



The University of
Nottingham

Department of Civil Engineering

**Hysteretic response of an innovative blind
bolted endplate connection to concrete
filled tubular columns**

by

ZHIYU WANG

Thesis submitted to the University of Nottingham for
the degree of Doctor of Philosophy

January 2012



IMAGING SERVICES NORTH

Boston Spa, Wetherby
West Yorkshire, LS23 7BQ
www.bl.uk

**MISSING PAGE/PAGES
HAVE NO CONTENT**



IMAGING SERVICES NORTH

Boston Spa, Wetherby
West Yorkshire, LS23 7BQ
www.bl.uk

**ORIGINAL COPY TIGHTLY
BOUND**



IMAGING SERVICES NORTH

Boston Spa, Wetherby
West Yorkshire, LS23 7BQ
www.bl.uk

BEST COPY AVAILABLE.

VARIABLE PRINT QUALITY

ABSTRACT

Concrete filled steel tubular (CFT) columns can employ the advantages of both materials: steel and concrete. Connection to such columns, however, is problematic. This is especially so if the required connection is both bolted and moment-resisting.

To address this issue, a novel blind-bolted and moment-resisting connection to CFT column has been developed. This connection uses an innovative blind-bolt, introduced in previous research at the University of Nottingham and is termed the Extended Hollobolt (EHB). The EHB has been developed to provide sufficient tensile resistance and stiffness for the connection to develop resistance to moment. Previous research work has studied the performance of this connection under monotonic loading. The performance of such connection under cyclic loading, however, is not yet investigated. The work presented in this thesis addresses this gap in knowledge.

This thesis reports on a series of full scale testing of joints consisting of beam endplates connected to CFT columns using this blind bolt. The test connections were constructed with relatively thick endplate so as to isolate the CFT column and the blind bolt as the relatively weak elements in the connection system. This study focuses on the behaviour of the connections with principal failure modes attributed by the blind bolt and the CFT column.

The experiments were conducted to obtain insights into the hysteretic moment-rotation relationship, available ductility & energy dissipation capacity, observe typical failure modes, and develop relevant understandings of the

Extended Hollobolt-endplate connection subjected to cyclic loading. The selected connection details were chosen to examine the influential parameters of the joint hysteretic moment-rotation behaviour.

From the experimental results, two representative failure modes, bolt fracture and column face bending failure, were observed and categorized in relation to the connection configuration. The connection behaviour are described and compared with respect to the influences of bolt grade, cyclic loading procedure, tube wall thickness and concrete grade.

Based on the experimental hysteretic moment-rotation relationships, an evaluation of the cyclic characteristics and an analysis of the cumulative damage were carried out for the two representative connection categories. The joint hysteretic moment-rotation response was assessed in term of degradations of strength, stiffness, ductility, and energy dissipation. The use of damage levels and stages in the interpretation of damage evolutions for the connection behaviour is also described in this thesis. The findings of cumulative damage analysis suggest that the energy based cumulative damage index outweighs the other indices in characterizing the progressive damage process of the connections in this study. This is especially the case for those related to hysteresis loops at repeated cycles of each loading amplitude.

Following the experimental study, 3D nonlinear finite element models of the connections were developed to analyse the mechanical response of the connection. The comparison of the numerical and experimental moment-rotation envelope curve is discussed with respect to related geometric and material parameters. The connection failure modes and displacement

distributions were further examined as a supplement to the experimental findings that were necessarily limited by instrumentations.

This work also presents mathematical models for the hysteretic moment-rotation relationships simulating the loading, unloading and reloading segments of the hysteresis loops. Characterizing parameters were introduced to allow for the softening slope, linear segment slope, and degradations of strength and energy dissipation.

This study concluded that the proposed finite element model simulates well the behaviour of the connection with good prediction of the moment-rotation envelope curves and of the failure mode. It is also concluded that the proposed mathematical models define well the non-linear loading and unloading paths with reasonable accuracy. It is finally claimed that the Extended-Hollobolt endplate connection provides a stable improvement in strength and stiffness under cyclic loading compared with other similar connections.

LISTS OF CONTENTS

ABSTRACT.....	ii
LISTS OF CONTENTS.....	vi
LISTS OF TABLES.....	xii
LISTS OF FIGURES.....	xiii
NOTATIONS.....	xx
ABBREVIATIONS.....	xxiii
TRADEMARKS.....	xxii
ACKNOWLEDGEMENT.....	xxiii
DECLARATION.....	xxiv
CHAPTER 1.....	1
1.1 BACKGROUND.....	1
1.2 JUSTIFICATION FOR THIS RESEARCH.....	5
1.3 RESEARCH QUESTIONS.....	9
1.4 RESEARCH AIM AND OBJECTIVES.....	10
1.5 RESEARCH METHODOLOGIES.....	10
1.6 OUTLINE OF CONTENTS.....	11
CHAPTER 2.....	15
2.1 INTRODUCTION.....	15
2.2 PREVIOUS STUDIES ON TENSILE BEHAVIOUR OF BLIND BOLTED CONNECTIONS.....	15
2.3 PREVIOUS STUDIES ON MONOTONIC BEHAVIOUR OF BLIND BOLTED BEAM TO COLUMN MOMENT CONNECTIONS.....	28

2.4	PREVIOUS STUDIES ON CYCLIC BEHAVIOUR OF BOLTED ENDPLATE BEAM TO COLUMN CONNECTIONS.....	39
2.5	PREVIOUS NUMERICAL STUDIES OF BLIND BOLTED CONNECTIONS	55
2.6	PREVIOUS ANALYTICAL MODEL STUDIES OF BEAM-TO-COLUMN JOINTS 56	
2.7	CONCLUSION AND NEEDS FOR FURTHER RESEARCH	58
CHAPTER 3		62
3.1	INTRODUCTION	62
3.2	TESTING PROGRAM	63
3.2.1	<i>Connection details</i>	63
3.2.2	<i>Material properties</i>	67
3.2.3	<i>Fabrication of test specimens</i>	71
3.2.4	<i>Test set-up</i>	73
3.2.5	<i>Instrumentation</i>	79
3.2.6	<i>Quasi-static cyclic loading procedure and control system</i>	88
3.3	MEASUREMENT OF JOINT ROTATION AND MOMENT.....	91
3.3.1	<i>Joint rotation measurement</i>	91
3.3.2	<i>Joint moment measurement</i>	93
3.4	DETERMINATION OF YIELD POINT FROM FORCE-DISPLACEMENT CURVES	96
3.5	CONCLUDING REMARKS	99
CHAPTER 4		100
4.1	INTRODUCTION	100
4.2	FAILURE MODES.....	100
4.3	HYSTERETIC MOMENT-ROTATION RELATIONSHIPS.....	114

4.3.1	<i>General moment-rotation behaviour</i>	114
4.3.2	<i>Effect of blind bolt grade</i>	123
4.3.3	<i>Effect of cyclic loading procedure</i>	124
4.3.4	<i>Effect of tube wall thickness</i>	125
4.3.5	<i>Effect of concrete grade</i>	126
4.4	STRAIN PROFILES OF RELEVANT CONNECTION COMPONENTS	127
4.4.1	<i>Strain profile of steel beam and endplate</i>	128
4.4.2	<i>Strain profile of tube sidewall face and connecting face</i>	133
4.4.3	<i>Strain profile of blind bolt</i>	138
4.5	CONCLUDING REMARKS	140
CHAPTER 5	142
5.1	INTRODUCTION	142
5.2	CYCLIC CHARACTERIZING PARAMETER ANALYSIS	143
5.2.1	<i>Resistance ratio</i>	145
5.2.2	<i>Energy dissipation ratio</i>	148
5.2.3	<i>Stiffness deterioration ratio</i>	150
5.3	ASSESSMENT OF CONNECTION DUCTILITY	152
5.4	CUMULATIVE DAMAGE MODEL ANALYSIS	154
5.4.1	<i>Basic procedures in the definition of damage model</i>	154
5.4.2	<i>Damage indices</i>	158
5.4.3	<i>Damage model analysis of experimental results</i>	166
5.5	CONCLUDING REMARKS	179
CHAPTER 6	182
6.1	INTRODUCTION	182
6.2	GENERAL DESCRIPTION OF FINITE ELEMENT MODEL	184

6.2.1	<i>Element type</i>	184
6.2.2	<i>Concrete failure criteria and modelling</i>	190
6.2.3	<i>Material model</i>	193
6.2.4	<i>Boundary condition and modelling techniques</i>	197
6.2.5	<i>Finite element model illustration</i>	199
6.2.6	<i>Loading condition and solution</i>	204
6.3	FINITE ELEMENT ANALYSIS RESULTS	206
6.3.1	<i>Blind bolt preload</i>	207
6.3.2	<i>Stress distribution and failure modes identification</i>	209
6.3.3	<i>Comparison of strain results</i>	219
6.3.4	<i>Comparison of moment-rotation curves</i>	223
6.3.5	<i>Comparison of tube deformation results</i>	228
6.3.6	<i>Summary of FE modelling results</i>	235
6.4	PARAMETER VARIATION ANALYSES	235
6.4.1	<i>Influence of concrete grade</i>	236
6.4.2	<i>Influence of tube wall thickness</i>	238
6.4.3	<i>Discussion on combined influence of concrete grade and tube wall thickness</i>	239
6.5	CONCLUDING REMARKS	241
CHAPTER 7		244
7.1	INTRODUCTION	244
7.2	MATHEMATICAL REPRESENTATIONS OF MOMENT-ROTATION ENVELOPE	245
7.2.1	<i>Eurocode 3 based trilinear representation</i>	246
7.2.2	<i>Power representation</i>	248

7.2.3	<i>Exponential representation</i>	251
7.3	RELATED MATERIAL CYCLIC MODELS FOR CONNECTION COMPONENTS	253
7.4	DEVELOPMENT OF HYSTERETIC MOMENT-ROTATION MODEL	255
7.4.1	<i>Basic envelope curve</i>	255
7.4.2	<i>Hysteretic moment-rotation models</i>	256
7.5	VALIDATION OF PROPOSED HYSTERETIC MOMENT-ROTATION MODEL	273
7.6	CONCLUDING REMARKS	277
CHAPTER 8	280
8.1	CONCLUSIONS FROM CURRENT RESEARCH PROGRAMME	280
8.2	RECOMMENDATIONS AND FUTURE WORK.....	284
REFERENCES	288
PUBLICATIONS	304
APPENDIX A	Rotation measurements in reported cyclic loading tests.....	306
APPENDIX B	Bolt shank tensile test.....	311
APPENDIX C	General yield and failure criteria for finite element analysis	312
APPENDIX D	Cyclic material models of steel and concrete.....	318
D1.	MATERIAL CYCLIC MODEL OF STEEL	318
D2.	MATERIAL CYCLIC MODEL OF CONCRETE.....	320

LISTS OF TABLES

Table 1.1 Classification of connection components in terms of ductility and dissipative capacity (Faella et al, 2000).....	8
Table 2.1 Typical blind fasteners (Corus Tubes library, 2005)	16
Table 2.2 Representative experimental studies on blind bolted T-stub connection subjected to tensile loading.....	19
Table 2.3 Representative experimental studies on blind bolted beam to column moment connections subjected to monotonic loading.....	29
Table 2.4 Representative experimental studies on bolted endplate moment connections subjected to cyclic loading.....	42
Table 2.5 Representative experimental studies on bolted endplate moment connections subjected to low cyclic fatigue loading.....	52
Table 3.1 Details of the test connections.....	65
Table 3.2 Details of SHS and beam section.....	66
Table 3.3 Geometric details of a sample M16 Extended Hollobolt.....	67
Table 3.4 Material properties of connection components.....	69
Table 3.5 Concrete mixture proportions and curing condition.....	71
Table 3.6 Concrete infill compressive strengths (N/mm ²).....	71
Table 3.7 Summary of electrical resistance strain gauges used in the tests....	81
Table 3.8 Summary of representative yield point determination methods.....	96
Table 4.1 Connection categories, test failure modes and yield rotation & moment.....	117
Table 4.2 Test moment & rotation at maximum moment & peak rotation...	117
Table 4.3 Test initial and secant stiffnesses.....	118
Table 5.1 Summary of cyclic characterizing parameter expressions.....	145
Table 5.2 Classification of damage level and related index (Park <i>et al.</i> 1985).	157
Table 5.3 Observed damage stages for connection category I (weak blind bolt & strong CFT column).	173
Table 5.4 Observed damage stages for connection category II (strong blind bolt & weak CFT column)	174
Table 6.1 Comparison of experimental and numerical maximum moment...	223

Table 6.2 Comparison of experimental and numerical initial stiffness.....	224
Table 6.3 Ratios of experimental and numerical results.....	224
Table 6.4 Model limitations.....	243
Table 7.1 Parameters for mathematical representations.....	250
Table 7.2 Summary of test calibration parameters.....	274

LISTS OF FIGURES

Figure 1.1 Components of an Extended Hollobolt.....	3
Figure 2.1 Representative tensile test of blind bolted (Lindapter Hollobolt) T-stub assembly (Barnett, 2001).....	19
Figure 2.2 Representative tensile test of blind bolted (Lindapter Hollobolt) T-stub to SHS column without concrete infill (Barnett, 2001).....	20
Figure 2.3 Representative tensile and compression test of blind bolted (Ajax One-side) T-stub to SHS column without concrete infill (Lee <i>et al</i> , 2010)....	22
Figure 2.4 Representative tensile test of blind bolted (Standard bolt, Lindapter Hollobolt, Extended Hollobolt) T-stub to CFT column (Ellison & Tizani, 2004)	23
Figure 2.5 Load-displacement relationship of tensile pull-out tests (Ellison & Tizani, 2004)	23
Figure 2.6 Representative tensile test of blind bolted (Ajax One-side with cogged extensions) T-stub to CFT column (Gardner and Goldsworthy, 2006)	25
Figure 2.7 Cyclic loading history used in Gardner & Goldsworthy's test (2005)	25
Figure 2.8 Representative tensile test of blind bolted (Ajax One-side with cogged extensions) T-stub to CFT column (Yao <i>et al</i> , 2008).....	28
Figure 2.9 Representative test of blind-bolted (Lindapter Hollobolt) beam-to-column moment connections under monotonic loading (Loh <i>et al</i> , 2006).....	32
Figure 2.10 Representative test set-up for blind-bolted (Lindapter Hollobolt) beam-to-column moment connections under monotonic loading (Wang <i>et al</i> , 2009)	33
Figure 2.11 Representative test of blind-bolted (Extended Hollobolt) beam-to-column moment connections under monotonic loading (Al-Mughairi, 2009)	35
Figure 2.12 Representative test of blind-bolted (Lindapter Hollobolt) beam-to-column angle connections under monotonic loading (Elghazouli <i>et al</i> , 2009)	38
Figure 2.13 Representative test of blind-bolted (Ajax One-side) beam-to-column moment connections under monotonic loading (Lee <i>et al</i> , 2011).....	38
Figure 2.14 Representative test of bolted (standard bolt) endplate beam to column connections under cyclic loading (Nogueiro <i>et al</i> , 2006).....	50

Figure 2.15 Representative test of bolted (standard bolt) endplate beam to column connections under cyclic loading (Shi et al, 2007).....	50
Figure 2.16 Cyclic loading histories for cyclic loading and low-cycle fatigue tests (Note: references are given in text)	53
Figure 3.1 Illustration of joint configuration and loading arrangement.....	63
Figure 3.2 Illustration of blind bolt tightening sequences.....	72
Figure 3.3 Tightened blind bolts in SHS column.....	72
Figure 3.4 Illustration of a representative test set-up.....	75
Figure 3.5 Photograph of a representative test set-up.....	76
Figure 3.6 Photograph of loading arrangement.....	78
Figure 3.7 Illustration of reaction buttress designed for actuator.....	78
Figure 3.8 Illustration of representative test instrumentations.....	80
Figure 3.9 Representative strain gauged blind bolt before tightening.....	81
Figure 3.10 Photograph of strain gauge pattern on tube connecting face.....	84
Figure 3.11 Photograph of strain gauge pattern on tube sidewall face.....	84
Figure 3.12 Photograph of potentiometer arrangement on tube connecting face.....	85
Figure 3.13 Photograph of LVDT arrangement on steel beam.....	85
Figure 3.14 Calibration of the load cell fitted into actuator.....	87
Figure 3.15 Data logger and computer link system.....	87
Figure 3.16 Illustration of cyclic loading procedures.....	89
Figure 3.17 Display of Servocon loading controller.....	90
Figure 3.18 Schematic graph of joint rotation relationships.....	93
Figure 3.19 Illustration of geometric relationship of linkage system and steel beam.....	94
Figure 3.20 Illustration of force transfer relationship of linkage system and steel beam.....	95
Figure 3.21 Illustration of representative yield point determination methods.....	98
Figure 4.1 Representative deformation mode of connection category I.....	102
Figure 4.2 Representative deformation mode of connection category II.....	103

Figure 4.3 Bolt shank failure mode.....	104
Figure 4.4 Representative yielding propagation on CFT column faces for connection category I.....	105
Figure 4.5 Representative yielding propagation on tube for connection category II (Specimen: BBEC-5-8.8-50-LII)	106
Figure 4.6 Representative yielding propagation on tube for connection category II (Specimen: BBEC-6.3-8.8-25-LII)	107
Figure 4.7 Representative failure mode of concrete infill after stripping away local tube faces (Specimen: BBEC-6.3-8.8-50-LII).....	108
Figure 4.8 Representative failure mode of concrete infill after stripping away local tube faces (Specimen: BBEC-6.3-8.8-25-LII).....	109
Figure 4.9 Photograph series for joint response of specimen BBEC-8-10.9-50-LI (connection category I)	112
Figure 4.10 Photograph series for joint response of specimen BBEC-5-8.8-50-LII (connection category II)	113
Figure 4.11 Comparison of calculated moments based on the LVDT measurement and theoretical prediction.....	115
Figure 4.12 Comparison of moment-rotation relationships of specimen BBEC-6.3-8.8-25-LII based on the measurement of LVDT-DB1 and DB2.....	116
Figure 4.13 Hysteretic moment-rotation curves for test specimens.....	121
Figure 4.14 Comparison of hysteretic moment-rotation relationships of specimens BBEC-8-8.8-50-LI and BBEC-8-10.9-50-LI.....	123
Figure 4.15 Comparison of hysteretic moment-rotation relationships of specimens BBEC-8-10.9-50-LI and BBEC-8-10.9-50-LII.....	124
Figure 4.16 Comparison of hysteretic moment-rotation relationships of specimens BBEC-5-8.8-50-LII, BBEC-6.3-8.8-50-LII and BBEC-8-8.8-50-LI.....	125
Figure 4.17 Comparison of hysteretic moment-rotation relationships of specimens BBEC-6.3-8.8-25-LII and BBEC-6.3-8.8-50-LII.....	126
Figure 4.18 Representative beam & endplate strain profile of BBEC-6.3-8.8-50-LII (connection category I)	129
Figure 4.19 Representative beam & endplate strain profile of BBEC-6.3-8.8-25-LII (connection category II)	132
Figure 4.20 Representative tube strain profile of BBEC-8-10.9-50-LI (connection category I)	135

Figure 4.21 Representative tube strain profile of BBEC-5-8.8-50-LII (connection category II)	136
Figure 4.22 Representative bolt strain profile of BBEC-8-10.9-50-LI (connection category I)	139
Figure 4.23 Representative bolt strain profile of BBEC-5-8.8-50-LII (connection category II)	140
Figure 5.1 Basic parameters of an idealized hysteretic cycle (ATC-24, 1992; ECCS, 1986)	144
Figure 5.2 Relationships of resistance ratio versus partial ductility ratio.....	147
Figure 5.3 Relationships of energy dissipation ratio versus partial ductility ratio for connection category I.....	148
Figure 5.4 Relationships of energy dissipation ratio versus partial ductility ratio for connection category II.....	149
Figure 5.5 Relationships of stiffness degradation ratio versus partial ductility ratio.....	151
Figure 5.6 An example of comparing ductility classified indices versus test hysteretic moment-rotation relationships.....	153
Figure 5.7 Relationship of damage index and damage parameter.....	155
Figure 5.8 Illustration of <i>PHC</i> and <i>FHC</i> in Kraetzig damage index.....	163
Figure 5.9 Damage model evaluations for specimen BBEC-8-8.8-50-LI.....	168
Figure 5.10 Damage model evaluations for specimen BBEC-8-10.9-50-LI..	168
Figure 5.11 Damage model evaluations for specimen BBEC-5-8.8-50-LII..	171
Figure 5.12 Damage model evaluations for specimen BBEC-6.3-8.8-25-LII.....	171
Figure 5.13 Comparison of observed damage stages and Park & Ang damage levels for connection category I.....	176
Figure 5.14 Comparison of observed damage stages and Park & Ang damage levels for connection category II.....	177
Figure 5.15 Comparisons of damage index ratio versus partial ductility ratio relationships.....	179
Figure 6.1 Typical procedure for finite element analysis.....	183
Figure 6.2 Schematic of SHELL181 (ANSYS@Academic Research, 2009)	185
Figure 6.3 Schematic of SOLID65 (ANSYS@Academic Research, 2009)..	186

Figure 6.4 Schematic of SOLID185 (ANSYS@Academic Research, 2009)	187
Figure 6.5 Schematic of BEAM188 (ANSYS@Academic Research, 2009)	188
Figure 6.6 Schematic of contact pair (ANSYS@Academic Research, 2009)	188
Figure 6.7 Schematic of PRETS179 (ANSYS@Academic Research, 2009) and preload action in blind bolted connection	190
Figure 6.8 Concrete cracking condition adopted in ANSYS (ANSYS@Academic Research, 2009)	191
Figure 6.9 Failure surface in principal stress space in nearly biaxial stress state (ANSYS@Academic Research, 2009)	193
Figure 6.10 Actual and true stress-strain relationship for tubular columns	195
Figure 6.11 Actual and true stress-strain relationship for beam and endplate (Al-Mughairi, 2009)	195
Figure 6.12 Actual and true stress-strain relationship for blind bolts (Al-Mughairi, 2009)	195
Figure 6.13 Stress-strain relationship of concrete with varying grades	197
Figure 6.14 Typical finite element meshes for blind bolt assembly	200
Figure 6.15 Typical finite element model with partitioned components	202
Figure 6.16 Finite element models of blind bolts anchored in concrete infill	203
Figure 6.17 Stress contours of tube connecting face, endplate and blind bolt (bolt preload phase)	208
Figure 6.18 Strain contours of overall connection and concrete infill (bolt preload phase)	208
Figure 6.19 Comparison of strains obtained from experiments, finite element analysis and literature report (Al-Mughairi, 2009)	209
Figure 6.20 Von Mises stress contours of test connections	212
Figure 6.21 Von Mises stress contours of blind bolts	213
Figure 6.22 Von Mises stress contours of tube sidewall and connecting faces	217
Figure 6.23 Von Mises stress contours of concrete infill	218
Figure 6.24 Comparison of experimental and numerical moment versus strain curves for tube connecting face of specimen BBEC-8-10.9-50-LI	220

Figure 6.25 Comparison of experimental and numerical moment-strain curves for blind bolts.....	222
Figure 6.26 Sensitivity analysis- No. elements of tube wall (T) & concrete (C)	224
Figure 6.27 Comparison of test and numerical moment-rotation curves.....	226
Figure 6.28 Illustration of representative path at the first bolt row.....	229
Figure 6.29 Comparison of tube UX displacements along assigned path at the first bolt row.....	230
Figure 6.30 Comparison of maximum deformation of tube connecting face at the first bolt row.....	232
Figure 6.31 Comparison of tube UX displacement along assigned path at the first bolt row.....	234
Figure 6.32 Comparison of numerical results for varying concrete grades...	237
Figure 6.33 Comparison of numerical results for varying tube wall thickness.....	238
Figure 6.34 Numerical results of maximum moment capacity with varying tube wall thickness and concrete strength.....	240
Figure 6.35 Comparison of monotonic moment-rotation relationships of similar connections with varying tube wall thickness (Al-Mughairi, 2009)..	241
Figure 7.1 Trilinear representation of moment-rotation curve suggested by Eurocode 3 (2005)	247
Figure 7.2 Comparison of trilinear representations and test envelope curves (Test No.1 & No.4)	248
Figure 7.3 Illustration of representative moment-rotation curves.....	249
Figure 7.4 Comparison of power representations and test envelope curves (Test No.1 & No.4).....	250
Figure 7.5 Comparison of finite element model based power representations for the curve with or without softening branch (Test No.4).....	251
Figure 7.6 Comparison of representative exponential representations and test envelope curves (Test No.1 & No.4)	252
Figure 7.7 Comparison of exponential representations for the curve with or without descending branch (Test No.4)	253
Figure 7.8 Illustration of linear assembling method of connection components.....	254
Figure 7.9 Envelope curves for hysteretic moment-rotation models.....	255

Figure 7.10 Hysteretic moment-rotation model for the connection category I.....260

Figure 7.11 Strength degradation ratio and energy degradation ratio versus partial ductility ratio for the connection category I (Note: test data are obtained from related experiments)263

Figure 7.12 Hysteretic moment-rotation model for the connection category II.....267

Figure 7.13 Relation between $K_{0,i}$ and μ'_i for the connection category II.....269

Figure 7.14 Strength degradation ratio and energy degradation ratio versus partial ductility ratio for the connection category II.....270

Figure 7.15 Hysteretic moment-rotation experimental and numerical curves for the connection category I.....275

Figure 7.16 Hysteretic moment-rotation experimental and numerical curves for the connection category II.....276

NOTATIONS

Special symbols adopted are not summarized below, but their explanations are included in the text

δ_y	yielding displacement
δ_c	calculated displacement value for damage index
δ_i	plastic deformation
δ_{it}, δ_{uc}	threshold displacement value and critical displacement value of basic damage parameters
δ_M	maximum response deformation
F_y	joint yielding force
θ_y	joint yielding rotation
θ_j	joint rotation
θ_o	overall rotation
θ_b	beam deformation
θ_c	column rotation
θ_{xd} & θ_{cd}	rotation corresponding to the moment first reaching maximum load level and final part of the curve ends respectively
θ_{ru}	reloading rotation at loading stage 2
$\theta_{ec,i}$	rotation corresponding to the point on the envelope curve
$\theta_{ul,i}$	Rotation for this linear segment
ξ	calibration parameter suggested in Eurocode 3
$\lambda_{s,h}$	strain hardening coefficient for hardening modulus
$\theta_{o,i}^+ \text{ \& } \theta_{o,i}^-$	Rotation at beginning of excursion i^+ & i^-
$(\Delta\theta_p)_{i^+}, (\Delta\theta_p)_{i^-}$	Un-deteriorated plastic deformation range of excursion i^+ & i^-
$(\Delta\theta_{pm})_{i^+}, (\Delta\theta_{pm})_{i^-}$	Measured plastic rotation range of excursion i^+ & i^-
$(\Delta\theta_t)_{i^+}, (\Delta\theta_t)_{i^-}$	Total rotation range for excursion i^+ & i^-
A_w	area of the beam web
A	strength constant for cyclic model of bolt in tension
L_b	distance along the beam from the column flange face to loading point
δ_{ac}	horizontal movement of the hydraulic actuator
T	horizontal force from hydraulic actuator.
F_n	Linkage transferred force normal to beam flange
F_t	Linkage transferred force tangent to beam flange
F_l	Linkage axial force
$F_{Rd,b}$ & $\delta_{Rd,b}$	design resistance and its associated displacement for bolt
$F_{Rd,c}$	design resistance of the CFT column faces
f_t	ultimate uniaxial tensile strength
f_c	uniaxial compressive strength
f_l	ultimate compressive strength for a state of biaxial compression superimposed on hydrostatic stress state

C	experimental constant in general fatigue based linear cumulative damage index
E_i	energy dissipated at i th cycle
$E_{pi}^{+/-}$ & $E_{fi}^{+/-}$	energy dissipated in primary cycles and follower cycles respectively
$E_{s,b}$	Young's modulus of the bolt material
$E_{s,c}$	initial tangent modulus of elasticity
dE	incremental absorbed hysteretic energy
E_c	elastic modulus of concrete
n_i	cycle number for damage model
n_{si}	number of cycles at the i -th displacement amplitude
N	shape factor for curve correlation
N_{fi}	average number of cycles to failure at the i -th displacement amplitude
N_c	scaling exponent controlling the smoothness of the transition of excursion branch
a, b	calibrating parameters for damage indices calculation
ϕ and c	angle of internal friction and cohesion respectively
β	calibrating parameter for cyclic loading
Δ_i & Δ_{fi}	displacement amplitudes corresponding to n_{si} and N_{fi} respectively
J_2	second invariants of the deviatoric stress tensor for yield criteria analysis
I_1	second invariants of the deviatoric stress tensor
$D_{(...)}$	damage indices described in Chapter IV
$\sigma_1, \sigma_2, \sigma_3$	principal stresses
$\sigma_x, \sigma_y, \sigma_z, \tau_{xy}, \tau_{xz}, \tau_{zy}$	stress tensor components
$\sigma_{xp}, \sigma_{yp}, \sigma_{zp}$	stresses on failure surface in principal stress space relating to concrete material model
σ_e	yield stress
σ_t & ϵ_t	true stress & strain
σ_{en} & ϵ_{en}	engineering stress & strain
σ_i	true stress & strain
σ_r^* & ϵ_r^*	residual stress and strain respectively
σ_y^t & σ_y^c	yield stresses for tension and compression loading respectively
ϵ_0	concrete strain corresponding to the peak compressive strength
ϵ_{cm} & ϵ_{20c}	unloading strain on the envelope curve and the strain at which stress drops to $0.2 f_c'$ respectively
μ_M & μ_u	ductility ratios corresponding to δ_M and δ_u respectively
μ_i	partial ductility ratio
$d\epsilon^{pl}$	plastic strain increment tensor
d_d & d_e	ductility component and energy component for damage indices
λ	plastic multiplier which defines the amount of plastic straining

λ_f	consecutive stiffness deterioration and energy dissipation reduction factor when ε is greater than ε_0
Q	function of stress termed the plastic potential which determines the direction of plastic straining
β_s	shear transfer coefficient in concrete material model
F	a function of the principal stress state (σ_{xp} , σ_{yp} , σ_{zp})
S	failure surface expressed in terms of principal stresses and five input parameters

ABBREVIATIONS

CFT	concrete filled steel tube (tubular)
AISC	American Institute of Steel Construction
ECCS	European Convention for Constructional Steelwork
FEMA	US Federal Emergency Management Agency
SHS	square hollow section
BBEC	blind bolted endplate connection
ND	nominal geometric details
AD	actual geometric details
LVDT	Linear Variable Differential Transformer
DCL	low ductility class
DCM	medium ductility class
DCH	high ductility class
PHC	primary half cycle
FHC	follower half cycle
FE1	finite element model with solid elements
FE2	finite element model with solid & beam elements

TRADEMARKS

Huck High Strength Blind Bolt (HSBB) and Huck Blind Oversized Mechanically Locked Bolt (BOM) are trademarks of Huck International, USA

Flowdrill is a trademarks of Flowdrill B.V, The Netherlands

Ajax One-side is a trademarks of Ajax Fasteners, Australia

Lindapter Hollobolt is a trademarks of Lindapter International, UK

ACKNOWLEDGEMENT

First I would like to thank my supervisor, Dr. Walid Tizani, for his thoughtful guidance, patience, and constructive criticism throughout the course of this study. I would also like to acknowledge helpful suggestions provided by Dr. John Owen, and Dr. Iman Hajirasouliha for experimental work and Prof. Carlo Sansour for numerical modelling.

There are some special thanks extended to the technical staff who helped in the development of the project, notably Mr. Gordon Hardy who helped with coordination for the fabrication of reaction buttress and debugging testing equipments, Mr. James Bellis and Mr. Bal Loyla who constructed the test rig and installed instrumentations for the experimental work. Also, sincere gratitude is extended to, Mr. Michael Langford, Mr. Nigel Rook, Mr. Damien Goy, and Mr. Andrew Maddison, for their general assistance.

This research work is supported with resources from Tata Steel (formally Corus) and Lindapter International. The helpful advice and support of Mr Trevor Mustard and Mr Andrew Orton of Tata Steel and of Mr Neil Gill of Lindapter are gratefully acknowledged.

Financial support from 'UK/China Scholarship for Excellence' programme that sponsored me for this project is gratefully acknowledged. I would also like to thank Prof. Qingyuan Wang of Sichuan University for his support.

My deepest appreciation and love are extended to my family members for their kind concern and warm encouragement.

DECLARATION

I declare that, except where cited in the text, all work contained within this thesis is my own original work, under the direction of my supervisors and the industrial sponsors. The work presented herein was performed at the University of Nottingham between September 2008 and January 2012. This thesis has not been submitted to any institution other than the University of Nottingham for the degree of Doctor of Philosophy.

CHAPTER 1

INTRODUCTION

1.1 Background

In this research, there are three related structural engineering issues: the use of concrete filled steel tubular (CFT) columns, the use of blind bolts for moment resisting beam to column connection system under monotonic and cyclic loading conditions. A brief description of these three issues will be presented below.

In the building industry, steel moment resisting frames (also called moment frames) are gaining popularity for the clear span and architectural freedom they provide. The open section and closed section columns are mostly used in the frame system. The use of circular and rectangular hollow sections as typical closed sections has attracted more attentions in recent years due to high strength to weight ratio and lower fire protecting costs (AISC Steel Construction Manual, 2005). The concrete infill into the closed section columns as CFT columns greatly enhances the load carrying capacity as compared with bare steel columns. The merits of steel and concrete are favourably employed as the concrete infill effectively prevents local buckling of the steel hollow section tube and the confinement of the hollow section tube. The available stiffness and compressive strength of the concrete are also improved. Moreover, the material costs of composite sections will be reduced through the use of reduced column size. Additionally, the presence of the concrete infill acts as a heat sink enhancing the fire resistance of the composite

section. Hence, the CFT columns combine the advantages of the ductility of steel hollow section tube and the compressive strength of concrete infill. In steel moment resisting frames, CFT columns have been considered in design as vertical structural elements with a high strength to weight ratio. The excellent monotonic resistance of CFT column under biaxial bending and axial force has been recognized in reported experimental studies (Tsai *et al*, 2003).

The beam to column connections in steel moment resisting frames tend to introduce welding and bolting configurations, favoured by industry and academia in different regions. With regard to the moment resisting frames with open section column, most American and Japanese investigations were concerned about the welded connections (AISC Steel Construction Manual, 2005), while the typical European practices prefer shop welding and on site bolting to site welding so as to avoid welding errors and minimize labour costs. The good practice of bolted connection in the construction with open section columns has encountered a problem in extending its further use to hollow section columns due to the lack of free access, unless the connections are located in the vicinity of the open end of a closed section member. This problem was well recognized in the late 1990s. As a solution, blind bolts have been developed to be used in applications where access for installation is from one side of the connection only, as in the case of connecting the endplate of a beam to a hollow section (Tabsh *et al*, 1997; Barnett, 2001).

More recently, an innovative blind bolt have been developed on the basis of the Lindapter Hollobolt at the University of Nottingham (Tizani & Ridley-Ellis, 2003). The configuration of this blind bolt is featured by extended bolt

shank and an anchorage in concrete infill, which is also labelled as 'Extended Hollobolt', as shown in Figure 1.1. It was intended to provide sufficient tensile resistance and stiffness for such connection to CFT column and allow its use for moment resisting connections. This blind bolt is used in the connection system studied in this thesis.

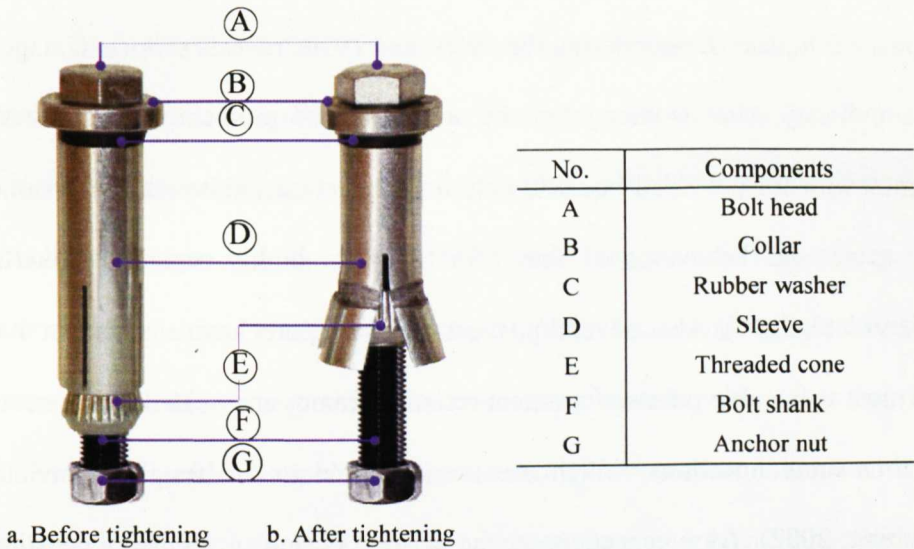


Figure 1.1 Components of an Extended Hollobolt

The beam-to-column connections are known as one of the most important structural elements in a building construction system due to the fact that the reliability and efficiency of the connections have great influence not only on the structural components but also on the behaviour of the whole structure. The steel moment resisting frames have advantages of good ductility and been regarded as a type of ideal structures for construction in seismic regions. Related evidences are available in recent design codes. The moment resisting steel frames in Eurocode 8 (2003) are designed with the largest behaviour factor which leads to lowest seismic design loads. As suggested by the code of

AISC (2005), the structural elements of steel moment resisting frames are required to exhibit sufficient resistance against lateral load, with expected plastic hinges development at critical sections. The corresponding connection details are designed to move the plastic hinge on the beam a short distance away from the beam-to-column connection.

A post earthquake survey during the 1980s and 1990s reveals serious damages of previously what is thought to be well-designed moment resisting steel frames with fully welded beam to column connections, although the seismic resistance and behaviour of these frames were highly regarded hitherto (Mazzolani, 2000). Also, several post earthquake reports have also shown that the most vulnerable points of moment resisting frames are welded components in moment connections, which are unsusceptible to the fragile behaviour (Dubina, 2002). As a consequence, the seismic design of moments resisting connections have been adjusted and updated to reduce structural seismic damages. Following the Northridge (1994) and Kobe (1995) earthquakes, an issue in the code of AISC (2005) is the introduction of pre-qualified moment connections in the design of moments resisting steel frames as to avoid beam-to-column connections becoming vulnerable points under cyclic loading. With regard to the concern of structural energy dissipation, the concept of dissipated structure has been introduced into Eurocode 8 (2003) to take into account the inelastic material behaviour in predefined zones. As a solution for the poor seismic performance of flange-welded moment connections (previously widely used in America), endplate moment connections have been regarded as an alternative connection of interests to engineers and researchers. Since the

late 1990s, attempts have been made by US Federal Emergency Management Agency (FEMA355E) to develop a database of behaviour curves and design guides for bolted endplate connection (Mahin *et al*, 2002).

The excellent performance of CFT columns in moment resisting frames under cyclic loading has been tested and confirmed by researchers (Beutel *et al*, 2002; Tsai *et al*, 2003). Most moment resisting connections to CFT columns refer to typical configurations of welded connections with internal and external diaphragm plates so as to transfer the cyclic loads from the girders directly to the tube wall or to the tube wall and concrete core simultaneously, as documented in a CIDECT publication (2004). To extend the use of blind bolts for moment resisting connections, there are recent investigations reported referring to extended endplate connections to hollow section column without concrete infill (Lee *et al*, 2010) and extended/flush endplate connections to CFT column (Wang & Han, 2009; Al-Mughairi, 2009). It is not possible, however, to comment further on the behaviour of these connections subjected to cyclic loading as there are limited reports available in the literature.

1.2 Justification for this research

This study attempts to investigate the cyclic behaviour of an innovative blind bolted endplate connection to CFT column by focusing on the constituent components of the blind bolt and the CFT column. The practical relevance will be the understanding of such connection under cyclic loading as a basis for seismic design.

The application of bolted simple beam to hollow section column connections has been documented in design book published by the Steel Construction Institute & the British Constructional Steelwork Association Limited (2005) and Corus Tube Library Publication (2009). The simple connections using blind bolts have already been used in design to resist and transmit shear and axial loads in beams. With regard to their use in moment resisting connections, there are limited reports about their related behaviours. As a part of a series of investigations on this innovative blind bolted endplate connection to CFT column, the present study was based on a thorough review of previous work related to the monotonic behaviour of the connection. This provides a basic understanding of the connection in this study and experimental plan reported here. In this study, the blind bolts are connected with a flush endplate constituting a typical flush endplate connection. The flush endplate connections are widely used in the UK for their ease in construction. The moment resisting behaviour of this innovative blind bolted endplate connection to CFT column has been investigated monotonically in previous research (Al-Mughairi, 2009) in which the connection is classified as rigid or semi-rigid based on Bjorhovde's classification. As a follow-up study, a similar geometric configuration of the connection was adopted in the present experiment. The failure mode of this innovative blind bolt in tension is firstly highlighted in this study.

As mentioned earlier, the pre-qualified moment connections are required by AISC (2005) in the design of moments resisting steel frames. This philosophy is based on the viewpoint that the behaviour of connections under severe

cyclic loading cannot be reliably predicted by analytical means alone. The laboratory testing of the connections under cyclic loads is further needed to evaluate the performance of the connections for seismic design. This point justifies the significance of the use of quasi-static cyclic loading test in this study for the cyclic behaviour of this innovative blind bolted endplate connection to CFT column.

By assembling the contributions of individual components the recognized component method (Jaspart *et al*, 1995) provides a practicable simplified mechanical model representing the characteristics of bolted connections. Based on characterizing force-deformation curves, the component method can be further introduced for the evaluation of the ductility of each component, which may be classified into three main groups: high ductility, limited ductility, and brittle (Simões da Silva L *et al*, 2000). The cyclic behaviour of the connection is determined by the constituent components performed plastically. The dissipative and non-dissipative components are usually distinguished for further assessment (Faella *et al*, 2000).

The components of a traditional bolted endplate connection to open section (I or H section) column are classified in terms of ductility group and dissipative capacity, as indicated in Table 1.1. With regard to ductile and dissipative components, it can be seen that they almost related to the plate elements where plastic yielding occurs. In order to develop an understanding of the ductile behaviour of this innovative blind bolted endplate connection to CFT column, it was felt that it is necessary to incorporate similar evidences into consideration. It is noted that the components of endplate and CFT column

connecting face may similarly contribute to the ductile behaviour of the connection due to the flexibility of plate elements. The flexibility of endplate in bending is not the focus of this study as considerable research work have been reported regarding the issue in the literature (e.g. Adey, *et al*, 2000). Instead, the test specimens were designed with relatively thick endplate so as to isolate the CFT column and the blind bolt as relatively weak elements in the connection system studied herein. On the other hand, this configuration can be used to provide practical evidence for an unlikely event study which is involved with over-strength beam and endplate but relatively weak connection to CFT column. It is worth exploring the cyclic behaviour of the connections under this aspect which can be further combined with the current codified design considerations of endplate and beam to give a good picture of the complexity of the connection system. Some more details will be given later.

Table 1.1 Classification of connection components in terms of ductility and dissipative capacity (Faella et al, 2000)

Connection components*	Ductility group	Dissipative capacity
Column flange in bending	High ductile	Dissipative
Endplate in bending		
Column web panel in shear	Limited ductile	Dissipative or Non dissipative**
Column web in tension		
Column web in compression		
Bolts in tension	Brittle	Non dissipative
Bolt in shear		
Welds fracture		

Note: The connection herein refers to a bolted endplate connection to open section column.

** Dissipative capacity of column web in compression also depends on local buckling

Due to complicated configuration of this innovative blind bolt and the connection system, finite element modelling is regarded in this study as a necessary supplement to experimental study. It provides not only more

evidences for local stress distribution but also moment-rotation response. For example, the bolt shank in tension is more prone to fracture at the section between the bolt head and threaded cone, where are difficult to access for instrumentation in physical test. In this case, finite element modelling can be used as an advantageous way to capture the stress distribution at this location and associate with moment-rotation relationship. Also, the powerful parametric study will enable a full understanding of the connection behaviour within a given range. The experimental study and finite element analysis in this study can be added together to the body of knowledge of understanding the cyclic characteristics of this innovative blind bolted endplate connection to CFT column.

1.3 Research questions

Although the behaviour of the standard bolted endplate connections under monotonic loading has been understood and applied to the study of blind bolted connections, it is not possible to comment further on the cyclic behaviour of this innovative blind bolted endplate connection to CFT column due to a significant gap of knowledge. As an attempt to provide basic understanding contributes to fill that gap, this research programme outlined in this thesis is intended to answer two fundamental questions:

- What are the cyclic characteristics of this innovative blind bolted endplate connection to CFT column?
- How can we simulate the hysteretic moment-rotation relationship of this innovative blind bolted endplate connection to CFT column and provide comments on main influencing parameters for the hysteretic behaviour of such connection?

1.4 Research aim and objectives

The intention of this research program is to test an innovative blind bolted endplate connection to CFT column under cyclic loading with the aims of obtaining insights into the hysteretic moment-rotation relationship, available ductility & energy dissipation capacity, observing typical failure modes, developing relevant understandings for the hysteretic behaviour of this connection.

The overall objectives of this research are highlighted as follows:

- To evaluate the hysteretic performance of the connection system in terms of strength & stiffness degradation, ductility and energy dissipation capacity.
- To examine the progressive damage evolution of the connection systems by introducing cumulative damage models.
- To develop a validated finite element model to trace the distinct local damage of the connection and undertake parametric study to allow for the dependence of connection behaviour on the relevant geometric and material variables.
- To establish a mathematical model for the prediction for the hysteretic moment-rotation relationship of the connections under cyclic loading.

1.5 Research methodologies

The objectives of this research will be achieved through following steps:

- Literature review to examine previous investigations in the related areas and comment further on the most beneficial aspects to direct the study.
- Full-scale experimental quasi-static cyclic loading test to get data of the moment & rotation capacities and failure modes of the connection for the

first objective of this study. The hysteretic moment-rotation relationship to be analysed for the second objective of this study, i.e. evaluate the cyclic characterizing parameters and the evolution of progressive damage during inelastic range of cyclic loading. The highlighted failure modes to be discussed covering the connection categories of strong blind bolt & weak CFT column and weak blind bolt & strong CFT column.

- 3D nonlinear finite element modelling to simulate the experimental response in further details which serve for the third objective of this study. The finite element model to be validated against the experimental moment-rotation envelope curves under positive and negative bending moments. Parametric study to investigate the main geometric and mechanical variables influencing the behaviour of this innovative blind bolted endplate connection to CFT column.
- Mathematical models to be developed and incorporated into the hysteretic moment-rotation models for the representation of hysteretic loops for the fourth objective of this study.

1.6 Outline of contents

This thesis consists of seven chapters including current chapter as the introduction. A brief description of these chapters is presented as follows.

Chapter 1: This chapter outlines research background, justification, research questions, research aims & objectives and research methodology.

Chapter 2: This chapter contains a literature review of three closely related topics, including the tensile behaviour of blind bolted connections, the

monotonic behaviour of blind bolted beam to column moment connections and the cyclic behaviour of bolted endplate beam to column connections. It includes current advances of experimental studies in these areas. As a conclusion remark of this chapter, the efforts needed for further understanding are highlighted for this innovative blind bolted endplate connection studied herein.

Chapter 3: This chapter presents the details of experiment in this study. It covers the objectives and design of the testing programme. The general configuration of tested specimens, material properties, test apparatus and instrumentation are presented. The quasi-static cyclic loading procedure is described with a brief overview of the yield point determination methods.

Chapter 4: This chapter presents the experimental results including failure modes, and hysteretic moment-rotation relationship. Using codified cyclic characterizing parameters, the cyclic characteristics of the connection system is evaluated in terms of ductility, energy dissipation, resistance and stiffness.

Chapter 5: This chapter demonstrates the use of cumulative damage models in evaluating the progressive damage modes of this innovative blind bolted endplate connection to CFT column. This analysis is presented based on the experimental data outlined in Chapter 4.

Chapter 6: This chapter describes 3D nonlinear finite element modelling of this innovative blind bolted endplate connection to CFT column. Related modelling theories and techniques are reviewed. Following the validation of finite element results with experimental data, the local damage of the

connection are further clarified based on the analysis of stress distribution which in turn provides further evidences for the failure modes indicated in Chapter 4 and Chapter 5. The parametric study is presented based on the validated finite element model. It provides further comments on the influences of tube wall thickness and concrete strength on the moment-rotation response of the connections.

Chapter 7: This chapter discusses further modelling of hysteretic moment-rotation relationship. Based on the moment-rotation envelopes predicted by finite element analysis, the mathematical models are adopted to represent hysteretic loops of the curves.

Chapter 8: This chapter highlights the main conclusions obtained from experimental study and finite element analysis. It also provides general comments and recommendations for the application and further research of this innovative blind bolted endplate connection to CFT column under cyclic loading.

CHAPTER 2

LITERATURE REVIEW

2.1 Introduction

In this research, an innovative blind bolt and CFT column were incorporated in the bolted endplate connection system to resist moment. The present chapter is organized along distinct lines of focus and describes the previous experimental researches relevant to this connection system. The respective focus areas in the literature review are directed to provide general understanding of the behaviour of the connection component or assembly. A brief overview of the focus and related methodology of each study is presented. The results obtained from previous investigations are not completely listed but selected to shed light on how the connection assembly and associated system are investigated. This chapter also includes recent work of a series of investigations on the behaviour of this innovative blind bolt. This chapter concludes with comments highlighting the needs for further research of this topic.

2.2 Previous studies on tensile behaviour of blind bolted connections

Several types of blind fastener have been developed commercially and adopted for beam-to-column connections, including the Huck High Strength Blind Bolt (HSBB) and Huck Blind Oversized Mechanically Locked Bolt (BOM) (Huck International-USA), the Flowdrill (Flowdrill B.V-The Netherlands), the Ajax One-side (Ajax Fasteners-Australia) and the Lindapter

Hollobolt (Lindapter International-UK), as indicated in Table 2.1. The behaviour of these blind fasteners has been widely investigated in the literature.

Table 2.1 Typical blind fasteners (Corus Tubes library, 2005)

Item	Configuration illustration	Installation procedure
BOM fastener	<p>Labels: Drive, Nut, Washer, Grip sleeve, Bulb sleeve</p>	<p>Labels: 1st stage, 2nd stage, 3rd stage</p>
HSBB fastener	<p>Labels: Pin, Primary sleeve, Second sleeve, Clamp, Washer, Collar, Pintail</p>	<p>Labels: 1st stage, 2nd stage, 3rd stage</p>
Flowdrill	<p>Labels: Tool, Collar, Flowdrill bit</p>	<p>Labels: 1st stage, 2nd stage</p>

Table 2.1 continues

Item	Configuration illustration	Installation procedure
Lindapter Hollo- bolt		
Ajax One-side		

For a bolted endplate beam to column connection, the moment mechanism is formed by tensile force developing on the beam flange and transfers to the compression zone of the connection. The tension zone of the bolted connection is often regarded as the major source of deformity. The equivalent bolted T-stub originally introduced by Zoetemeijer (1974) has been recognized as a fundamental approach for the idealization of the performance of the tension zone of the bolted joints. Also, an understanding of the overall connection behaviour in bending was established. For example, the bending of the column flange and the endplate can be described using equivalent bolted T-stub models as illustrated in Figure 2.1. The strength and stiffness of bolted connections is then determined using both the component method and the T-s

tub models (Agerskov *et al*, 1976, Yee *et al*, 1986; Jaspart *et al*, 1995; Shi *et al*, 1996). Also, this simplified analytical method has been adopted in modern codes, such as Eurocode 3 (2005). With regard to the blind bolted connection, most concerns were given to its tensile behaviour. Although the blind bolt is susceptible to undergo shear action, this configuration of assembly with large cross-section area could be inherently strong enough to resist such action. This is especially true for the Hollobolt, whose large cross sectional area due to the flaring sleeves produces a great shear resistance. Accordingly, the T-stub connection model was adopted in literature above for the preliminary study of strength and stiffness of the blind bolted connection in tension. Typical experimental studies in recent years for blind bolted T-stub connections are listed in Table 2.2. This section will present a brief overview of relevant experimental work on T-stub connections at the University of Nottingham and the University of Melbourne. The main focus of review in this section is given to the Lindapter Hollobolt and the Ajax One-side based blind bolts.

Barnett (2001) conducted an early experimental study at the University of Nottingham on blind bolted T-stub assemblies, as shown in Figure 2.1. The ultimate performance and failure modes of different types of the blind bolts were observed and compared. The reported stiffness of the connections with the Lindapter Hollobolt was lower than those with the standard bolt. It was observed early ductile shearing of the flaring sleeve caused axial bolt deflection prior to the preload being overcome and then this ductile shearing continued until fracture of the flaring sleeve, as shown in Figure 2.1(b). Due to limited number of tests, no analytical models were given to characterize the

performance of the blind bolt and its connection.

Table 2.2 Representative experimental studies on blind bolted T-stub connection subjected to tensile loading

Reference	Blind bolt types	Details of the tube (mm)	Details of the T- stub flange (mm)	Test number	Test limitations
Tanaka (1996)	Huck high strength one side bolt (BOM)	SHS300×300×12 Without concrete infill	250×250×25 250×302×34	4	Complicate installation
Barnett (2001)	Lindapter RMH bolt and Hollobolt	SHS 200×200×8 SHS 200×200×10 SHS 200×200×12.5 Without concrete infill	250×200×25	12	Sleeve shearing failure
Ellison (2004)	Standard bolt, Lindapter RMH bolt, Hollobolt and Extended Hollobolt	SHS 200×200×10 With concrete infill	200×200×50	4	Without accounting for cyclic loading
Gardner (2005)	Ajax One-side	CHS* 219.1×4.8 With concrete infill	200×230×16	5	Connecting welds fracture
Yao (2008)	Ajax One-side	CHS* 323.9×6 With concrete infill	280×280×20	6	Connecting welds fracture
Lee (2010)	Ajax One-side	SHS 150×150×6 Without concrete infill	270×150×10	2	Tube wall damage

Note: * CHS denotes circular hollow section

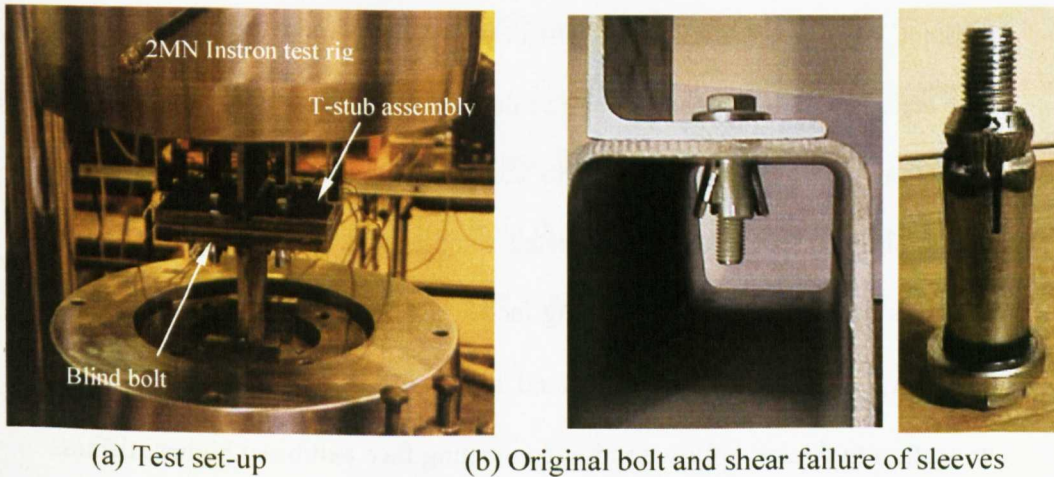


Figure 2.1 Representative tensile test of blind bolted (Lindapter Hollobolt) T-stub assembly (Barnett, 2001)

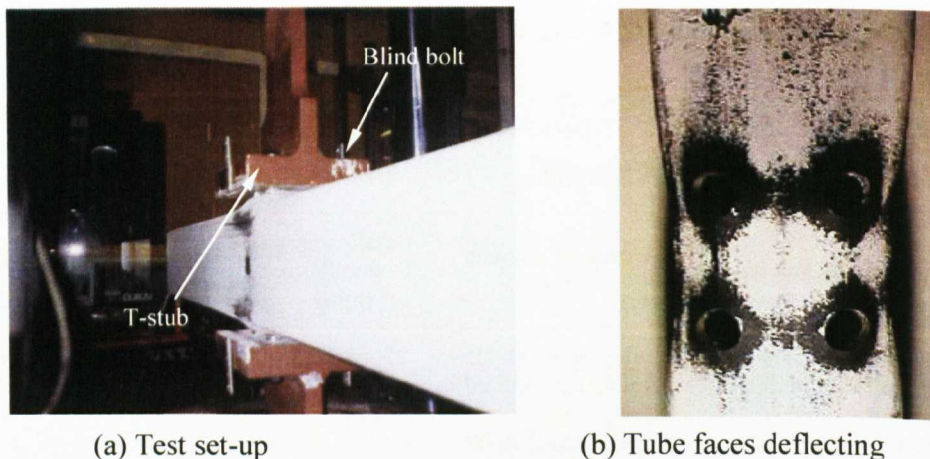
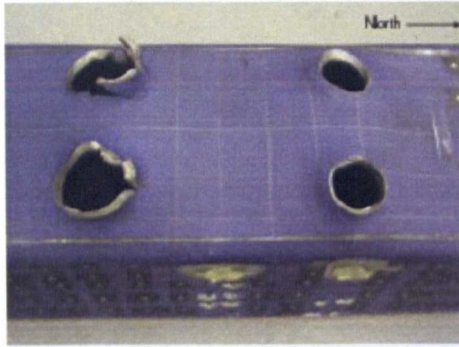


Figure 2.2 Representative tensile test of blind bolted (Lindapter Hollobolt) T-stub to SHS column without concrete infill (Barnett, 2001)

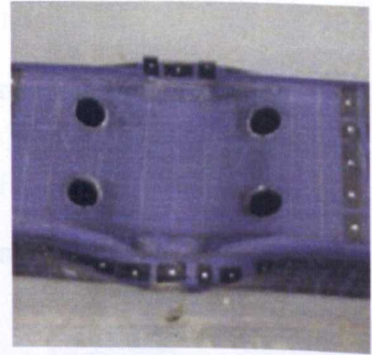
The research conducted by Barnett (2001) also expanded the research of T-stub assembly for the blind bolted T-stub connection to square hollow section (SHS) column without concrete infill, which is similar to previous test performed by Tanaka & Tabuchi (1996). The ductile shearing of the flaring sleeve against the underside of the connections was again observed as the predominant cause of damage for the blind bolt. The expansion of the clearance hole was reduced as the stiffness of SHS column wall is increased. More serious ductile shearing failure of the flaring sleeve was observed for the connection with 12.5 mm thick SHS column wall than those with 8mm or 10mm. The connection failure of tested samples was also due to significant deflection observed on the connecting face and lateral face of SHS column, as shown in Figure 2.2 (b). It was found in the reported tests that the T-stub connection to thicker hollow section connecting face exhibited higher stiffness than those to thinner ones. The flexibility of hollow section column face was

recognized as a limiting factor for the use of the blind bolted connection to hollow section column as moment resisting connections.

Lee *et al* (2010) studied blind bolted T-stub connections to hollow section columns for low rise construction. As mentioned earlier, the blind bolt studied at the University of Melbourne was the Ajax One-side, which was used as fastener with T-stub to build a moment connection. The tension test showed that the bolt failure followed a different failure mode in which the tube face around the bolt hole area tore open, resulting in bolt pullout as plotted in Figure 2.3 (a). The compression test showed that the tube underneath the endplate crushed and the sidewall bulged outwards as plotted in Figure 2.3 (b). Besides the deformation of the blind bolt and tube face, the endplate also deformed in a bow shape and produced plastic hinges. The numerical moment-rotation curves were converted and compared with moment-rotation curves related to Eurocode 3 classification. This connection classification was introduced by EI_b (flexural stiffness) and L_b (span of the beam); and then given as (1) rigid- $K_{j,ini} > k_b EI_b / L_b$, where $k_b = 8$ (braced frames) and $k_b = 25$ (sway frames); (2) nominal pinned, if $K_{j,ini} < 0.5 EI_b / L_b$; (3) semi-rigid: for cases in between the rigid and nominally pinned. By evaluating the stiffness properties of the connections, it was concluded in this work that the Ajax One-side could be used as an alternative to welded connections in residential or low rise commercial frames.



(a) Punching failure of bolt hole



(b) Tube face crushing

Figure 2.3 Representative tensile and compression test of blind bolted (Ajax One-side) T-stub to SHS column without concrete infill (Lee *et al*, 2010)

From the work referred above, it is noted that the deformability of a blind bolted connection to tubular column greatly depends on the flexibility of connecting face and sidewall of hollow section column. The introduction of concrete infill into this area of study was performed by early researchers. France *et al* (1999) compared the blind bolted connection with flowdrilled connectors and concluded that the concrete infill dramatically increased the strength and stiffness of the blind bolted connections. Later, Tizani & Ridley-Ellis (2003) reported a similar observation when compared with the bolted connections with RMH (Reverse Mechanism Hollobolt).

Due to the efficient stiffening effect of concrete infill, the CFT column has attracted more attention for its use in moment resisting beam to column connections. The blind bolts, on the other hand, have been improved to employ the beneficial effect of anchorage provided by concrete infill. Early practice at the University of Nottingham was made for the Lindapter Hollobolt by extending the bolt shank and adding a nut at the end to be anchored in concrete infill, which is also labelled as 'Extended Hollobolt'. Ellison &

Tizani (2004) conducted a practical experimental study for the blind bolted connections to CFT column. There were four different types of blind bolts tested for comparison.

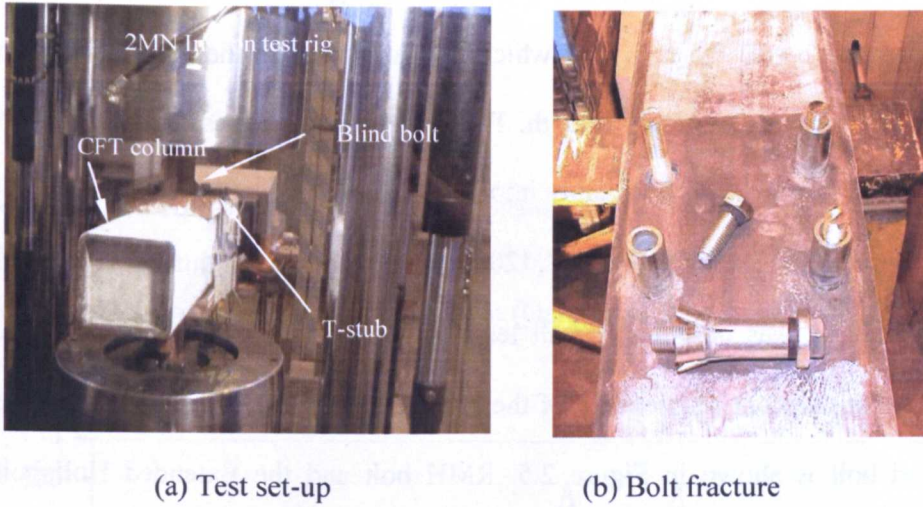


Figure 2.4 Representative tensile test of blind bolted (Standard bolt, Lindapter Hollobolt, Extended Hollobolt) T-stub to CFT column (Ellison & Tizani, 2004)

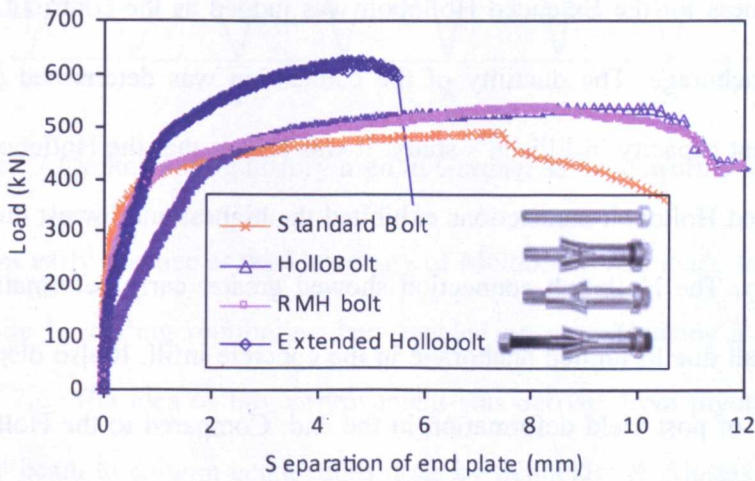
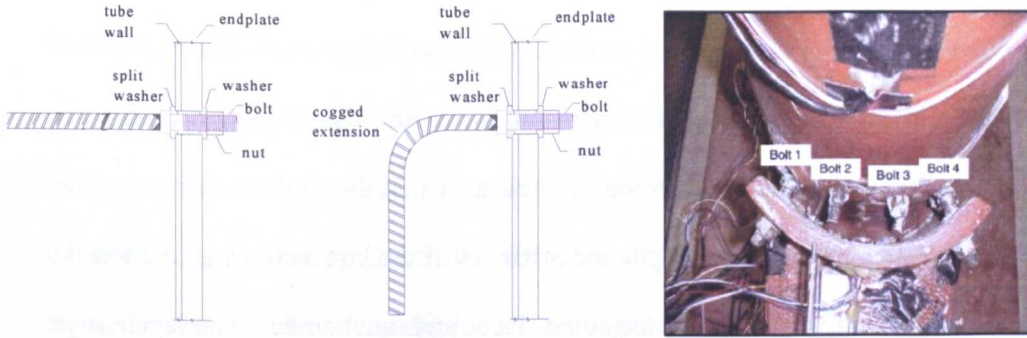


Figure 2.5 Load-displacement relationship of tensile pull-out tests (Ellison & Tizani, 2004)

The test set-up reported by Ellison & Tizani (2004) is shown in Figure 2.4. The main failure modes for all the connections were featured by bolt fracture.

This observation is also different from previous test on the Hollobolt connection, in which the Hollobolt was partially pulled through the hole prior to the development of the tensile capacity (Barnett, 2001). The standard bolt failed near the middle of the shank length. The Extended Hollobolt connection showed little early deformation which was attributed to the extra anchorage provided by the extra shank length. The strength and stiffness for all types of the blind bolt were again notably improved when compared with similar tests without concrete infill (Barnett, 2001). As such, a minimum tube wall deformation was observed for all tests. A representative comparison of the load-displacement relationship of the connections with different types of the blind bolt is shown in Figure 2.5. RMH bolt and the Extended Hollobolt connections exhibit similar stiffness to those of the standard bolt while the Hollobolt connection displays much lower stiffness. The improvement of initial stiffness for the Extended Hollobolt was judged as the contribution of concrete anchorage. The ductility of the connection was determined as the displacement capacity in Ellison's study. It was shown that the Hollobolt and the Extended Hollobolt connections exhibited the highest and lowest ductility respectively. The Hollobolt connection showed greater early deformation of the tube wall due to limited anchorage in the concrete infill. It also displayed higher rate of post yield deformation in the end. Compared to the Hollobolt, the standard bolt connection developed less early deformation. Based on the reported test results, the connection with the Extended Hollobolt was suggested as a type of moment-resisting connections to hollow sections and a feasible alternative for traditional expensive and cumbersome welded connections.



(a) Blind bolt with straight & cogged extensions (b) Bolts bend & fracture

Figure 2.6 Representative tensile test of blind bolted (Ajax One-side with cogged extensions) T-stub to CFT column (Gardner and Goldsworthy, 2006)

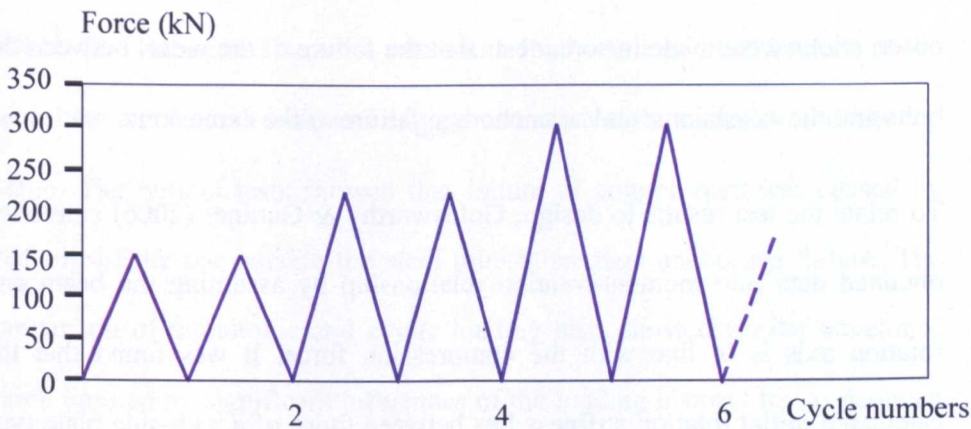


Figure 2.7 Cyclic loading history used in Gardner & Goldsworthy's test (2005)

Another early practice at the University of Melbourne was made for the Ajax One-side by adding reinforcing bars welded on as extensions as shown in Figure 2.6. The idea of this improvement was derived from pivotal work of welded beam to column connections done by Schneider & Alostaz (1998), in which reinforcing bars were welded onto the top of the flange and anchored into the concrete so as to avoid the excessive distortion of the tube wall and retain the plastic moment capacity of beam. In Goldsworthy & Gardner's work (2006), the blind bolted connections were studied with different extension

types, such as straight and cogged, and with different length as shown in Figure 2.6. The tension load applied to the connections consisted of monotonic load and unidirectional cyclic loads, in which the cyclic loading history is shown in Figure 2.7. It was found in their tests that that the extensions lead to an improvement in the strength and stiffness of the connections as the tensile loads are shared between the tube face and anchorage. The anchorage provided by the reinforcing bar extensions prevented excessive localized column yielding or shearing, or bolt pull-out. Although it was assumed that the desired failure as the bolts reached their full capacity and fracturing, observations were made in some tests that the failure of the welds between the bolts and the extensions, and/or anchorage failure of the extensions.

To relate the test results to design, Goldsworthy & Gardner (2006) converted obtained data into moment-rotation relationship by assuming the beam end rotation axis is in line with the compression force. It was found that the calculated initial rotation stiffness lies between those of a web-side plate type connection and a rigid endplate connection. The initial stiffness of the connection was increased with the provision of better anchored extensions. As conclusions of this work, they confirmed that effectiveness of the extensions, especially the cogged ones, in increasing the strength and stiffness of this T-stub connection in tension. As for the consideration of extension in design, they suggested a limit be prescribed on the load taken by extensions to ensure sufficient anchorage under ultimate condition.

Thereafter, Yao *et al* (2008) further studied the blind bolt of Ajax One-side with extension used for moment resisting connection, as shown in Figure 2.8.

The tests consisted of a large scale T-stub connection with full instrumentation tested to failure in tension and some pullout tests to study the anchorage behaviour of cogged bars. The test was considered under monotonic and cyclic loading, in which the cyclic loading history was similar to the test reported by Gardner & Goldsworthy (2005) but referred with more cycles. Again, it was shown in their test that the addition of the cogged extension to the blind bolt increased the tensile strength and stiffness of the T-stub connection. It was estimated that 65% of the tension was carried by the cogged extensions and 35% was taken by hoop stress within the steel tube wall at the load level of 500kN. The failure mode at the maximum load was again the fracture of the welds between the bolt head and cogged extension at the middle bolt of the top T-stub. The pullout tests showed that failure of cogged bars was caused by breaking of the bar outside the steel tube other than anchorage failure. The comparison of monotonic and cyclic loading tests showed similar envelopes which implied no significant influences of the loading history. It was deduced that from load slip of pull out test that the tube with 6mm thickness was able to provide sufficient confinement.

The tensile response of the blind bolted T-stub connection was later simulated by a finite element model. The cogged bar were divided by two parts: the straight portion and the cogged portion as the interaction between reinforcing bar and the surrounding concrete was modelled. These two parts were modelled with couple elements & bond element and a single spring element respectively.

Following the T-stub connection test, another test was conducted to validate a strong and stiff blind bolted connection rather than ductile moment resisting ones. Once again, the test was terminated when the weld fracture between the blind bolt head and the cogged extension. Similar to the comment given by Goldsworthy & Gardner (2006), Yao *et al* (2008) suggested an one-piece combination of the cogged extension and the blind bolt as to avoid brittle fracture. The connection was concluded with favourable strength and stiffness in moment-resisting frames to resist lateral loads, however, this study was not related with the connection ductility. The comparison of the cyclic performance of the Extended Hollobolt and the Ajax One-side bolt will be commented later.

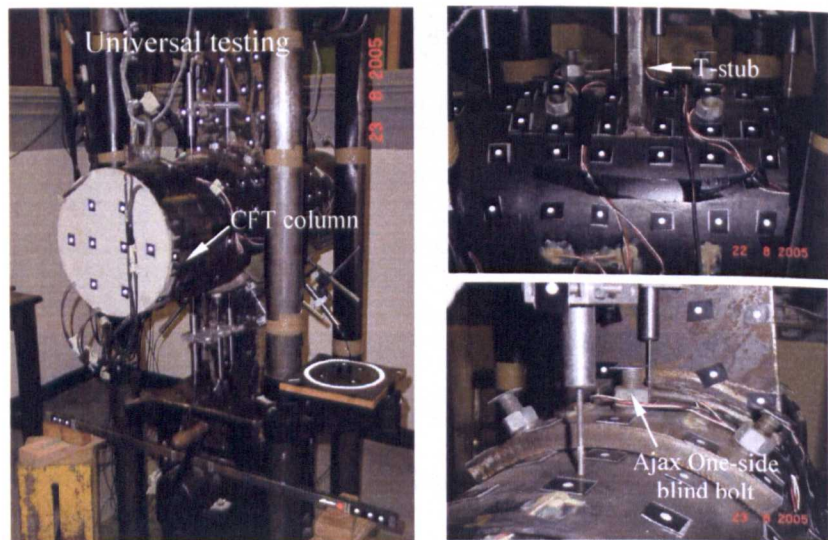


Figure 2.8 Representative tensile test of blind bolted (Ajax One-side with cogged extensions) T-stub to CFT column (Yao *et al*, 2008)

2.3 Previous studies on monotonic behaviour of blind bolted beam to column moment connections

Recent experimental investigations on the blind bolted moment connection to tubular column have been carried out on a variety of connection with

configuration parameters of tube shape, concrete infill and blind bolt, as listed in Table 2.3. Similar to the experimental studies on T-stub connections, the research work at early stage concerns the blind bolted beam-to-column connections with hollow section columns without concrete infill and later expanded for the connections with CFT columns.

Table 2.3 Representative experimental studies on blind bolted beam to column moment connections subjected to monotonic loading

Reference	Bolt types	Column details (mm)	Beam details (mm)	Number of test
Ghobarah (1993)	Huck BOM Huck HSBB	SHS203×203×12.7 SHS254×254×11.13 With/Without concrete infill	W360×33	6
Korol (1993)	Huck BOM Huck HSBB A325	SHS203×203×12.7 SHS254×254×9.53 SHS254×254×11.13 Without concrete infill	W360×33	5
Tanaka (1996)	Huck BOM	SHS300×300×12 Without concrete infill	H400×200×8×13	4
France (1999)	Flowdrill	SHS200×200×8 SHS200×200×10 SHS200×200×12.5	UB356×171×67	6
Harada (2002)	Torque controlled high strength blind bolt (TCBB)	SHS350×350×12 Without concrete infill	H400×200×9×19	4
Loh (2006)	Lindapter Hollobolt	SHS200×200×9 With concrete infill	250UB25.7	6
Wang (2008)	Lindapter Hollobolt	SHS200×200×8 CHS200×8 With concrete infill	H300×150×6.5×9	4
Al-Mughairi (2009)	Extended Hollobolt	SHS200×200×8 SHS200×200×10 SHS200×200×12.5	UB356×171×67	8
Elghazouli (2009)	Lindapter Hollobolt	RHS200×100×5 SHS150×150×6.3 SHS150×150×10 SHS200×200×10	UB305×102×25 UB305×165×40	10
Lee (2011)	Ajax One-side	SHS 150×150×6 Without concrete infill	310UB32	1

Early study by Ghobarah *et al* (1993) and Korol *et al* (1993) indicated that an appropriate use of the blind bolts in the connections to hollow section tubular column could achieve similar moment capacity as those of the standard bolts.

Also, the moment capacity of the blind bolted connection can be improved by changing the bolt pitch and endplate thickness so as to reduce the blind bolt bending and the prying action. An basic analytical model was given by Ghobarah *et al* (1993) to evaluate the initial stiffness and plastic moment capacity of the blind connections to SHS column with and without column infill. This study proved that initial stiffness of the blind bolted moment connections increases with the effect of concrete infill. The prediction of connection's moment-rotation relationship was shown at various load levels.

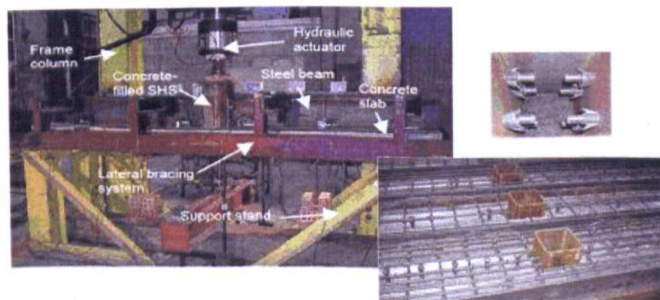
France *et al* (1999) investigated the moment behaviour of flowdrill connections to tubular columns without and with concrete infill with the aim to assess the joint's semi-rigid behaviour and acceptability of the flowdrill connector as a method for onsite bolting of beam to the column connections. The related parameters examined in the experiment referred to tube wall thickness, material properties, and endplate thickness. The moment tests of the connections with no concrete filled tubular column showed that the majority of the joint rotation occurred due to flexural action of the tube walls and the flowdrill connector was not sufficient to restrain the column face when in tension. The sidewall buckled outwards in the compression zone with yielding across the full width of tube sidewall. However, an uncertainty was expressed if this extensive yielding influenced the response of the joint connected to the adjacent face of the column. When compared the moment behaviour of the connections, the depth of the connections was suggested as more efficient than that the tube wall thickness in achieving strong and stiff joint. The results from experimental studies showed flowdrill connector was able to achieve full

strength for moderately thick endplate connections of flush endplate details. The later studies on the connections with tubular columns with concrete infill indicated that the concrete provided sufficient stiffness at the corners of the tubular column to prevent any inward deformation of the lateral face (France *et al*, 1999). There were not any visible deformations of the column in the compression zone. The strengthening effect of concrete infill caused the axis of rotation of the joint shifting towards the compression of the flange of the beam. As a result of the joint response, the increased initial stiffness and post yield stiffness were observed for such connections to tubular columns with concrete infill than those without concrete infill. However, the ductility of the connection was reduced with the concrete infill.

Harada *et al* (2002) studied the cyclic behaviour of a type of blind bolted connections using split-T to rectangular hollow section column. The blind bolts used in reported tests were torque controlled high strength blind bolt (TCBB). The performance of the connection was assessed by experimental load-deformation relationship curves, which showed stable spindle-shaped hysteresis loops. This type of connection was concluded with capacity of possessing sufficient deformation capacity.

Loh *et al* (2006) tested cruciform blind bolted (Lindapter Hollobolt) composite connections to CFT column under hogging bending, as shown in Figure 2.9 (a). This study aimed to simulate the internal regions of a semi-continuous frame. Comparative studies were taken for bare steel joints and composite joints with concrete slab, in which the latter type was explored by examining the influence of shear connections and reinforcement on the joint behaviour. The

beneficial effect of using the concrete filled column sections was observed as the prevention of the local tube failure. The experimental results showed that the failure of bare steel joint was caused by excessive deformation of tube face and pull out of the Hollobolts, as shown in Figure 2.9 (b). The failure of the composite joints was induced by the local buckling of compressive beam flange, which attributed to the reduction of moment resistance and rotational capacity of the joints. However, there was no failure of the Hollobolts although the larger clearance bolthole deformation was observed. The test results also showed the influences of shear connection level and reinforcement ratio on the behaviour of the composite joint. In the former case, the rotation capacity was enhanced by a slight compromise of stiffness and resistance, while in the latter case, a notable effect on the joint performance was observed. As for the issue of using partial shear connection in design, suggestions were given for appropriate shear levels and reinforcement ratios.

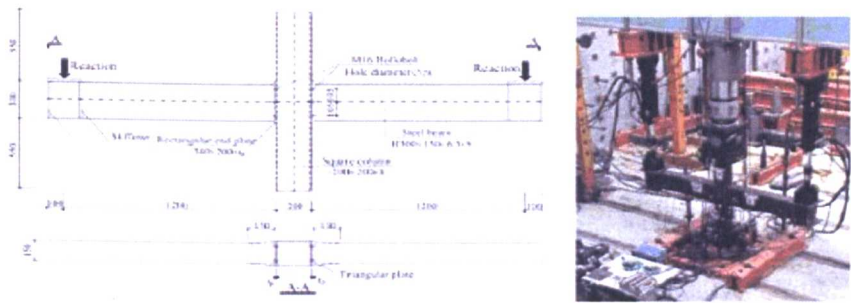


(a) Test set-up

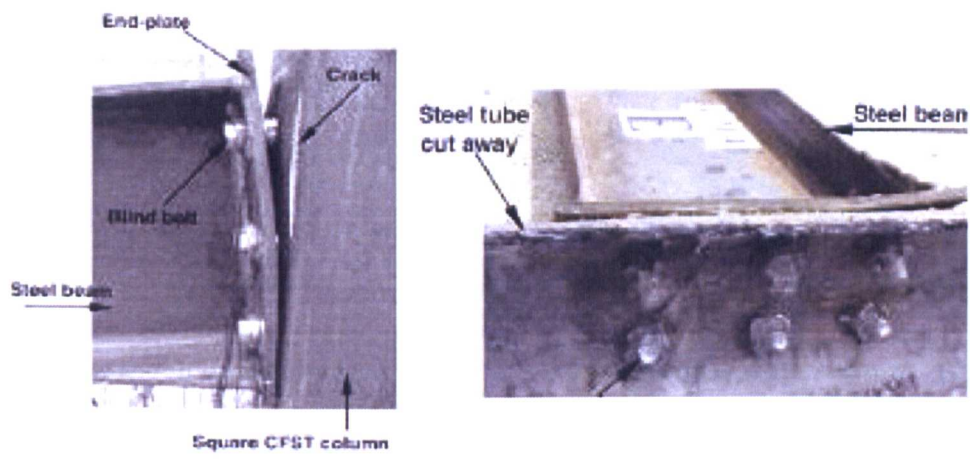


(b) Failure modes

Figure 2.9 Representative test of blind-bolted (Lindapter Hollobolt) beam-to-column moment connections under monotonic loading (Loh et al, 2006)



(a) Test set-up



(b) Failure modes

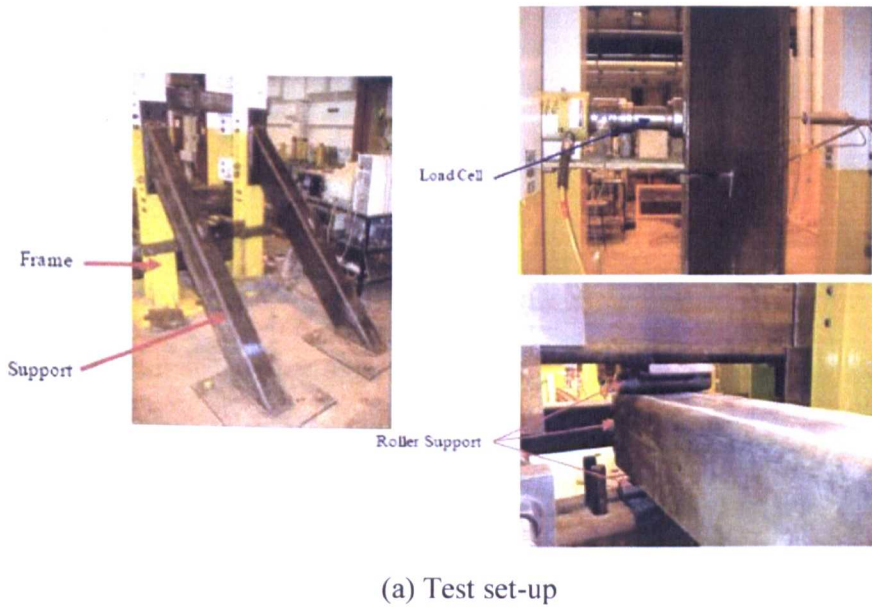
Figure 2.10 Representative test set-up for blind-bolted (Lindapter Hollobolt) beam-to-column moment connections under monotonic loading (Wang *et al*, 2009)

A similar experimental study was conducted by Wang *et al* (2009) for the monotonic behaviour of the cruciform blind bolted connections to CFT columns, as shown in Figure 2.10 (a). Limited number of tests was performed taking column section type (square and circular CFT columns) and the thickness of endplate as parameters. As the column section used in the tests were cold-formed, the failure mode was shown as longitudinal cracks on the corner of the square CFT column, as shown in Figure 2.10 (b). Despite concrete crack at the ultimate state, no failure sign of the Hollobolt was observed. A comparison was made for the influence of selected parameters on

the strength and stiffness of the connections. The thickness of endplate was observed having an effect on the connection behaviour, i.e., the increased thickness of endplate produces increased strength and stiffness but decreased rotation capacity of the connections. The connection performance was assessed on the basis of moment-rotation relationship. According to the Eurocode 3 classification, it was concluded that this type of connection behaved in a partial strength and semi-rigid manner with reasonable strength and stiffness.

Al-Mughairi (2009) investigated the monotonic behaviour of the blind bolted endplate connection to CFT column using the Extended Hollobolt, as shown in Figure 2.11 (a). As already mentioned in the first chapter, this work is a pilot study on the beam to column moment resisting behaviour of this innovative blind bolted endplate connection in this study. Hence, it was intended to present a little more details about experimental set-up and analysis herein as a basic reference for present study. This experimental work aimed to study the suitability of the use of the Extended Hollobolt for a moment resisting connection. The parameters in this report include concrete strength, tube thickness, bolt pitch and endplate type. The I-beam connected was designed with larger capacity than the connection. As such, thick endplate with sufficient strong welds was used to avoid any plastic deformation so that the blind bolt failed in the end. The monotonic load was applied 1m away from the connection with load control. It was observed in the reported test that the failure mode for all the connections was the bolt fracture in tension rather than pullout. From the strain gauge reading on the bolt and related experimental

observation, the concrete gripped the anchored part of the bolt such that the bolt was not pulled out from concrete, i.e., nothing indicates bond failure between concrete and bolts. The deformations on the tube walls, beam section and endplate were rarely noticeable during nearly all the tests. Similar yield line pattern was observed at the corner of 8mm thick tubes.



(b) Failure mode of bolt fracture

Figure 2.11 Representative test of blind-bolted (Extended Hollobolt) beam-to-column moment connections under monotonic loading (Al-Mughairi, 2009)

As for the parametric study, it was found that the concrete strength had little influence on the behaviour of the connection with Extended Hollobolt. This point can be understood based on the fact that relatively thick tube face (varying tube thickness from 10mm to 12.5mm) greatly restrains bolt pullout and its interaction with concrete infill, i.e., bolt anchorage or bond between

bolt and concrete. The non-negligible influence of tube thickness on the connection behaviour was confirmed in this report. It was found that the increase of bolt pitch leads to an increase of moment capacity and ductility of the connection. As for the endplate configuration, it was reported the extended endplate thickness had more significant effect on the increase of connection capacity than tube wall thickness.

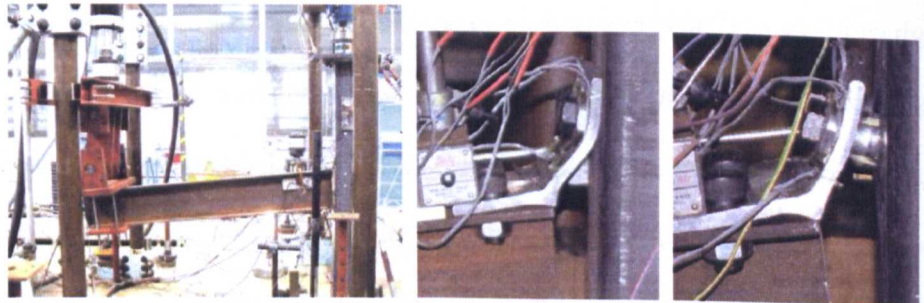
The rigidity of the connection was analysed using secant stiffness and related classifications. The secant stiffness was estimated from Eurocode 3 method and beam line analysis to specify the connections among the categories of rigid, semi-rigid and flexible. By using the classifications suggested by Eurocode 3 and Bjorhovde, it was concluded that the connections with given beam ranges (length and section) can be classified as rigid or semi-rigid (Al-Mughairi, 2009). This classification system is based on the stiffness criteria which can be referred to review work conducted by Chen (2000). This indicated those connections within the category of semi-rigid or rigid connection. The ultimate limit state study showed tested connections were neither full strength nor flexible. By changing the beam section and length, it was found that full strength connections were achieved.

The 3D finite element models in the report were developed to validate against test results with a great confidence. The bolt preload was found to be a significant factor in determining the behaviour of the connections. It was also reported the parametric study of the effects of relevant parameters on the monotonic behaviour of the connections, including tube thickness, bolt pitch, and bolt gauge. The stiffness of the connections was more affected by tube

thickness than bolt pitch and bolt gauge. As a general remark in reported work, this type of the blind bolted connection owned similar failure mode which was comparable to that of a standard bolt. The tested connections with this innovative blind bolt met the requirements which can be classified as a rigid or semi-rigid connection in moment resisting frame system.

Elghazouli *et al* (2009) reported an experimental study on top seat and web angle connections blind bolted to hollow section columns under monotonic and cyclic loading, as shown in Figure 2.12 (a). The focus in this study was given to the influence of bolt grade, gauge distance, column thickness, beam width and presence of web angles. These related parameters were discussed in relation with connection stiffness, capacity and failure mechanisms, and their implication on performance & design. The deformation mode of the connection tension zone is shown in Figure 2.12 (b). The direct tension test displayed that the bolt axial stiffness was increased with the increase of bolt grade. This was also shown in joint tests in which the relatively higher stiffness and capacity of the angles were used, i.e., the blind bolt plays direct roles in the response. The gauge distance showed the interrelation between the influence of the stiffness of angle and blind bolt, in which the reduced distance between the blind bolts and the beam flange increased the connection stiffness and capacity. The reduction of column wall thickness caused lower stiffness and capacity of the connections. The beam width was found as important in related with the width of column face, for which the effect of flexibility of column face in compression became significant when the column face is wider than the beam. The use of web angles was found to be effective in improving

the stiffness and capacity of the connection. This report also included an analytical model examination and comparison with Eurocode 3 methods. This further coupled with experimental results indicated the suitability of this connection as semi-rigid and partial strength for secondary or primary frame systems.



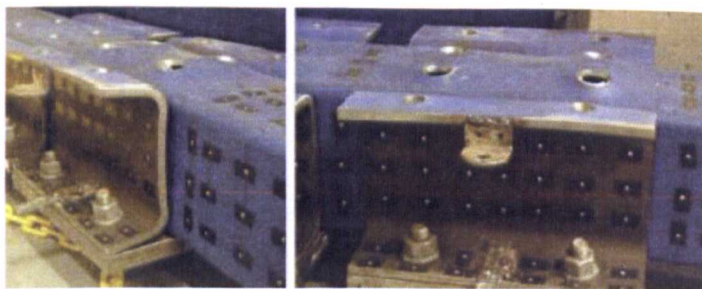
(a) Test set-up

(b) Deformation mode of connections

Figure 2.12 Representative test of blind-bolted (Lindapter Hollobolt) beam-to-column angle connections under monotonic loading (Elghazouli *et al*, 2009)



(a) Test set-up



(b) Deformation of tube face and channels

Figure 2.13 Representative test of blind-bolted (Ajax One-side) beam-to-column moment connections under monotonic loading (Lee *et al*, 2011)

Lee *et al* (2011) examined the monotonic behaviour of a new bolted moment connection comprising of T-stubs connecting the top and bottom flanges of the beam to the column face and channels connecting the T-stubs to a back-plate at the back-face of the hollow section column, as shown in Figure 2.13 (a). The typical deformation mode of the connection occurred at the corners of the channels, as shown in Figure 2.13 (b). Similar to the T-stub connection test reported before (Lee *et al*, 2010), Eurocode 3 classification was used for assessing initial rotation response of the connection which can be referred to Lee *et al* (2010). It was shown that this connection has the potential to be classified as a rigid connection for a brace frame system and even stiffer than the T-stub connection tested before (Lee *et al*, 2010). Finite element analysis was also used in the sensitivity analyses. It was found that the T-stub and back-plate thickness were crucial for the connection stiffness. In this report, a simplified analytical model was also developed for the study of stiffness.

2.4 Previous studies on cyclic behaviour of bolted endplate beam to column connections

Traditionally, beam to column connections including bolted endplate connections are often assumed to be fully rigid to transfer moment in steel frame design. Early studies on the cyclic behaviour of bolted endplate moment connections followed the similar methodology adopted in the full welded connections and focused on the stress and force distributions in the connection. The configuration of the connection in these studies refers to small beam sections with un-stiffened endplates. The subsequent study revealed that the connection may carry monotonic loads even after a significant rotation

(Nethercot *et al*, 1988), which in turn have influence on the frame stiffness and cause an increase in the frame drift. As a result, the bolted endplate connections could undergo relatively large cyclic rotation. Concerns have been extended for the inelastic response of such connections. Another motivation for the study of bolted endplate connection under cyclic loading derives from the post earthquake survey, especially following the Northridge (1994) and Kobe (1995) earthquakes, relating to the poor performance of traditional welded connections, whose fragile behaviours were identified. As a consequence, the bolted endplate beam to column connection was considered as an alternative to traditional welded counterpart. Till now, considerable experimental studies have been reported in the literature on a wide range of this type of connections under cyclic loading. The highlights of these studies are related to the inelastic performance of the bolted endplate connection, including ductility, rotation capacity, energy dissipation capacity...etc.

Most early tests involve with the bolted endplate beam to column connection to open section column. In contrast, there are only few cyclic loading tests reported on the blind bolted endplate connection to hollow section column, such as Mourad (1995). The work to date are presented by Wang, *et al* (2009) and Mirza, *et al* (2011), which refer to the blind bolts of the Lindapter Hollobolt and the Ajax One-side respectively. A summary of these tests is indicated in Table 2.4, which includes the connection type (i.e., flush or extended endplate and standard bolt or blind bolt), details of column & beam and main parameters in each investigation. As a closely related topic of the connection subjected to seismic loading, the research on the low cycle fatigue

Chapter 2: Literature review

behaviour of the bolted endplate moment connection is also briefly outlined at the end of this section. The representative cyclic loading history used in these tests is compared with codified procedures, such as ECCS (1986) and ATC-24 (1992).

Table 2.4 Representative experimental studies on bolted endplate moment connections subjected to cyclic loading

Reference	Connection types	Column details (mm)	Main parameters investigated	Number of test
Korol (1990)	Extended endplate A490, M25 bolt	Column details: W360×64, W360×79 Beam details: W360×45, W360×57	Examination of the factors that influence the cyclic behaviour of the joint, such as end-plate thickness, bolt pre-tension forces, column flange slenderness and column flange stiffeners. Evaluation of strength, stiffness, ductility and energy dissipation capacity.	7
Chobarah (1990)	Extended endplate A490, M25 bolt	Column details: W360×45 Beam details: W360×64, W360×79	Assessment of the contribution of the individual components to the overall response of the joint under cyclic loading. Evaluation of strength, ductility and energy dissipation capacity.	5
Tsai (1991)	Extended endplate A325 bolt	Column details: W18×40 Beam details: W18×40, W21×44	Effort to determine the adequate bolt and endplate strength for attaining the adequate ductility behaviour. Evaluation of strength, ductility and failure modes.	3
Mourad (1995)	Extended endplate HSBB fastener	Column details: RHS590×230×22/19 Beam details: W360×33	Study of the cyclic behaviour of the blind bolted extended endplate connections for HSS (hollow structural steel) columns and investigation on the effect of joint flexibility on the response of the frame when subjected to dynamic loading. Evaluation of stiffness and ductility.	2
Dunai (1996)	Extended endplate SBPR 80/105 bolt	Column details: H300×150×9×6.5 Beam details: H300×150×9×6.5	Investigation on the axial force-rotational stiffness relationship and cyclic behaviour of the connection zone excluding the joint region. Evaluation of strength, ductility and failure modes.	3

Table 2.4 continues

Bernuzzi (1996)	Flush endplate Extended endplate in one/ both sides	Column details: Rigid base Beam details: IPE 300	Assessment of the influence of the loading history on the cyclic behaviour of the joint associating with the main strength and stiffness parameters. Evaluation of strength, ductility and energy dissipation capacity.	16
Adey (2000)	Extended endplate A325/A490 bolt	Column details: W310×118, W310×143 Beam details: W610×125 W360×51, W460×97	Researches undertaken to assess the significance of some design parameters, including: beam size, bolt layout, endplate thickness, use of extension stiffeners, welding process, and weld preparation. Evaluation of strength, rotation and energy dissipation capacity.	15
Yorgun (2001)	Extended endplate M16 & 10.9 grade bolt	Column details: H160×135×5.5×12 Beam details: H110×195×8×10	Study on the effect of a gap between the endplate and the column face on the cyclic behaviour of the extended endplate connection. Evaluation of strength and ductility.	2
Simões (2001)	Extended endplate in one side M20 & 8.8grade bolt	Column details: HEA 220 Beam details: IPE 270	Investigation on the contribution of the concrete confinement in composite columns to the cyclic behaviour of the joint, on internal and external nodes, together with an assessment of degradation of strength and stiffness in successive loading cycles.	4
Dubina (2001)	Extended endplate in two side M20 & 10.9 grade bolt	Columns details: HEB 300 Beam details: IPE 360	Comparison made between the connections under symmetrical and anti symmetrical loading condition. Study on the initial stiffness, moment capacity and plastic rotation capacity of the connection.	2
Summer (2002)	Extended endplate in one side M32 bolt (ASTM A490 or ASTM A325)	Column details: W14×120 (I93) (257) Beam details: W24×68, W30×99 W36×150	Research on the strength, stiffness and ductility of the connections for use in seismic force resisting moment frames.	6

Table 2.4 continues

Greca (2004)	Extended endplate 20mm diameter & 10.9 grade bolt	Column details: HEB 300 Beam details: IPE 360	Assessment of the joint rotation capacity relationship between monotonic and cyclic loading. Evaluation of strength, stiffness and ductility.	12
Kovács (2004)	Extended endplate 16mm diameter bolt & 8.8 and 10.9 grade bolt	Column details: HEA 200	Study on the typical cyclic behaviour modes of the joint, characterized by the cyclic moment-rotation relationships. Evaluation of strength, stiffness and ductility.	9
Nogueiro (2006)	Extended endplate 24mm diameter & 8.8 grade bolt	Column details: HEA 320 Beam details: IPE 360	Investigation on the energy dissipation, the maximum joint strength, the initial and post-limit stiffness so as to further analysis of the current prescription of Eurocode 8.	6
Shi (2007)	Extended endplate 20/24 mm diameter & 8.8 and 10.9 grade bolt	Column details: H300×250×8×12 Beam details: H300×200×8×12	Examination of the factors that influence the cyclic behaviour of the joint, such as endplate thickness, bolt diameter, endplate extended stiffener, column stiffener, type of flush and extended endplate. Evaluation of moment capacity, rotation stiffness, rotation capacity and hysteretic curves.	8
Wang (2009)	Flush endplate Lindapter Hollobolt	Column details: SHS200×200×8 CHS200×8 With concrete infill Beam details: H 300 × 150 × 6.5 × 9	Research on the effect of the endplate thickness and column cross-section type on the cyclic behaviour of the joint. Evaluation of strength, ductility and energy dissipation capacity.	4
Mirza (2011)	Flush endplate Ajax One-side	Column details: SHS300×300×12 With concrete infill Beam details: 610UB101	Verifying the connection can perform satisfactorily under cyclic loading from the aspects of yielding, maximum strength capacity and ultimate displacement ductility. Parametric study on concrete slab thickness, stud spacing, reinforcement spacing, column axial load.	1

An early study conducted by Korol, *et al* (1990) revealed that proper design and detailing of bolted endplate connections could produce sufficient energy dissipation without substantial loss of strength or stiffness. Both endplate and column flange as important structural components in the connection system have great influences on the connection failure under cyclic loading. It was reported that the bolt force deterioration induced by thin endplate could allow reduced connection stiffness. It was suggested the adequacy of column (open section) flange should be checked beforehand, even if the column stiffeners are considered, to avoid excessive yielding of column flange which would further lead to low cycle fatigue.

The experiments reported by Ghobarah, *et al* (1990) and Tsai, *et al* (1991) demonstrated that well designed bolted endplate connections can be considered suitable for moment-resisting frames in severe seismic service. They did not recommend un-stiffened column flange for seismic design of bolted endplate connections. To avoid significant failures of the bolt and endplates during cyclic loading, the connections were advised capable of sustaining the moment of $1.3M_p$, in which M_p is the plastic moment of the beam. They also presented design recommendations for bolts used in these connections as a supplement for AISC codes.

Mourad, *et al* (1995) continued Ghobarah's research on the bolted extended endplate connections (using HSBB fasteners) to hollow section columns in moment resisting steel frame. The beam yielding was avoided in the pre-design of the test to examine the behaviour of the connections under cyclic loading. This assumption was achieved in their tests. The nonlinear frame analysis showed that the flexibility of such connections increased lateral

deflection, decreased the number of beam plastic hinges and plastic rotation, thereby reducing the cyclic loading induced damage and increasing the plastic rotations experienced by the columns at fixed bases.

Thereafter, Dunai, *et al* (1996) and Bernuzzi, *et al* (1996) studied the influences of axial force and loading history on the cyclic behaviour of bolted endplate connections respectively. Dunai's tests concentrated not on the joint region but on the local connection region (omitting of the actual column configuration outside the connection). The rotational stiffness of the connection was investigated under different levels of compressive axial loads applied on the beam end. It was observed that the rotational stiffness is increased significantly at higher ratio of axial load to yield load of the steel section, depending on the compression to tension zone stiffness ratios. The rigidity of this connection was reduced to the 'hinge' range after the failure of the concrete in the surface. The investigations carried out by Bernuzzi (1996) allowed for the influence of loading history on the cyclic behaviour of the bolted endplate connections. The test results exhibited the cyclic loading history has significant influence on the shape of hysteretic curves, but moderate influence on the envelopes of the cyclic response. It was suggested a cyclic loading procedure with too rapid increment might cause an overestimation of the energy dissipation capacity of the connection. It was also recommended that two cycles at the same maximum amplitude are sufficient to quantify the resistance deterioration.

Adey, *et al* (2000) investigated several full sized endplate moment connections under cyclic loading. This test was designed to trigger failure in

the endplate rather than in the beam and column. It was revealed that the endplate energy dissipation capacity decreases as the beam size increases. Meanwhile, the extended endplate stiffener increases the endplate dissipation capacities. If the endplate thickness remains unchanged, it was reported that the connection with relaxed bolts possess greater flexibility than counterpart connections with tight bolt configuration. Thus, it was concluded that extended endplate connections with relaxed bolt and extension stiffeners are able to dissipate more energy than the connections with a tight bolt configuration, and no extension stiffeners, thus demonstrate good potential for use in seismic zones.

Yorgun, *et al* (2000) carried out an experimental study on the extended endplate connections under cyclic loading. An innovative connection configuration was used in this reported study by placing a short I-shaped element (cut from the beam section) between the endplate and the column flange. The thickness of the panel zone was chosen as twice that the column web to reduce the deformation occurred in the panel zone of the column thereby economising the design in the critical cross-sections and connections without additional web-plate or diagonal stiffeners. The experimental results of such connection were compared with the standard endplate connections. It was found that the column flange and the endplate behaved as weakest elements in the tested connections, and no bolt fracture occurred in the test. The innovative connection used in this test exhibited better cyclic performance than the standard counterparts.

Simões, *et al* (2001) performed a series of cyclic loading tests on the

composite bolted endplate connections. The samples consisted of reinforced concrete slab and concrete encased column besides steel connection. It was observed from this study that the stiffness degradation was low in internal node tests, while significant in the external node tests. By comparing the cyclic behaviour of the joints with steel columns and those with composite columns, it was concluded that the differences are not pronounced as concrete cracking decreases considerably the advantage of the column web confinement. The analytical models were validated against the tests results and corresponding accuracies were also discussed.

Dubina, *et al* (2001) studied the effect of cyclic loading type (symmetrical and anti-symmetrical) on the response of beam to column connections used in steel moment-resisting frames. The endplate connections were designed as semi-rigid and partially resistant according to Eurocode 3. The test showed that the joints which are classified as rigid and full strength under symmetrical loading might become partially resistant and semi-rigid under anti-symmetrical loading. This was observed from hysteresis loops with increased ductility, stable energy dissipation, and decreased moment capacity & initial stiffness. The connection failures were influenced by various factors, such as connection detailing, welding procedure, and weld access hole, which are the possible sources of stress concentration.

Sumner & Murray (2002) performed cyclic loading tests on bare and composite slab extended endplate connections with the purpose of evaluating their feasibility for use in seismic load resisting moment frame. The bare steel connections and composite connections were tested in horizontal and vertical

positions respectively. The connections were designed to be stronger than the connecting beam to ensure the resistance of the beam to column connection assembly is relieved from local buckling of beam flange and web. The tests met the design requirements. Finally, a design formula, which based on the yield and tensile stress of steel, was suggested for predicting connecting beam strength under cyclic loading.

Kovács, *et al* (2004) expanded the knowledge of bolted endplate beam to column connections to column-base joints. The test samples were chosen with varying endplate thickness, column section and bolt diameter so as to observe their influences on the cyclic behaviour of the connections. From this study, the hysteretic behaviour of the connections was evaluated on the basis of the moment-rotation diagrams. The cyclic parameters, such as partial and full ductility ratio, rigidity ratio, resistance ratio and absorbed energy ratio were calculated and compared. The representative cyclic behaviour was defined as pure bolt failure, pure plate failure, combined bolt-plate failure and plate buckling failure of column ends. From their study, the combined mode was determined to act as the most advantageous ones in energy absorption, rotational and load carrying capacity.

Nogueiro, *et al* (2006) reported an experimental study on the cyclic behaviour of the double extended bolted endplate joints to I-section column with transverse stiffeners at web panel, as shown in Figure 2.14. The monotonic tests showed that the failure mode was the column web panel in shear until the endplate fails as the fracture in heat-affected zone. Similar failure mode was also observed from cyclic loading tests. It was demonstrated from hysteretic

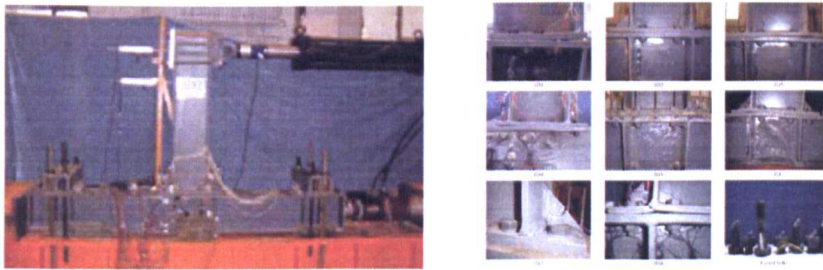
curves that neither joint slippage nor significant strength and stiffness deterioration occurred. This behaviour was attributed to the joint configuration of transverse column web stiffeners and the extended endplate geometry.



(a) Test set-up

(b) Failure modes

Figure 2.14 Representative test of bolted (standard bolt) endplate beam to column connections under cyclic loading (Nogueiro *et al*, 2006)



(a) Test set-up

(b) Failure modes

Figure 2.15 Representative test of bolted (standard bolt) endplate beam to column connections under cyclic loading (Shi *et al*, 2007)

Shi, *et al* (2007) presented an experimental study on a series of bolted endplate beam to column connections subjected to cyclic loading, as shown in Figure 2.15. The joint failure modes include the bolt rupture, endplate yielding, endplate stiffener fracture and buckling of column web and flange in compression, as shown in Figure 2.15 (b). A standard detail of bolted endplate moment connections was suggested for seismic design. Also, the failure

modes and related calculation methods were referred so as to ensure enough rotation capacity and energy dissipation capacity of the connections under seismic loading. In view of pinching and stiffness degradation involved with the connections under cyclic loading, it was recommended that the use of extended endplate connections for moment resisting frames in their study.

Wang, *et al* (2009) reported a study with limited number of tests on the blind bolted endplate connections to CFT column subjected to cyclic loading. The test set-up and joint configuration were the same with their former monotonic test, as shown in Figure 2.10. This study consisted of four full-scale test of joints with square and circular cross sections as an interior joint of moment resisting frame. The significant failure mode of the connection was the cracks at the corner of the square steel tubes (cold-formed) around the first row of the tensile bolts, which is the same as that in monotonic test. The sleeves of the blind bolt exhibited no failure signs, but only loosening. It was indicated that the blind bolted endplate connections to CFT column satisfied the ductility requirement for seismic design. This type of connection was thus judged to be suitable for moment resisting structures.

The post earthquake (Northridge earthquake, 1994) investigations indicated that the local failures of beam to column connections did not induce the collapse of the steel frames but produce non-negligible structural damages. This point seems to imply the understanding of low-cycle fatigue phenomenon for beam to column connections subjected to cyclic loading. The reported European investigations on the low cycle fatigue behaviour of the steel beam to column connections has been conducted in the 1990s at the universities of

Liege, Lisbon, Milan, and Trento (Calado *et al*, 1995; Ballio *et al*, 1997; Bernuzzi *et al*, 1997; Plumier *et al*, 1998). A brief summary of these tests is indicated in Table 2.5. This part of research, mostly involving with the deterioration of structural behaviour under cyclic loading with constant amplitude range, is often regarded as a follow-up study from those outlined in previous section. Figure 2.16 shows a brief summary of cyclic loading history adopted in these studies along with two widely used cyclic loading procedures suggested by ECCS (1986) and ATC-24 (1992).

Table 2.5 Representative experimental studies on bolted endplate moment connections subjected to low cyclic fatigue loading

Reference	Connection types	Column details (mm)	Beam details (mm)	Number of test	Loading pattern
Calado (1995) Ballio (1997) Bernuzzi (1997)	Flush endplate Extended endplate 16mm diameter & 8.8 grade bolt	HEA120	HEA120	4	No. 1 No. 2
Plumier (1998)	Extended endplate 16mm diameter & 8.8 grade bolt	HE300B	IPE150	4	No. 3

Note: Loading pattern refers to Figure 2.16

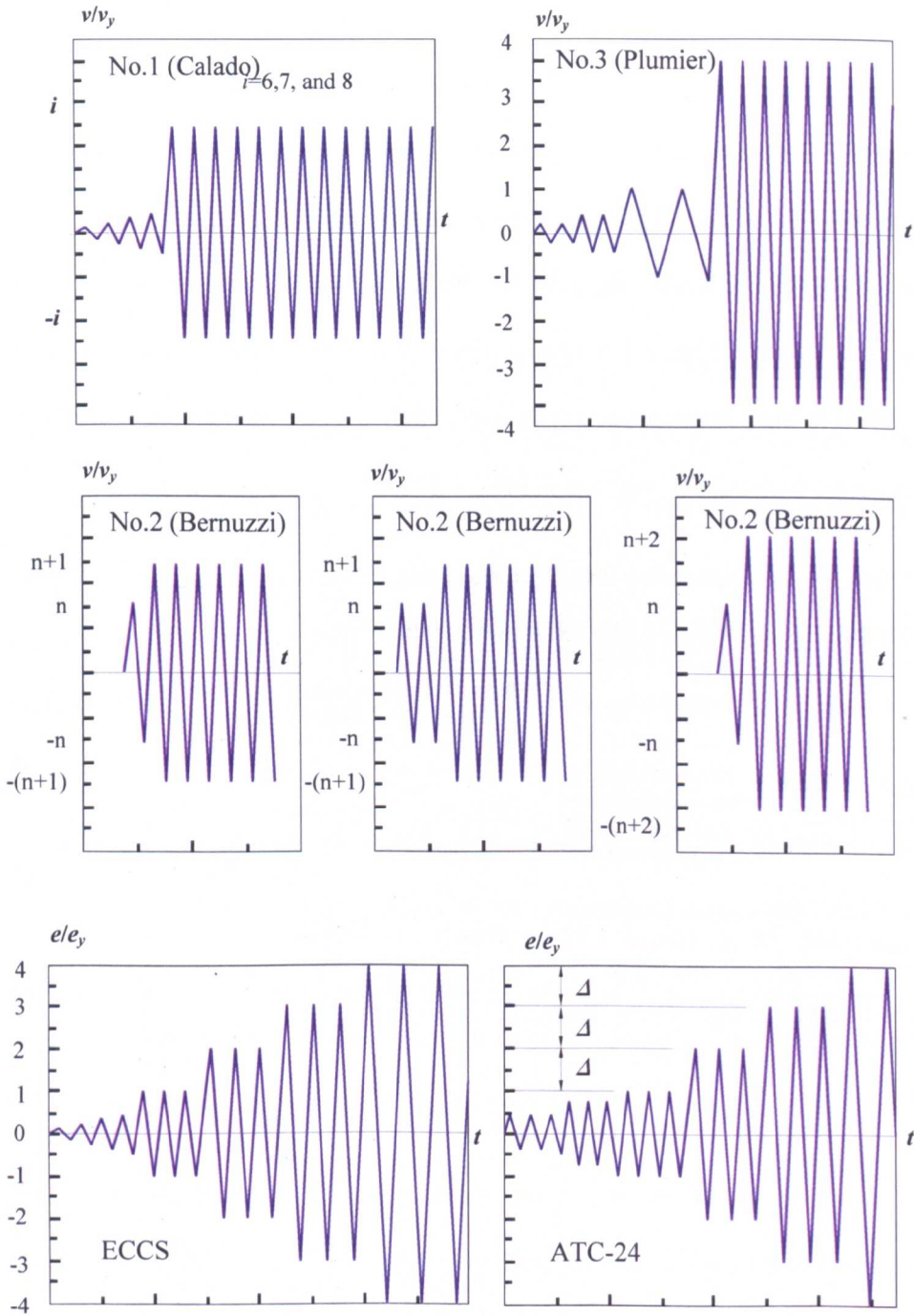


Figure 2.16 Cyclic loading histories for cyclic loading and low-cycle fatigue tests (Note: references are given in text)

Most specimens tested by previous researchers were designed as rigid full strength connection. In case of extended endplate connections, the

low-cycle fatigue failure took place as the beam flange buckling and cracking close to the welds. Bernuzzi *et al* (1997) observed that plastic hinges developed in the beam for all extended endplate connections and located at certain distance equal to the height of the beam profile. Large plastic deformation in the beam web presented an increased resistance to low cycle fatigue (Plumier *et al*, 1998). In case of flush endplate connections, on the other hand, the connections failed by welds fracture and collapsed by one bolt fracture in the end. In order to evaluate the low cycle fatigue, related fatigue curves can be compared with *S-N* lines indicated by design codes for high cycle fatigue. Based on the Miner's rule, unified failure criteria for such connections were proposed by previous researchers. It was concluded that these failure criteria have a general validity in evaluating the low cycle fatigue of the bolted endplate connections (Plumier *et al*, 1998).

The choice of a test program and associated cyclic loading history depends on the purpose of experiments, the type of test specimen, and the type of anticipated failure mode (ATC-24, 1992). With regard to cyclic loading history, it was assumed in most current tests that the strength deterioration is slow and strain rate developed is not high to exert great influence on the material property. The concept of cumulative damage at inelastic excursions, which is also featured by the memory of past structural damages, is often highlighted as an overriding issue in the application of appropriate cyclic loading history. As shown in Figure 2.16, the codified cyclic loading procedures suggested by ATC-24 (1992) and ECCS (1986) are similar in general forms in which the yield deformation is used as reference for two or

three cycles at each amplitude of stepwise increasing (multiple steps) deformation cycles in the inelastic range. On the other hand, the loading histories used for low cycle fatigue test contain most cycles at a given deformation amplitude. It appears that the procedures for low cycle fatigue indicate main outcomes in the resistance deterioration while the codified procedures allow for tested structure achieving its potential strength and providing implicit information related ductility level and energy dissipation. In the present study, the ECCS (1986) cyclic loading procedure was adopted and modified for quasi-static cyclic loading test, which will be indicated in Chapter 3. The cumulative damage evaluation of this innovative blind bolted endplate connection to CFT column will be described in Chapter 5 as a further analysis of the test data.

2.5 Previous numerical studies of blind bolted connections

Use of finite element modelling for the behaviour of bolted endplate connection can be dated back to 1970s (Krishnamurthy & Graddy, 1976). Earlier analyses mostly focused on the elastic behaviour of the connections through simplified 2D or 3D models (Abolmaali *et al*, 1984). Thereafter, the advance of computer technology leads to more sophisticated modelling of the joint behaviour, such as the incorporation of inelastic material behaviour and contact condition between connection components (Gebben *et al*, 1994; Bahaari & Sherbourne, 1996; Choi & Chung, 1996; Bose *et al*, 1997). Also, the modelling of bolt preload condition in the estimation of the moment-rotation behaviour of the connection was reported (Bursi & Jaspart, 1998; Sumner, 2003; Shi *et al*, 2008). Although considerable work described in the

literature related to the modelling the traditional bolted endplate connection to open section column, there are only limited number of reports referring to the modelling of the blind bolted connections. In contrast to the standard bolts, in fact, more complicated configuration and boundary condition are inevitably introduced for the blind bolts. Lee *et al* (2011) presented a 3D finite element model for a blind bolted moment connection to unfilled hollow section column using Ajar ONESIDE blind bolts. Yao *et al* (2008) proposed a numerical blind bolt model with solid element plus spring element for Ajar ONESIDE blind bolts and cogged extensions respectively in their study of the tensile behaviour of blind bolted T-stub connections to concrete filled circular columns. As for the blind bolted connections studied herein, however, there are no detailed reports available in the literature regarding related modelling approaches for them. The attempts of modelling the connection behaviour in this study will be presented in Chapter 6.

2.6 Previous analytical model studies of beam-to-column joints

Based on the available literature, several sophisticated mathematical representations for the prediction of the monotonic joint behaviour have been proposed (Abdalla *et al*, 1995). To characterize the joint moment-rotation relationships in this study, the test moment-rotation envelope curve for the representative tests are modelled using various representations, such as polynomial representation (Frye & Morris, 1975), three-parameter power representation (Richard & Abbott, 1975; Colson & Louveau, 1983; Kishi & Chen, 1990), and exponential representation (Yee *et al*, 1986; Lui & Chen, 1986; Wu & Chen, 1990).

The hysteretic moment-rotation curves are often used for representing the cyclic response of beam-to-column joints with the aid of mathematical models. These models are based on the curve fitting thereby correlating with the experimental curves as the range of application agrees with the structural details tested (Faella *et al*, 2008). Various mathematical models for hysteretic behaviour of beam-to-column joints and components have been developed. As the hysteretic loops under repeated and reversed loading are assumed to be stable and reproducible, the static monotonic moment-rotation curves are used and extended to the cyclic loading analysis (Chui & Chan, 1996). For example, the Ramberg-Osgood model was early adopted by Mazzolani (Mazzolani, 1988) in the simulation of the hysteretic behaviour of the connection with slippage. A literature review and an application of such models together with the Richard-Abbott model were provided by Chui & Chan (1996) and Simões & Silva (2001). Bernuzzi (1998) extended the tri-linear representation suggested by Eurocode 3 (2005) to the case of beam-to-column joints under cyclic loading in which the unloading and reloading phases are based on the Massing assumption. Deng *et al* (2000) proposed a nonlinear hysteretic connection element for the simulation of extended endplate connection. This model was formulated by introducing a multilinear cyclic skeleton followed by curvilinear cyclic relationship as well as degradation and pinching schemes. More recently, Ibarra *et al* (2005) developed relatively simple hysteretic models that include the strength and stiffness degradations for high inelastic systems. Based on the mathematical models available in the literature, this study also indicates analytical simulation of moment-rotation hysteresis loops

in Chapter 7.

2.7 Conclusion and needs for further research

From above literature review, it is indicated that the use of blind bolt for moment resisting connections has been under investigation, especially for its relevant behaviour under tension. However, very limited investigations have been carried out on the cyclic behaviour of such connections. As a closely related topic, in contrast, considerable work have been carried out on the cyclic behaviour of bolted endplate connections to open section columns using standard bolts.

The key findings obtained from previous studies relevant to the present study may be summarized as follows:

- Early tensile tests of blind bolts showed that the Hollobolt is likely to be partially pulled through the bolt hole with ductile shearing of the flaring sleeves. When the hollow section column is introduced into the bolted connection assembly, a significant deformation can be expected for the compression region of the connection with tube sidewall bulged outwards.
- For the blind bolted connection to hollow section column, the reduction of column wall thickness leads to lower stiffness and capacity of the connection. The relation of beam endplate width with the width of column face plays an important role in developing joint behaviour, for which the effect of flexibility of column face in compression became significant when the column face is wider than the beam endplate.

- The introduction of concrete infill into the blind bolted connections to hollow section column greatly enhances the strength and stiffness of the hollow section column. The Extended Hollobolt as an innovative blind bolt adopted in this study furthermore employs the beneficial effect of anchorage provided by concrete infill thereby improving the tensile strength of the connection assembly in contrast with the Hollobolt counterpart.
- The monotonic loading test showed that this innovative blind bolted endplate connection to CFT column can be used as a type of rigid or semi-rigid beam to column connection. The ultimate limit state study showed that tested connections were neither full strength nor flexible, and furthermore, the stiffness of this innovative blind bolted endplate beam to column connections was greatly affected by tube thickness and bolt pitch.
- An adequate design and detailing of bolted endplate connections could achieve good energy dissipation without substantial loss of strength or stiffness. Endplate in bending as a ductile component can be employed to achieve energy dissipative bolted endplate connection.

Despite the understandings generated from recent investigations reviewed above, the knowledge gap is still significant for the understanding of the cyclic behaviour of this innovative blind bolted endplate connection to CFT column with unavailable data existing on the mechanical characteristics and hysteretic moment-rotation relationship of the connections. There are still further research work remain to be done in this field. Some of these works are introduced below as the main contributions of the present study. The rest of

work will be outlined in the last chapter as suggestions for future work.

- Although the concrete anchorage effect of a similar blind bolt (i.e., Ajax One-side) with extension has been studied under several loading and unloading cycles (Goldsworthy & Gardner, 2006; Yao *et al* 2008), it is not sufficient to import reported observations for the connection with this innovative blind bolt (Extended Hollobolt). This is because the extension welded to Ajax One-side often posed undesired weld fracture under cyclic loading as reported in the literature. In contrast, it appears this weakness may be effectively avoided for this innovative blind bolt studied herein which is featured by one pieced bolt shank as the extension part. The failure modes of the connection with this innovative blind bolt are to be understood through cyclic loading tests.
- From theoretical point of view, the CFT column face as a plate element in flexible deformation represents a ductile component in the study of the blind bolted endplate connection to CFT column. Wang *et al* (2009) reported an investigation of similar connection system using the Hollobolt, however, the cold-formed steel tubes produced early cracks at the tube corner which limited the flexibility of CFT column face. The contribution of the CFT column face with hot-rolled tube section and associated interaction with the concrete infill to the ductile performance of this innovative blind bolted endplate connection is to be investigated.
- The CFT column and the blind bolt have combined effects on the connection behaviour. The understanding of their roles in the cyclic characteristics of this innovative blind bolted endplate connection to CFT

column is to be further accounted for.

- The failure modes of this innovative blind bolted endplate connection will be clarified through gaining the evidences from the stress & strain distributions and related observations. As a supplement for experimental instrumentations, finite element models are to be developed and related parametric study is to be conducted for this understanding.
- The hysteretic moment-rotation curves are often used for representing the cyclic response of beam-to-column joints with the aid of mathematical models. Allowing for different degrees of complexity of the connection system, the hysteretic models are to be proposed in this study for the moment-rotation relationship of this innovative blind bolted endplate connection.

CHAPTER 3

EXPERIMENTAL STUDY-TEST PREPARATION

3.1 Introduction

The need for further experimental study on the cyclic behaviour of this innovative blind bolted endplate connection to CFT column has been identified from background literature. To achieve the research objectives introduced in Chapter 1, an experimental program consisting of six full-scale blind bolted connection tests was conducted. The purpose of this test programme was to investigate the moment behaviour of multiple bolt-rowed beam to column connection under quasi-static cyclic loading.

This chapter will be presented as follows. First, the test program is outlined including the connection details, material properties, specimen details, test set-up, instrumentation and cyclic loading procedure. Second, the joint rotation measurement method is presented based on the instrumentation adopted in the experiment. As the yield displacement determination approaches vary with the test programs and connection configurations, it was decided to clarify this issue through a brief discussion and then present an appropriate method for this study. The content in this chapter will join the following chapter and constitutes the overall description of experimental study in this research programme.

3.2 Testing program

3.2.1 Connection details

The specimens of this innovative blind bolted endplate connection to CFT column are identified consisting of steel beam, endplate, CFT column and blind bolt, as indicated in Figure 3.1. For these test specimens, the flush endplate were bolted to the CFT column with this innovative blind bolt. As a follow-up study, the geometric configurations of the joints in this experiment were similar to former monotonic test conducted by Al-Mughairi (2009).

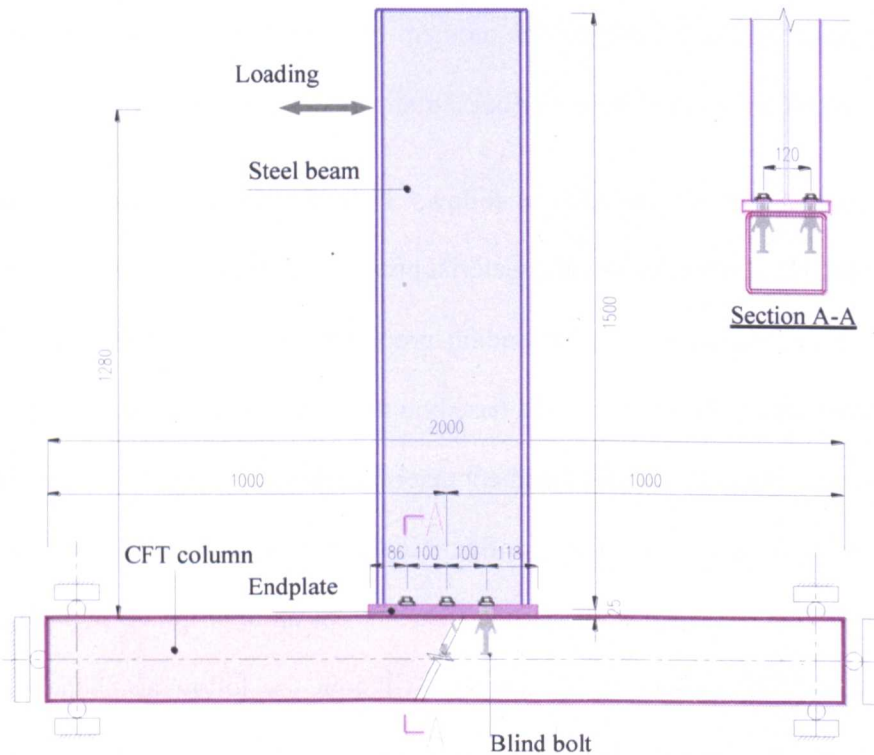


Figure 3.1 Illustration of joint configuration and loading arrangement

The details of tested specimens are listed in Table 3.1. Parameters indicated in test reference are indicated by BBEC- t_c - b_{gr} - c_{gr} - l_p , where, BBEC denotes the blind bolted endplate connection, and other parameters are represented by t_c

(tube wall thickness), b_{gr} (blind bolt grade), c_{gr} (Concrete grade), and l_p (Loading procedure). For instance, Test 4 in Table 3.1, which is referred as BBEC-5-8.8-50-LII, stands for a tested specimen with CFT column of expected concrete strength of 50N/mm^2 and 5 mm thick tube connected using 8.8 Grade blind bolt and tested using cyclic loading procedure type II. The description of the material and loading procedure will be given in Section 3.2.2 and 3.2.6 respectively.

Steel beam with UB 356×171×67 section and 25mm thick endplate were used for all test joints. This configuration was determined to provide sufficient capacity and stiffness of the beam & endplate and eliminate their failure and significant likelihood to influence the connection behaviour. That is eliminating the failure modes of steel beam and endplate in bending, fracture of beam to endplate welds, local beam flange and web in buckling. As mentioned in Chapter 1, it was intended to investigate the cyclic behaviour of the connection in the case of strong beam & endplate with under-strength blind bolt & CFT column. Consequently, the configurations of SHS column section and blind bolt were varied as indicated in Table 3.1. The beam flange and web were connected with fillet welds. Through careful calculation including the safety factor, the size of fillet legs was taken as 12mm along the beam flange and web (Al-Mughairi, 2009). Given the use for cyclic loading, the surfaces of the welds were patiently ground smooth to eliminate possible minute discontinuities which may cause local stress concentration.

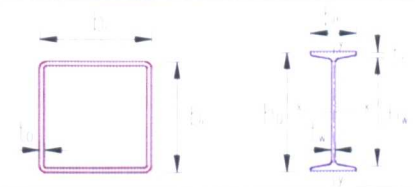
Table 3.1 Details of the test connections

Test No.	Specimen reference	SHS column section		Blind bolt			
		ND $b_e \times b_e \times t_0$ (mm)	AD $b_e \times b_e \times t_0$ (mm)	Bolt grade	Tightening torque (Nm)	Clamping thickness (mm)	
						ND	AD
1	BBEC-8-8.8-50-LI	200×200×8	201.5×201.5×7.91	8.8	190	33	32.6
2	BBEC-8-10.9-50-LI	200×200×8	201.5×201.5×7.91	10.9	300	33	32.6
3	BBEC-8-10.9-50-LII	200×200×8	201.5×201.5×7.91	10.9	300	33	32.6
4	BBEC-5-8.8-50-LII	200×200×5	201.2×201.2×4.92	8.8	190	30	29.62
5	BBEC-6.3-8.8-50-LII	200×200×6.3	201.1×201.1×6.27	8.8	190	31.3	30.97
6	BBEC-6.3-8.8-25-LII	200×200×6.3	201.1×201.1×6.27	8.8	190	31.3	30.97

Note: ND and AD denote nominal and actual geometric details respectively. All steel beam size: UB 356×171×67. All endplate size (mm): 404×220×25. All blind bolt size: M16. Basic case: Test 1. Expected failure modes: I and II. Variables: bolt grade, loading amplitude, tube wall thickness and concrete grade.

Hot-rolled steel hollow sections were adopted for the CFT column. Unlike cold-formed structural hollow sections used in a previously reported test (Wang *et al*, 2009), the hot-rolled counterparts have smaller corner radii, particularly for higher wall thickness tubes, thereby providing better moment capacity and eliminating cracks at the corners of the tube. It was expected that the strength and flexibility of steel SHS column under outward loads are influenced by the thickness and width of the tube wall. Due to the concrete infill, it is apparent that the tube sidewall deformation of hollow section is greatly restrained, thus the flexibility of the CFT column is mostly determined by tube connecting face. Although the slenderness of tube connecting face depends on the tube width and thickness, only the latter effect was chosen as a varying geometric parameter for SHS column. The section sizes were carefully measured using a vernier caliper (metric scale) prior to testing. The actual values were obtained as the mean values of three times measurements at specific locations. The related comparisons against nominal sizes are also listed in Table 3.1. The standard details of steel hollow section are shown in Table 3.2.

Table 3.2 Details of SHS and beam section



SHS column section $b_c \times b_c \times t_0$ (mm)	Area of section (cm^2)	Ratio for local buckling		Second moment of area (cm^4)		Radius of gyration (cm)		Elastic modulus (cm^3)	
		b_c/t_0		x-x	y-y	x-x	y-y	x-x	y-y
201.2×201.2×4.92	38.63	37.60		2481.65		8.02		246.7	
201.1×201.1×6.27	48.86	28.84		3094.52		7.96		307.76	
201.5×201.5×7.91	61.25	22.25		3832.29		7.91		380.38	
Steel beam section ($h_0 \times b_f \times t_w \times t_f$) (mm)	Area of section (cm^2)	Ratio for local buckling		Second moment of area (cm^4)		Radius of gyration		Elastic Modulus (cm^3)	
		b_f/t_f	h_w/t_w	x-x	y-y	x-x	y-y	x-x	y-y
UB 356×171×67 (363.4×173.2×9.1×15.7)	85.5	5.52	34.2	19500	1360	15.1	3.99	1070	157

Note: SHS column section and steel beam section refer to codes BS 5950-1:2000, BS EN 10210-2: 1997 and BS 5950-1:2000, BS EN 4-1: 1993 respectively.

The blind bolts used in the presented test program are the Extend Hollobolt devised at the University of Nottingham and provided by Lindapter International Ltd. The assembly of this innovative blind bolt is shown in Figure 1.1 and its measured geometric details are indicated in Table 3.3. The size for all bolts adopted in the tests was M16. The bolt shank is 150mm long with an end anchor nut. To prevent unexpected rotation and removal of the anchor nut in the process of placing and vibration of the concrete, a secure method called 'lock tight' was used. Three bolt rows were considered for all test specimens with 100mm pitch width and 120mm gauge width. The blind bolts with two bolt grades were used: grade 8.8 and grade 10.9. The layout of bolt rows is slightly asymmetry along the neutral axis of the steel beam, introducing a deviation of 16mm, as shown in Figure 3.1. The intentions for using this asymmetrical arrangement are two-fold. Firstly, the geometric

configurations of beam to column connections in actual structural engineering are mostly in asymmetry due to the presence of slab, which to some extent affects the moment behaviour of the connection. On the other hand, the strength, stiffness and ductility are inherently affected by the bolt pitch distance (Barnett, 2001). Using slightly asymmetric arrangement of bolt rows with respect to the beam neutral axis, the strong side and weak side of the connection can be easily foreseen in relation with positive or negative moment. For the purpose of simplicity, the behaviours of the weak side and strong side of the connections are assumed to undergo positive and negative bending moments respectively. In this study, a comparative observation was also made for the moment behaviours of the connection under both moment directions.

Table 3.3 Geometric details of a sample M16 Extended Hollobolt

Blind bolt components		Size (mm)	Blind bolt components		Size (mm)
Bolt head	hexagon side length	18.12	Upper cone	Upper cone height	12.37
	Height	10.25		Lower cone height	5.47
Bolt shank	Length	150.02	Threaded cone	Upper diameter	20.56
	Diameter	15.81		Middle diameter	25.13
Collar	Outer diameter	36.94		Lower diameter	19.32
	Inner diameter	17.26	Rubber washer	Outer diameter	26.34
	Height	8.06		Inner diameter	16.22
Sleeve	Outer diameter	25.37	Anchor nut	Height	4.85
	Inner diameter	17.13		hexagon side length	15.59
	Overall length	63.06	Height	12.46	
	Slot length	36.87			

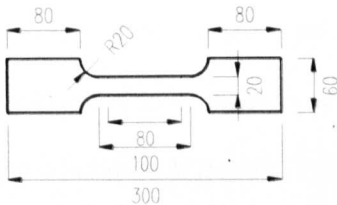
3.2.2 Material properties

In structural design, the nominal material strengths are often used and indexed according to the material grades. Apparently, the actual material strengths in an experiment may present certain discrepancies with nominal ones. For the sake of analysis and comparison of tests results, it is of importance to measure the actual strengths of the test materials. This is especially significant for the

connection featured by the tensile behaviour. For this purpose, the material properties of the steel beam, SHS column and bolt shank were all tested according to the relevant standards such as BS 5950-1 (2000), BS EN 10210-2 (1997) and BS 4-1 (1993). As several structural components in the present tests were shared from the same batch of the materials used for former monotonic tests, the material properties of these components were referred from previous reports (Al-Mughairi, 2009; Fang, 2010). The test material properties described herein only include Young's modulus and strength values. Related stress-strain relationships will be presented in Chapter 6 in contrast with those adopted for finite element models.

To determine the fundamental properties of the steel of SHS columns, a series of tensile coupon tests were carried out. The tensile coupons were designed according to EN 10002-1:2001, as indicated in Table 3.4. Then, the coupon pieces were cut from the same SHS tube used for actual connection tests and shaped with flats at the ends. The 8mm thick hollow section tubes used in the connection tests were in the same batch used for the monotonic tests carried out by Al-Mughairi (2009). The tensile coupon tests were conducted using Zwick/Roell 1484 computer controlled universal test machine. The overall length of the coupon pieces was loaded including the parallel length portion and the transition between the gripped and parallel portions. The loading was controlled with the rate of 20mm/min, and continued until the tensile failure happened. The test were monitored and data recorded using Zwick/Roell PC version 5.50a software, which has basic data processing features in exporting Young's modulus, maximum and ultimate tensile forces. The stress producing 0.2% residual strain was used to define the material yield strength.

Table 3.4 Material properties of connection components



SHS column					
Test No.	Specimen reference	Section $b_c \times b_c \times t_0$ (mm) Bolt grade	Young's modulus (N/mm ²)	Yield strength (N/mm ²)	Ultimate strength (N/mm ²)
1	BBEC-8-8.8-50-LI	200×200×8	199114	435	511
2	BBEC-8-10.9-50-LI	200×200×8			
3	BBEC-8-10.9-50-LII	200×200×8	197194	433	522
4	BBEC-5-8.8-50-LII	200×200×5			
5	BBEC-6.3-8.8-50-LII	200×200×6.3	190512	423	514
6	BBEC-6.3-8.8-25-LII	200×200×6.3			
Steel beam					
-	All specimens	UB 356×171×67	194205	500	581
Bolt shank					
1	BBEC-8-8.8-50-LI	Grade 8.8	194204	752	918
2	BBEC-8-10.9-50-LI	Grade 10.9	209722	883	1082
3	BBEC-8-10.9-50-LII	Grade 10.9			
4	BBEC-5-8.8-50-LII	Grade 8.8	194204	752	918
5	BBEC-6.3-8.8-50-LII	Grade 8.8			
6	BBEC-6.3-8.8-25-LII	Grade 8.8			

Note: the data of steel beam and 8mm thick SHS column, and the modulus and yield stress of bolt are taken from Al-Mughairi (2009).

As a blind bolted connection in tension, the important role of bolt shank for the connection strength was expected. The tensile tests were also performed to obtain the tensile strength of the bolt shank. According to BS EN ISO-898-1, the Young's modulus & yield strength and ultimate strength of the bolt shank can be obtained from the tensile tests of a machined bolt and a full-size bolt respectively. In view of the blind bolts used in the present tests are taken from the same batch as those in former monotonic tests, only the ultimate strengths of full-sized bolts were tested. Likewise, the Zwick 1484 computer controlled universal test machine was used in this test. As the size of a bolt sample is different from flat shape of a coupon, a set of specially fabricated grips was

used to clamp the bolt properly on the machine. After the test, the ultimate tensile stresses were taken as the mean values for the tested bolt samples as indicated in Table 3.4.

The concrete infill was assumed to affect the behaviour of the connection by limiting the tube sidewall deformation and accommodating anchorage to this innovative blind bolt. The strength of concrete infill was expected as an influential factor of the connection performance. In practical design, the mix to achieve required concrete strength should be designed according to related standard recommendations. The recent design guide (Corus Tube Library Publication, 2009) suggests the concrete infill with plain concrete mix is in the condition that the maximum size of aggregate being 10mm for 100mm minimum section columns, 20mm for 140 to 180mm minimum section columns and 40mm for 200mm minimum section columns. The concrete in the present tests was made with Portland limestone cement and Trent Valley aggregate of 40mm maximum size. The details of concrete mixture proportion and curing condition are indicated in Table 3.5. According to the procedure of standard cube tests, the concrete cubes of 100×100×100mm were cast at the same time as the connection specimens and cured in water at the temperature of approximately 20°C. The compressive strength of concrete was obtained from the concrete cube compression tests using a Denison compression test machine. Test results are summarized in Table 3.6, including the data for the concrete curing after 7 days, 28 days and the day of full-scale joint test.

Table 3.5 Concrete mixture proportions and curing condition

Concrete mixture proportions			
Material	Mix ratio		Descriptions
	Test No.1 to No. 5	Test No. 6	
Cement	1	1	Portland limestone cement
Coarse aggregate	2.35	3.63	Trent Valley aggregate maximum 40mm
Fine aggregate	1.65	3.33	2mm river sand
Water	0.43	0.74	Tap water

Curing condition:
Cured with room temperature 20°C; cubic compressive strength at 28 days.

Table 3.6 Concrete infill compressive strengths (N/mm²)

Test No.	Specimen reference	Compressive strengths (N/mm ²)		
		7 days	Test days	28 days
1	BBEC-8-8.8-50-LI	47.03	53.20	53.50
2	BBEC-8-10.9-50-LI	43.15	47.40	52.35
3	BBEC-8-10.9-50-LII	46.60	51.55	54.73
4	BBEC-5-8.8-50-LII	45.73	49.13	56.33
5	BBEC-6.3-8.8-50-LII	49.30	52.75	56.50
6	BBEC-6.3-8.8-25-LII	17.77	20.77	26.23

3.2.3 Fabrication of test specimens

The test specimens were fabricated starting from steel components assembling to concrete casting. As the welding between the steel beam and endplate was performed in the workshop, the assembly work here refers to the bolt tightening in the laboratory. The beam endplate was lifted using crane and aligned above the bolt holes located tube connecting face to ensure the blind bolts placed through the bolt holes of endplate and SHS column. Thereafter, the blind bolts were initially tightened with a spanner and then at later stage with a torque wrench in accordance to the required torque values given in Table 3.1. Given the contact surfaces between the endplate and the SHS column face may not be exactly flat, the blind bolts were tightened using side interval orders. As shown in Figure 3.2, the top left bolt above the beam web was tightened first (label 1) and then the bottom middle below the beam web

(label 2), preceding the top right bolt above the beam web again (label 3). As the procedure continues until label 6, a tightening cycle was finished. Figure 3.3 shows blind bolt rows subsequent to this tightening procedure.

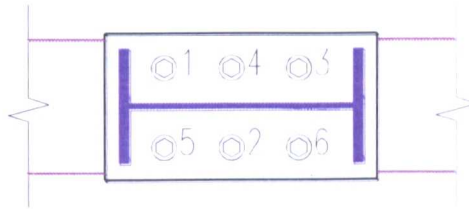


Figure 3.2 Illustration of blind bolt tightening sequences

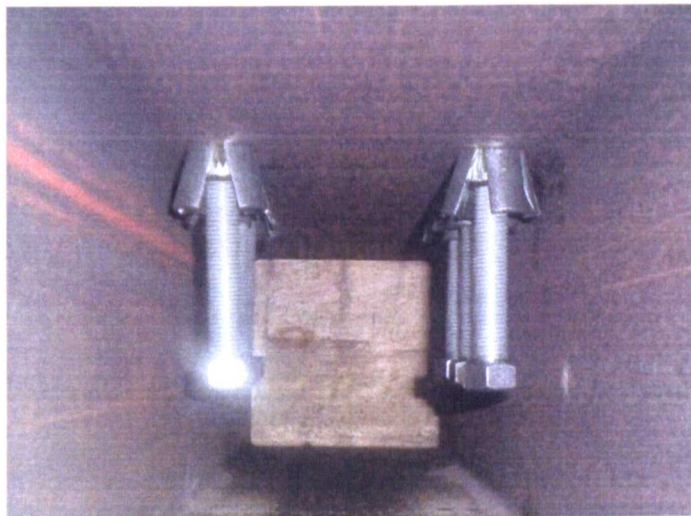


Figure 3.3 Tightened blind bolts in SHS column

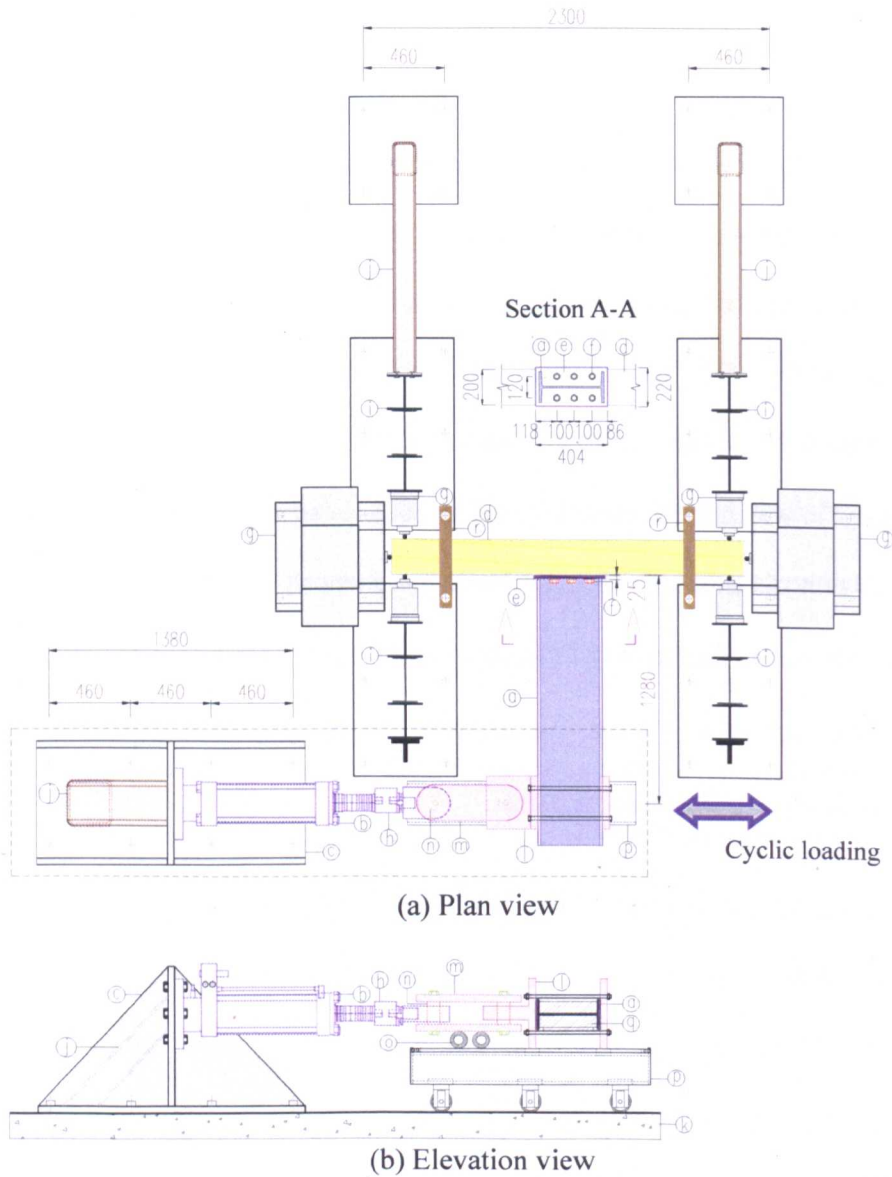
Following the bolt tightening, all loose material and debris produced during the previous installation process and transportation were removed to clear the internal surface of SHS columns. The popular ways of filling concrete in hollow section refer to top filling and bottom pressure filling. Although the latter way has become popular in several recent reported Australian projects (Goldsworthy & Gardner, 2006), the former way was used in this experiment for its simplicity without special equipments required. Prior to concrete

placing, a beam-to-column connection specimen was erected with adequate bracing and ready for concrete mix dropping into the column from the top. The bottom end of the column was plate padded with polystyrene gluing up around the perimeter of the hollow section to avoid the mix running out. The filling was simultaneously carried out by placing concrete mix placed using hand trowels and compacting using vibrating poker. The vibrating poker should be moved up in time as concrete surfaces rises. This is especially important for the concrete infill at the bottom column where insufficient amount of coarse aggregate may cause voids between aggregate particles.

3.2.4 Test set-up

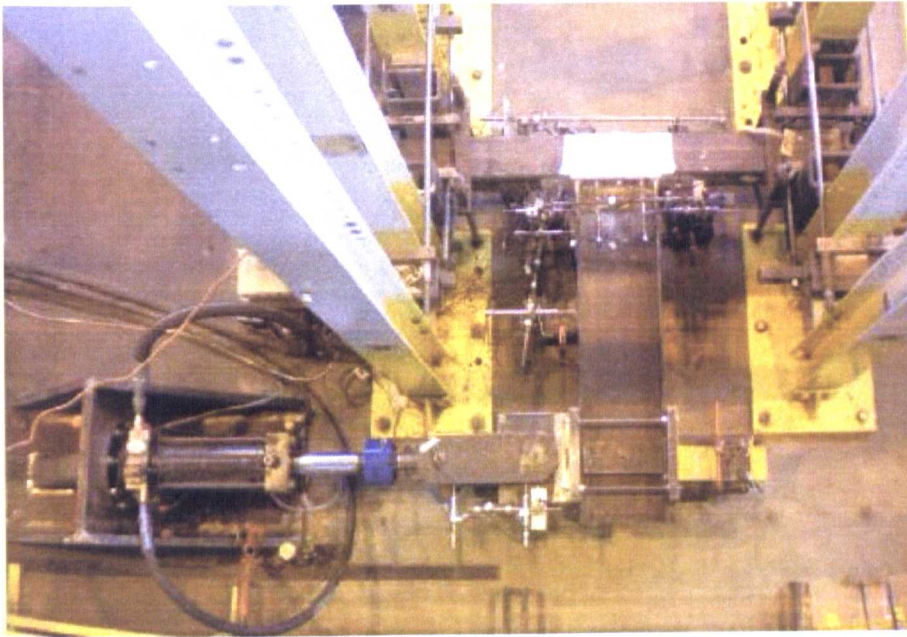
From the literature review, there are two representative test set-ups usually used by recent researchers, i.e., test in the vertical plane incorporating the gravity vector and test in the horizontal plane normal to the direction of the gravity vector. The former test set-up was used in several recently reported experiments regarding the blind bolted beam to column connections (Elghazouli, *et al*, 2009; Lee, *et al*, 2011). The uses of latter test set-up were reported by Ryan (1999) and Sumner & Murray (2002) at Virginia Polytechnic Institute and State University in testing bare steel bolted endplate connections. Both set-ups in the test of joint behaviour have their own merits. The first set-up is relatively simple in the configuration of loading point on the cantilever beam and better accommodating composite joints. In contrast, the second set-up lowers the height of the actuator from ground level which reduces the loading demand for reaction frames fixed on the strong floor.

To make good use of available apparatus in the department's laboratory, the beam to column connection specimens in the present study were tested in the horizontal plane normal to the direction of the gravity vector. A representative test-up in the present experimental study is shown in Figure 3.4. The main point in the design of test set-up was the intention of minimizing the stress and deformation in the test frame members and connections. Another consideration in the test apparatus was the floor anchoring pattern in the laboratory, in which the anchor points distributed in square grid with a centre-to-centre unit distance of 460 mm. The M24 anchor bolts were available at each anchor point. The layout of Lateral & end blocks (g), reaction buttress (c) and frame columns (i) are pre-designed with sufficient precision to accommodate the grid of anchor points.



No. Test specimen & apparatus	No. Test specimen & apparatus
a Test steel beam	h Load cell
b Horizontal actuator	i Frame column
c Reaction buttress	j Lateral brace
d Test CFT column	k Strong floor
e Test endplate	l Head cap
f Blind bolts	m Rigid link
g Lateral & end blocks	n Link roller: rotation
o Link roller: translation	
p Sliding base	
q Local support & packing	
r Out-of-plane restraint & tie-downs	

Figure 3.4 Illustration of a representative test set-up



(a) Plan view



(b) Rear view

Figure 3.5 Photograph of a representative test set-up

The CFT column (d) of a test specimen was securely fastened into the test rig by roller supports positioned at both column ends to prevent any sideway and

horizontal movements. To avoid local crushing of concrete, two smooth surface plates were attached at the surfaces of both column ends in contact with roller supports. The column lateral restraints (r) in the vicinity of the column ends stopped the CFT column from out of horizontal plane lifting by bolting tied to the anchorage points on strong floor. To ensure global stability and integrity of the frame system, the frame columns (i) were restrained with long bolts in the transverse direction of the test column and externally braced (j). A photograph of these details of test rig is shown in Figure 3.5. As the CFT column face was expected to undergo local deformations induced by the blind bolt in tension, the tube connecting face and sidewall face of the CFT column were coated with a hydrated lime solution for the purpose of observing yield line formation patterns.

A photograph of overall loading system used in the test set-up is described in Figure 3.6. A 450kN actuator provides horizontal cyclic loads to the steel beam at 1.28m from the column face which give rise to bending moment for the blind bolted connection. The actuator was connected with a 40mm thick rectangular middle plate on an especially designed reaction buttress as shown in Figure 3.7. The reaction buttress with 40mm thick rectangular side plates and reinforced with a compression braced (150×150×10mm) was designed to ensure sufficient strength and stability.

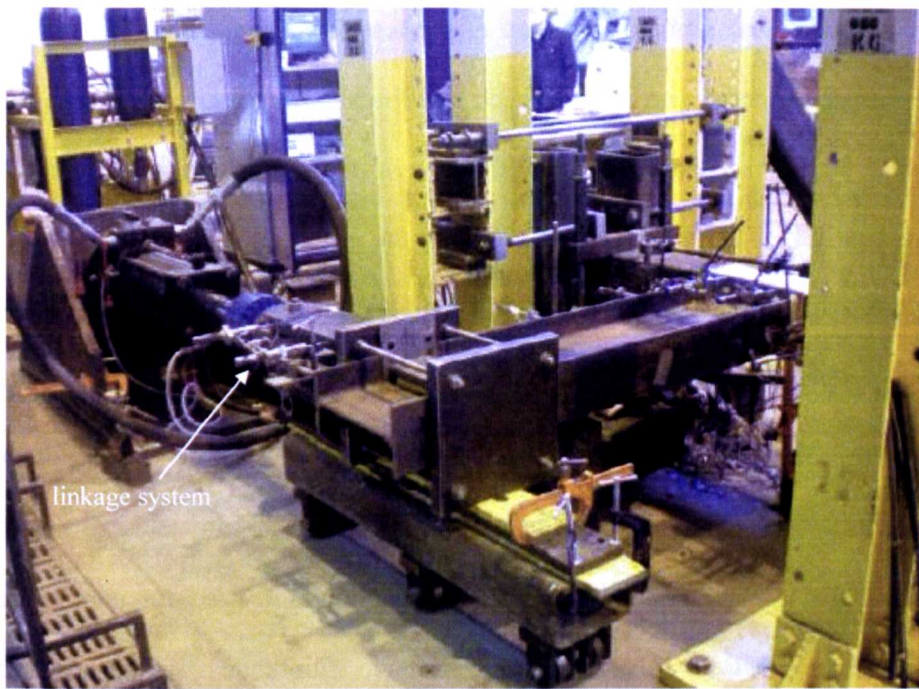


Figure 3.6 Photograph of loading arrangement

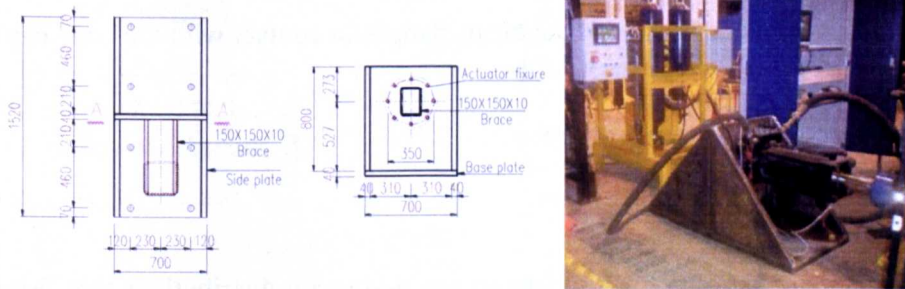


Figure 3.7 Illustration of reaction buttress designed for actuator

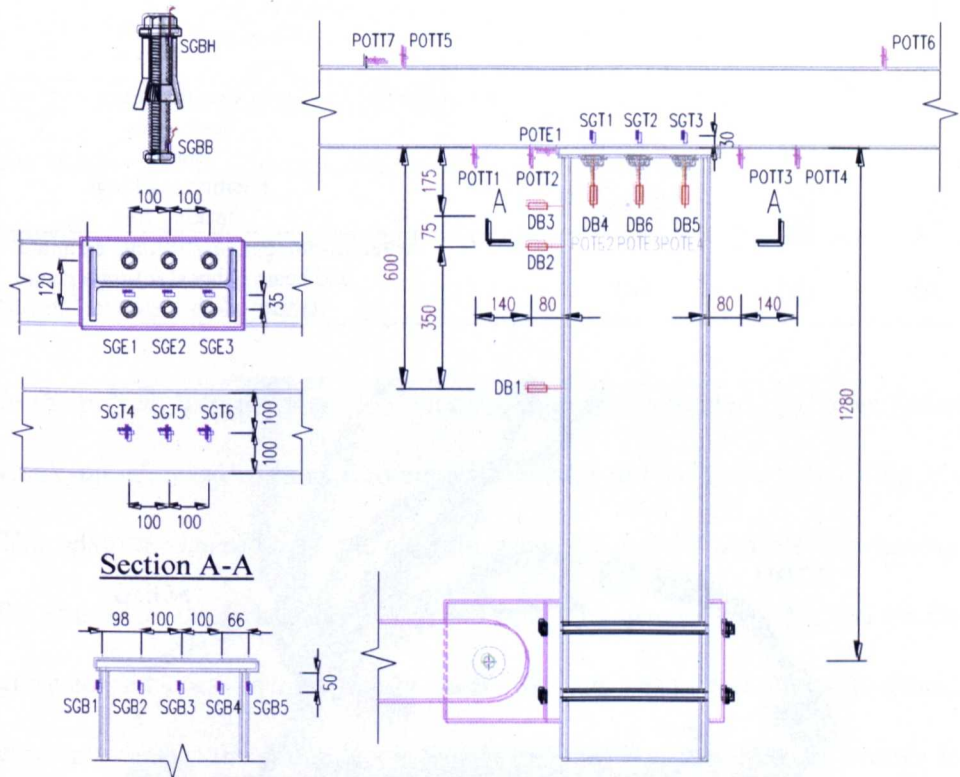
For the purpose of properly transferring the load supplied by the actuator, a linkage system was constructed between the actuator and the test beam. As the horizontal load on the tip of the beam, the original loading point on the beam would not remain at same location horizontally as the beam rotates. Rather, it would translate in the direction parallel and normal to the original horizontal axis. Consequently, the linkage system should be able to accommodate this variation such that it will not deform the horizontal extension of the actuator. As a section view shown in Figure 3.4, a sliding base attached by three pairs of horizontal rollers underneath was applied to carry the gravity and

accommodate the global movement of the test beam and the linkage system. To ensure the test beam moving back and forth, a head cap supported by the sliding base was used to clamp the free end of the beam. A rose joint (i.e., rod end bearing or heim joint) at the end of the extension of the actuator was connected with the head cap (l) using a couple of rigid links (m). To avoid any load produced by the gravity of the rigid links, two small horizontal rollers (o) were also considered together with the rigid link couple for the purpose of carrying the local translation and rotation of the test beam and the linkage system respectively. Additionally, the lubrication was used for compressed components within this linkage system to eliminate friction between constituent parts. Whist the load is transferred to the test beam, two plates were tightly padded between the beam flanges in contact with the head cap as stiffeners.

3.2.5 Instrumentation

In order to obtain the load, displacement, and strain distributions that feature the response of the connection, a range of instrumentation was used to monitor the response of the specimens during the test procedure. A representative layout of the instrumentation adopted in the test is shown in Figure 3.8, including strain gauges, potentiometers and LVDTs for steel beam, bolted endplate, and steel tube. The details of instrumentation will be described below.

3.2.5.1 Strain gauges



Instruments	No.	Label	Measured quantity	Units
Load cell	1	-	Applied load	kN
LVDT	3	DB	Beam displacement	mm
	3	DE	Endplate displacement	mm
Potentiometer	7	POTT	Tube displacement	mm
	1	POTE	Endplate displacement	mm
Strain gauge	3	SGE	Endplate strain	
	6	SGT	Tube connecting face strain sidewall face strain	$\mu \epsilon$
	5	SGB	Beam strain	
	4	SGBH,SGBB	Bolt shank local strain near bolt head and anchor nut	

Figure 3.8 Illustration of representative test instrumentations

Table 3.7 Summary of electrical resistance strain gauges used in the tests

	Labels	Gauge type	series	Gauge factor
	(a)	Single element	FLA-6-11	2.10
	(b)	Single element	FLG-1-11	2.08
	(c)	Two element cross	FCA-6-11	2.10
Labels	Components			
i	lead wires			
ii	Grid			
iii	Position markings			
iv	Backing film			
Note: (a)-bolt gauge; (b)-tube, endplate and beam gauges; (c)-tube gauge				

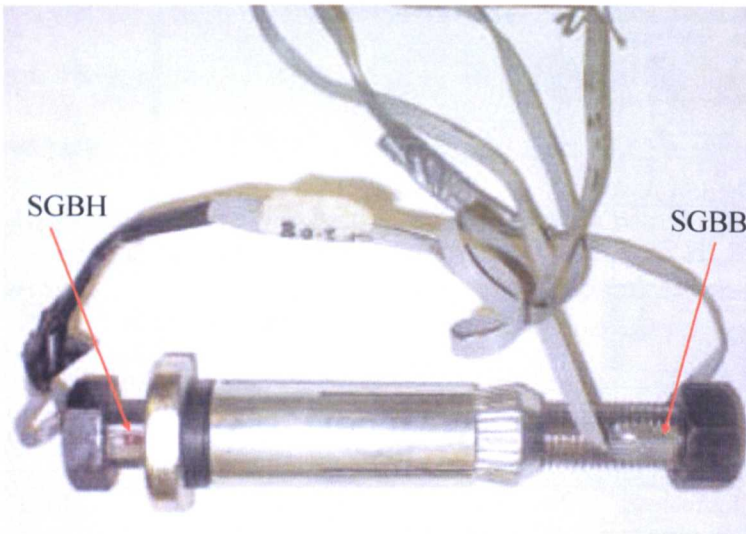


Figure 3.9 Representative strain gauged blind bolt before tightening

The electrical resistance strain gauge has been widely used today as a relatively simple and inexpensive instrumentation to precisely measure surface strain. The work principal of the electrical resistance strain gauge is based on the fact that the electrical resistance of metal wire changes with strain. A representative configuration of a strain gauge consists of lead wires, an etched foil grid, position markings and a piece of backing film as indicated in Table

3.7. The single element gauges are configured to measure strain in single direction (also called linear gauges), while the two element gauges measure strains in two directions perpendicular to each other (i.e., 0° and 90°). Gauge factor (also called strain sensitivity), which is defined as the ratio of relative change in electrical resistance to mechanical strain, is an important parameter for strain results. To achieve accurate measurement, it is prerequisite to carefully install the strain gauges according to the procedures specified in related product documents.

In the present test, three types of strain gauges manufactured by Tokyo Sokki Kenkyujo Co., Ltd were used to measure surface strains, as listed in Table 3.7. The relatively small sized one element gauge FLA-6-11 was used to monitor the strains on the bolt shank of a blind bolt. The gauges were bonded on the grooved surfaces symmetrically near the top and bottom bolt shank, corresponding to the gauge labels SGBH and SGBB respectively, as shown in Figure 3.9. Without similar free spaces of the bottom shank, the wires connected to the gauges at the top shank should be passed through slots on the bolt head. The gauges at the top shank are used to measure changed strain values for preload estimation. During the bolt tightening process, it is advisable to turn the spanner and torque wrench with caution to prevent any damages of the connecting wires. The grooved surfaces near the top shank may cause reduced cross-section of the shank and weakened the bolt tensile capacity. Consequently, the strain gauged blind bolt was only installed at the middle bolt row of the connection.

The single element strain gauges (FLG-1-11) on the surfaces of the flange and

web of steel beam and endplate were used to monitor strains and check if the beam and endplate were in elastic state as assumed in the pre-design of the connection. As shown in Figure 3.8, there are five gauges in line on the steel beam: two on the upper and lower flanges, and three on the web corresponding to each bolt row. The arrangement on the endplate also consists of three gauges located in line at each bolt row.

The strain distributions on the column were of interest for both tube connecting face and sidewall face. To allow for the strains in the directions parallel and perpendicular to the bolt row, two elements cross gauges (FCA-6-11) were mounted on the tube connecting face as shown in Figure 3.10. The endplate in contact with the connecting face of the tube has three circular grooves underneath which in place accommodate strain gauges in the middle of each bolt row. The slots connecting to the grooves were also made through the endplate so that the wires could pass through properly. Due to limit spaces involved with the grooves and related gauges, it is worth checking the gauges with caution before and after bolting the endplate during the test preparation. The strain gauges to monitor the strains on the tube sidewall surfaces were placed 30mm away from the connecting face level and related with the each bolt row. It was felt the un-necessity to measure the strains deeper down the tube sidewall face due to very small strains at the middle of the tube sidewall face as formerly reported by Al-Mughairi (2009). Moreover, only the single element gauge was adopted for this measurement on the tube sidewall face as shown in Figure 3.11.

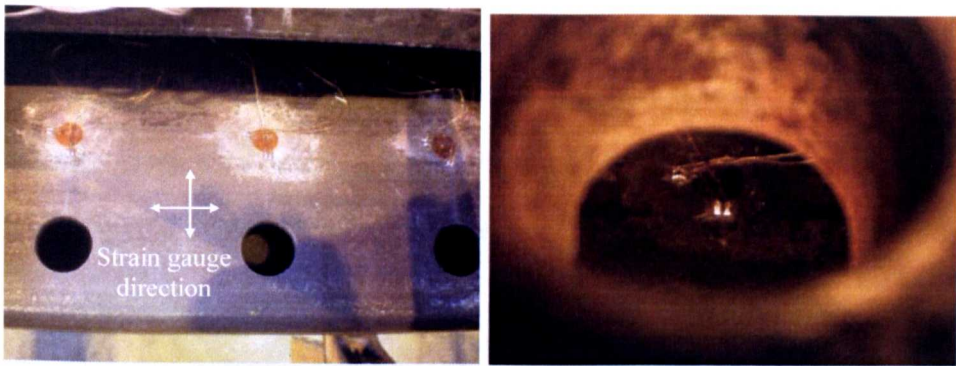


Figure 3.10 Photograph of strain gauge pattern on tube connecting face

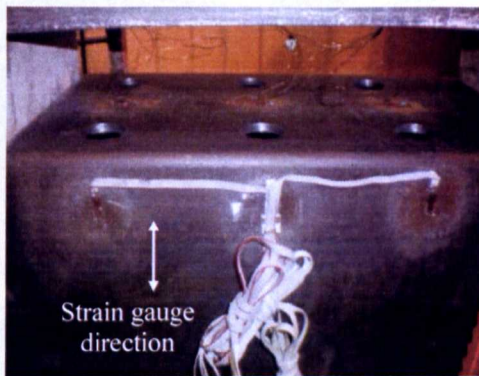


Figure 3.11 Photograph of strain gauge pattern on tube sidewall face

3.2.5.2 Potentiometers

Potentiometers are position sensors that are often used to provide an accurate measurement of displacement. The measuring configuration of potentiometers is based on the moving contact between the wiper and the resistance strip. As the measurement ranges of available potentiometers are up to 15mm, it should be kept in mind to monitor the position variation on the related structural component within this range. As shown in Figure 3.12, the potentiometers were installed near the supports and on the tube connecting face adjacent to the endplate monitoring the horizontal and transverse displacements. Also, a further potentiometer (POTE1) was used to record any possible slippage between the endplate and the CFT column. These potentiometers were determined to record the data for global model rotation and local deformation.

The related consideration for calculation will be presented in Section 3.3. For the test specimens without too large rotation capacity expected for the connection (e.g. test specimen No 2), the potentiometers were considered on the endplate at each bolt row, as the dashed line label shown in Figure 3.8.



Figure 3.12 Photograph of potentiometer arrangement on tube connecting face

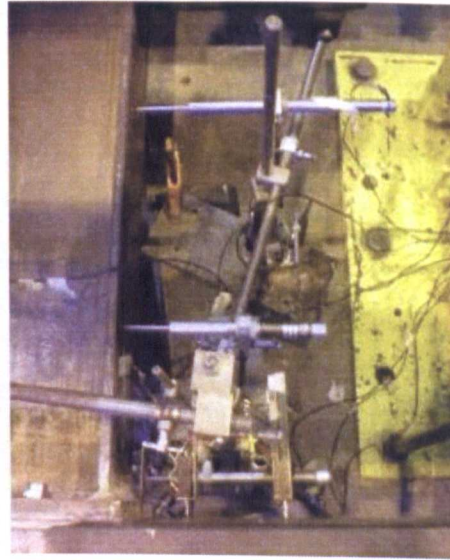


Figure 3.13 Photograph of LVDT arrangement on steel beam

3.2.5.3 LVDTs

Linear Variable Differential Transformers (LVDTs) are widely used for reliable displacement and position measurements. Unlike potentiometers, the LVDTs have no physical contact between the moving and stationary parts which reduce the possible consequences of wearing out or corrosion. Moreover, LVDTs are often used with wider range of measurement than potentiometers. The measurement ranges of available LVDTs in this study were within $\pm 60\text{mm}$ and $\pm 25\text{mm}$ for DT1 and the other LVDTs respectively

(referring to Figure 3.8). Three sets of LVDTs on steel beam (DB1, DB 2 and DB 3) and another three sets on endplate were used to monitor the displacements on the steel beam and endplate respectively for the test specimens with relatively large joint rotations. For the other specimens, on the other hand, only the steel beam was monitored with LVDTs (the endplate displacements were measured by potentiometer as mentioned previously). Although not plotted in Figure 3.8, multiple LVDTs were considered and employed to measure the displacements on the steel beam to provide redundant experimental data.

During LVDT installation process, it is a good practice to inspect that the original location of needles are in appropriate condition for positive and negative displacements, and replace the LVDT if it is found any damage or unreasonable output readings. If possible, it is advisable to monitor the performances of all potentiometers and LVDTs while applying a small number of elastic load cycles to the specimen, prior to formal test.

3.2.5.4 Load cell

In the test rig of this research, a 450kN load cell (Model: 1232AF) manufactured by Interface Inc was used to monitor the load applied by the actuator as shown in Figure 3.4. Before fitting it into actuator, the load cell was calibrated in accordance with relevant specifications. Figure 3.14 briefly illustrates the load cell in calibration process. To account for possible eccentric loads involved in the test, a calculation was made to check if the capacity of the load cell and the actuator could be satisfied.

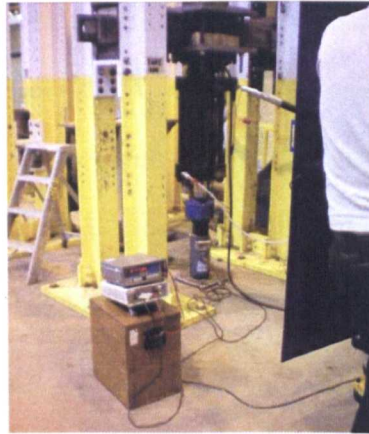


Figure 3.14 Calibration of the load cell fitted into actuator

3.2.5.5 Data logger

The data loggers were used in this test for the data acquisition during the blind bolt tightening process and the connection test. The Orion delta data logger was used for blind bolt tightening process. As mentioned in sub-Section 3.2.5.1, the variations of strains before and after bolt tightening at the top shank were recorded by this logger. The calculation and comparison of bolt preload using these bolt strain readings will be presented in sub-Section 6.3.1.



(a) Orion delta data logger



(b) Schlumberger data logger

Figure 3.15 Data logger and computer link system

For the connection tests, the Schlumberger data logger was used in all tests to collect the data electronically from the strain gauges, potentiometers, LVDTs and load cell. As a backup, the Data Taker DT 800 acquisition system was also used in tests No. 1 and No. 2 for LVDT recordings. Both logger systems have powerful operating system and internal file structure. Controlled by computer, the data was recorded automatically. Meanwhile, the recordings were displayed by live plotting a group of selected data during the test. For instance, the readings from the load cell and a LVDT furthest from tube face were plotted as a x-y plot on the computer screen. The recording papers were also printed as a hard copy every 40 seconds. This allows the performance of the test being in time monitored immediately and saved on backup papers. After the test, all the data were transferred by Schlumberger package to Microsoft EXCEL spreadsheet formats for further data analysis.

3.2.6 *Quasi-static cyclic loading procedure and control system*

As mentioned earlier, the cyclic loading history is determined on the basis of the purpose of the experiment. Considerable loading histories have been proposed in cyclic tests to assess the force-deformation or moment-rotation characteristic of the structure. The loading procedure suggested by ECCS (The European Convention for Constructional Steelwork, 1986) was adopted in this experiment for cyclic loading test.

The ECCS loading procedure has been accepted in academia as one of standardized methods relating interpretative parameters to the demand of seismic recommendation. In the research of bolted endplate beam-to-column connections, the ECCS loading procedure has been widely adopted in recent

investigations for endplate connections with standard bolts (e.g. Kovács *et al*, 2008) and blind bolts (e.g. Elghazouli *et al*, 2009). In the standard ECCS recommendations, at least four levels of displacements are performed before the yielding displacement of the joint (δ_y). As for the subsequent inelastic phase, the loading procedure is performed in three cycles at each loading amplitude as even multiplier of δ_y , i.e., $2\delta_y$, $4\delta_y$, $6\delta_y$, $8\delta_y$. . . In this study, a small adjustment is also made to the increment of loading amplitude as $0.5\delta_y$ instead of $2\delta_y$ in ECCS procedure for tests No. 1 and No. 2. This was considered as limited rotation capacity for both specimens with the relatively strong CFT columns. The adjusted procedure is labelled as cyclic loading procedure type I, as indicated in Table 3.1. On the other hand, the standard ECCS procedure applied for the other specimens is labelled as cyclic loading procedure type II. Both loading procedures are illustrated in Figure 3.16. The cyclic loading was applied within the displacement range of the stroke.

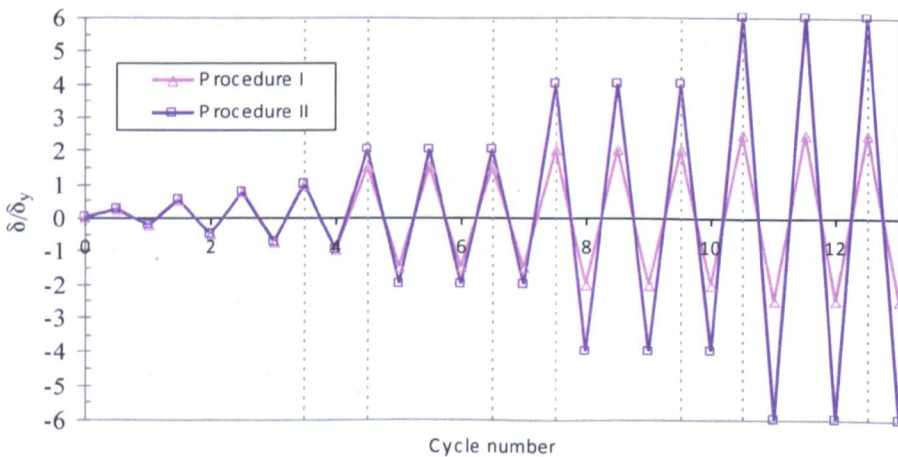


Figure 3.16 Illustration of cyclic loading procedures

The loading system manufactured by Servocon Systems Ltd. was used in this experiment. The control was assisted by a set of computer programmed

system to coordinate the movement of the hydraulic actuator, the load data acquisition and the instant display of selected data. Figure 3.17 shows a representative display of the system input screen. This screen presents basic information of load and displacement recorded by the system on the right. The primary input information is displayed in the middle screen including the load/displacement target for each loading process, the loading rate per second, and the hold time after each loading. Using this input, the control system imposes the required cyclic loading procedure on the hydraulic actuator.



Figure 3.17 Display of Servocon loading controller

3.3 Measurement of joint rotation and moment

Due to the complexity of the joint system and test apparatus used in the test, it was difficult to obtain the joint rotation and moment from the instrumentation at a given measuring point. Rather, the measurements of joint rotation and moment are based on the geometric relationships related to the instrumentation on the joint as well as the test apparatus. This section describes the measurements of joint rotation and moment, which were used to analyse the data recorded through the test.

3.3.1 Joint rotation measurement

The approaches for joint rotation measurement reported in the literature (referring to Appendix A) vary in terms of joint configurations (single sided or double sided configuration) and loading patterns (symmetrical or unsymmetrical loading). It is noted that the joint rotation measurements in most of these studies refer to the rotation due to the beam displacement as the main rotation source. There are still some other studies in which the relative deformation between the column flange and endplate was recorded to calculate the joint rotation (referring to Shi *et al*, 2007). Due to unavailable space inside the CFT column for instrumentation, only the former approach was considered in the present study. Given the contribution of joint components to the rotation, from the theoretical point of view, the overall rotation, θ_o , consists of three components, i.e., the beam deformation induced rotation (bending and shearing effects), θ_b , the joint rotation, θ_j , and the column rotation, θ_c , as shown in Figure 3.18.

As the loading is applied on the beam side, the overall rotation is the rigid body rotation of the beam relative to the column centreline. The magnitude of the overall rotation can be calculated as the ratio of the counterpart rigid displacement on the beam, excluding the local endplate slippage and column rigid displacement along the centreline direction, to the distance from the column flange face (L_b) as shown in Figure 3.19.

It is apparent that the beam rotation (bending and shearing effects) can be ignored when L_b is relatively small and the area of the beam web (A_w) is relatively large. Consequently, most LVDTs on the beam flange in this test were located adjacent to the CFT column connecting face (referring to Figure 3.8). The beam section area was checked to satisfy the requirement of elasticity (i.e., beam remains elastic at maximum load applied). This consideration was also in agreement with the suggestions indicated in previous report (Al-Mughairi, 2009). Thus, the beam rotation (bending and shearing effects) is not included in this study for the joint rotation.

The column rotation takes place as the translation of the rigid body induced by the unbalanced moment. To allow for the column rigid body rotation, the aforementioned two potentiometers were used near the transverse supports of the column. The magnitude of the column rigid body rotation can be obtained by dividing the difference of displacement by the distance between both of potentiometers.

The joint rotation consists of the components in the beam-to-column connection system. Figure 3.18 indicates the joint rotation (θ_j) relationship with respect to θ_b and θ_c . As already mentioned, θ_b was assumed to

benegligible such that the joint rotation can be calculated as:

$$\theta_j = \theta_o - \theta_c \quad \text{Equation 3.1}$$

The related relationship is schematised in Figure 3.18.

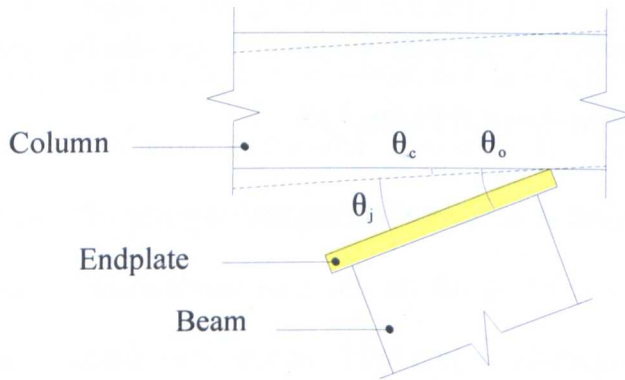


Figure 3.18 Schematic graph of joint rotation relationships

3.3.2 Joint moment measurement

The moment of a joint with a cantilever beam is generally obtained by the product of the applied force normal to the beam flange and the loading point lever arm. Due to the introduction of the linkage system, the forces applied on the steel beam were taken into account by appropriate conversion of the horizontal force provided by the hydraulic actuator (T), as shown in Figure 3.19.

Figure 3.19 shows a schematic graph of transforming geometric relationship of the linkage system and the steel beam. Assuming that the rigid links have no self-deformations, the horizontal movement of the hydraulic actuator (δ_{ac}) produces the beam rotation as well as the rigid links spinning around link roller (Point: D) which result in the rotation angles θ_j and γ respectively. Based on the theoretical trigonometric relationship, γ can be obtained from the

function: $\gamma = \sin^{-1}[L_{EA} \sin(\theta_j) / L_{DE}]$, in which L_{EA} and L_{DE} are the rigid link length and head cap depth respectively. Given two points on the rigid link (Points: f and g), on the other hand, the related trigonometric relationship can be obtained using measured displacements δ_{ff} and δ_{gg} at points f and g respectively. Then, $\theta_j + \gamma$ can be calculated as: $\sin(\theta_j + \gamma) = (\delta_{ff} - \delta_{gg}) / L_{fg}$. As such, it was determined to install two LVDTs at these two points on the rigid link. Once the displacements are obtained, the γ can be calculated as $\{\text{asin}[(\delta_{ff} - \delta_{gg}) / L_{fg}] - \theta_j\}$. As indicated above, it is noted that γ can be obtained by two methods, as trigonometric relationship calculation and LVDT measurement of $(\theta_j + \gamma)$. Based on the test results, a contrast of γ from both methods will be presented in sub-Section 4.3.1.

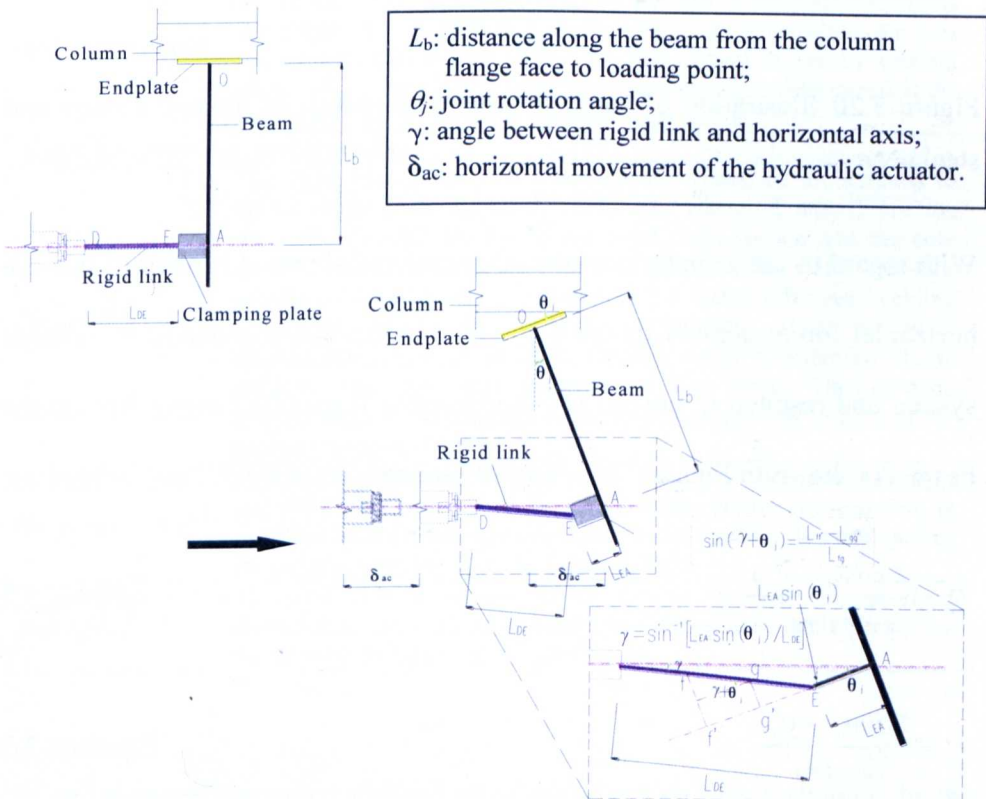


Figure 3.19 Illustration of geometric relationship of linkage system and steel beam

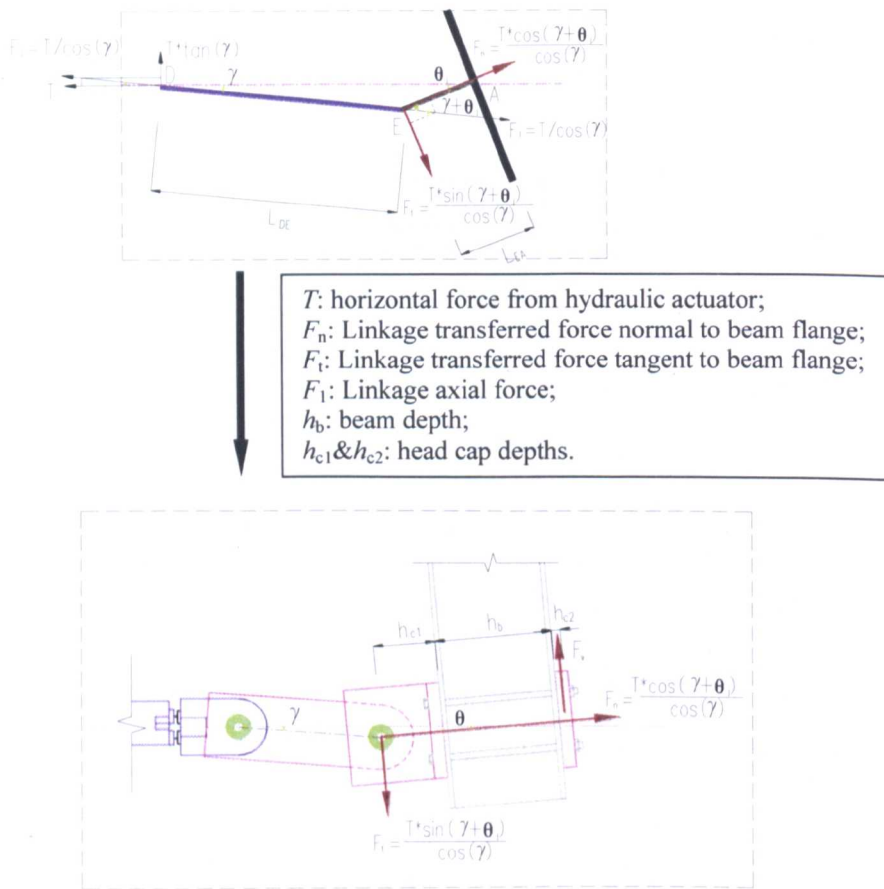


Figure 3.20 Illustration of force transfer relationship of linkage system and steel beam

With regard to the geometric relationship outlined above, it is obvious that the horizontal forces applied by the hydraulic actuator are transferred by linkage system and resulted in normal (F_n) and tangent force (F_t) components on the beam. As shown in Figure 3.20, F_n and F_t are converted from T and written as:

$$F_n = \frac{T \cos(\gamma + \theta_j)}{\cos(\gamma)} \quad \text{Equation 3.2}$$

$$F_t = \frac{T \sin(\gamma + \theta_j)}{\cos(\gamma)} \quad \text{Equation 3.3}$$

Thus, the joint moment can be calculated as:

$$M = F_n L_b + F_t (h_b + h_{c1} + h_{c2})$$

Equation 3.4

where, h_b and h_{c1} & h_{c2} are the beam depth and head cap depths respectively with reference to Figure 3.20.

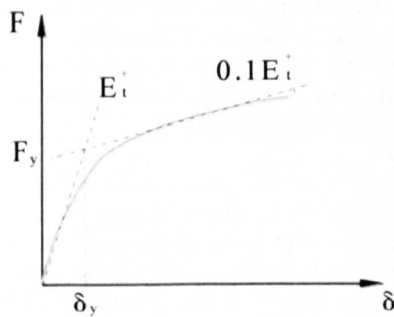
3.4 Determination of yield point from force-displacement curves

Table 3.8 Summary of representative yield point determination methods

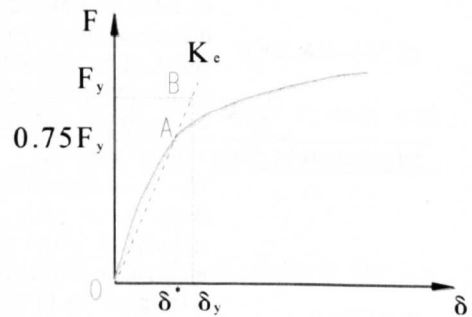
Code recommendations	
ECCS, 1986	δ_y is determined as the intersection between the tangent at the origin of the curve E_t^* and that with a slope of $E_t^*/10$ (Figure 3.21a).
ATC-24, 1992	Based on the forced control procedure, the structural element is loaded up to a level of $0.75F_y$, δ^* (control deformation). The F_y may be estimated from the results of a monotonic test or by employing established design equation (using measured material yield strengths). The elastic stiffness is obtained from the line OA, then δ_y is determined by extending the line from A to B (Figure 3.21b).
FEMA-356, 2000	The determination of yield value is based on target displacement and its related idealized bilinear relationship with secant slope intersects the actual curve at 60% of assumed yield load. Meanwhile, the area enclosed by this bilinear curve should be equal to that by original curve within the range of target displacement. δ_y is determined at the intersection of bilinear relationship (Figure 3.21f).
Suggestions by some other researchers	
Han (2004)	The yield displacement for load control is based on the stiffness in elastic stage (K_e): $K_e = 6(E_s I_s + 0.6 E_c I_c) / L$, where, I_s and I_c are the moment of inertia for the hollow steel cross section and the core concrete cross section respectively, E_s and E_c are the elastic modulus corresponding to I_s and I_c respectively, L is the effective buckling length of column in the plane of bending. Then, the yield displacement, δ_y , is obtained by the intersection of extended elastic stiffness line and load capacity of the curve. The ultimate displacement, δ_u , is obtained as the load capacity falls to 85% of the ultimate strength (Figure 3.21c).
Shannag (2005)	The elastic stiffness is defined as the line drawn between the origin and 50% load capacity of the curve. Then elastic stiffness line is extended to 80% load capacity, and the intersection is presumed as the point corresponding to δ_y (Figure 3.21d).
Park (2007)	The yield point is defined as the area enclosed by the idealized elastoplastic envelope curve which was the same as that enclosed by the actual envelope curve (Figure 3.21e).

The yield values are often defined in relation to significant yielding in the critical region of connections, which represent a clear nonlinearity in a force-

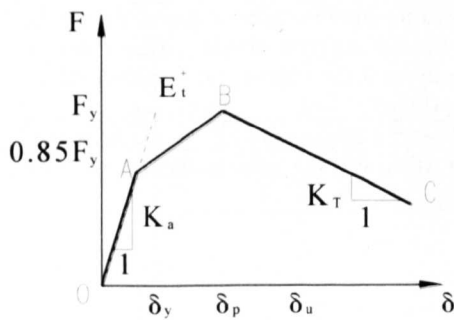
deformation relationship. Referring to cyclic loading procedures suggested by recent codes (ECCS, 1986; AISC, 2005), the yield displacement of the joint should be determined from monotonic loading test or predicted analytically beforehand as a control parameter for cyclic loading procedure. As commented by ATC-24 (1992), however, none of the different methods for obtaining ‘yield points’ for component behaviour given in the literature provides satisfactory results for all cases since judgement is involved in all definitions. Table 3.8 and Figure 3.21 indicate some representative yield displacement determination methods suggested by recent design codes and adopted by some other researchers. Related explanations are also presented for these methods.



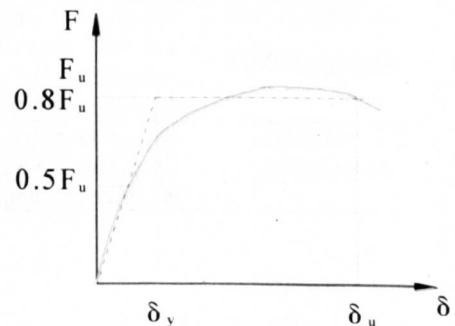
(a) ECCS method



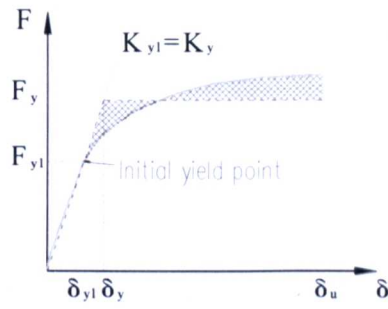
(b) ATC-24 method



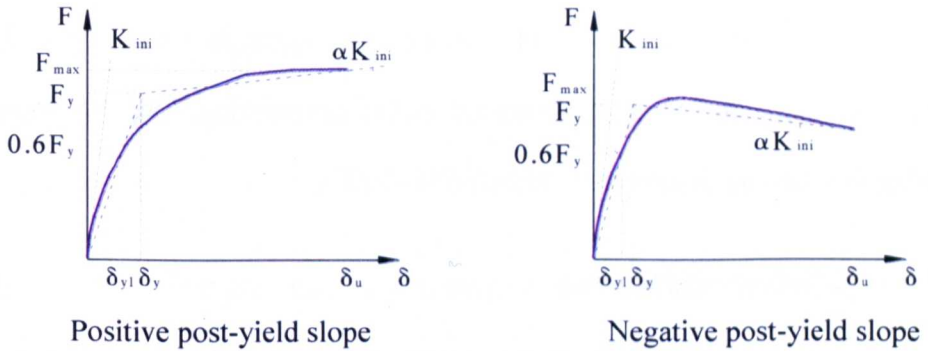
(c) Han *et al*, 2005



(d) Shannag *et al*, 2004



(e) Park *et al*, 2007



(f) FEMA-356 based method

Figure 3.21 Illustration of representative yield point determination methods

Each method for the determination of the yield point (yield displacement) from a force-displacement curve has its merits. Most of these determination methods are based on the elastic stiffness or secant stiffness line associated with a given force ratio which refers to the intersection point between stiffness line and actual curve to the yield point. Notwithstanding simple expressions, their applications are influenced by specific provisions. It is worth noting that an alternative approach of determination of yield point is through introducing the energy dissipation. For example, Park *et al* (2007) adopted a yield point determination approach based on the concept of equal plastic energy, as shown in Figure 3.21 (e). The procedures outlined in the FEMA-356 (2000) provide a method in which idealized bilinear force-displacement relationships are compared against the nonlinear force versus displacement relationship to

estimate the effective lateral stiffness and yield strength of a building. Moreover, the bilinear relationships are plotted to fit the actual curves with positive and negative post-yield slopes (αK_{ini}). As outlined in Table 3.8, this method seems to provide a compromise of the considerations of secant stiffness, i.e., the secant stiffness linear up to 60% of assumed yield force, and energy dissipation, i.e., the requirements of approximate area balances between line segments above and below the actual curve. In the present study, the yield force and yield displacement of the connections were determined using this method suggested by FEMA-356 (2000).

3.5 Concluding remarks

The experiment preparation of this research programme has been described in this chapter. The design intension of the test specimens has been introduced and discussed in details. Relevant information of specimen fabrication, test set-up, instrumentation, and loading procedure has been presented in this chapter. The yield displacement determination approach adopted for this study has been described and discussed. The work mentioned above have a close relation with the experimental data processing in this study. The test results will be given and discussed in the following chapter.

CHAPTER 4

EXPERIMENTAL STUDY-TEST RESULTS

4.1 Introduction

In conjunction with the previous chapter, it is the purpose of this chapter to evaluate the results obtained from full-scale beam-to-column connection tests. The approaches mentioned in the previous chapter are taken for post-processing test data. The verifications of test design assumption are also presented.

The results will be presented in this chapter as in the following order. First, two representative failure modes of the connections are outlined together with the test observations recorded in the experiments. Second, the hysteretic moment-rotation relationships are described in relation with the relevant influential parameters which were considered as the bolt grade, cyclic loading procedure, tube wall thickness and concrete grade. Third, relevant discussions are made for these influences on the hysteretic moment-rotation relationships of this innovative blind bolted endplate connection to CFT column. Fourth, the representative strain profiles of the connection components including the steel beam, tube sidewall face & connecting face, and bolt shank are described. Finally, concluding remarks are presented.

4.2 Failure modes

As mentioned earlier, the connection specimens were designed in this study to isolate the CFT column and the blind bolt as relatively weak components and eliminate the plastic deformation of the steel beam and endplate. The

connection failures in the tests were supposed as the results of blind bolt shank and CFT column face. These failure modes relate to the predominant influential factor for the basic behaviour modes observed in the tests. The actual failure mode of the connection may also be the failure of the blind bolt whilst the CFT column is subjected to local damage. The test in this study considers both the material and geometric influences on the failure modes of the blind bolt and the CFT column. During the cyclic loading process, it is important to observe and record the failure modes which are related to damage evolution. This section will begin with a brief indication of typical failure modes and connection categories. The figures are then illustrated for both individual components and overall connections, including typical failure mode snapshots and photo series.

Based on the experimental observations, two typical failure modes in relation with counterpart connection categories are summarized as follows:

- Failure mode I (FI): bolt shank fracture with limited CFT column face yielding. As the bolt shank elongation is the primary source of deformation, the CFT column is presumed to possess higher strength and stiffness than those of the blind bolt, i.e., relatively thick tube face and/or high strength concrete infill. The connection category in this case is labelled as 'CI' or 'weak blind bolt & strong CFT column'.
- Failure mode II (FII): CFT column face with moderate flexible deformation, local damage of concrete infill and moderate bolt pullout with likely local cracking in the sleeves. As the blind bolt assembly in this case undergoes greater deformation, the CFT column is presumed to be much weaker in

strength and stiffness than the blind bolt, i.e., relatively thin tube face and/or low concrete strength. The connection category in this case is labelled as 'CII' or 'strong blind bolt & weak CFT column'.

As a general observation of overall joint response, the deformation modes of connection category I and II at the ultimate rotation of the connections are shown in Figure 4.1 and Figure 4.2 respectively. For connection category I, it is obvious that the endplate rotates as a rigid body around the compressed beam flange. The gap between the endplate and the flat CFT column connecting face (noticeable sleeve of the blind bolt) are distributed linearly with its corresponding distance to the rotation point. For connection category II, on the other hand, the CFT column connecting face at the first and second bolt rows almost deforms along with the moderate bolt pullout, thereby inducing nearly invisible gaps between the endplate and the CFT column connecting face. The blind bolts in this case did not undergo bolt shank fracture unlike those in failure mode I.

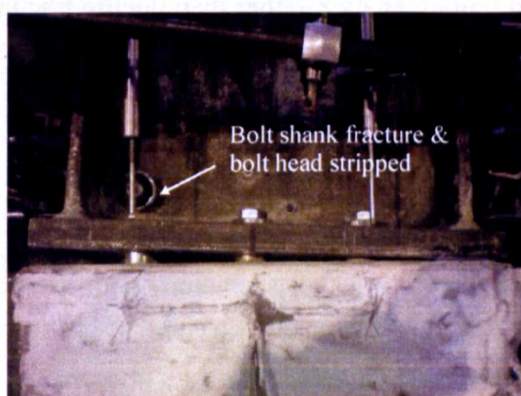


Figure 4.1 Representative deformation mode of connection category I

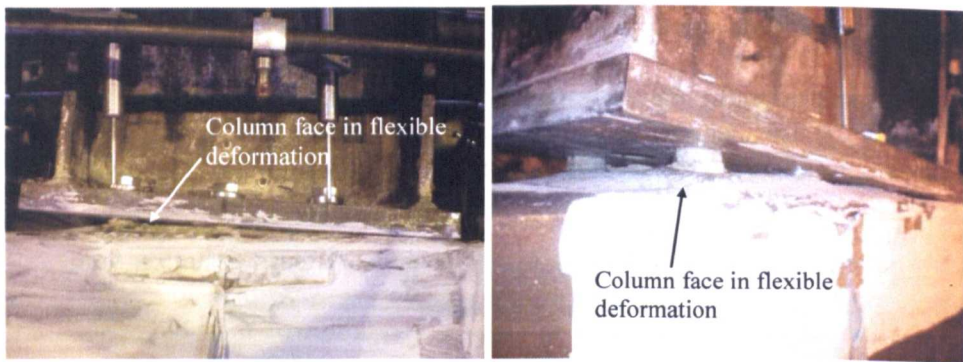


Figure 4.2 Representative deformation mode of connection category II

The connections of tests No.1, No.2, No.3 and No.5 failed in mode I. The bolt shanks in tension at outer bolt row fractured very suddenly with the bolt heads stripped. Figure 4.3 shows a comparison of the fractured parts with an original full sized blind bolt. It is observed that the bolt shank fracture section locates ranging approximately 15mm~28mm from the bottom surface of the bolt head, which is expected within the bolt clamping length (equal to the sum of the thicknesses of the endplate and the tube connecting face). Upon a closer examination, all the bolt shanks indicate very limited necking, which demonstrate limited bolt elongation rather than ductile fracture failure pattern. Additionally, it can be seen from the photograph that rubber washers were almost squashed in contact with the bottom bolt head. This observation suggests the mechanical interlock effect of the blind bolt threaded cone and sleeve still remained effective for all specimens until the fracture of the bolt shank.

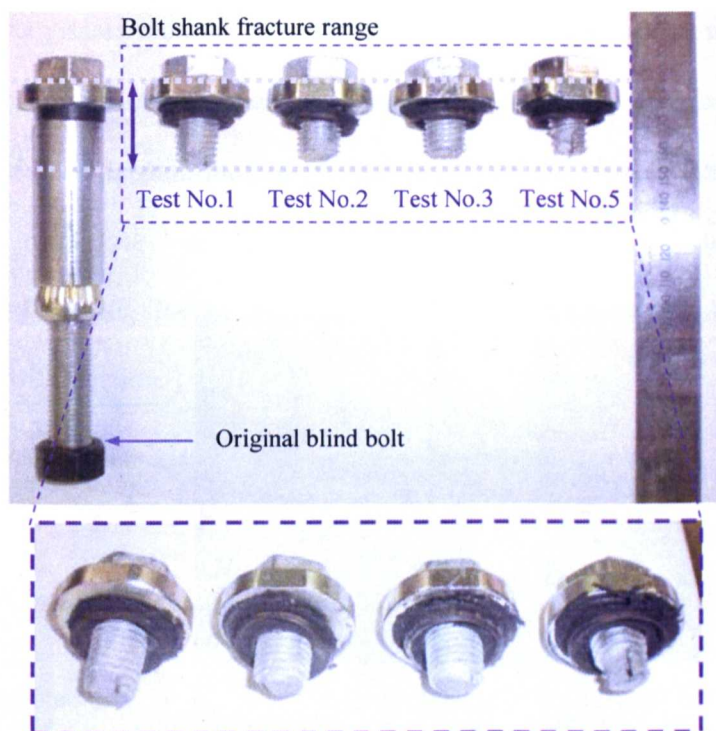


Figure 4.3 Bolt shank failure mode

For the purpose of examining the CFT column faces involved with the connection failure, the connections were dismantled by cutting off the remaining bolt heads and removing the steel beam and the endplate. Figure 4.4 a&b shows three photographs of the CFT columns after testing in which the connections failed in mode I. The deformations on the tube connecting face and sidewall face are almost invisible, however, the local yielding patterns are revealed on the tube connecting face coated with hydrated lime solution. The typical distribution of yield line pattern at outer bolt row agrees with those described by Kurobane *et al* (2007), as displayed in Figure 4.4c.

For specimen BBEC-8-10.9-50-LI, the yield line patterns are visibly displayed at the edges between the tube connecting face and the sidewall face, especially at outer bolt rows which attract more tension. For specimen BBEC-6.3-8.8-50-

LII with thinner tube wall, the yield lines are shown more clearly around bolt clearance holes. Also, local concrete crushing can be observed in the vicinity of bolt clearance holes, which agrees with the assumptions as blind bolt pulled outwards.

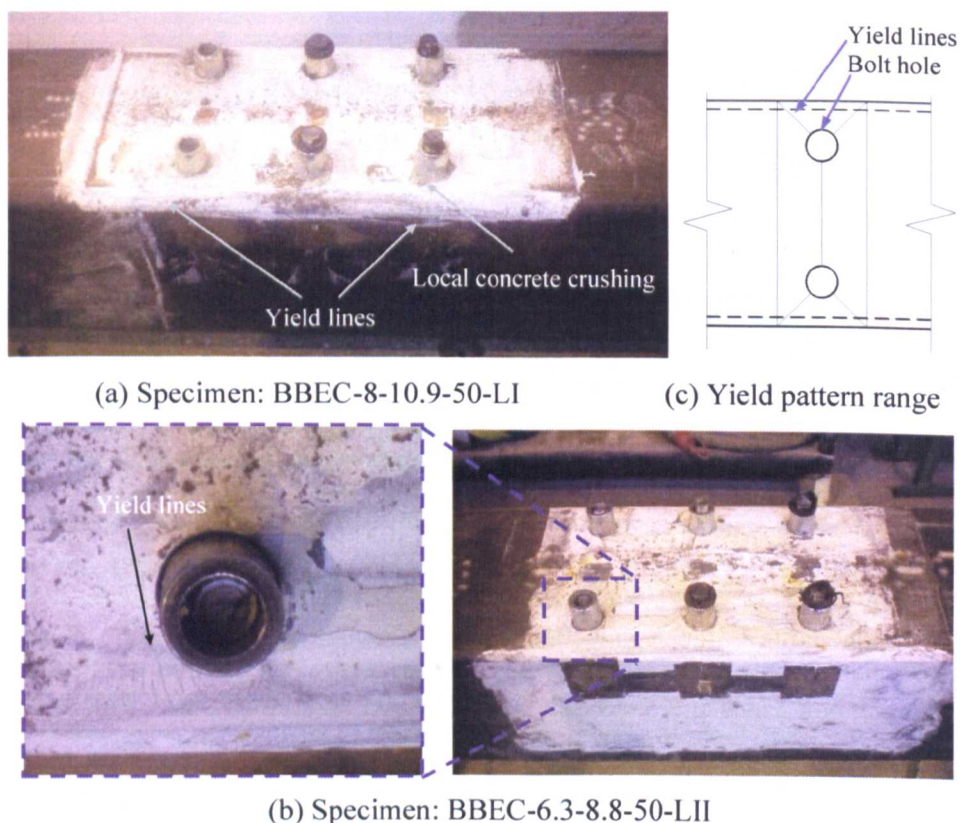


Figure 4.4 Representative yielding propagation on CFT column faces for connection category I

To compare the damages on the CFT column faces of the connections failed in mode II, observations were made for specimens BBEC-5-8.8-50-LII and BBEC-6.3-8.8-25-LII. As shown in Figure 4.5, an obvious flexible deformation of the CFT column connecting face can be seen at each bolt row while the yield fan patterns developed around the bolt clearance holes and extended to the edges between the tube connecting face and the sidewall face.

In contrast, greater local concrete crushing can be observed around the bolt clearance holes. More evidences will be described with regard to this issue later. As a closer look at the blind bolt, the cracks are seen deriving from the slots and propagate longitudinally along the sleeve. This trend is more pronounced for the sleeves at top bolt row which are supposed to undergo greater tensile traction.

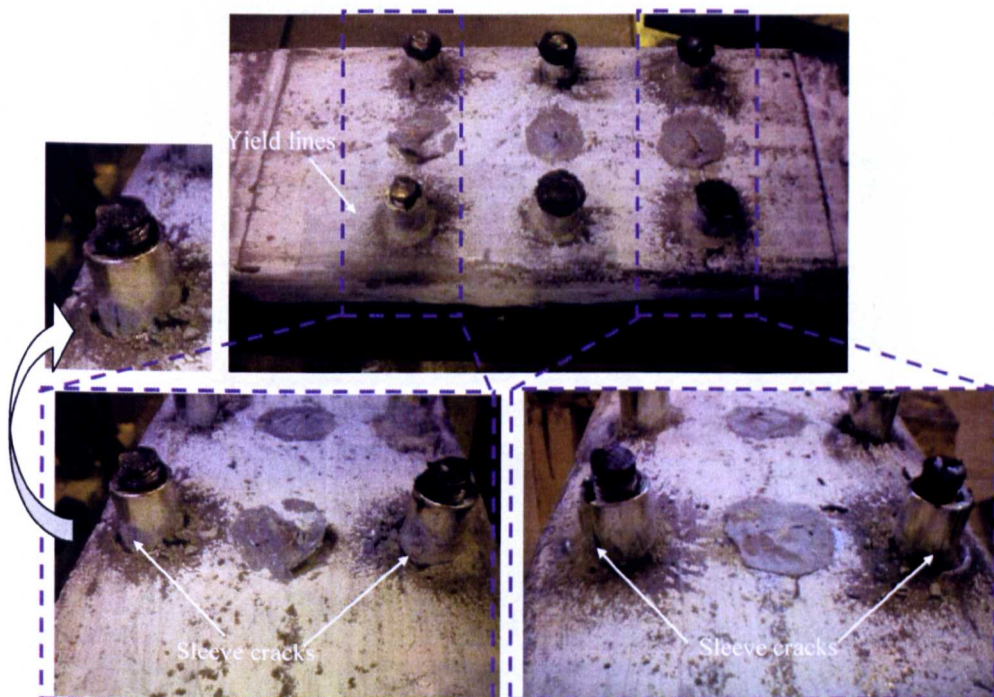


Figure 4.5 Representative yielding propagation on tube for connection category II (Specimen: BBEC-5-8.8-50-LII)

A similar yielding on the CFT column connecting face can be seen for specimen BBEC-6.3-8.8-25-LII with relatively weak concrete, as plotted in Figure 4.6. However, less significant cracks are seen propagating on the sleeve although both connections were subjected to similar rotation at ultimate stage. The observations above can be attributed to the evidence of consecutive damage of CFT column as the moderate pullout of the blind bolt. The concrete

strength, on the other hand, has great influence on the anchorage of the blind bolt components. It appears that high strength concrete infill would produce greater partial restraining effects on the sleeves so that the interlocked threaded cone is more prone to over-squeeze the flaring sleeve as the connection is subjected to greater rotation. Also, it is expected that the anchorage at the bolt extension part underwent greater deterioration.

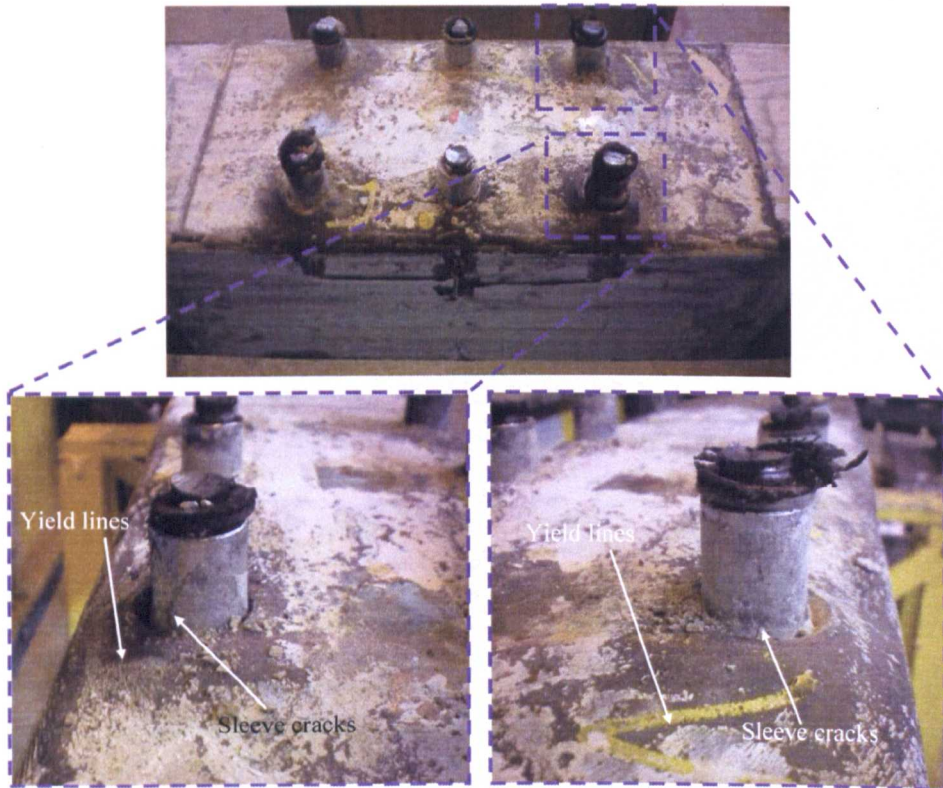


Figure 4.6 Representative yielding propagation on tube for connection category II (Specimen: BBEC-6.3-8.8-25-LII)

In view of the local concrete crushing through the bolt clearance holes, it was felt necessary to strip away the local tube face so as to have a closer look at the damage of the concrete infill. For specimen BBEC-6.3-8.8-50-LII failed in mode I, most concrete infill surface areas are kept intact except for some local damages around the bolt sleeves, as shown in Figure 4.7. It seems that the

concrete infill efficiently restrained the bolt from pulling out which results in the bolt shank fracture in the end. This observation also indicates an agreement with the test observations reported in former monotonic tests (Al-Mughairi, 2009), in which the strong bond between the blind bolt and concrete infill was concluded.

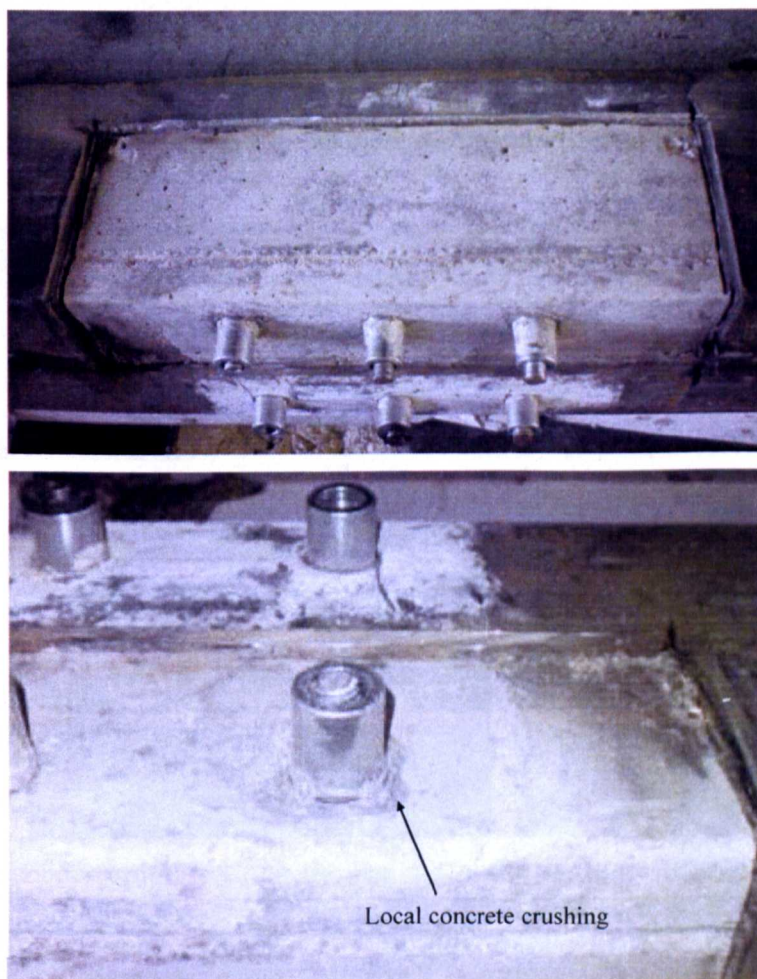
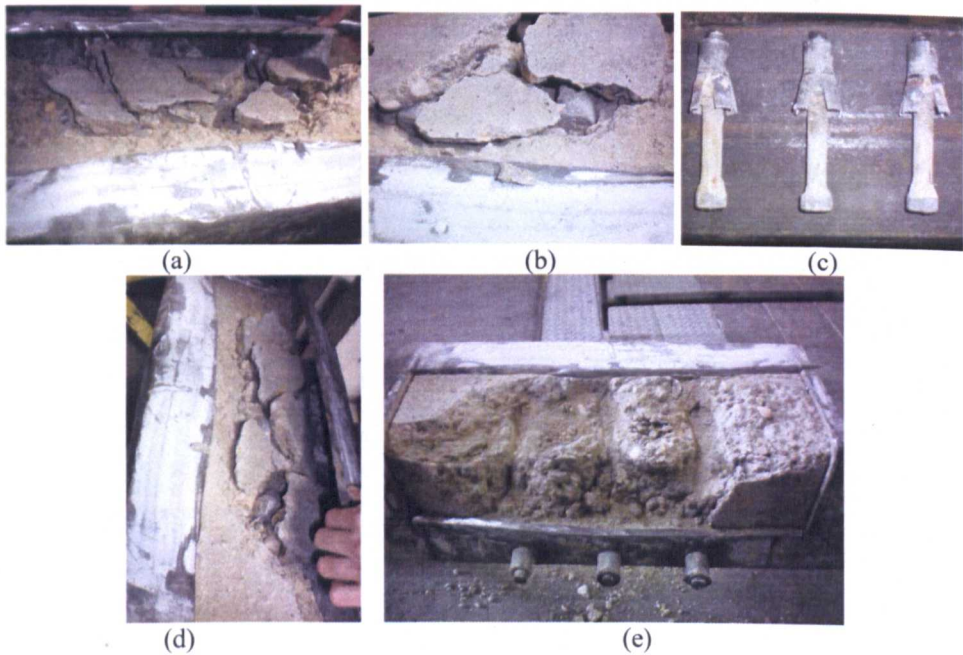


Figure 4.7 Representative failure mode of concrete infill after stripping away local tube faces (Specimen: BBEC-6.3-8.8-50-LII)

For specimen BBEC-6.3-8.8-25-LII which failed in mode II, most of the concrete infill in the vicinity of the blind bolt was damaged. This is

fundamentally difference is from the case of failure mode I. Due to the presence of relatively widespread concrete damage, the post test survey was conducted with care in removing the tube face piece cut beforehand. After cleaning the rubbles of the concrete infill, several photographs of the remaining concrete infill around the blind bolt are shown in Figure 4.8. It is evident that the local concrete crushed not only near the anchor nut but also along the bolt shank which indicates significant loss of anchorage and bond for the blind bolts as the connection underwent large rotation.



Graph No.	Observations	Graph No.	Observations
(a)	Overview of concrete infill crushing after testing	(d)	Side view of concrete infill crushing after testing
(b)	Local concrete crushing around anchor nut	(e)	Remaining concrete infill after cleaning
(c)	Blind bolts after testing		

Figure 4.8 Representative failure mode of concrete infill after stripping away local tube faces (Specimen: BBEC-6.3-8.8-25-LII)

The inspection also shows that the concrete infill in contact with tube sidewall face cracked into several pieces rather than that in contact with tube connecting face. This implies that the crushing of concrete infill along longitudinal direction of the CFT column is more severe than that in transverse direction, which can be explained by the fact that the blind bolts are controlled by the endplate rotation around the transverse rotation axis. The examination was also made on the blind bolts after removing from the damaged concrete infill. Other than damage to the local sleeves, no noticeable damages are seen at the interlocked assembly parts of the blind bolt. This observation agrees with previous remarks that in the failure mode II relatively large extent of cracking occurring at the concrete infill with moderate bolt pullout. Moreover, it seems that the anchorage part of the bolt shank as well as the anchor nut remains intact after the cyclic loading. This implies no significant damage at the blind bolt in the anchorage portion.

As this blind bolted endplate connection to CFT column is featured by cumulative failure development, the photograph series of specimens BBEC-8-10.9-50-LI and BBEC-5-8.8-50-LII have also been recorded for the joint response under progressive cyclic loading. A further analysis relating to the cumulative damage model will be described in chapter 5. The photograph series plotted herein represent failure modes I and II as follows:

Specimen BBEC-8-10.9-50-LI: this specimen failed in mode I. Due to the overheating of the pump system at early stage of loading, the cyclic loading procedure was paused for system adjustment and resumed from the positive moment direction. As shown in Figure 4.9, the endplate bottom face is in

alignment with the CFT column face during initial loading cycles. Also, the deformation of blind bolts is not significant. As the rotation becomes increasingly greater than the yielding rotation capacity of the connection, the endplate rotates as a rigid body with the blind bolt shank elongation. Finally, the failure of the connection is observed as a sudden fracture of the bolt shank at the outer bolt row under negative moment. This failure mode is expected due to larger lever arm distances from the rotation axis of the connection under negative moment than that under positive moment, i.e., the failed blind bolts are subjected to greater tensile force in this case.

Specimen BBEC-5-8.8-50-LII: this specimen failed in mode II. As the presence of great rotation at the connection, two photographs are displayed at each point to feature the global view of the connection and localized view of outer bolt row in tension, as shown in Figure 4.10. Prior to the yielding of the connection, the rotational response of the connection are seen to be similar with that of the specimen BBEC-8-10.9-50-LI. A noticeable deformation can be seen since the connection was loaded at 8~10 cycles. Thereafter, the rotation of the connection is featured by the consecutive deformation of the connecting face of the CFT column as well as moderate blind bolt pullout. At ultimate loading, it is observed that the endplate undergoes significant rotation while the tube connecting face deforms outwards with moderate blind bolt pullout.

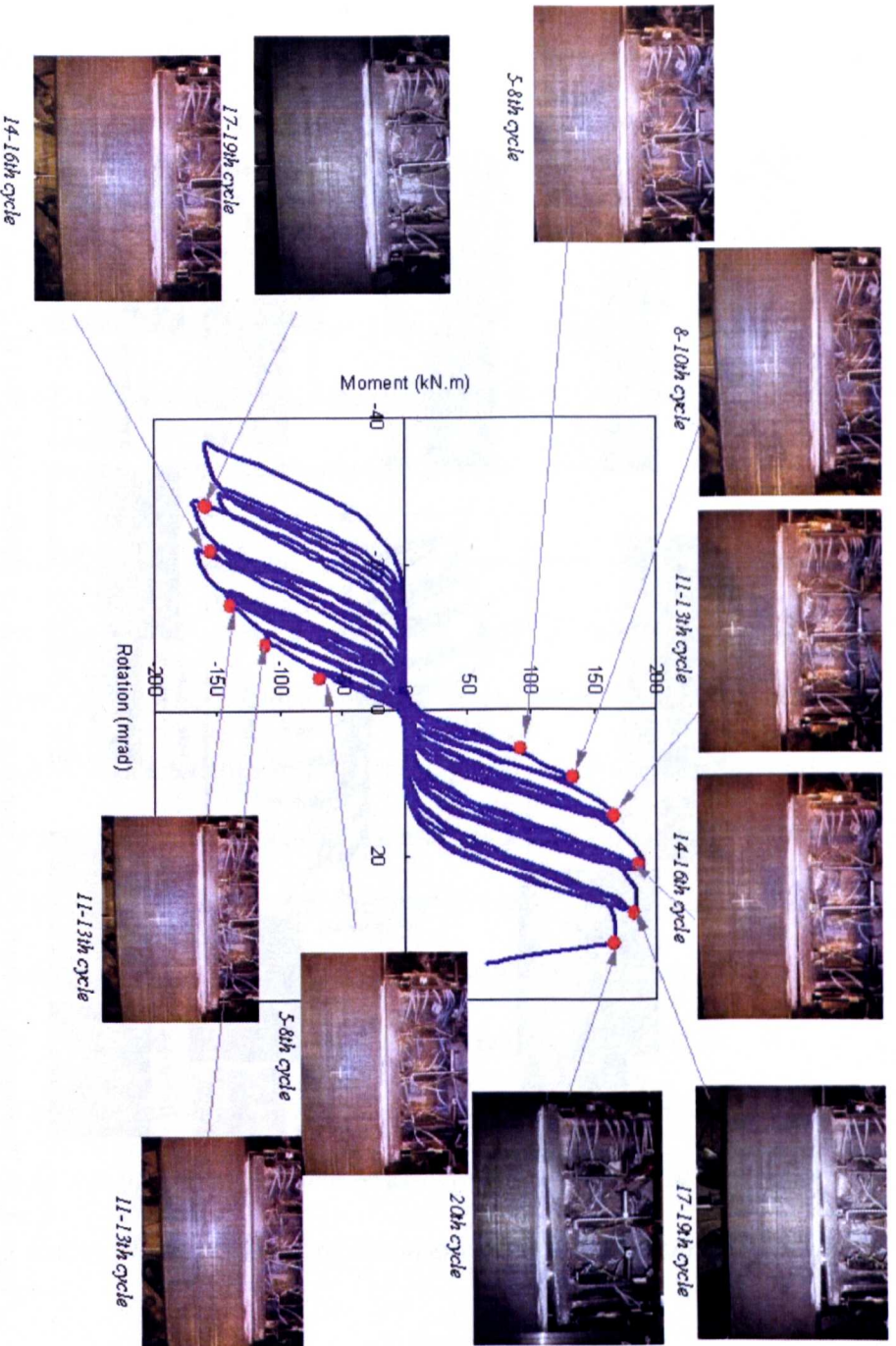


Figure 4.9 Photograph series for joint response of specimen BBEC-8-10.9-50-L1 (connection category I)

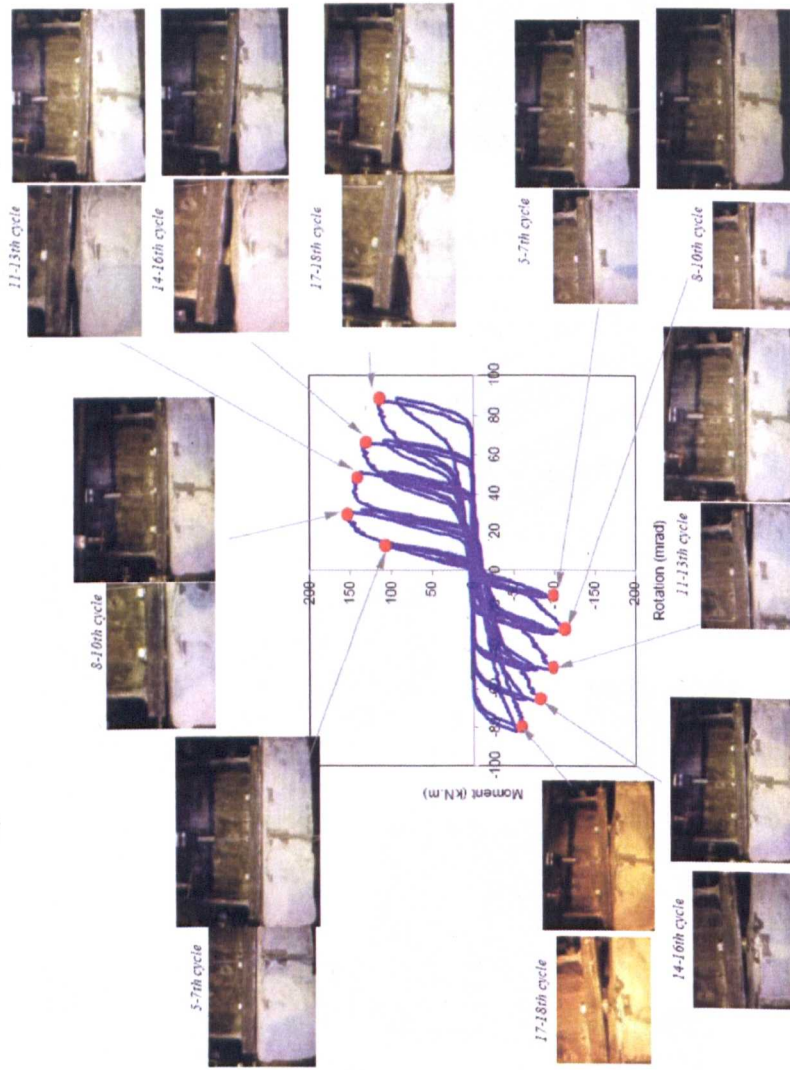


Figure 4.10 Photograph series for joint response of specimen BBEC-5-8.8-50-LII (connection category II)

4.3 Hysteretic moment-rotation relationships

4.3.1 General moment-rotation behaviour

The moment-rotation relationship is the principle means of evaluating and characterising the behaviour of beam-to-column connections. Based on the hysteretic moment-rotation relationships, the main characteristics of the connection, such as resistance, rotation capacity, and stiffness, can be evaluated. In this study, the moment-rotation relationships served as a basis for further assessment of cyclic characteristics and cumulative damage of this blind bolted endplate connection to CFT column.

The moment and rotation of the connections are calculated from corresponding load and displacement data obtained from the test instrumentations. The calculated results should allow for the geometric and mechanical characteristics of the test system as discussed previously in Section 3.3. The test results of moment-rotation relationships are summarized in Tables 4.1~4.3, which indicate the moment, rotation and stiffness of hysteresis envelope curves at yield point, maximum moment point and peak rotation point. The hysteresis envelope herein is taken as the curve of a generalized relationship that envelopes response data obtained from cyclic loading of a structural component or assembly (Deierlein *et al*, 2010). Related failure modes of the connections are also included as a contrast within each group.

To examine the geometric relationship of linkage system and steel beam outlined in Section 3.3.2, a comparison was made for the calculated moment

of the specimen BBEC-6.3-8.8-50-LII as an example. Firstly, γ was calculated from trigonometric relationship based prediction and LVDT measurement at points f and g as shown in Figure 3.19. Then, the moments are calculated according to Equation 3.4 and compared in Figure 4.11. The obtained results satisfy a standard deviation no more than 3% in validation.

To examine the rotation response of the joint, a comparison was made for the hysteretic moment-rotation relationships based on different measuring points on the steel beam. The displacement measurements from DB1 and DB2 (referring to Figure 3.8) were adopted in this comparison. Both curves are, not surprisingly, in very close agreement as shown in Figure 4.12, except a slight variation near the peak rotation of the connections. This confirms the previous pre-design assumptions and the beam deformation induced rotations can be neglected whist the measuring points on the steel beam were assigned for the joint rotation response.

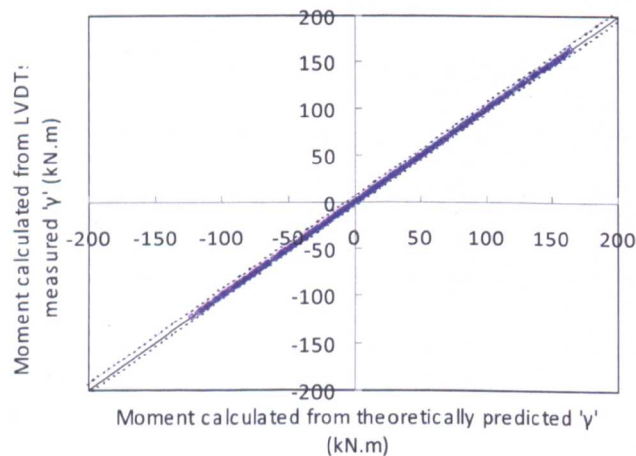


Figure 4.11 Comparison of calculated moments based on the LVDT measurement and theoretical prediction

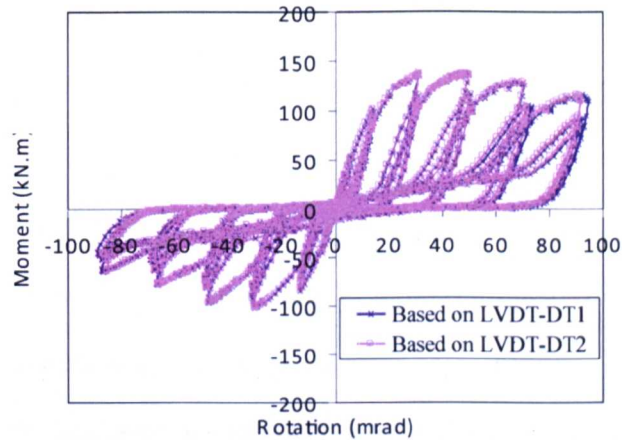


Figure 4.12 Comparison of moment-rotation relationships of specimen BBEC-6.3-8.8-25-LII based on the measurement of LVDT-DB1 and DB2

All hysteretic moment-rotation relations plotted in Figure 4.13 show certain hysteretic pinching and gradual nonlinear yielding at the loading branch of the hysteresis envelopes. The hysteresis loops are not in a general plump shuttle shape as reported in former experiments of bolted endplate connections involved with the endplate in bending. On the other hand, different hysteretic moment-rotation responses can be identified from two connection categories, corresponding to the failure modes I and II respectively. By relating to the failure modes of the connection described in previous section, the general observations of hysteretic moment-rotation relationships are made (referring to Tables 4.1~4.3 and Figure 4.13) as follows:

Failure mode I: this representative response is observed from the test specimens BBEC-8-8.8-50-LI, BBEC-8-10.9-50-LI, BBEC-8-10.9-50-LII and BBEC-6.3-8.8-50-LII. By referring to Figure 4.13 (a), (b), (c) and (e), the hysteretic moment-rotation curves present significant hysteretic pinching, which is represented as all the hysteresis loops intersected at a point. These connection specimens failed by bolt shank fracture and limited CFT column

face yielding with peak rotation at 29mrad~33mrad. An obvious rotation increment along zero moment axis of loading and unloading excursions indicates that the joint rotation is governed by bolt shank elongation rather than plate flexibility. It can be deduced from the curves that the loading of these specimens was terminated at the first loading cycle of ultimate loading amplitude. Moreover, the areas enclosed by the cyclic excursion produced by the first loading cycle of each amplitude are rather larger than those generated by subsequent cycles. Further discussion for this phenomenon will be given in a topic of energy dissipation later. As the bolt tensile capacity was fully utilised and failed by bolt fracture ultimately, it is supposed that the tube wall and/or the concrete anchorage provide strong restraints during the loading process. This justifies the previous assumption of details of connection category I as well as the failure modes described in Section 4.2.

Table 4.1 Connection categories, test failure modes and yield rotation & moment

Test No.	Specimen reference	Yield point				Connection categories	Failure modes*
		Yield moment		Yield rotation			
		M_v^- (kN.m)	M_v^+ (kN.m)	θ_v^- (mrad)	θ_v^+ (mrad)		
1	BBEC-8-8.8-50-LI	120.65	154.01	12.40	12.09	CI	FI
2	BBEC-8-10.9-50-LI	149.04	173.02	12.03	11.30	CI	FI
3	BBEC-8-10.9-50-LII	151.07	177.02	11.92	11.23	CI	FI
4	BBEC-5-8.8-50-LII	107.2	132.5	15.47	14.43	CII	FII
5	BBEC-6.3-8.8-50-LII	116.5	144.78	13.51	13.06	CI	FI
6	BBEC-6.3-8.8-25-LII	97.12	121.2	15.44	14.93	CII	FII

Note: * refers to related descriptions in Section 4.2

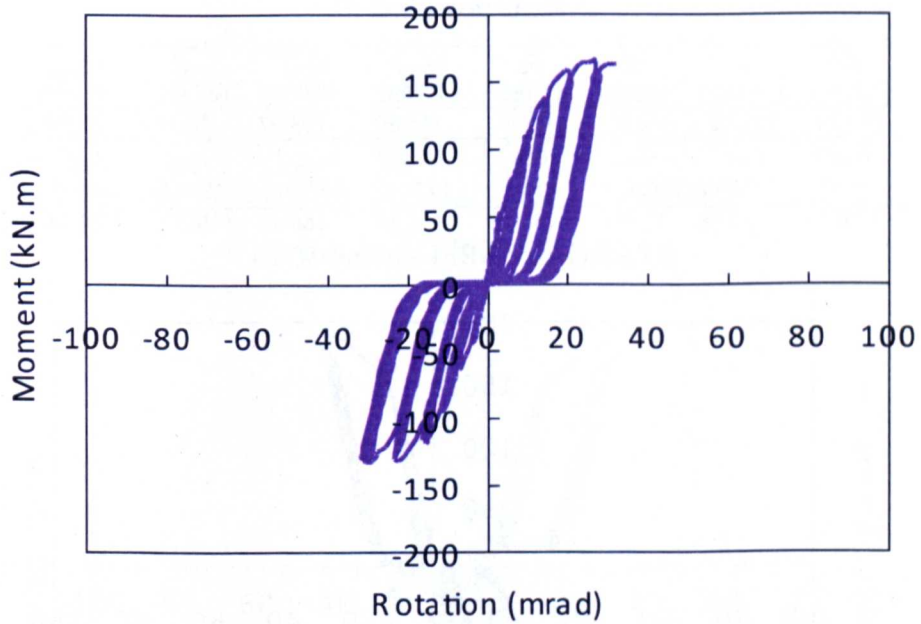
Table 4.2 Test moment & rotation at maximum moment & peak rotation

Test No.	Specimen reference	Maximum moment point				Peak rotation point			
		Moment		Rotation		Moment		Rotation	
		M_{max}^- (kN.m)	M_{max}^+ (kN.m)	$\theta_{m,max}^-$ (mrad)	$\theta_{m,max}^+$ (mrad)	$M_{r,peak}^-$ (kN.m)	$M_{r,peak}^+$ (kN.m)	θ_{peak}^- (mrad)	θ_{peak}^+ (mrad)
1	BBEC-8-8.8-50-LI	133.79	163.89	30.55	27.31	130.80	161.75	31.33	32.17
2	BBEC-8-10.9-50-LI	164.69	188.97	22.33	21.79	154.56	166.39	36.74	34.94
3	BBEC-8-10.9-50-LII	171.89	189.17	29.35	27.72	156.87	180.13	29.83	31.64
4	BBEC-5-8.8-50-LII	115.80	157.72	32.14	30.54	62.17	116.71	77.20	86.54
5	BBEC-6.3-8.8-50-LII	120.39	160.95	31.13	30.26	108.87	147.46	32.34	35.74
6	BBEC-6.3-8.8-25-LII	102.95	137.28	30.57	30.38	64.59	110.24	83.32	92.81

Table 4.3 Test initial and secant stiffnesses

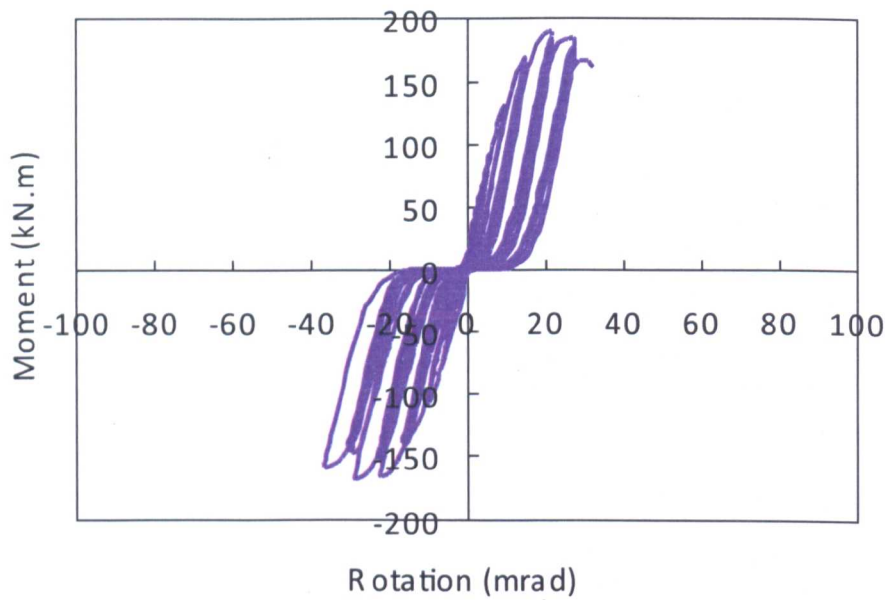
Test No.	Specimen reference	Approximate yield point			
		Initial stiffness		Secant stiffness for yield point determination**	
		K_{ini}^- (KN.m/mrad)	K_{ini}^+ (KN.m/mrad)	K_{sec}^- (KN.m/mrad)	K_{sec}^+ (KN.m/mrad)
1	BBEC-8-8.8-50-LI	16.92	23.51	9.73	12.74
2	BBEC-8-10.9-50-LI	20.11	27.06	12.39	15.31
3	BBEC-8-10.9-50-LII	20.18	28.62	12.68	15.76
4	BBEC-5-8.8-50-LII	14.06	17.95	6.93	9.19
5	BBEC-6.3-8.8-50-LII	15.78	19.15	8.62	11.08
6	BBEC-6.3-8.8-25-LII	13.66	16.18	6.29	8.12

Note: ** denotes secant stiffness adopted in the yield point determination as indicated in Section 3.4



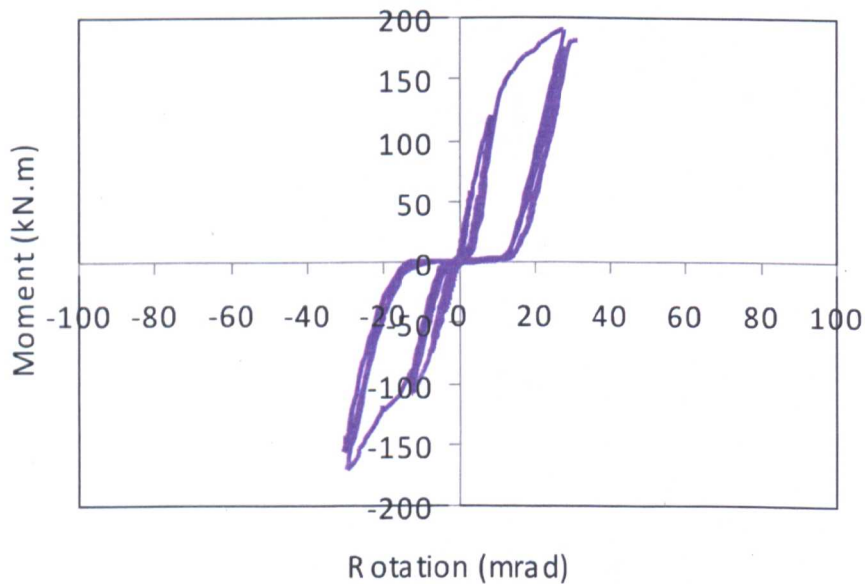
M_v^- (kN.m)	M_v^+ (kN.m)	θ_v^- (mrad)	θ_v^+ (mrad)	M_{max}^- (kN.m)	M_{max}^+ (kN.m)	$\theta_{m,max}^-$ (mrad)	$\theta_{m,max}^+$ (mrad)
120.65	154.01	12.40	12.09	133.79	163.89	30.55	27.31
K_{ini}^-	K_{ini}^+	K_{sec}^-	K_{sec}^+	$M_{r, peak}^-$ (kN.m)	$M_{r, peak}^+$ (kN.m)	θ_{peak}^- (mrad)	θ_{peak}^+ (mrad)
16.92	23.51	9.73	12.74	130.80	161.75	31.33	32.17

(a) Specimen: BBEC-8-8.8-50-LI



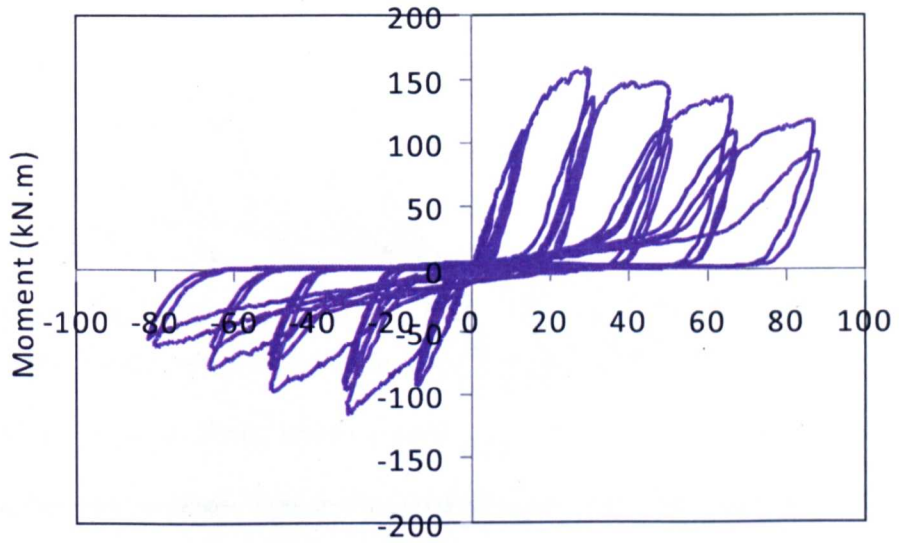
M_v^- (kN.m)	M_v^+ (kN.m)	θ_v^- (mrad)	θ_v^+ (mrad)	M_{max}^- (kN.m)	M_{max}^+ (kN.m)	$\theta_{m,max}^-$ (mrad)	$\theta_{m,max}^+$ (mrad)
149.04	173.02	12.03	11.30	164.69	188.97	22.33	21.79
K_{ini}^-	K_{ini}^+ (KN.m/mrad)	K_{sec}^-	K_{sec}^+	$M_{r, peak}^-$ (kN.m)	$M_{r, peak}^+$ (kN.m)	θ_{peak}^- (mrad)	θ_{peak}^+ (mrad)
20.11	27.06	12.39	15.31	154.56	166.39	36.74	34.94

(b) Specimen: BBEC-8-10.9-50-LI



M_v^- (kN.m)	M_v^+ (kN.m)	θ_v^- (mrad)	θ_v^+ (mrad)	M_{max}^- (kN.m)	M_{max}^+ (kN.m)	$\theta_{m,max}^-$ (mrad)	$\theta_{m,max}^+$ (mrad)
151.07	177.02	11.92	11.23	171.89	189.17	29.35	27.72
K_{ini}^-	K_{ini}^+ (KN.m/mrad)	K_{sec}^-	K_{sec}^+	$M_{r, peak}^-$ (kN.m)	$M_{r, peak}^+$ (kN.m)	θ_{peak}^- (mrad)	θ_{peak}^+ (mrad)
20.18	28.62	12.68	15.76	156.87	180.13	29.83	31.64

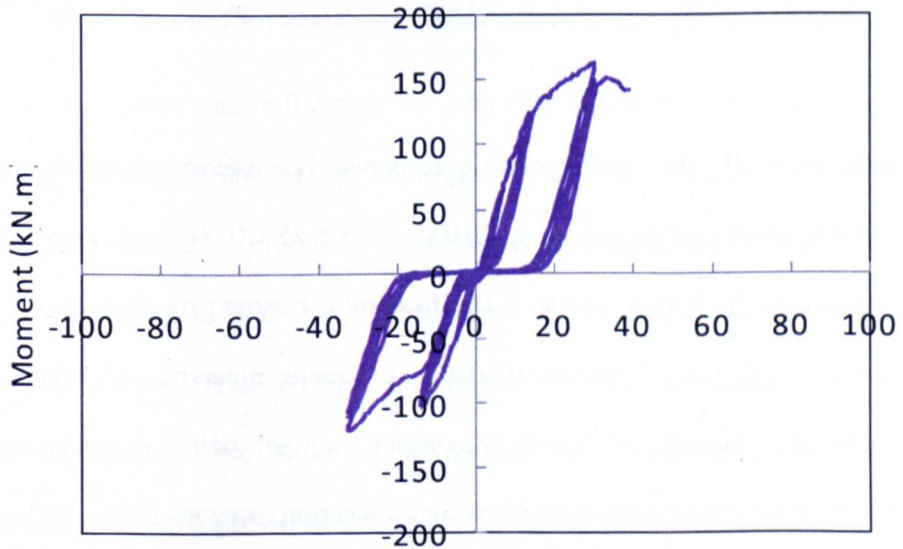
(c) Specimen: BBEC-8-10.9-50-LII



Rotation (mrad)

M_v^- (kN.m)	M_v^+ (kN.m)	θ_v^- (mrad)	θ_v^+ (mrad)	M_{max}^- (kN.m)	M_{max}^+ (kN.m)	$\theta_{m,max}^-$ (mrad)	$\theta_{m,max}^+$ (mrad)
107.2	132.5	15.47	14.43	115.80	157.72	32.14	30.54
K_{ini}^-	K_{ini}^+	K_{sec}^-	K_{sec}^+	$M_{r, peak}^-$ (kN.m)	$M_{r, peak}^+$ (kN.m)	θ_{peak}^- (mrad)	θ_{peak}^+ (mrad)
14.06	17.95	6.93	9.19	62.17	116.71	77.20	86.54

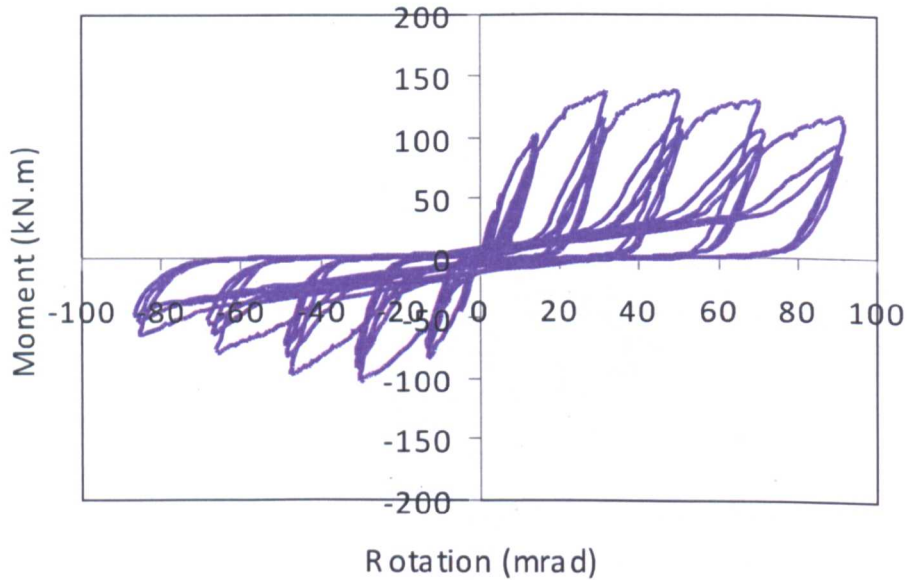
(d) Specimen: BBEC-5-8.8-50-LII



Rotation (mrad)

M_v^- (kN.m)	M_v^+ (kN.m)	θ_v^- (mrad)	θ_v^+ (mrad)	M_{max}^- (kN.m)	M_{max}^+ (kN.m)	$\theta_{m,max}^-$ (mrad)	$\theta_{m,max}^+$ (mrad)
116.5	144.78	13.51	13.06	120.39	160.95	31.13	30.26
K_{ini}^-	K_{ini}^+	K_{sec}^-	K_{sec}^+	$M_{r, peak}^-$ (kN.m)	$M_{r, peak}^+$ (kN.m)	θ_{peak}^- (mrad)	θ_{peak}^+ (mrad)
15.78	19.15	8.62	11.08	108.87	147.46	32.34	35.74

(e) Specimen: BBEC-6.3-8.8-50-LII



M_v^- (kN.m)	M_v^+ (kN.m)	θ_v^- (mrad)	θ_v^+ (mrad)	M_{max}^- (kN.m)	M_{max}^+ (kN.m)	$\theta_{m,max}^-$ (mrad)	$\theta_{m,max}^+$ (mrad)
97.12	121.2	15.44	14.93	102.95	137.28	30.57	30.38
K_{ini}^-	K_{ini}^+	K_{sec}^-	K_{sec}^+	$M_{r, peak}^-$ (kN.m)	$M_{r, peak}^+$ (kN.m)	θ_{peak}^- (mrad)	θ_{peak}^+ (mrad)
13.66	16.18	6.29	8.12	64.59	110.24	83.32	92.81

(f) Specimen: BBEC-6.3-8.8-25-LII

Figure 4.13 Hysteretic moment-rotation curves for test specimens

Failure mode II: this representative response is observed from the test specimens BBEC-5-8.8-50-LII and BBEC-6.3-8.8-25-LII. By comparing with the specimens in Failure mode I, the hysteretic moment-rotation curves in Figure 4.13 (d) and (f) present moderate hysteretic pinching and relatively large rotation capacity. Prior to maximum moment point, the shapes of hysteretic moment-rotation excursions for connection category II are similar to those for connection category I. Thereafter, the differences between the areas enclosed by the cyclic excursions deriving from the first loading cycle of each amplitude and those generated by the subsequent cycles are increasingly reduced as the joint rotation becomes larger. Meanwhile, the maximum

moments of the excursions within given loading amplitude are reduced significantly from the first cycle to the subsequent cycles which can be explained as the result of consecutive concrete deterioration. It is also observed that the unloading cyclic excursions in the specimens of connection category II have a short branch along the zero moment axis (horizontal branch), but deviate with small inclined angle from the horizontal afterwards (inclined branch). Based on the experimental observation, the short horizontal branch and further longer inclined branch can be attributed to the consequences of bolt shank elongation and the CFT column face flexible deformation respectively. For this reason, the brittle fracture of the bolt shank is avoided with an adding contribution of the tube connecting face in bending. Notwithstanding that, it is worthy of note that the local crack in the sleeves with bolt pullout could take place at this stage.

To further study the influences of material, geometric configuration and loading procedure on the cyclic responses of this blind bolted endplate connection to CFT column, a series of comparisons were made for the experimental hysteretic moment-rotation relationships and counterpart envelope curves. Based on the experimental observations, related comments and explanations for these influences on the cyclic behaviour of the connections will be presented as below.

4.3.2 Effect of blind bolt grade

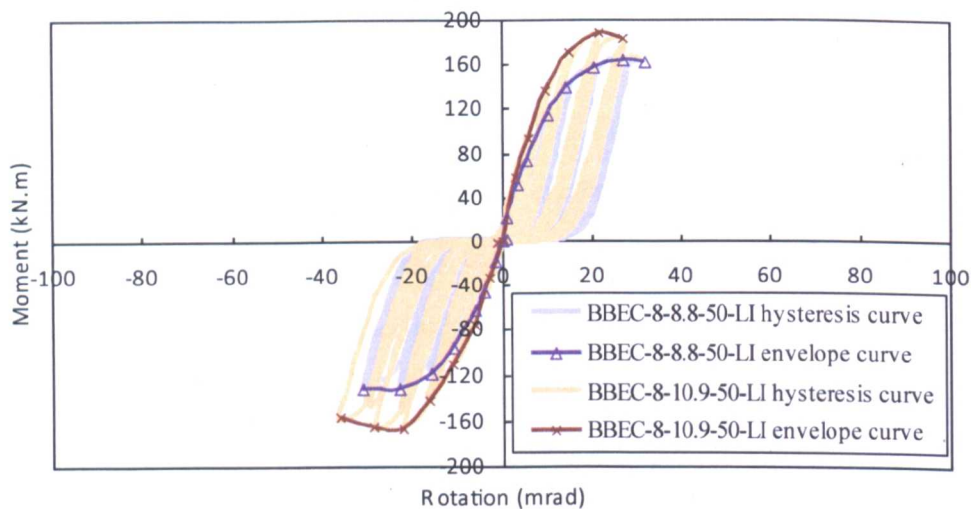


Figure 4.14 Comparison of hysteretic moment-rotation relationships of specimens BBEC-8-8.8-50-LI and BBEC-8-10.9-50-LI

It was expected that the bolt grade influences the tensile strength and preload of the blind bolt. The comparison of hysteretic moment-rotation relationships in Figure 4.14 indicates that, in contrast to the specimen BBEC-8-8.8-50-LI, the use of higher bolt grade in the specimen BBEC-8-10.9-50-LI enhances the moment and initial stiffness of the blind bolted connection, but slightly reduces the rotation capacity of the connection for the same load level. As mentioned previously, both specimens failed as the results of bolt shank fracture, thereby fulfilling the tensile capacity of the bolt shanks in the tensile regions of the connections. Hence, the evidence of this comparison can be attributed to the blind bolts that the increase of the strength and preload of the bolt shank improves the strength and stiffness of the connection.

4.3.3 Effect of cyclic loading procedure

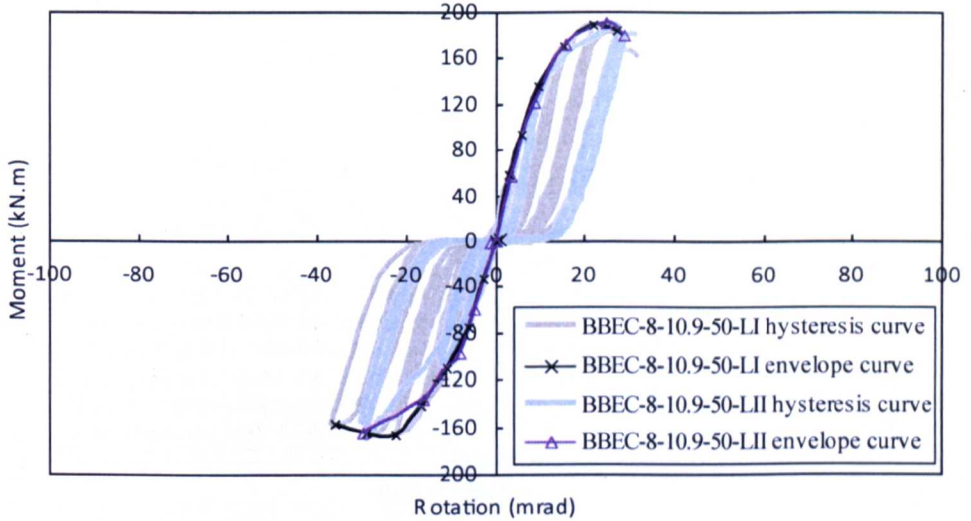


Figure 4.15 Comparison of hysteretic moment-rotation relationships of specimens BBEC-8-10.9-50-LI and BBEC-8-10.9-50-LII

Figure 4.15 presents experimental hysteretic moment-rotation relationships of the specimens (BBEC-8-10.9-50-LI and BBEC-8-10.9-50-LII) under cyclic loading procedures I and II. Both hysteresis envelope curves in both cases show a close agreement except a slight variation at the bottom of the negative excursion. This observation indicates the cyclic loading amplitudes adopted in this study differ in the generation of hysteresis loops but has slight influence on the hysteretic moment-rotation envelopes of the connection which is similar with former experimental results reported by Bernuzzi *et al* (1996) in the study of bolted flush endplate connections to open section columns. In other words, a direct comparison of hysteretic moment-rotation envelopes can be taken for the specimens under different cyclic loading amplitudes.

4.3.4 Effect of tube wall thickness

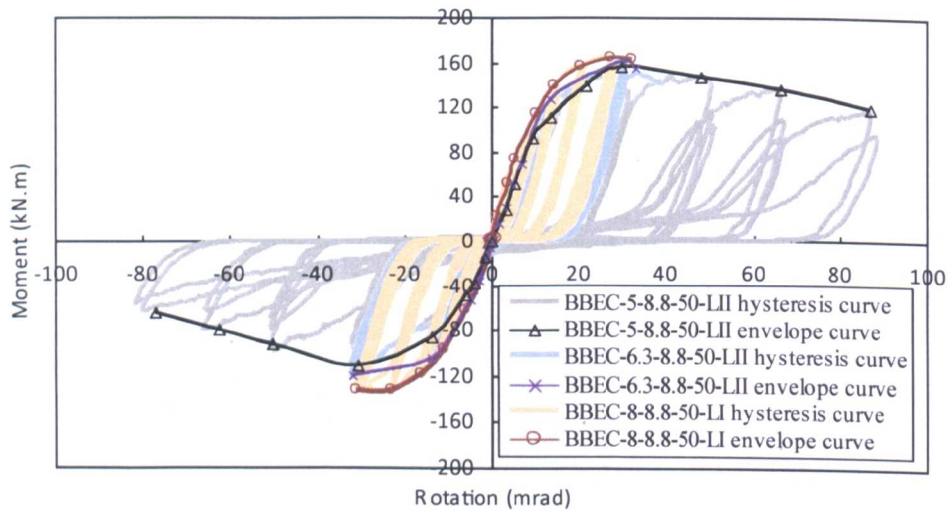


Figure 4.16 Comparison of hysteretic moment-rotation relationships of specimens BBEC-5-8.8-50-LII, BBEC-6.3-8.8-50-LII and BBEC-8-8.8-50-LI

Related to the tube wall slenderness ratio, the tube wall thickness was expected to influence the strength and flexibility of the SHS column face as a primary component of the connection. Figure 4.16 illustrates the comparison of hysteretic moment-rotation relationship of specimens (BBEC-8-8.8-50-LI, BBEC-6.3-8.8-50-LII and BBEC-5-8.8-50-LII) with varying tube wall thickness. Prior to the maximum moment of the connections, as expected, the strength and stiffness of the connections decreased with reduced tube wall thickness. It is noted that the failure mode of the connections was altered from mode I to mode II as the tube wall thickness reduces to 5 mm which represents weaker confining effect to the concrete infill and higher local flexibility of SHS column faces under in-plane bending moment. In this case, the ultimate rotation capacity of specimen BBEC-5-8.8-50-LII increases nearly 2.5 times compared to those of specimen BBEC-8-8.8-50-LI and BBEC-6.3-8.8-50-LII.

Additionally, further details of hysteretic moment-rotation relationships with failure modes I and II can be referred to the comments presented earlier in this section.

4.3.5 Effect of concrete grade

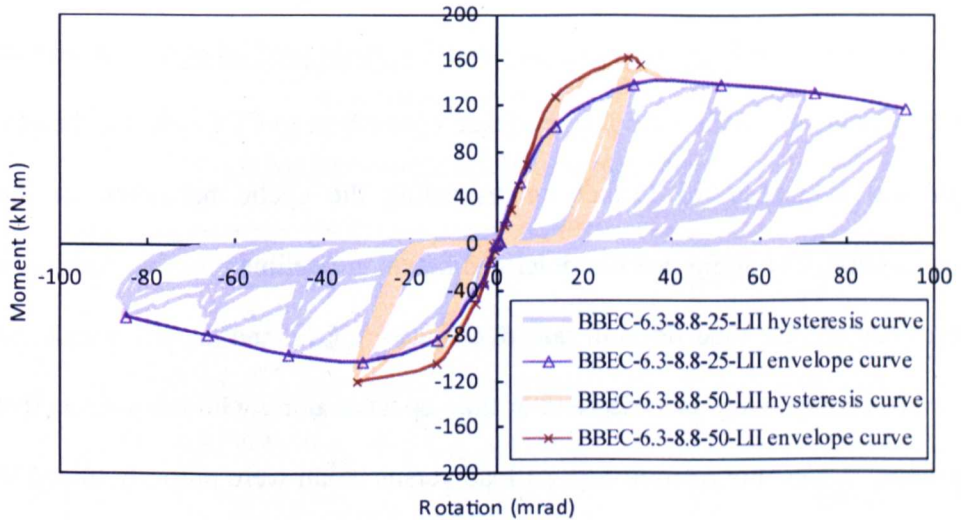


Figure 4.17 Comparison of hysteretic moment-rotation relationships of specimens BBEC-6.3-8.8-25-LII and BBEC-6.3-8.8-50-LII

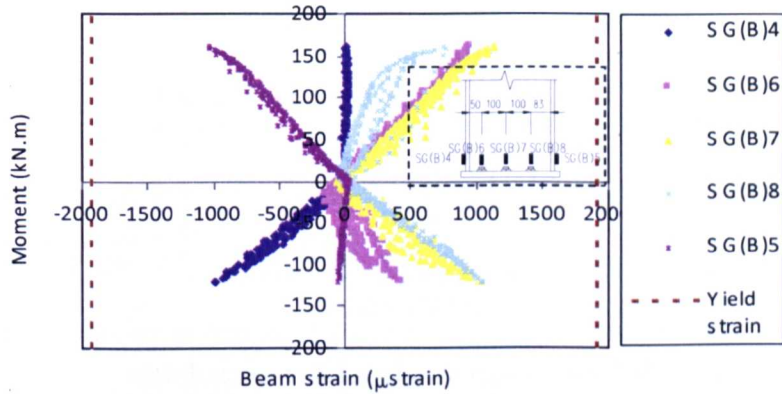
The concrete grade was expected to influence the strength of the concrete infill of CFT column. The moment-rotation relationship comparison of specimens BBEC-6.3-8.8-25-LII and BBEC-6.3-8.8-50-LII with varied concrete grade is plotted in Figure 4.17. The increase of the strength and stiffness is evident for the connection as the concrete grade is increased. It is also interesting to note that the connection with CFT column of weak concrete presents greater rotation capacity with obvious unloading branch rather than the bolt shank fracture subsequent to very limited necking development. Apart from expected effect of concrete grade on the compressive strength CFT column, it seems

that the bolt anchorage provided by concrete infill has significant influence on the blind bolt strength and deformability thereby indicating the relation of concrete grade with the failure modes of this blind bolted endplate connection to CFT column.

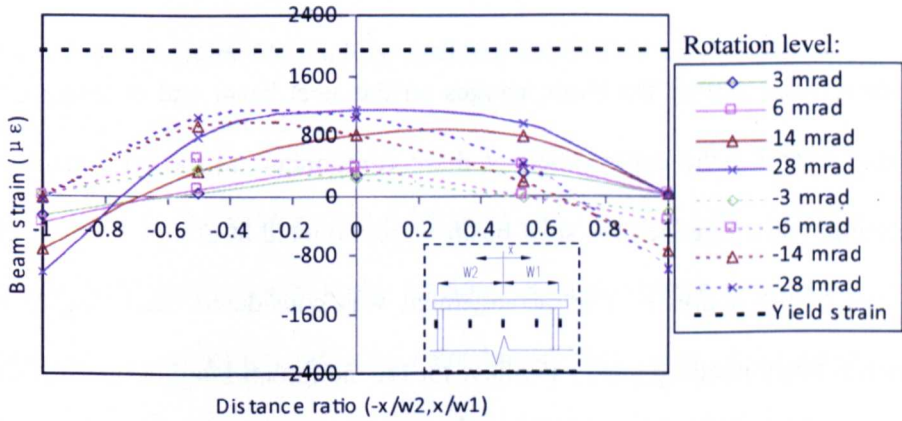
4.4 Strain profiles of relevant connection components

Strain gauge recordings were used to depict the strain profiles of the constituent components of this blind bolted endplate connection to CFT column, thereby gaining evidences for further understanding the cyclic behaviour of the connection. The strain profiles described herein are outlined for the steel beam, the endplate, the tube sidewall face & connecting face, and the bolt shank. As strain readings were recorded and in time updated along with the consecutive loading cycles, the relationships of load versus strain were properly traced in this study. To feature the strain distributions in the vicinity of the connection, the strain profiles corresponding to the maximum rotation at each loading amplitude were plotted against dimensionless location ratios. The load versus strain relations are also plotted for steel beam and endplate. The yield strains were calculated using relevant test data of coupon samples and plotted against the strain profile curves. The strain profiles illustrated below were selected from all test specimens representing the connection categories I and II.

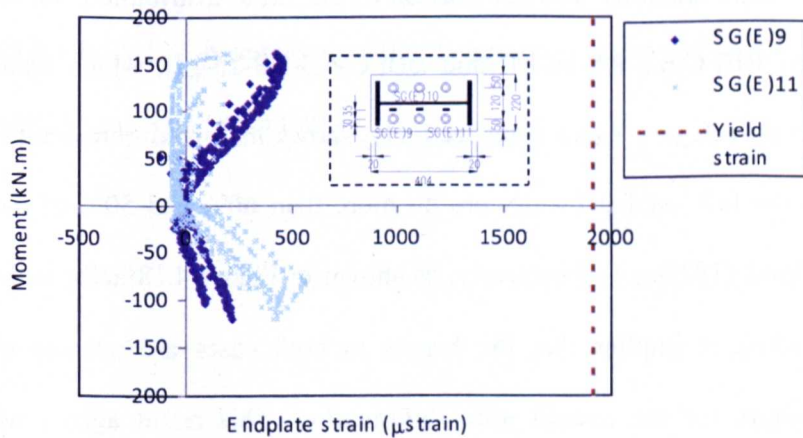
4.4.1 Strain profile of steel beam and endplate



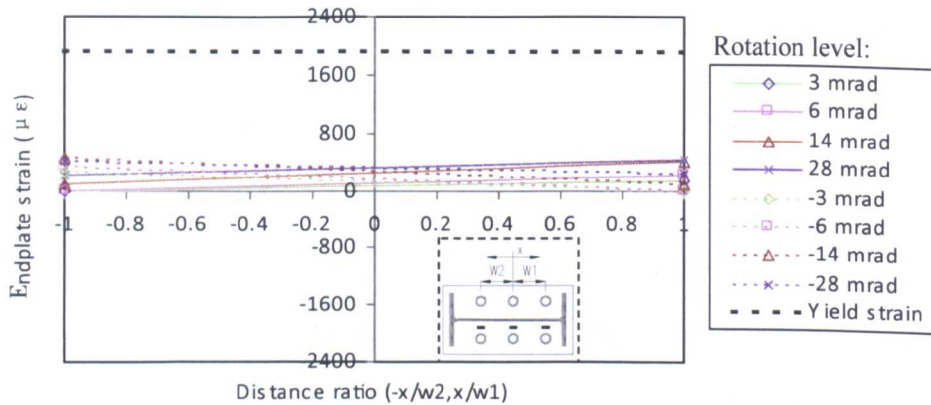
(a) Moment-strain relation on steel beam



(b) Strain-distance ratio relation on steel beam



(c) Moment-strain relation on endplate



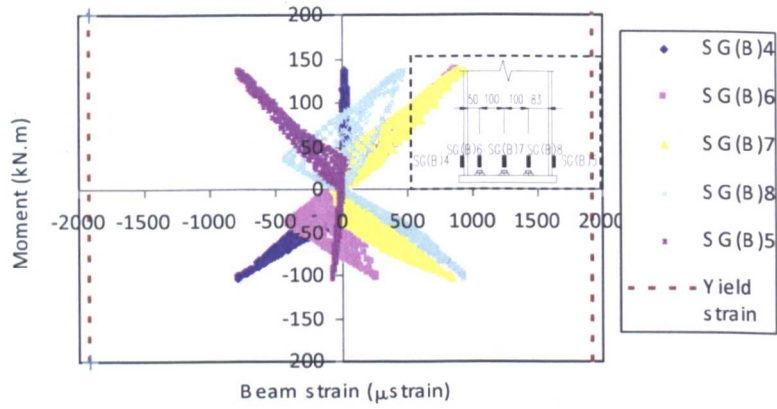
(d) Strain-distance ratio relation on endplate

Figure 4.18 Representative beam & endplate strain profile of BBEC-6.3-8.8-50-LII (connection category I)

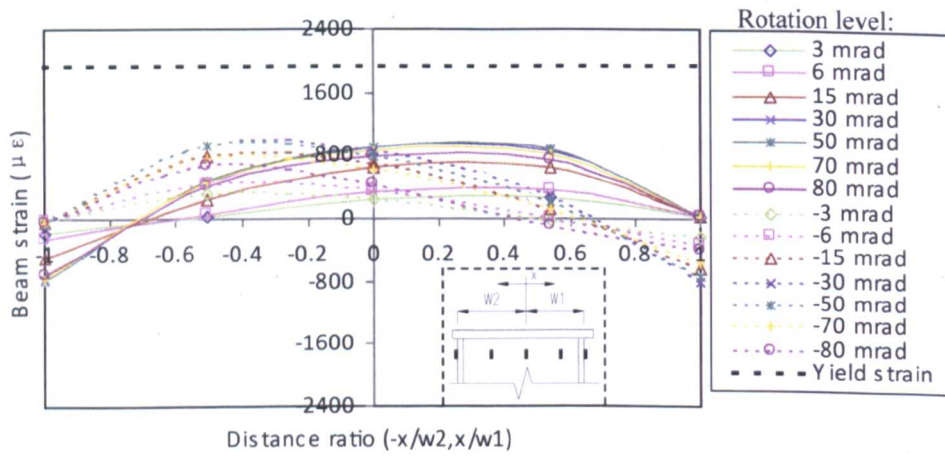
As mentioned earlier, the strain gauges on the steel beam and endplate were used to examine the contribution of these components to the joint response. The single strain gauges for steel beam were mounted at 50mm from welded surface of the endplate. This arrangement was considered according to the classical beam bending theory to allow for the maximum longitudinal strain on the cantilever beam. The strain results are plotted in moment-strain and strain-distance ratio relations. The comparison of the strain distributions on the steel beam of BBEC-6.3-8.8-50-LII and BBEC-6.3-8.8-25-LII, which feature the connection category I and II respectively, shows that maximum beam strains during the full loading history are no more than 60% and 50% of the yield strain level ($1922\mu\epsilon$) respectively, as shown in Figure 4.18(a&b) and Figure 4.19 (a&b). It implies that the beams in both cases are not the obvious contributors for the overall joint deformation. This result agrees with the connection design assumptions that the beams in both connection categories were in elastic state as the connections underwent cyclic loads.

The moment-strain relations are shown in Figure 4.18(a) and Figure 4.19(a). The strain distribution on the steel beam is expected as follows. When the outer and middle bolt rows are in tension, the corresponding steel beam web regions are obviously strained. It can be seen that similar strain gauge readings of SG(B)6&SG(B)7 and SG(B)7&SG(B)8 are around $1000\mu\text{strain}$ when the joints are subjected to negative and positive bending moments respectively. In contrast, the strains of the steel beam web near the compression flange are much lower (roughly between $350\sim 550\mu\text{strain}$). As for the beam flange, the compression counterparts have significant negative strain recordings while the opposite counterparts are slightly strained, such as SG(B)4 and SG(B)5 for negative bending moments.

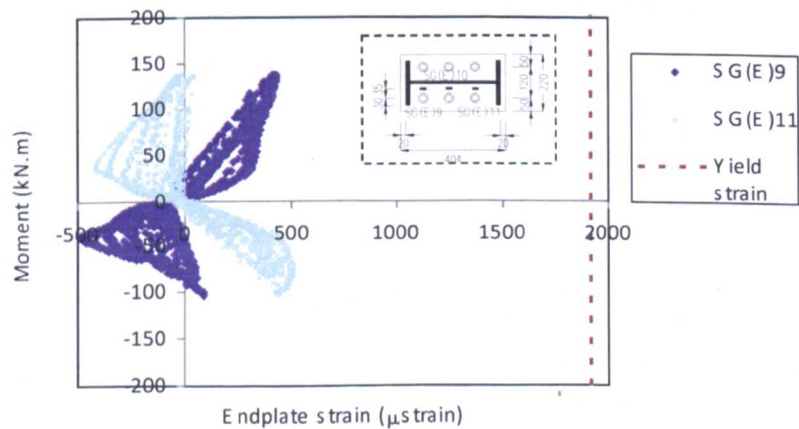
The comparison between Figure 4.18(a&b) and Figure 4.19(a&b) shows that the maximum beam strains under tension and compression measured for the specimens of connection category I are higher than those of the connection category II. This is in agreement with the moment ratios of the connection to that of the beam, i.e. 0.29 and 0.25 for specimens BBEC-6.3-8.8-50-LII and BBEC-6.3-8.8-25-LII respectively (the bending moment of the beam is transmitted by the tension flange).



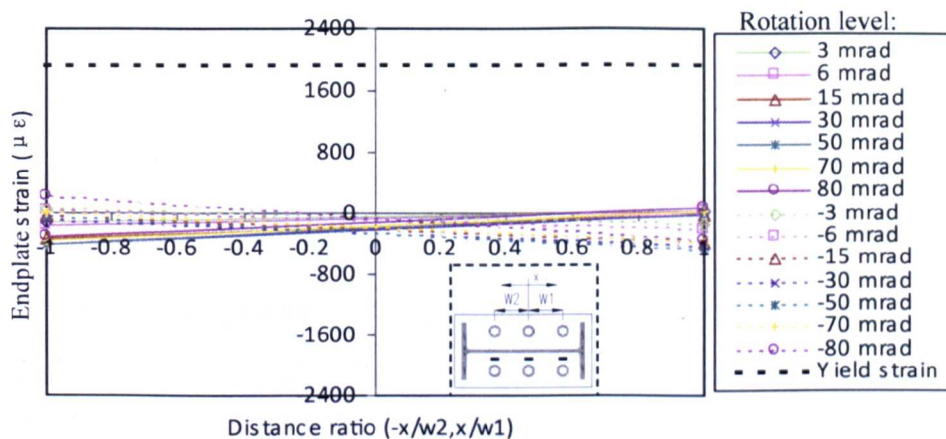
(a) Moment-strain relation on steel beam



(b) Strain-distance ratio relation on steel beam



(c) Moment-strain relation on endplate



(d) Strain-distance ratio relation on endplate

Figure 4.19 Representative beam & endplate strain profile of BBEC-6.3-8.8-25-LII (connection category II)

The strain gauges were installed on the endplate at each bolt row to capture the deformation induced by endplate in bending. The strain distributions on the endplate of BBEC-6.3-8.8-50-LII and BBEC-6.3-8.8-25-LII are shown in Figure 4.18(c&d) and Figure 4.19(c&d) respectively. Due to improper recording problem of SG(E)10, only the strain results of SG(E)9 and SG(E)11 are plotted here. As the connections underwent increasingly larger rotation, only a slight variation of the strains can be seen for specimens of the connection category I and II. The plotted maximum endplate strains during the full loading history are around $500\mu\text{strain}$ which is far below yield strain level. When comparing Figure 4.18(c) and Figure 4.19(c), it can be seen that the maximum compression strains of the endplate are almost equivalent to tension counterpart for the connection category II. However, the maximum compression strains are very low (around $50\mu\text{strain}$) for the connection category I. This is because of the development of the compression state in the connection category II in contrast to that in the connection category I.

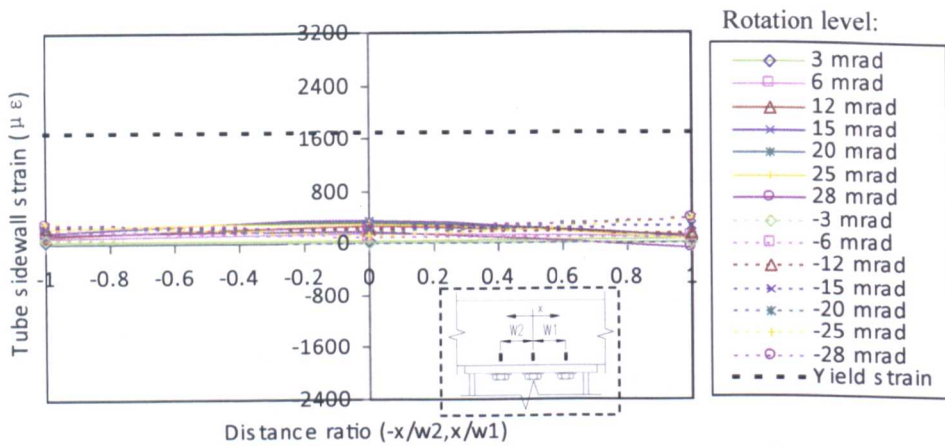
Again, the comparison of yielding strain level indicates that the design assumptions of the connection have been satisfied as the endplates are in pure elastic state. Also, the specimens of connection category I exhibit higher strains distribution than that of connection category II. Along with the steel beam, this observation can be attributed to the restraints provided by the connection rigidities.

4.4.2 *Strain profile of tube sidewall face and connecting face*

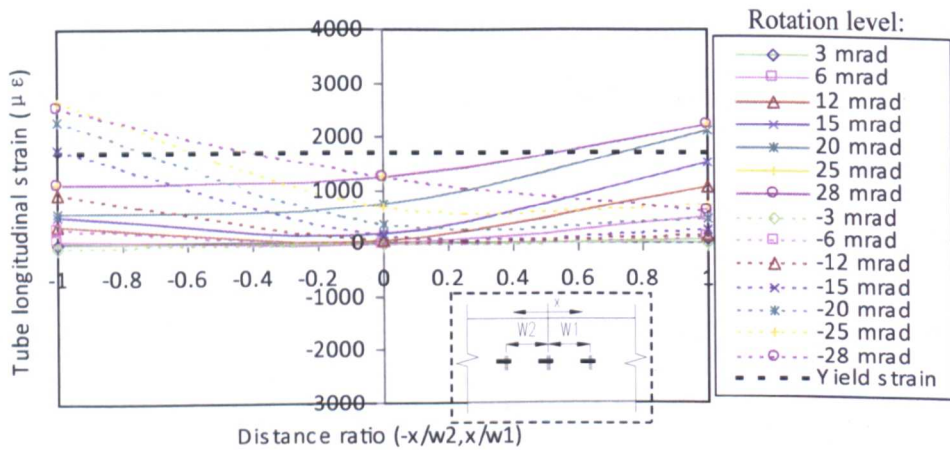
As reviewed in Chapter 2, the concrete infill has beneficial effect in strengthening the tube sidewall face from inside thereby reducing the blind bolt pullout induced deformation of tube sidewall faces as reported in the literature. Consequently, only the strains on the tube sidewall face directed towards the connecting face were studied by mounting single element strain gauges at the locations of 30mm from the connecting face corresponding to each bolt row. It is shown that the strains of tube sidewall face under overall loading history relating to the specimen of connection category I, as plotted in Figure 4.20 (a), are varied slightly and far below the yield strain level. The increase of strain at each position is almost linear. The maximum strain of $350\mu\text{strain}$ was recorded from the strain gauges corresponding to the outer and middle bolt rows in tension. In contrast, the specimen of connection category II, as plotted in Figure 4.21 (a), shows a significant strain increase (rotation larger than 15mrad) until straining beyond yield point (rotation larger than 50mrad). The maximum strain for the connections under negative and positive bending moments are $3000\mu\text{strain}$ and $2200\mu\text{strain}$ respectively. In this case, the strain recordings at outer bolt row in tension are higher than the others.

As the CFT column face is subjected to the tensile traction of the blind bolt, the connecting face at the each bolt row is supposed to be significantly strained. Accordingly, the two elements cross strain gauges were mounted at these locations for relevant measurements. Figure 4.20 (b) and Figure 4.21 (b) show that the longitudinal strain distribution on the tube connecting face for BBEC-8-10.9-50-LI and BBEC-5-8.8-50-LII, which feature the connection categories I and II respectively. For each loading cycle, the surface strain magnitude distributes with ascending curve from compression to tensile regions. The maximum strain occurs when the rotation and/or bending moment of the connection reaches the maximum, i.e. $2200\mu\text{strain}$ and $3300\mu\text{strain}$ for the connection categories I and II respectively.

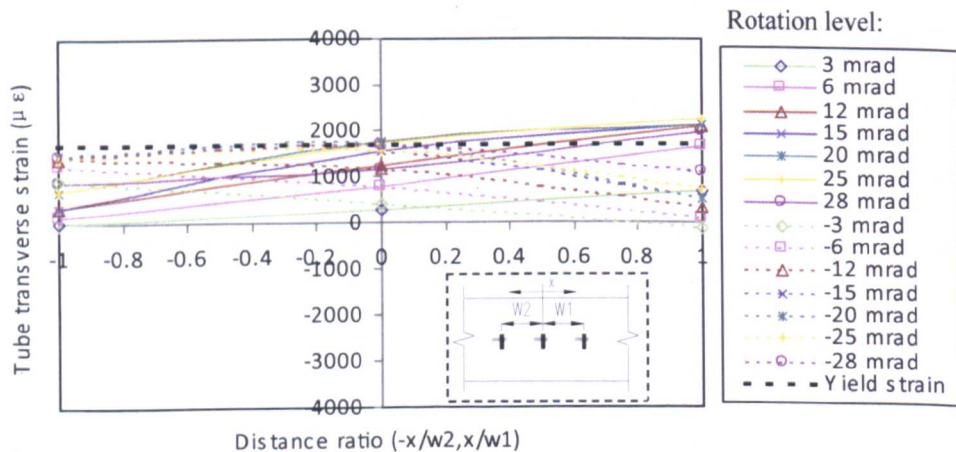
The specimen BBEC-8-10.9-50-LI represents a consistently increased longitudinal strain between three parallel bolt rows, slightly exceeding the yield strain level at the rotation beyond 20 mrad . In comparison, the specimen BBEC-5-8.8-50-LII under greater rotation action shows relatively higher strains, in which the maximum value is nearly twice the yield level. The strain development in the middle bolt row for the connection category II is much higher than that for the connection category I. This is especially the case as the strain reading ranging between $2500\mu\text{strain}$ and $2800\mu\text{strain}$ when the connection rotates greater than 30 mrad . The explanation for this observation can be related to the significant flexible deformation of the tube connecting face under relatively large bending moment. As a result, the tube face regions between the middle and outer bolt rows in tension are significantly strained.



(a) Strain distribution on tube sidewall face

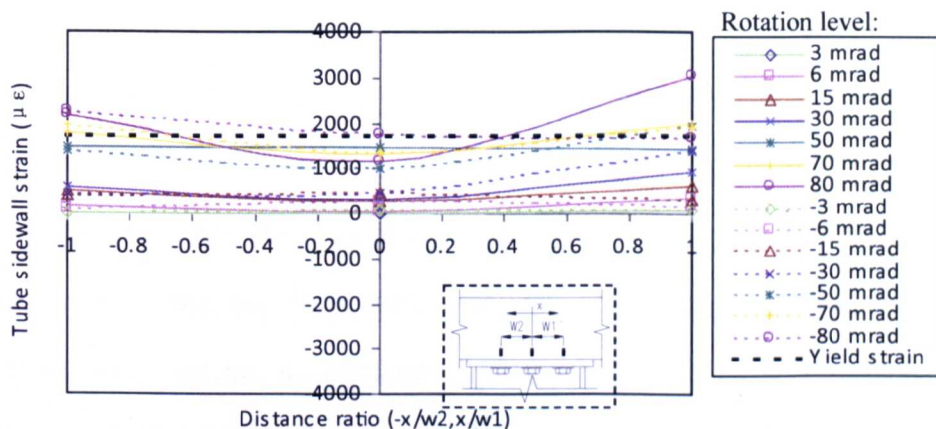


(b) Longitudinal strain distribution on tube connecting face

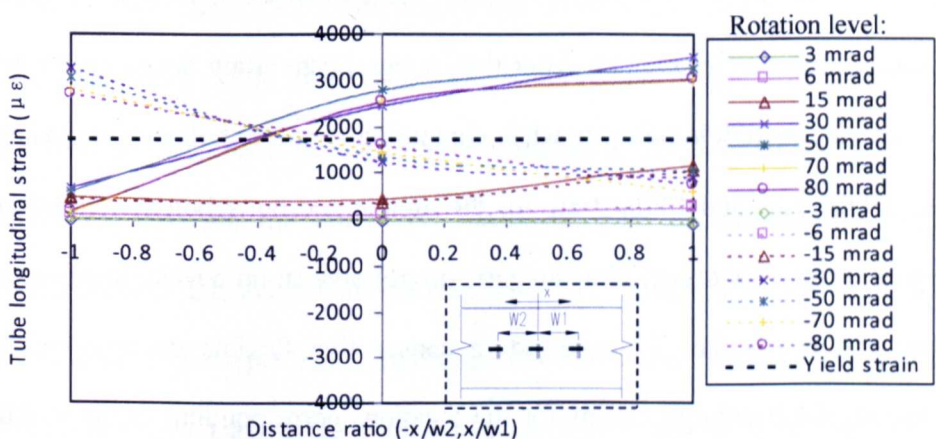


(c) Transverse strain distribution on tube connecting face

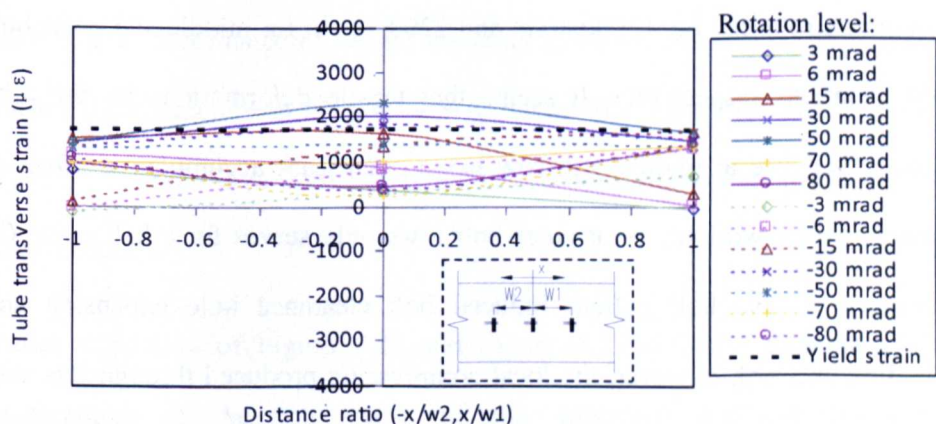
Figure 4.20 Representative tube strain profile of BBEC-8-10.9-50-LI (connection category I)



(a) Strain distribution on tube sidewall face



(b) Longitudinal strain distribution on tube connecting face



(c) Transverse strain distribution on tube connecting face

Figure 4.21 Representative tube strain profile of BBEC-5-8.8-50-LII (connection category II)

The transverse strain distribution on the tube is illustrated in Figure 4.20 (c) and Figure 4.21 (c). It can be seen that a linear increase of strain related to distance ratio when the rotation level is below 15mrad for both connections. For specimen BBEC-5-8.8-50-LII, the maximum transverse strain values of the overall cycles exceeding the yield strain level are much lower than longitudinal ones, i.e. 2200 μ strain~3300 μ strain. It appears that strains developed at the middle bolt row of the specimen BBEC-5-8.8-50-LII are higher within the gauge arrangement than those of BBEC-8-10.9-50-LI as the rotation increases to 30mrad. After that, a significant strain development can be seen at the middle bolt row when comparing the outer bolt row in tension, i.e. 2300 μ strain and 1400 μ strain for the middle and outer bolt row locations respectively. This observation suggests progressive strain development as the tube connecting face is subjected to consecutive flexible deformation. In contrast, the transverse strains for the locations corresponding to the middle and outer bolt row in tension become close as the connections are subjected to maximum rotation, i.e. 1700 μ strain and 2200 μ strain for middle and outer bolt row locations respectively. It seems that tensile deformations on the tube connecting face at middle bolt row has a significant accumulative effect at overall cycles while those at outer bolt rows only serves for a half cycle (in tension). As the bolt pullout induced bolt clearance hole expansion and bending outward, however, the local compression produced through this way compensates for the tensile strain.

4.4.3 Strain profile of blind bolt

The gauged bolt was installed only at the middle bolt row with moderate tensile loading as to avoid the presence of premature tensile fracture at the grooved shank section. The strain development on the blind bolt was recorded by strain gauges mounting symmetrically near the top and bottom shank. Each bolt strain was taken as the mean value of both strain gauge readings at related cross-section. The top shank strain gauges (SGBH) were used to record the strains at two stages, i.e., tightening of the blind bolt with preload and full-scale quasi-static cyclic loading test. The strain results of bolt preload are not described here, but will be indicated in Chapter 6. The bottom shank strain gauges (SGBB), on the other hand, were adopted to monitor the strain development on the shank with the anchorage of concrete infill. Likewise, the test results of the specimens BBEC-8-10.9-50-LI and BBEC-5-8.8-50-LII were selected to feature the connection category I and II respectively. To illustrate the response of the blind bolt, the bolt force was introduced and calculated in accordance of design methods in which an assumption is made that the force depends on the distances to the rotation centre for each bolt row (l_1, l_2, l_3), i.e. bolt force $B_i=0.5M_c/(l_1+ l_2+ l_3)$, where, M_c is bending moment of the connection.

Visual inspection of Figure 4.22 and Figure 4.23 indicates that the strain development at the top shank of the specimen BBEC-8-10.9-50-LI (connection category I) is very limited across the yield strain level, while that of the specimen BBEC-5-8.8-50-LII (connection category II) displays relatively larger strain distribution beyond the yield strain level. As for the

bottom shank measurement, the strain results of the specimen BBEC-8-10.9-50-LI were fully recorded, however, those of the specimen BBEC-5-8.8-50-LII displayed some reading errors when the rotation became larger than 40 mrad. This problem was attributed to the large local friction and sliding of the bottom shank across concrete rubbles thereby damaging the strain gauges or connecting cables. Notwithstanding that, the comparison of the bottom shank strains under 40 mrad rotation indicate that maximum strains at the specimen BBEC-8-10.9-50-LI (connection category I) are generally larger than those at the specimen BBEC-5-8.8-50-LII (connection category II). This observation suggests that the amount of deformity provided by the bolt shank in connection category I is very limited at the top shank as well as that at bottom shank anchored in concrete infill. In contrast, the top bolt shank in connection category II reveals greater amount of deformity whilst the bottom shank presents reduced strain distribution as the concrete crushing to some extent releases strained bottom shank.

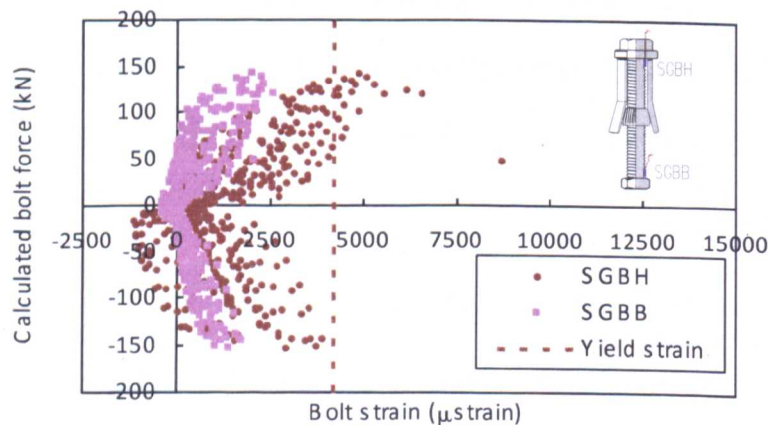


Figure 4.22 Representative bolt strain profile of BBEC-8-10.9-50-LI (connection category I)

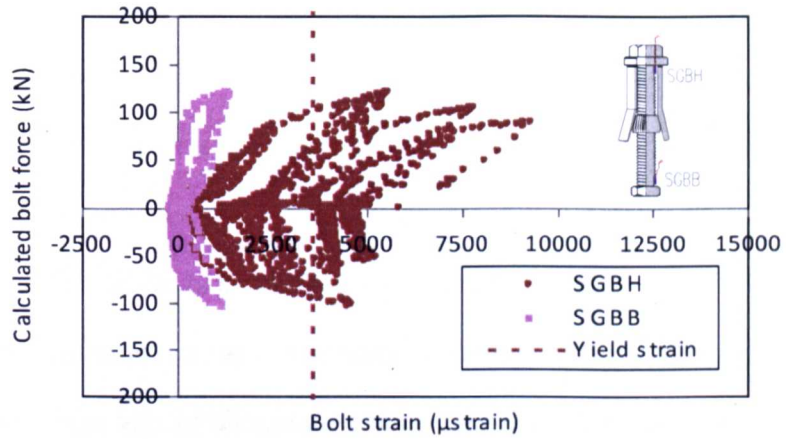


Figure 4.23 Representative bolt strain profile of BBEC-5-8.8-50-LII (connection category II)

4.5 Concluding remarks

A series of full-scale quasi-static cyclic loading tests were performed to study the cyclic behaviour of the connections. The joints have been demonstrated to exhibit nonlinear hysteretic moment-rotation response. The failure of the blind bolt or the CFT column took place as a direct consequence of adopting relatively thick endplate and strong steel beam. Two representative failure modes were observed in the experiments as: Mode I-bolt shank fracture with limited CFT column face yielding; Mode II-CFT column face moderate flexible deformation, local damage of concrete infill and moderate bolt pullout with likely local crack in the sleeves. The former failure mode is associated with relatively weak bolt, thick tube face and/or high strength concrete infill while the latter failure mode is referred to relatively strong bolt, thin tube face and/or low concrete strength. Consequently, the loading for the failure mode II was terminated with relatively large deformation.

For the overall test series, the influences of bolt grade, cyclic loading procedure, tube wall thickness and concrete grade on the hysteretic moment-rotation relationship have been described and compared in terms of failure modes, strength, stiffness, and rotation capacity. It has been demonstrated that: the use of higher bolt grade increases the moment and initial stiffness of the connections, but slightly reduces counterpart rotation capacity; the cyclic loading procedures with different loading amplitude in this study has slight influence on the moment-rotation relationship; the decreased tube wall thickness and concrete grade may reduce the strength and stiffness of the connections and, on the other hand, change the connection failure from mode I to mode II which leads to significantly increased ultimate rotation.

The strain profiles of the connection components have been used to examine the test design assumptions and gain further evidences for the connection behaviour. Comparison of strain profiles related to the specimens of the connection category I and category II indicated that two distinct strain distributions on the counterpart connection components. The test hysteretic moment-rotation relationships were used to evaluate the cyclic characteristics and cumulative damage of the connections, which will be described in Chapter 5. The test results were also used to validate the finite element models which will be presented in Chapter 6.

CHAPTER 5

CYCLIC CHARACTERIZING PARAMETER & CUMULATIVE DAMAGE ANALYSIS

5.1 Introduction

The test results of hysteretic moment-rotation relationship presented in Chapter 4 will be further examined in this chapter in terms of cyclic characterizing parameter and cumulative damage analysis.

To study the structural performance under cyclic loading, a series of parameters has been suggested in the recent codes of ECCS (1986) and ATC-24 (1992) for quantitative evaluation of the cyclic test results. These parameters relate to the issues of resistance characteristics, stiffness characteristics, deformation ductility, and energy dissipation (absorption) capacity. The use of these parameters will serve to meet the research objectives and is also in line with other beam-to-column tests reported in the literature (Dunai & Fukumoto, 1996).

In the performance-based seismic design, it is known that the reliable evaluation of structural damage becomes a key issue. The damage evaluation provides a better way in contrast to elastic analysis methods to limit the damage under seismic loads. The damage of a structure incorporates three levels, i.e., structure, substructure and members, which can be quantified by different types of damage indices. The damage indices can also be used for the assessment of subsequent loss of structural performance and rehabilitation or

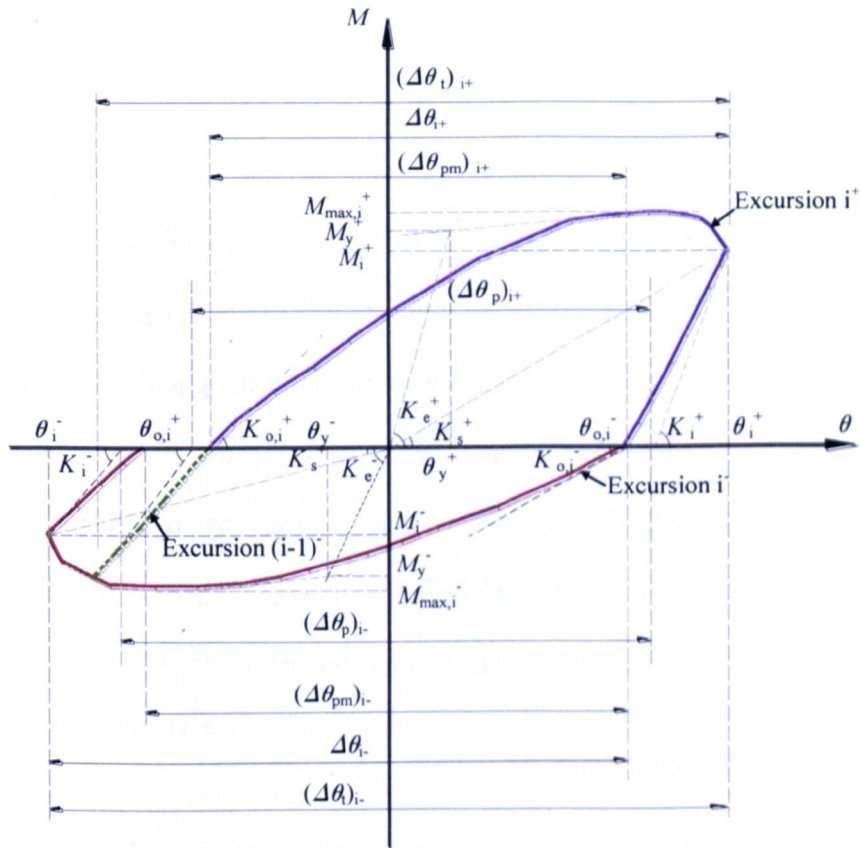
retrofitting programs. The test moment-rotation relationships along with representative failure modes were used in this cumulative damage analysis.

5.2 Cyclic characterizing parameter analysis

The values of cyclic performance quantities can be determined separately and jointly from positive and negative excursions of cyclic curves. According to ECCS (1986) and ATC-24 (1992), several basic parameters of an idealized hysteretic cycle are illustrated in Figure 5.1 and expressions for related cyclic characterizing parameters adopted in this study are indicated in Table 5.1, including those for resistance & rotation characteristics, ductility, energy dissipation capacity and stiffness characteristics. The moment and rotation at yield point, i.e., yield moment and yield rotation, were calculated based on the recommendation of FEMA-356 (2000) instead of ECCS (1986) and ATC-24 (1992), as discussed in Section 3.4.

For seismic design, it is of foremost importance to stress the concept of ductility, which is defined as the ability of the structure to undergo large plastic deformation without significant loss of strength (Mazzolani, 2000). The partial ductility ratio, which is defined as the ratio of the maximum rotation to the yield rotation of a positive or negative excursion, is often taken as a basic variable to plot against the other cyclic characterizing parameters. This is because the rotation is often used as a basic quantity of the progress of cyclic loading. Additionally, it is worth noting that characterizing cyclic behaviours are mostly used to feature the structural behaviour in the inelastic range. These parameters may be involved with unrealistic expression in the elastic range, so

the cyclic characterizing behaviour are usually studied with the partial ductility ratio no less than 1.0.



Moment	$M_{max,i}^+, M_{max,i}^-$	Maximum moment in excursion $i+$ & $i-$
	M_y^+, M_y^-	Yield moment in excursion $i+$ & $i-$
	M_i^+, M_i^-	Moment at peak rotation in excursion $i+$ & $i-$
Rotation	$\theta_{o,i}^+, \theta_{o,i}^-$	Rotation at beginning of excursion $i+$ & $i-$
	θ_y^+, θ_y^-	Yield rotation in excursion $i+$ & $i-$
	θ_i^+, θ_i^-	Peak rotation in excursion $i+$ & $i-$
	$(\Delta\theta_p)_{i+}, (\Delta\theta_p)_{i-}$	Un-deteriorated plastic deformation range of excursion $i+$ & $i-$
	$(\Delta\theta_{pm})_{i+}, (\Delta\theta_{pm})_{i-}$	Measured plastic rotation range of excursion $i+$ & $i-$
	$\Delta\theta_{i+}, \Delta\theta_{i-}$	Rotation range of excursion $i+$ & $i-$
Stiffness	$(\Delta\theta_t)_{i+}, (\Delta\theta_t)_{i-}$	Total rotation range for excursion $i+$ & $i-$
	$K_{o,i}^+, K_{o,i}^-$	Slope of $M-\theta$ diagram at the start of loading in excursion $i+$ & $i-$
	K_e^+, K_e^-	Initial stiffness of $M-\theta$ diagram in excursion $i+$ & $i-$
	K_i^+, K_i^-	Slope of $M-\theta$ diagram at the start of unloading in excursion $i+$ & $i-$
	K_s^+, K_s^-	Reduced secant stiffness at maximum rotation of excursion $i+$ & $i-$

Figure 5.1 Basic parameters of an idealized hysteretic cycle (ATC-24, 1992; ECCS, 1986)

Table 5.1 Summary of cyclic characterizing parameter expressions
(ECCS, 1986; Williams & Sexsmith, 1995)

Cyclic characterizing parameters	Expressions
Resistance ratio	$M_i^+/M_y^+, M_i^-/M_y^-$
Partial ductility ratio	$\theta_i^+/\theta_y^+, \theta_i^-/\theta_y^-$
Absorbed energy ratio	$A_i^+ / [M_y^+ (\theta_i^+ - \theta_y^+ + \theta_i^- - \theta_y^-)]$ $A_i^- / [M_y^- (\theta_i^- - \theta_y^- + \theta_i^+ - \theta_y^+)]$
Stiffness deterioration ratio	$K_s^+/K_e^+, K_s^-/K_e^-$

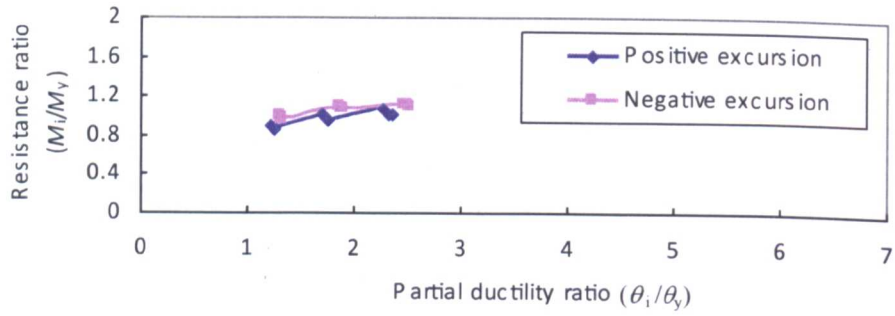
The cyclic behaviours of the connections in the positive and negative excursions are studied as follows with respect to the relationship of the cyclic characterizing parameters (referring to Table 5.1) versus partial ductility ratio. The significance of each parameter is also indicated along with the test results. For the sake of representing failure mode progression, the specimens BBEC-8-8.8-50-LI and BBEC-8-10.9-50-LI were chosen as representatives for connection category I, while the specimens BBEC-5-8.8-50-LII and BBEC-6.3-8.8-25-LII were chosen for connection category II.

5.2.1 Resistance ratio

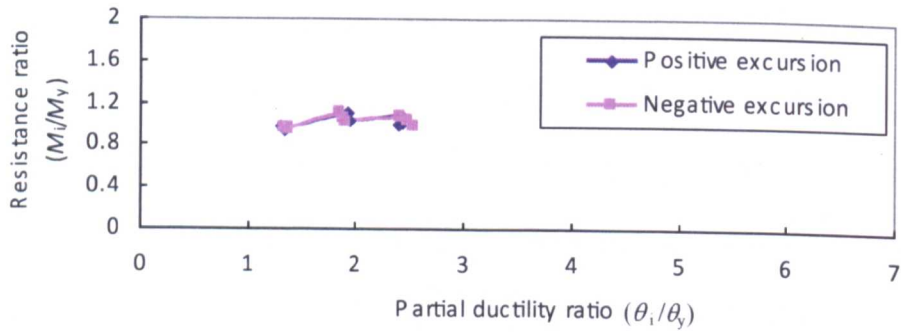
As the post yield behaviour acts as an important issue for connections subjected to cyclic loading, the resistance ratio is often used to indicate the post yield resistance with respect to yield resistance. This parameter was calculated based on the equations listed in Table 5.1. The relationships of the resistance ratio versus partial ductility ratio in the positive and negative excursions are plotted in Figure 5.2. The specimens of the identical connection category represent similar tendencies of resistance ratio variation when comparing the positive and negative excursions of cyclic curves. For specimens of connection category I (BBEC-8-8.8-50-LI and BBEC-8-10.9-50-LI), the resistance ratio is increased with increased partial ductility ratio,

without obvious moment resistance degradation at each loading amplitude level. When referring to section 4.2, it is known that the connections in this case failed as the bolt shank fractured at nearly the maximum resistance of the envelope. Although the connections with different bolt grade were used in this connection category, the steady trends of the resistance ratio versus partial ductility ratio are similar.

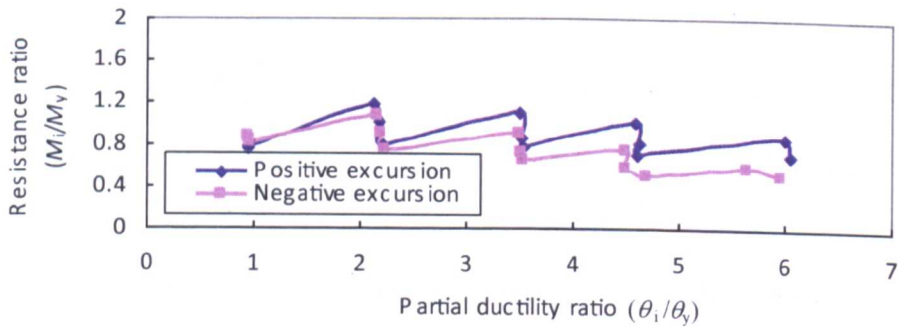
On other hand, the specimens of connection category II (BBEC-5-8.8-50-LII and BBEC-6.3-8.8-25-LII) illustrate decreasing resistances with significant drops at each loading amplitude level whilst the partial ductility ratio is increased greater than 2.0, as shown in Figure 5.2 (c) and (d). This observation in these graphs indicates a significant reduction of moment resistance at following consecutive cycles of relevant loading amplitude. The decrease of moment resistance can be attributed to the consecutive deterioration and crushing of concrete which lead to the loss of bolt anchorage. Both the steel tube wall thickness and concrete grade have direct influence on this behaviour. The former factor is related to the flexibility of the tube face and the confinement of concrete infill, while the latter factor is concerned with the strength of the concrete. Additionally, a greater decreasing tendency is shown at the negative excursion than that at positive ones for the connections in category II. This can be explained as weaker stiffness properties of the connections which produce more significant resistance degradation in connection category II than those in connection category I.



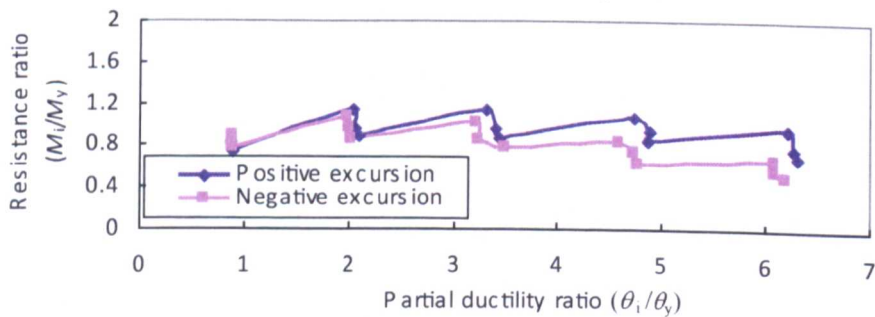
(a) BBEC-8-8.8-50-LI (Category I)



(b) BBEC-8-10.9-50-LI (Category I)



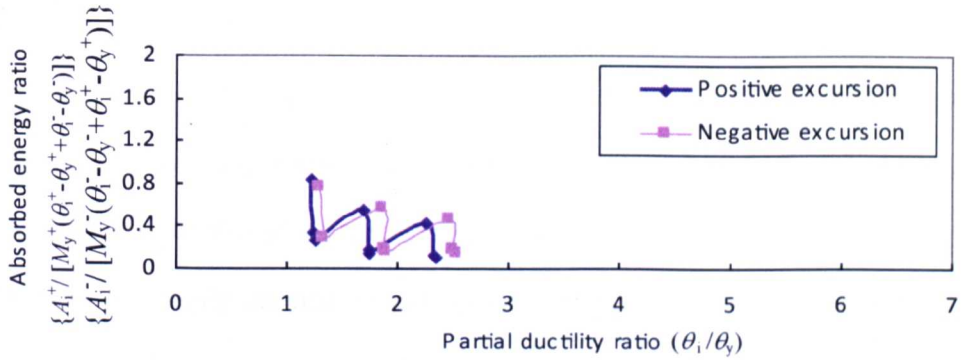
(c) BBEC-5-8.8-50-LII (Category II)



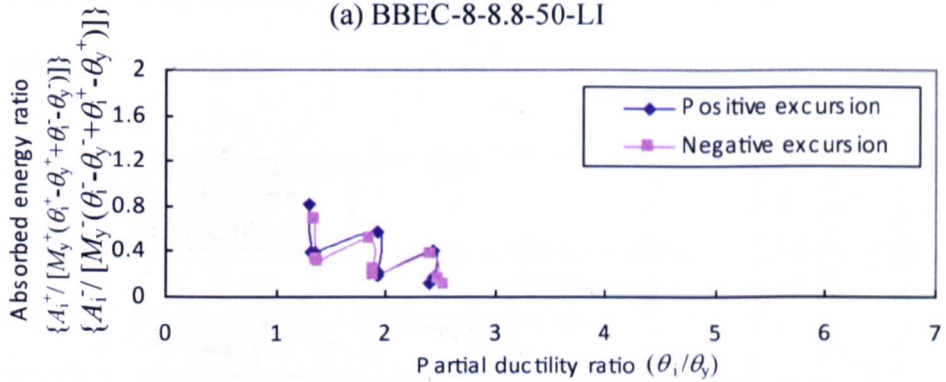
(d) BBEC-6.3-8.8-25-LII (Category II)

Figure 5.2 Relationships of resistance ratio versus partial ductility ratio

5.2.2 Energy dissipation ratio



(a) BBEC-8-8.8-50-LI



(b) BBEC-8-10.9-50-LI

Figure 5.3 Relationships of energy dissipation ratio versus partial ductility ratio for connection category I

Energy dissipation capacity is the ability of a structure or its component to dissipate energy through hysteretic behaviour which indicates the extent of ductility the joint possesses and describes its response to seismic stimulus. The amount of energy dissipation of the joint can be identified as the summation of the areas enclosed by hysteresis loops. The relationships of the energy dissipation ratio versus partial ductility ratio are plotted in Figures 5.3 & 5.4. For specimens of connection category I (BBEC-8-8.8-50-LI and BBEC-8-10.9-50-LI), the absorbed energy ratio decreases with increased partial ductility ratio. It is worth noting a dramatic drop of the absorbed energy ratio subsequent to the first cycle of each loading amplitude, which means the

dissipated energy reduces significantly during the repeated cycles. For example, the reductions in the positive excursion of the cyclic curve for specimen BBEC-8-8.8-50-LI are seen as approximately from 0.83 to 0.26, from 0.55 to 0.14, and from 0.42 to 0.10. Direct evidence can also be traced back to the hysteretic moment-rotation curves plotted in sub-Section 4.3.1, in which the hysteresis loop becomes rather narrow after the first cycle of each loading amplitude level. It seems that this tendency continues until the end of the test.

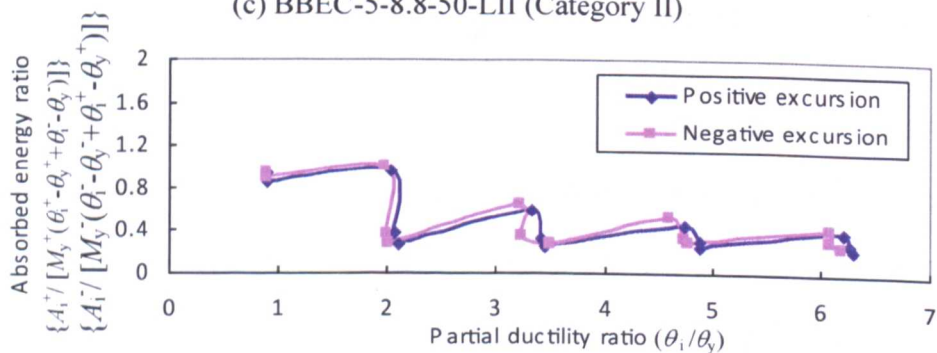
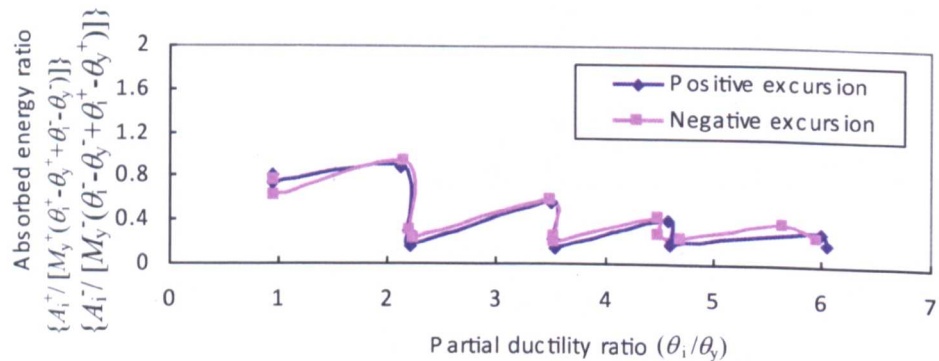


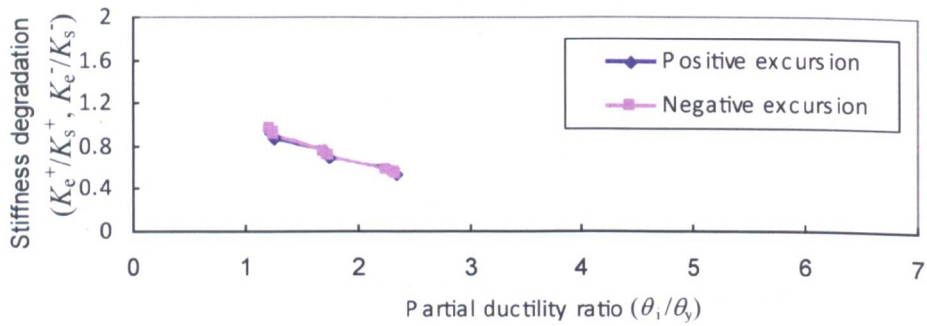
Figure 5.4 Relationships of energy dissipation ratio versus partial ductility ratio for connection category II

Along with increased partial ductility ratio, in contrast, the specimens of connection category II (BBEC-5-8.8-50-LII and BBEC-6.3-8.8-25-LII) demonstrate reduced amount of such reduction at follower consecutive cycles

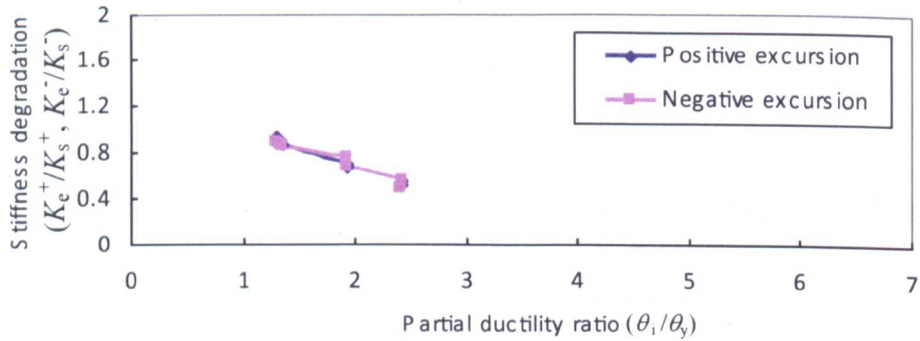
in the loading progress. e.g. For specimen BBEC-6.3-8.8-50-LII, the reductions in the positive excursion of the cyclic curve are seen as approximately from 0.95 to 0.25, from 0.59 to 0.24, from 0.44 to 0.25 and from 0.38 to 0.23. This phenomenon can be attributed to the energy dissipation of the tube connecting face as a plate element which underwent flexible tension and then compression as the load is reversed. Consequently, the energy dissipation capacity is somewhat improved for the specimens of connection category II.

5.2.3 Stiffness deterioration ratio

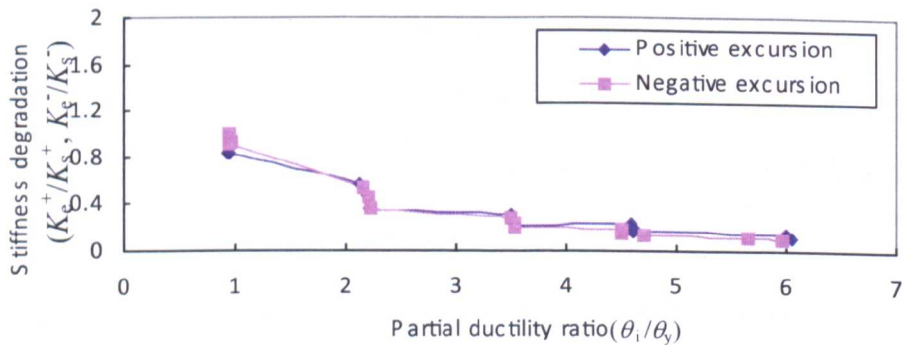
The stiffness deterioration ratio is taken as the ratio of the secant stiffness (K_{sec}) to the initial stiffness (K_e) of the connection which can be referred to Figure 5.1 and Table 5.1. A similar parameter was also used in the literature for damage measures (Williams & Sexsmith, 1995). As shown in Figure 5.5, the specimens of connection category I (BBEC-8-8.8-50-LI and BBEC-8-10.9-50-LI) demonstrate greater slopes of stiffness deterioration ratio than those of connection category II (BBEC-5-8.8-50-LII and BBEC-6.3-8.8-25-LII), i.e., higher possibility of earlier failure of the connection. For the connection category II (BBEC-5-8.8-50-LII and BBEC-6.3-8.8-25-LII), it is observed that the increase of stiffness deterioration during the overall loading progress becomes gradual as the connection partial ductility increases greater than 2.0. The similar observation can also be made for the stiffness deterioration corresponding to the cycles at the same loading amplitude.



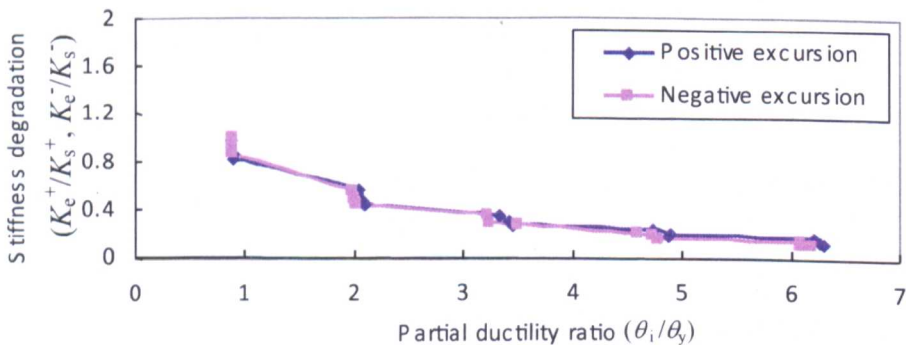
(a) BBEC-8-8.8-50-LI (Category I)



(b) BBEC-8-10.9-50-LI (Category I)



(c) BBEC-5-8.8-50-LII (Category II)



(d) BBEC-6.3-8.8-25-LII (Category II)

Figure 5.5 Relationships of stiffness degradation ratio versus partial ductility ratio

5.3 Assessment of connection ductility

The ductility issues of structural member and connection have attracted sufficient attention in recent seismic design of moment resisting frames. In Eurocode 8 (2003), a fundamental distinction is made between full strength connections and semi-rigid (and/or) partial strength connections. The related requirements are described as follows:

- The beam-to-column connection should be designed for the required degree of over-strength provided that the beam is designed as the dissipative component in the structure.
- Dissipative semi-rigid (and/or) partial strength connections are permitted provided that the subsequent conditions are satisfied: the connections have a rotation capacity consistent with global deformations; members framing into the connections are demonstrated to be stable at ultimate state; the effect of connections deformation on global drift is taken into account.

Eurocode 8 has also introduced three levels of ductility along with relevant design concepts, such as low ductility class (DCL), medium ductility class (DCM) and high ductility class (DCH). The rotation capacity of the plastic hinges is required for the connection design as: no less than 35 mrad for structures of high ductility class (DCH) and 25 mrad for structures of medium ductility class (DCM) with behaviour factor, q , larger than 2.0, which reflects that plastic deformation capacity of a structure. Although not explicitly indicated in Eurocode 8, the brittle failure of bolted flush endplate connections for less than 20 mrad rotation capacity was suggested by Bose & Hughes

(1995) and later adopted by Thomson & Broderick (2002). On the other hand, the rotation capacity of the plastic hinge includes not only the plastic hinge beam rotation but also deformation of the connection (Fardis *et al*, 2005). The latter contribution needs to be accounted for in semi-rigid and partial strength connections.

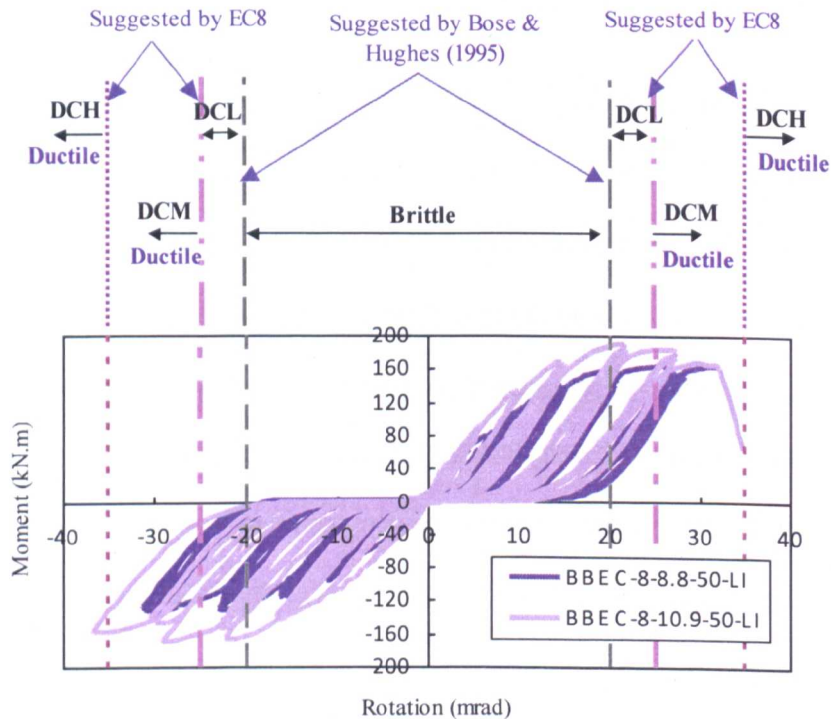


Figure 5.6 An example of comparing ductility classified indices versus test hysteretic moment-rotation relationships

The connection ductility in this study was further analysed by comparing experimental hysteretic moment-rotation relationships with suggested ductility classes mentioned above. An exemplified comparison of the specimens BBEC-8-8.8-50-LI and BBEC-8-10.9-50-LI is shown in Figure 5.6, which features connection category I. It is apparent that more than 25 mrad rotation can be provided by the connections in category I which may have potential to satisfy the connections in the frame classified as ductility class (DCM) with

$q > 2$. Using similar comparison, the specimens of connection category II are more likely to behave with more than 35 mrad rotation without significant strength and stiffness deterioration which may satisfy the connections in frames of ductility class (DCH). It is noted that the connections tested in this study relate to relatively thick endplate, i.e., the ductility contribution of endplate is ignored; otherwise further improved ductility may be obtained for the connections. However, this is beyond the scope of this work described herein.

5.4 Cumulative damage model analysis

Based on a specific damage rule, the operator that calculates damage index is defined as a damage model. So far great efforts have been made by contemporary researchers using damage indices based approaches for structural damage assessment. It should be pointed out that these approaches are not restricted to specific research topics of structural members and frames, but can be expanded to the research on beam to column connections, as reported in recent literature (e.g., Castiglioni *et al.* 2009). This approach was also adopted in this study for evaluating and comparing the behaviour of the connections by applying these damage indices and analysing the test results with respect to observed experimental failure modes.

5.4.1 Basic procedures in the definition of damage model

For the purpose of defining damage or collapse of a structural component, it is necessary to use damage parameters related to structural performance under cyclic loads in the inelastic domain. Powell & Allahabadi (1988) suggested

two basic procedures to calculate structural damage index, such as demand versus capacity procedure and degradation procedure. As for the demand versus capacity procedure, the structural performance related parameters, such as strength, displacement, deformation and energy can be used for analysis. The corresponding damage parameters may be based on a single maximum value, a maximum range or a cumulative value (using a history of values of the damage parameter). The calculated demand varies with its corresponding capacity (i.e., the demand increases monotonically as the structure is damaged). As for the degradation procedure, the structural performance related parameters, such as stiffness, strength, deformation and energy dissipation, are used for analysis. This procedure is based on the assessment of undamaged and damaged states.

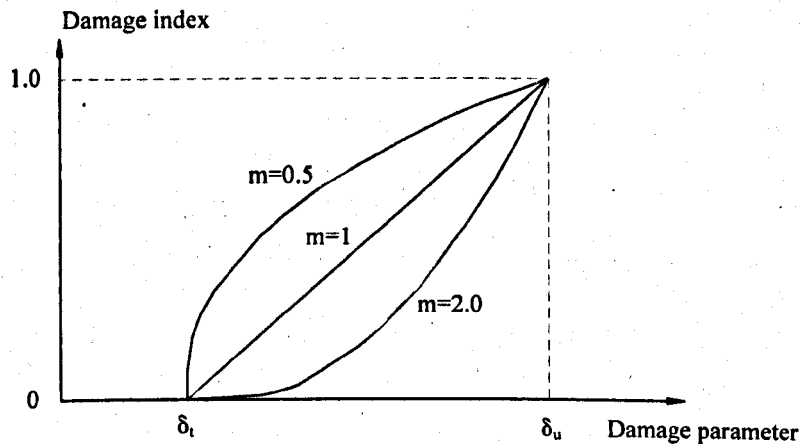


Figure 5.7 Relationship of damage index and damage parameter

As an early research in the damage functional expression, Powell & Allahabadi (1988) adopted a threshold value, δ_t , and a critical value, δ_u , as the basic damage parameters, as illustrated in Figure 5.7. It assumes that there is no significant structural damage if the structural damage index is zero,

whereas failure occurs if the structural damage index is unity. A simple linear function for structural damage index, D , is then written as:

$$D = \left(\frac{\delta_c - \delta_i}{\delta_u - \delta_i} \right)^m \quad \text{Equation 5.1}$$

where, δ_c is the calculated structural performance related parameter and m is a constant exponent. This relationship of damage index and damage parameter is illustrated in Figure 5.7. It is also worth noting that the damage index is a dimensionless scalar quantity.

Similar to Equation 5.1, Cosenza *et al.* (1993) suggested a general and practical expression for structural damage index, D , as:

$$D = \begin{cases} 0, & d \leq d_y \\ \left(\frac{d_i - d_y}{d_u - d_y} \right)^m, & d_y \leq d \leq d_u, m > 0 \end{cases} \quad \text{Equation 5.2}$$

The following steps were also recommended in the formulation of a damage functional expression as a further work following the model proposed by Powell & Allahabadi (1988):

- Definitions of d_i which are considered to be important in the definition of progressive collapse;
- Definition of the values d_y and d_u assumed by the state vector at the beginning of structural system yielding and at collapse under cyclic loads respectively. d_y can be considered similar to the threshold value, δ_i , in the model proposed by Powell & Allahabadi (1988).
- Introduction of a normalized damage functional expression D , defined on the space of the state vectors $\{d\}$; it assumes a value of zero at the

beginning of yielding and a value of 1.0 at failure. Also, the function should increase as damage increases;

- Evaluation of the value assumed by the functional expression, with reference to the structure examined and for the seismic events expected; the seismic verification will be satisfied if the result satisfies $D < 1$.

As already mentioned that a damage model refers to the calculation of the damage index through a specific damage rule, it is categorized based on the loading type and failure mechanism (Williams & Sexsmith, 1995). The non-cumulative damage model is load path independent and often calculated using the peak value of the performance as the basic variable which is normalized by the nominal capacity of the structural component. The envelope of structural response is usually used in the calculation of non-cumulative damage indices. Although it is simple for calculation, the non-cumulative damage model only presents an approximate measurement of the level of damage undergone during inelastic loading and is unable to account for the damage due to cyclic loading. The cumulative damage model and combined damage model, on the other hand, are regarded as operators that calculate the damage indices using damage rules related to cumulative damage, such as Park and Ang model. Cumulative energy dissipation, plastic displacement and deformation are usually used for cumulative damage indices. The generally adopted damage indices will be reviewed in the following subsection.

Table 5.2 Classification of damage level and related index (Park *et al.* 1985)

Damage levels	Damage indices	Referred observation of RC structure
I. No or slight	0~0.1	Sporadic concrete cracking
II. Minor	0.1~0.25	Slight concrete cracking and crushing
III. Moderate	0.25~0.4	Concrete extensive cracking and spalling
IV. Severe	0.4~1.0	Concrete crushing, reinforcement bucking
V. Collapse	>1.0	Loss of load carrying capacity

Using damage indices, it is possible to feature the structural damage mechanism and describe the evolution of structural damage states. Park *et al.* (1985) proposed a damage level classification relating to damage index. The structural damage level consists of five categories: slight, minor, moderate, severe, and collapse. The relation of damage level versus damage index is indicated in Table 5.2. Although the classification is based on the empirical experimental observations, the comparison against the ranges of damage indices has been adopted in the recent studies for beam to column connections (Altoontash *et al.* 2005) and moment resisting frames (Palazzo *et al.* 2004). As such, this classification will be further adopted in sub-Section 5.4.3 in the damage model analysis of experimental results.

5.4.2 Damage indices

Previous researchers have proposed a number of damage models for structural response related to three levels including structure, substructure and components. Although different failure criteria are involved in the structural response, it may be possible to use damage indices in a general form to carry out damage assessment. The damage indices reviewed herein are based on the characteristics of fatigue, energy and combined energy & ductility.

5.4.2.1 General fatigue based linear cumulative damage index

The Palmgren-Miner linear damage theory (Miner's rule) has been widely used to evaluate the cumulative damage and remaining fatigue life of a structure subjected to cyclic loading with constant or varying amplitudes. Miner's rule (Miner, 1945) states that, if there are k different stress amplitudes

each relating to n_i cycles, and N_i the number of cycles to failure of a constant stress S_i , then the failure occurs when:

$$\sum_{i=1}^k \frac{n_i}{N_i} = C \quad \text{Equation 5.3}$$

where, C is the experimental constant. In general, this constant is assumed to be equal to 1.0 when failure occurs. The application of Miner's rule for the study of beam to column connections has been reported by Ballio *et al.* (1995) and Castiglioni *et al.* (2009). As for cyclic loading test with non-constant displacement amplitudes, the expression for Miner rule (general fatigue) based damage index is written as:

$$D_{G,M} = \sum_{i=1}^k \frac{n_{s_i} \Delta_i}{N_f \Delta_f} \quad \text{Equation 5.4}$$

where, k is further modified as the number of displacement amplitudes. n_{s_i} is the number of cycles at the i -th displacement amplitude. N_f is the average number of cycles to failure at the i -th displacement amplitude. Δ_i and Δ_f are the displacement amplitudes corresponding to n_{s_i} and N_f respectively.

5.4.2.2 Low cycle fatigue based cumulative damage index

The parameters of plastic displacement and ductility are widely used to evaluate the low cycle fatigue damage by early researchers. Krawinkler & Zohrei (1982) adopted the simple Coffin-Manson model together with linear damage accumulation to account for the low cycle fatigue damage. The damage index is expressed with plastic deformation range as a variable:

$$D_{L,k} = A \sum_{i=1}^k (\delta_i - \delta_y)^c \quad \text{Equation 5.5}$$

where, δ_i and δ_y are the plastic deformation and yield deformation respectively. A and c are calibrating parameters. For parameter c , a general range of 1.6 to 1.8 can be used for steel structure (Cosenza *et al.* 1993) and reinforced concrete structure (Stephens & Yao, 1987), respectively. Let the value of $D_{L,k}$ be equal to 1.0 for the failure under monotonic loads, then parameter A can be obtained (Cosenza *et al.* 1993) and in turn substituted into the expression of $D_{L,k}$ as:

$$D_{L,k} = \sum_{i=1}^k \left(\frac{\delta_i - \delta_y}{\delta_u - \delta_y} \right)^c \quad \text{Equation 5.6}$$

where, δ_u is the monotonic ultimate deformation, c is taken as 1.6 in this study. It can be seen that this expression is similar to Equation 5.2 but relates to practical application. By introducing ductility ratio ($\mu_i = \delta_i / \delta_y$, $\mu_u = \delta_u / \delta_y$), $D_{L,k}$ can be transformed into the form as:

$$D_{L,k} = \sum_{i=1}^k \left(\frac{\mu_i - 1}{\mu_u - 1} \right)^c \quad \text{Equation 5.7}$$

Assuming c is equal to 1.0, the equivalent normalized ultimate damage index, $D_{L,k,u}$, in the definition of kinematic or cyclic ductility can be written as (Cosenza *et al.* 1993):

$$D_{L,k,u} = \sum_{i=1}^k \left(\frac{\mu_i - 1}{\mu_u - 1} \right) \quad \text{Equation 5.8}$$

In this case, the damage model is equally contributed by all plastic cycles

except ultimate ones. Based on the experimental results presented by Krawinkler & Zohrei (1982), Kumar & Usami (1996) suggested a greater value than unity which is more appropriate to feature the contribution of larger plastic deformation.

The low cycle fatigue based damage index has an advantage in its application incorporating plastic deformation range as a basic variable, which can be easily assessed by experimental study. Apart from envelope characteristics, however, it seems impossible to capture some detailed cyclic characteristics, such as the shape of hysteresis loop and strength deterioration.

5.4.2.3 Energy based cumulative damage index

One of the most important properties in evaluating the structural hysteretic performance is energy dissipation, which approximately incorporates the strength and plastic deformation of hysteresis loops. This provides certain merits as compared with low cycle fatigue based index which is primarily related to plastic deformation range. The energy based cumulative damage index used by early researchers (Banon *et al.* 1981, Darwin & Nmai 1986) is simply expressed as the normalization of energy dissipated (E_i) with respect to the elastic energy stored (the product of yield force, F_y , and yield deformation, δ_y). The damage index, $D_{E,D}$, is given as:

$$D_{E,D} = \sum_{i=1}^k \frac{E_i}{F_y \delta_y} \quad \text{Equation 5.9}$$

This equation also supplies a simple comparison of evaluated energy dissipation with design capacity.

Kraetzig *et al.* (1989) proposed a more complex formulation by applying the concept of primary half cycle (*PHC*) and the follower half cycle (*FHC*) to account for the cumulative damage corresponding to the excursions with maximum amplitude and the other smaller excursions, as illustrated in Figure 5.8. The damage index is calculated first by introducing intermediate variables as:

$$D_Q^+ = \frac{\sum E_{pi}^+ + \sum E_{fj}^+}{E_u^+ + \sum E_{fj}^+} \quad \text{Equation 5.10}$$

$$D_Q^- = \frac{\sum E_{pi}^- + \sum E_{fj}^-}{E_u^- + \sum E_{fj}^-} \quad \text{Equation 5.11}$$

where, $E_{pi}^{+/-}$ and $E_{fj}^{+/-}$ are the energy dissipated in primary cycles and follower cycles respectively. The displacement and deformation are often used to trace the progress of the primary and follower half cycles. At initiate stage of loading, the displacement or deformation remains zero. The damage progress continues until the energy dissipated in primary half cycles reach E_u^+ or E_u^- , where the damage index is assumed to be equal to 1.0. As for a combined action, the damage index is written by taken into account D_Q^+ and D_Q^- as:

$$D_{E,K} = D_Q^+ + D_Q^- - D_Q^+ D_Q^- \quad \text{Equation 5.12}$$

Given a primary half cycle is considered only when a half cycle reaches a new maximum amplitude, the magnitude of $D_{E,K}$ is greatly contributed by the energy dissipated in the primary cycles with respect to those in the follower cycles. The failure takes place when energy dissipated in primary half cycle is equal to the ultimate energy dissipated. In this study, an adjustment was made

for $E_{pi}^{+/-}$ and $E_{fi}^{+/-}$ which are presumed for first cycle and repeated cycles of each loading amplitude respectively. The dissipated energy was accounted as the area enclosed by the hysteresis loop excluding the elastic rotation energy which is recovered at unloading stage.

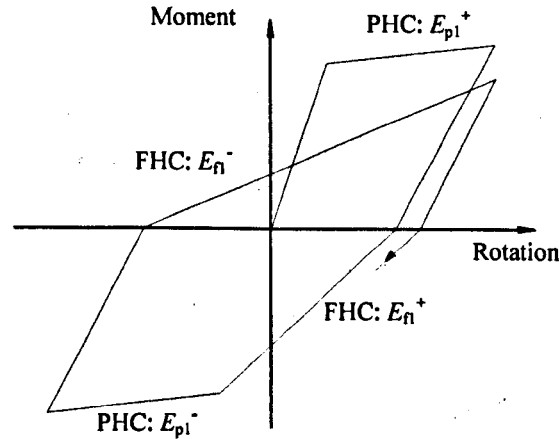


Figure 5.8 Illustration of *PHC* and *FHC* in Kraetzig damage index

5.4.2.4 Combined energy and ductility based cumulative damage index

Since the use of either ductility or energy index to quantify the structural damage has advantage of its own, some efforts have been made by early researchers to formulate them together as a linear combined damage index. The combined damage indices described herein refer to Park and Ang damage model (Park *et al.* 1985) and Banon damage model (Banon *et al.* 1981), which are widely used in the research field of concrete and steel structure.

The Park and Ang damage model was firstly proposed for the assessment of reinforced concrete building damage (Park *et al.* 1985). The original form of damage index is written as:

$$D_{C,PA} = \frac{\delta_M}{\delta_u} + \frac{\beta}{F_y \delta_u} \int dE \quad \text{Equation 5.13}$$

where, δ_M is the maximum response deformation. dE is the incremental absorbed hysteretic energy. β is a calibrating parameter for cyclic loading. F_y is the yield load. The range of β between -0.3 to 1.2, with a median of about 0.15 is suggested for concrete structure (Cosenza & Manfredi, 2000), while $\beta=0.025$ can be used for steel structure (Castiglioni *et al.* 2009). It is noted that this damage index is regarded as ductility based provided that β is small. Introducing ductility variable, this equation can be further transformed by dividing δ_y at its upper and lower parts and then becomes:

$$D_{C,PA} = \frac{\mu_M}{\mu_u} + \frac{\beta}{\mu_u} \frac{E_h}{F_y \delta_y} \quad \text{Equation 5.14}$$

where, μ_M and μ_u are the ductility ratios corresponding to δ_M and δ_u respectively. Using Park and Ang damage model for this analysis, a similar expression is written as:

$$D_{C,PA} = \frac{1}{\mu_u} \left[\mu_{i,\max} + \beta \sum_{i=1}^k (\mu_{i,j}^{\dagger} - 1) \right] \quad \text{Equation 5.15}$$

$$\mu_{i,j}^{\dagger} = 1 + \frac{E_i}{F_y \delta_y}$$

where, $\mu_{i,\max}$ is the ductility ratios similar to μ_M for i th cycle. It is worthy of note that the combination of ductility and energy in this way is linear which may cause difficulties in the analysis of highly nonlinear problem.

Banon *et al.* (1981) proposed another combined index in the analysis of RC elements and structures. This combined index was thereafter used by Cosenza *et al.* (1993) and Castiglioni *et al.* (2009) in their researches of concrete and

steel structures. The ductility component, d_d , and energy component, d_e , are introduced as:

$$d_d = \frac{\delta_{i,max} - \delta_y}{\delta_y} = \mu_{i,max} - 1 \quad \text{Equation 5.16}$$

$$d_e = a \left[\frac{2E_i}{F_y \delta_y} \right]^b = a [2(\mu_{e,i}^\dagger - 1)]^b \quad \text{Equation 5.17}$$

As reported in the literature, the calibrating parameters a and b are taken as 1.1 and 0.38 respectively. $\mu_{e,i}^\dagger$ can be referred to Equation 5.15. The Banon damage index, $D_{C,B}$, is then obtained by a nonlinear combination of these components as:

$$D_{C,B} = [(d_d)^2 + (d_e)^2]^{0.5} = \left\{ (\mu_{i,max} - 1)^2 + a^2 \sum_{i=1}^k [2(\mu_{e,i}^\dagger - 1)]^{2b} \right\}^{0.5} \quad \text{Equation 5.18}$$

It is known that the combined damage model may present incorrect results when the deformation range is close to yield value. This problem is more obvious as the loading under constant amplitude is concerned. From theoretical point of view, however, the structure has experienced small damage at the onset of inelastic deformation. Hence, common methods to tackle this issue is to neglect δ_y when it is much smaller than $\delta_{i,max}$ and δ_u . Kumar & Usami (1996) made similar observations and incorporated it into a proposed damage model to fit most types of structure. This simple consideration is also deemed acceptable for the tests with non-constant displacement amplitudes.

5.4.3 *Damage model analysis of experimental results*

The study of structural damage evolution progress with reference to each performance level is beneficial for better understanding the response of the connection under cyclic loading. To feature the typical progress, the tested specimens were categorized with due consideration of the failure modes observed in the tests. The damage indices outlined in previous subsection were adopted for the damage model analysis of the experimental results.

5.4.3.1 Tested specimen selection and damage definition

As reported in Chapter 3, the laboratory tests on 6 specimens are classified by two connection categories: (I) weak blind bolt & strong CFT column, and (II) strong blind bolt & weak CFT column. There are three primary considerations in the selection of tested specimens for damage analysis. First, it is possible to represent the typical damage modes of two categories of the connection. Second, the structural properties and numbers of loading cycles should be well recorded to establish related relationship of structural damage. Third, the assumed failure point of the tested specimen should be able to feature the local damage evolution and associate with the structural capacity parameters for structural damage definition.

The test results of the specimens BBEC-8-8.8-50-LI and BBEC-8-10.9-50-LI were selected to represent the failure with ultimate damage due to the brittle fracture of the bolt shank. The ultimate failure phenomenon is instantaneous with sudden drop of loading capacity preceded by the arrival of peak moment. Under this circumstance, the structural failure is obvious. In the other cases,

the test results of the specimens BBEC-5-8.8-50-LII and BBEC-6.3-8.8-25-LII were chosen to account for gradual failure mode. After peak moment, the connections went through continuous cycles and sustained degraded moments. The decrease of load carrying capacity is often adopted as the failure criteria to assume the failure of the connection. In this study, it is assumed that the maximum strength reduction of 30%~40% of the observed peak load as the severe failure of the connection. Although the connection may still be able to undergo some loads, it is better to assume the connection attain the failure state. In practice, the local failure observation at this stage might be apparent, e.g., the great losses of concrete anchorage, local concrete crushing, and excessive deformation around bolt hole on the tube connecting face and local bolt pullout.

5.4.3.2 Damage analysis and comparison of test specimens

Using damage indices outlined in Section 5.4.2, the relationships of progressive damage indices and loading cycle are shown from Figure 5.9 to Figure 5.12. For low cycle fatigue based damage model (Krawinkler & Zohrei, 1982), the calibrating exponent parameter (c) were taken as 1.0 and 1.6 for comparison, corresponding to the labels of 'Krawinkler 1' (K 1) and 'Krawinkler 1.6' (K 1.6) respectively. The normalized value of damage index was taken as the ratio of the results calculated by damage functional expressions at deterioration state to those at ultimate state. When the damage index ratio reaches 1.0, the failure of the connection is assumed to occur. For the purpose of relating structural performance level to physical damage, the damage level classification proposed by Park *et al.* (1985) was also used as a

reference in this comparison. In view of different cyclic behaviours involved with the connection under bending moment, the relationships for each specimen are described in terms of positive excursion which is critical for connection damage progress.

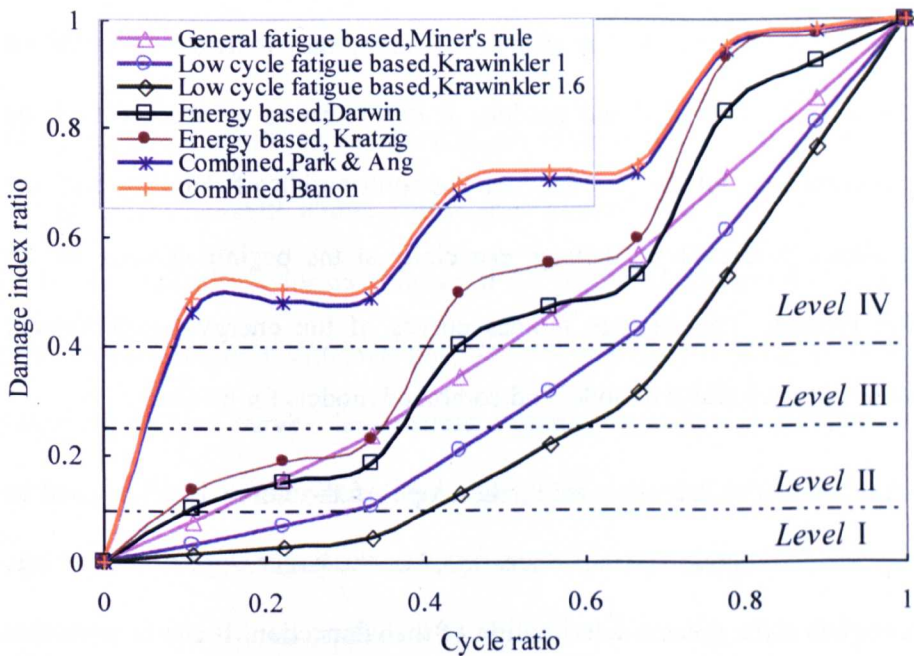


Figure 5.9 Damage model evaluations for specimen BBEC-8-8.8-50-LI

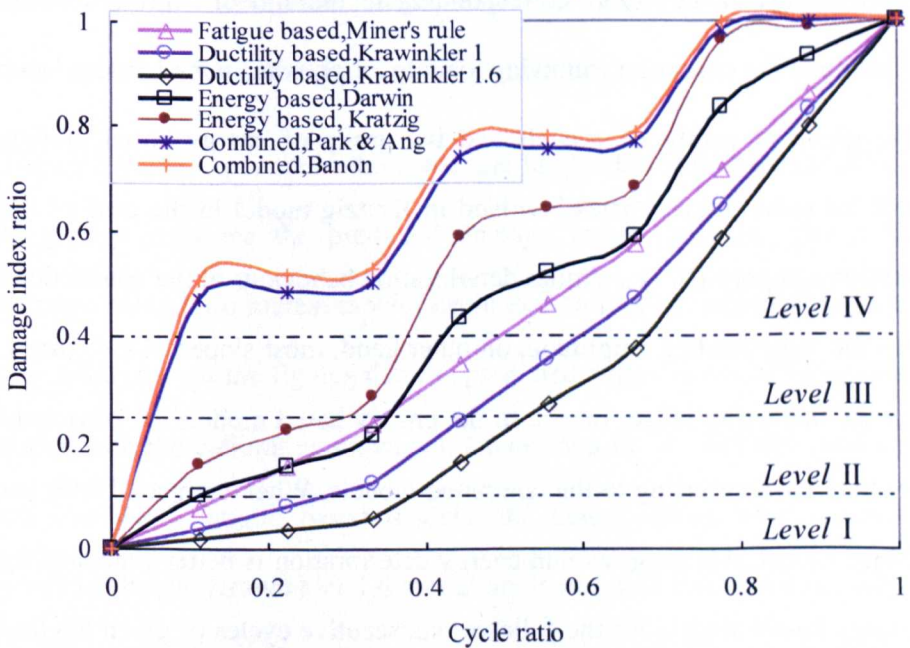


Figure 5.10 Damage model evaluations for specimen BBEC-8-10.9-50-LI

Visual inspection of Figure 5.9 to Figure 5.12 indicates an obvious stepwise increasing style for the energy based damage models and the combined models. This seems to display in similar manner with ECCS loading procedure, in which the displacement amplitude is increased step by step. For the combined models, the damage index ratios predicted by Banon are slightly larger than those by Park & Ang. When comparing the prediction of combined models with the energy based models, it is interesting to observe that the combined models, taking into account the contribution of ductility, indicate much higher prediction of damage especially at the beginning stage of the loading process. The damage indices curves of the energy based Kratzig model lie between Darwin model and combined models for all cases.

With regard to the damage model, the slope of the curve is often used to indicate the deterioration of the connection, i.e., the larger slope of the damage index variation the greater deterioration of the connection. It can be seen that the slopes between the points corresponding to the end of a given loading amplitude and the onset of a following loading amplitude are moderately close for the group of combined models and the group of energy based models (except for some discrepancies involved in Kratzig model in the case of the connection category II), i.e., similar deterioration behaviour of the connections. Within the same loading amplitude, on other hand, most slopes of the curves, except the beginning range, related to the energy based models are obviously higher than those referring to the combined models. When compared with the combined model, this suggests that energy deterioration is better evaluated by the energy based models for the follower consecutive cycles of given loading

amplitude. The energy based Darwin model prediction in most cases lie between the general fatigue based model and the combined models. By contrast, the energy based Krazzig model presents larger predictions of damage than Darwin model. In the cases plotted in Figure 5.11 and Figure 5.12, an even higher prediction of damage can be seen for the Krazzig model as the cycle ratio is greater than 0.5 as compared with the combined models.

The comparison of general fatigue and low cycle fatigue based models against the models discussed above show approximately linear and multi-linear increases respectively for most range of the predicted curves without obvious steps as the loading progressed into repeated cycles. For the general fatigue based model, the curves demonstrate a stable increase and distribute fairly close to the cater-corner across from origin to the endpoint of the graph. In comparison, the curves predicted by the low cycle fatigue based damage models are below those predicted by all the other models. This suggests that they might not well take into account the variation during the follower consecutive cycles due to the neglect of energy dissipation.

The calibrating exponent in the low cycle fatigue based damage model is seen to greatly influence the predicted damage index ratio, i.e., the predicted damage index ratio increases with decreased calibrating exponent values. It is also evident from the figures that the predicted deterioration of the connection varies with the calibrating exponent. Comparing the curve slope predicted by the low cycle fatigue based models, the deteriorations of the connection predicted by the Krawinkler 1.6 model are lower than that of the Krawinkler 1 model at the beginning stage of the loading process (Cycle ratio < 0.5).

However, a converse trend is featured by a rapid deterioration of the connection at the end of the loading process (Cycle ratio > 0.8).

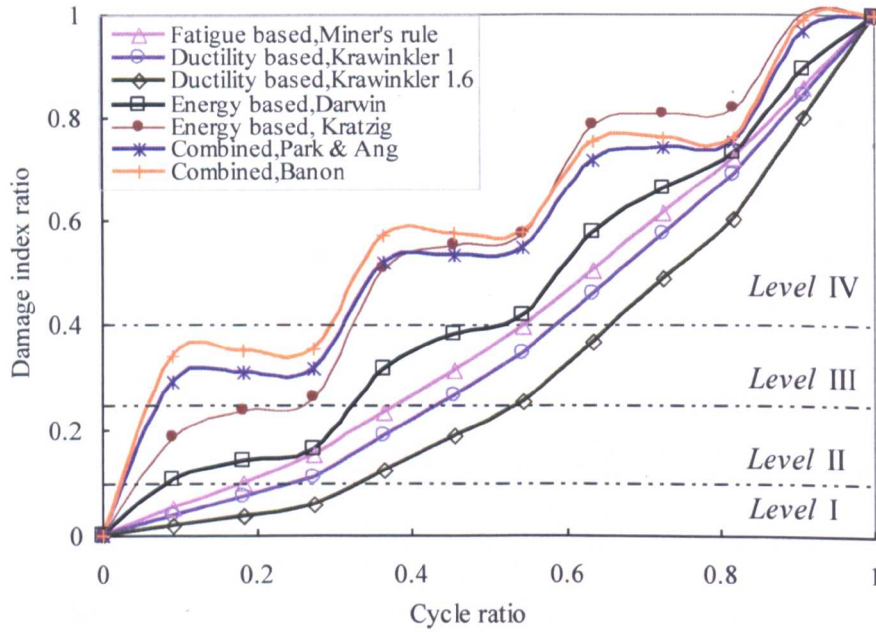


Figure 5.11 Damage model evaluations for specimen BBEC-5-8.8-50-LII

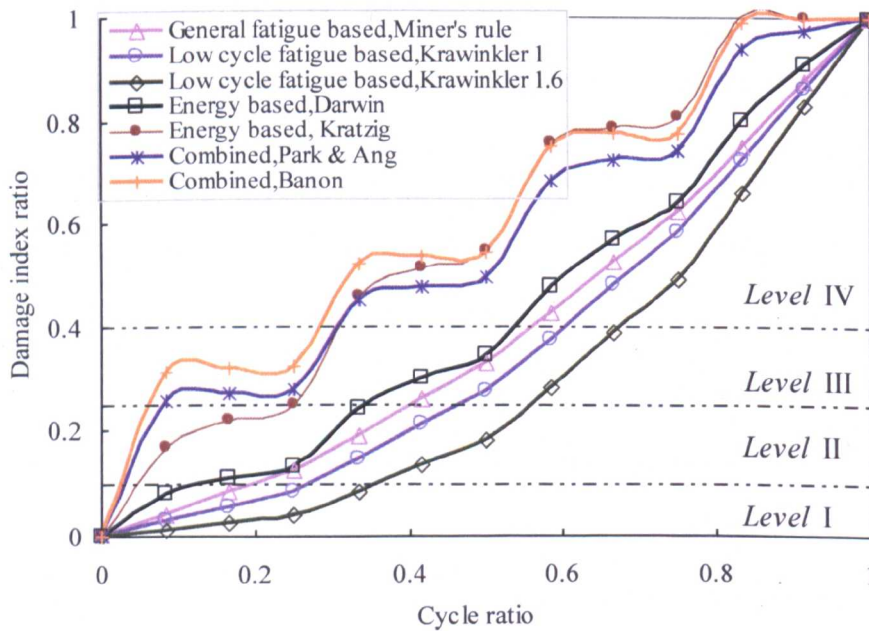


Figure 5.12 Damage model evaluations for specimen BBEC-6.3-8.8-25-LII

In order to have a closer look at the use of the damage model in evaluating the progressive damage, it was felt that the necessity to further the comparative study of different connection categories. For the connection category I (Weak blind bolt & strong CFT column), the comparison of Figure 5.9 and Figure 5.10 shows similar variations of damage indices for both cases, although a slight difference is indicated for the energy based damage indices. For the connection category II (Strong blind bolt & weak CFT column), it can be seen that the connections with CFT columns of weak tube face (Figure 5.11) present a slightly higher damage indices than those with lower concrete grade (Figure 5.12) as the cycle ratio ranges from 0 to 0.5. This trend is reversed for the curves with cycle ratio ranging from 0.7 to 1.0. Moreover, the damage indices curves predicted by the energy based and combined damage indices (Park & Ang, Banon) are more susceptible to change than those predicted by the other indices. This implies that the contribution of energy dissipation to the connection damage might be significantly influenced by altering concrete strength and tube face thickness.

When further comparing the damage indices between the connections of the two categories, it can be deduced that the combined damage indices (Park & Ang, Banon) would represent higher initial damage for the connection category I than those for the connection category II. For instance, the connections with cycle ratio ranging between 0.1 to 0.3 resulted in damage index value around 0.5 for category I (referring to Figure 5.9a) compared with a damage index value nearly 0.3 for category II (referring to Figure 5.12a). As for the energy based Darwin damage index, it can be seen that the curves for

the connection category I start and end with similar stepwise increasing styles, while those for the connection category II with regard to the follower consecutive cycles become smooth with increasing cycle ratio and terminate with almost linear growth. This trend seems to be in agreement with the cyclic characterizing parameter study presented in the Section 5.2, which can be justified in line with the decreased energy dissipation ratio of the first cycle to the follower consecutive cycles.

Table 5.3 Observed damage stages for connection category I (weak blind bolt & strong CFT column)

Stages	Moment-rotation behaviour	Experimental observations
1	Yielding of the connection	Rubber washer compressed outward, minor bolt shank elongation in the tension region of the connection
2	Full development of bolt plastic deformation	Rubber washer edge damaged, a seam between endplate and tube face in the tension zone of the connection
3	Achieving the peak load of the connection	Rubber washer locally squashed, a moderate gap between endplate and tube connecting face in the tension zone of the connection, slight local concrete crushing around bolt clearance holes
4	Gradual load descending from the peak strength	Rubber washer squashed, the gap distances between endplate and tube connecting face corresponding to each bolt row are almost in linear distribution, slight local concrete crushing around bolt clearance holes
5	Loss of load carrying capacity of the connection	Bolt shank tensile fracture, noticeable local concrete crushing around bolt clearance holes

Based on the experimental observations, the progressive failure evidence for the connection categories I and II are briefly summarized in Table 5.3 and Table 5.4 respectively. It can be concluded that the primary differences of the damage propagation between the connection categories I and II are the brittle and ductile responses developed after the peak moment respectively. For the sake of relating the Park & Ang damage level classification presented in Table

5.2 for damage model evaluation, the observed damage evidences are updated for tests and similarly divided into five stages.

Table 5.4 Observed damage stages for connection category II (strong blind bolt & weak CFT column)

Stage	Moment-rotation behaviour	Experimental observations
1	Yielding of the connection	Rubber washer compressed outward, minor bolt shank elongation in tension region of the connection
2	Full development of bolt plastic deformation	Rubber washer edge damaged, slightly bolt pull out at outer bolt rows, a seam between endplate and tube connecting face in the tension zone of the connection
3	Achieving the peak load of the connection	Rubber washer locally squashed, slight bolt pull out at the outer and the middle bolt rows, a moderate gap between endplate and tube connecting face in the tension zone of the connection, slight deformation of tube connecting face in the tension zone of the connection
4	Gradual load deterioration from the peak strength	Rubber washer squashed, noticeable bolt pull out, noticeable deformation of tube connecting face in the tension zone of the connection
5	Excessive deterioration of load carrying capacity of the connection	More excessive bolt pull out, deformation of tube connecting face in the tension zone of the connection, slight sleeve cracks initiating from the slot and propagating longitudinally

For further comparison, the observed damage stages are plotted based on the test observations and moment-rotation relations indicated in Tables 5.3 & 5.4. Also, the plots of Park & Ang damage levels are extended from aforementioned damage model evaluations and related level classification listed in Table 5.2. Comparisons of observed damage stage and Park & Ang damage level for the connection categories I and II are shown in Figures 5.13 & 5.14. The comments from these comparisons can be made as follows.

The predicted damage level curves related to combined damage models (i.e. Park & Ang, Banon) are almost coincident during the overall cycles. They also indicate higher damage levels and steep ascending branch to damage level III or IV in contrast to the other indices at the beginning stage of the cycle ratio

range. From the theoretical point of view, this can be explained by the fact that a relatively small energy contribution was allowed for in the combined damage models which implies somewhat overestimated predicted damage levels with respect to experimental observations. Conversely, the low cycle fatigue based models with no consideration of energy characteristics present relatively underestimated prediction of damage level in the most cycle ratio range. The damage level prediction in this group is also influenced by predefined calibration exponent, 'c', i.e. the predicted results of 'Krawinkler 1.6' model are much lower than those of the 'Krawinkler 1' model. By contrast, the energy based models (Darwin and Kratzig models) are seen to exhibit moderate progressive damage which correlate better with damage stages observed in the tests, such as the energy based Darwin model for the connection category I (except cycle ratio range 0.56~0.89) and the energy based Kratzig model for the connection category II (except cycle ratio range 0.18~0.36). Consequently, to feature the damage levels of such connections under cyclic loading, it is suggested to properly take into account the energy characteristics in the formulation of damage indices related. This is especially useful in accurately capturing slight and moderate damages of the connections although the severe damage level at the final stage could be unsurprisingly predicted by most referred damage models. Otherwise, the predicted damage levels could overestimate or underestimate actual damage levels observed in the experimental tests.

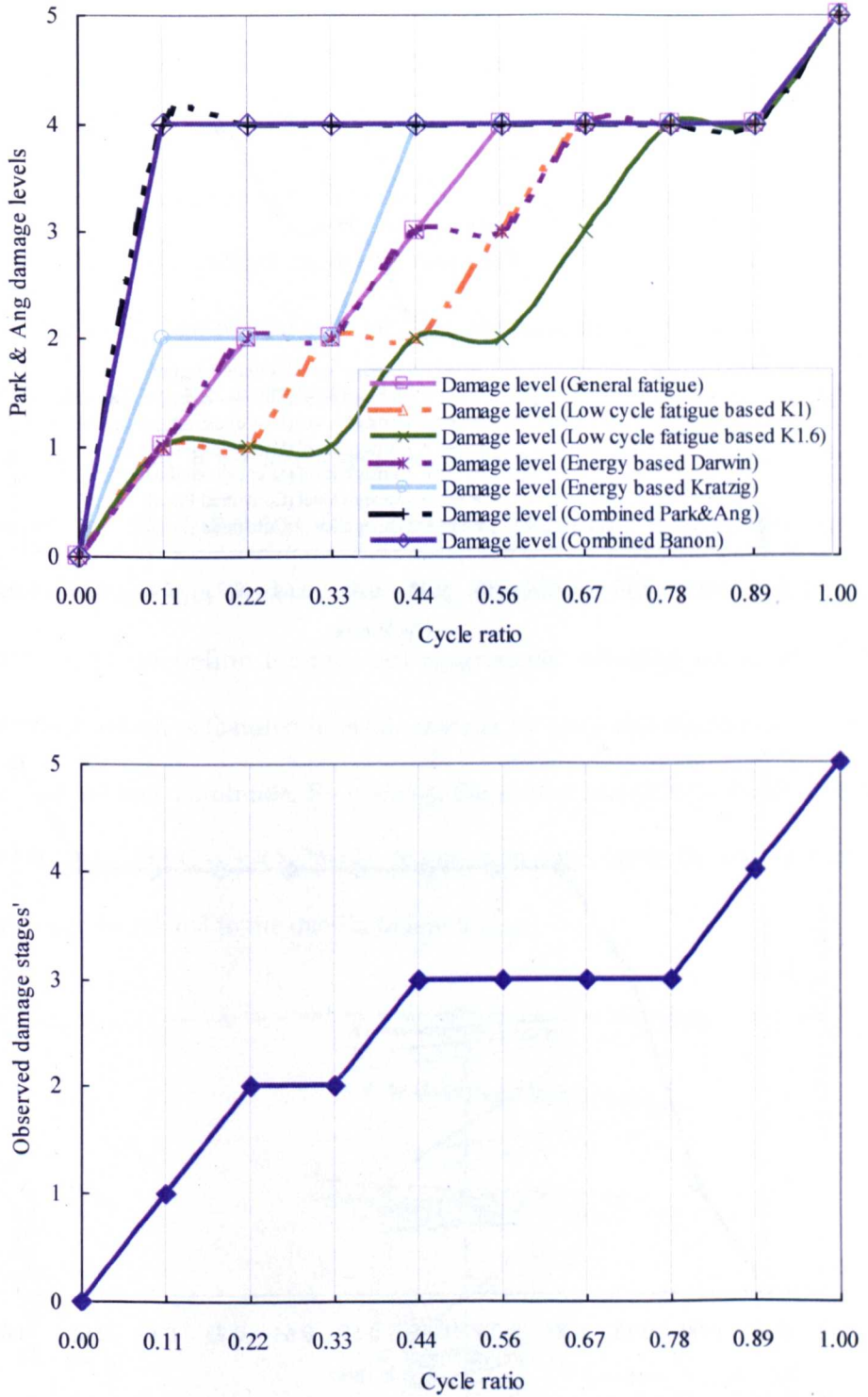


Figure 5.13 Comparison of observed damage stages and Park & Ang damage levels for connection category I

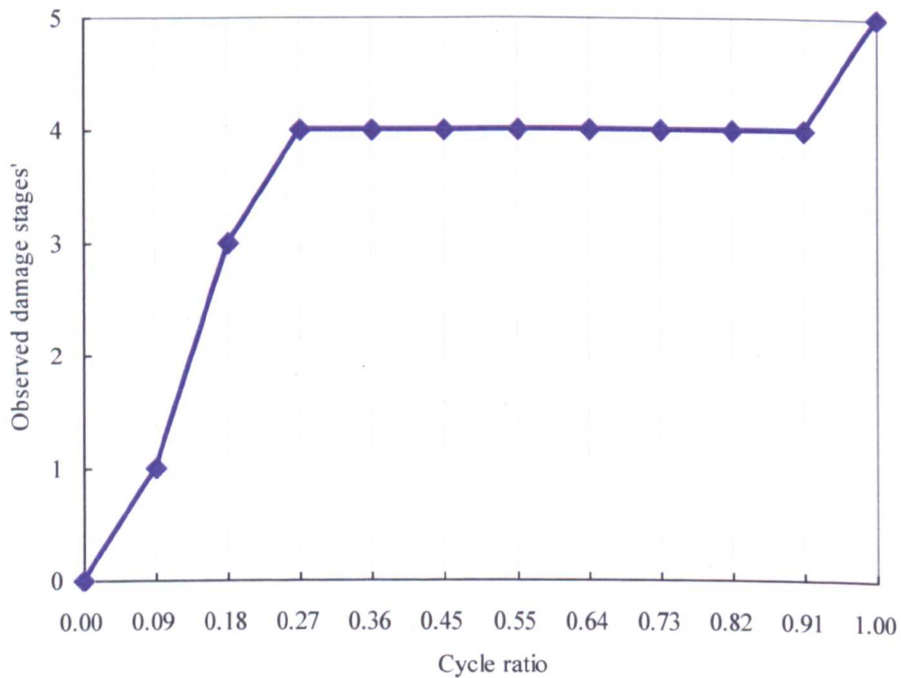
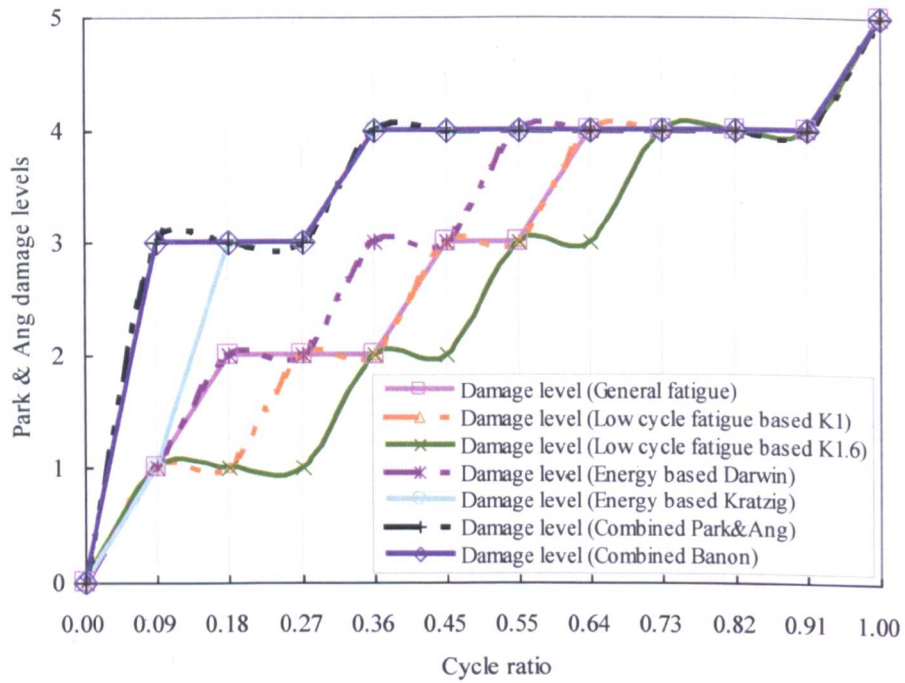
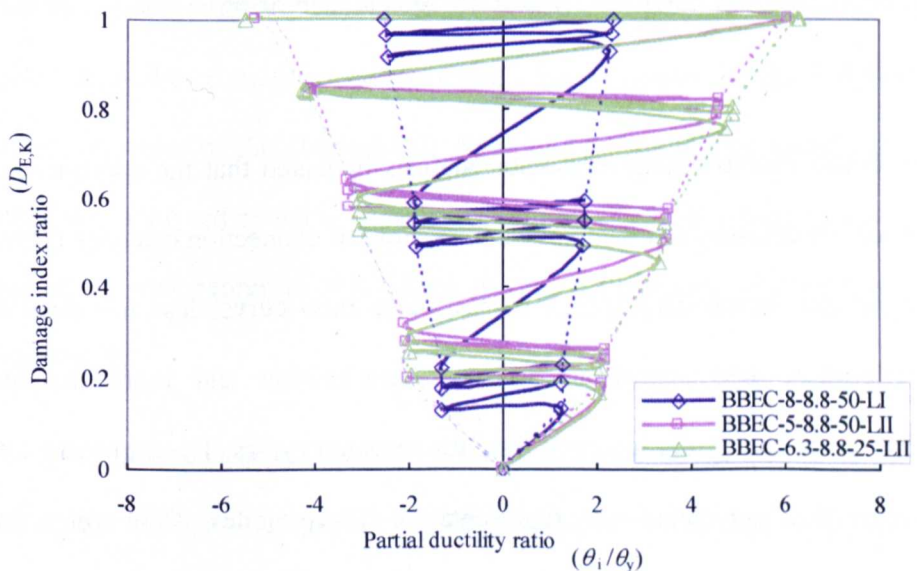


Figure 5.14 Comparison of observed damage stages and Park & Ang damage levels for connection category II

As observed above, the energy based indices are attractive for their simplified manners in the evaluation of cumulative damage. The comparison of damage evolutions of the connections (BBEC-8-8.8-50-LI, BBEC-5-8.8-50-LII and BBEC-6.3-8.8-25-LII) is further studied and shown in Figure 5.13 with the predicted damage indices against the partial ductility ratio. The actual and envelope curves are plotted with straight line and dash line respectively. The selected group of the connections allows for the connection categories I & II and keeps the bolt grade as constant. It can be seen that a dramatic increase of damage for BBEC-8-8.8-50-LI (connection categories I) when the partial ductility level varies from around 1.2 to 1.8 and then from 1.8 to 2.3. This result seems to confirm the previous experimental observations of BBEC-8-8.8-50-LI, which is featured in brittle manner by early bolt fracture at the first cycle of ultimate amplitude. By contrast, the similar increase for BBEC-5-8.8-50-LII and BBEC-6.3-8.8-25-LII (connection categories II) are moderate which can be related to the ductile failure mode.



(a) Energy based Kratzig model

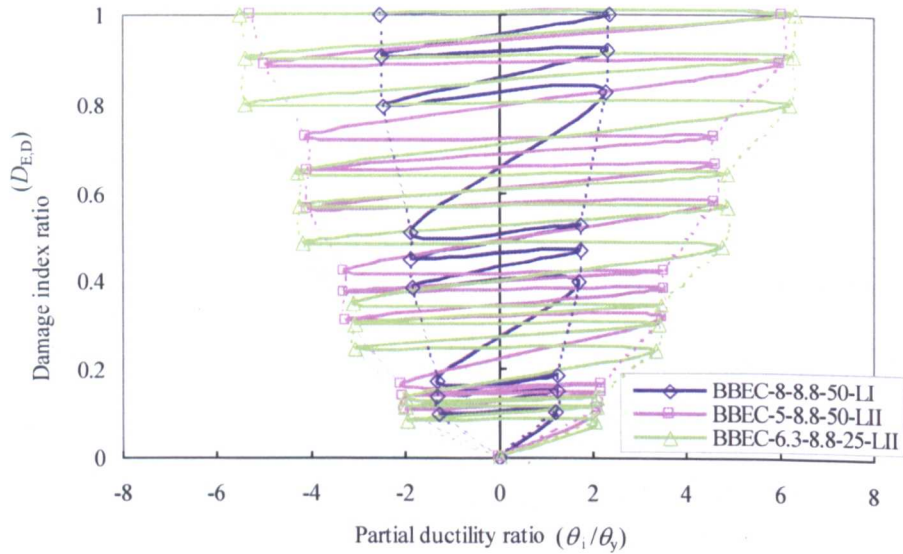


Figure 5.15 Comparisons of damage index ratio versus partial ductility ratio relationships

5.5 Concluding remarks

The study outlined in this chapter presented the cyclic characteristics evaluation and cumulative damage analysis for this innovative blind bolted endplate connection to CFT column. Given two representative failure modes of the connection categories I and II, related comparative study has been conducted.

The cyclic characterizing parameter analysis indicated that the specimens of connection category I in comparison with those of connection category II have insignificant descending branch of resistance ratio curve, less full ductility deterioration, less significant stiffness deterioration and more dramatic reduction of energy dissipation during the repeated cycles. These observations were in close agreement with representative failure modes of the connection recorded in the tests.

The observation in the comparison of hysteretic moment-rotation relationships with codified ductility levels has shown that the test specimens of connection category I and connection category II could satisfy the connections in the frame classified as medium ductility class (DCM) with behaviour factor (q) larger than 2.0 and the high ductility class (DCH) respectively.

Finally, the analysis of the experimental data was analysed using damage indices which are based on the characteristics of fatigue, energy and combined energy & ductility. Related comparative study was conducted with consideration of different damage evolutions for the connection categories I and II. It seemed that the energy based cumulative damage index is better than the other indices in featuring the progressive damage process of the connection. Given the failure modes of the connection during the inelastic range of cyclic loading, the relevant experimental observations were also summarized in terms of damage stages and compared with the general Park & Ang damage level classification. It has been demonstrated that the use of damage levels & stages in relation to the general fatigue based model, the low cycle fatigue based models and the energy based models for the analysis of cyclic behaviour of the connections. Additionally, the energy based damage model was analysed by using partial ductility ratio. The presented results were seemed to well represent the failure modes development observed in the experiments.

The cyclic characteristics evaluation and cumulative damage model analysis in this study were limited to the cyclic loading procedure as non-constant displacement amplitudes (as specified in ECCS recommendation). The failure

modes are also restricted to those of the connection categories I and II of this type of the connection.

CHAPTER 6

FINITE ELEMENT MODELLING

6.1 Introduction

The preceding chapter outlined an analysis of the connection behaviours using cyclic characterizing parameters and damage models. Although the outcomes provided by experimental approach are direct indications of the connection behaviour, they are limited in terms of the number and range of geometric and material parameters studied. It is also difficult to conduct costly and time-consuming experimental parametric studies. Moreover, the data that can be measured in experiments are necessarily limited by possible instrumentations. For example, it is not possible to measure with ease data relating to the flaring sleeves interlocking or to the anchored nut in the concrete. Fortunately, the recent development in finite element modelling technology has made it possible to simulate the behaviour of complex engineering problems. In other words, the finite element modelling with reasonable accuracy acts an efficient tool to supplement experimental study. Also, using finite element modelling for parametric study is a powerful means in developing the understanding of the structural behaviour of the connection.

Finite element modelling in this study was carried out using the ANSYS software (ANSYS version 12.1, 2009) which has been widely adopted for structural analysis by both academia and industry. This program provides powerful linear and nonlinear structural capabilities with a wide range of options regarding material, element and solution controls for high-quality and

reliable structural simulations. The finite element model can be developed through both the Graphics User Interface (GUI) and the ANSYS Parametric Design Language (APDL). The main feature of the GUI is the direct viewing with the aid of user commands. However, this may pose some difficulties in accurately picking certain nodes and key points, especially for irregular surfaces. Alternatively, the APDL can be used to automate common tasks or even build parametric model, including a wide range of other features such as repeating a command, macros, if-then-else branching, do-loops, and scalar, vector and matrix operations (ANSYS@Academic Research, 2009). There are three basic steps in the ANSYS analytical process as pre-processing phase, solution phase and post-processing phase as shown in Figure 6.1. As for a complicated analysis, it usually requires more than one iteration in an analytical process.

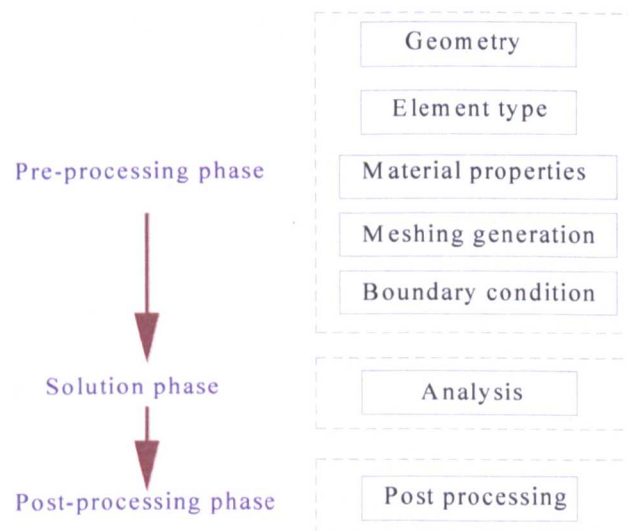


Figure 6.1 Typical procedure for finite element analysis

The finite element model in this study was developed with emphasis not only on the blind bolt but also on the connection system. The following section will

present a step-by-step procedure of the development of finite element model. In Section 6.2, the general description of the material model and related element type in ANSYS is presented. Then the boundary condition and loading case are outlined. The solution control method is also described for finite element analysis. Following the general description of the finite element model, the use of advanced analysis techniques to facilitate the simulation of the finite element model is indicated. The validation of the finite element model with experimental results is described in Section 6.3 including the comparison of moment-rotation relationship and strain distribution of the connection. The failure modes of the connection are then depicted and traced with the stress contours finite element model. The parametric study is presented in Section 6.4, including the comparison of geometric and mechanical influential parameters in the finite element analysis. The comparative study of the adopted modelling techniques is also outlined. Finally, a brief summary and discussion about the finite element analysis for the cyclic behaviour of the connection are presented in Section 6.5.

6.2 General description of finite element model

6.2.1 *Element type*

The element type is often considered to fit the geometry of the model. Two dimensional and three dimensional elements were adopted first in this study for finite element analysis. Shell elements are two-dimensional element that typically used for the structures where the thickness is negligible compared to its length and width. Solid elements are three-dimensional element that

typically used for the structures without any a priori geometric simplification (Zienkiewicz & Taylor, 2006). When comparing both elements, the solid elements are favoured by their advantages of directness and identical outlook as actual physical system. Nevertheless, the introduction of more nodes with degrees of freedom in solid elements often produces more computation cost for a complicated finite element model under multiple loading steps condition. Accordingly, a combination of shell elements and solid elements were selected in the finite element models as presented below.

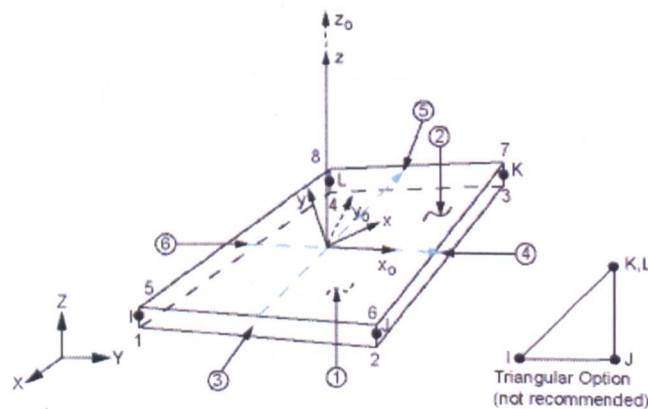


Figure 6.2 Schematic of SHELL181 (ANSYS@Academic Research, 2009)

The SHELL181 element was used for modelling of the steel beam. This is a four-node element with six degrees of freedom at each node: translations in the x , y , and z directions, and rotations about the x , y , and z -axes, as shown in Figure 6.2. The element is capable of linear, large rotation, and/or large strain nonlinear analysis. The different thickness of the shell can be defined using real constants as input at each node. The typical commands in the definition of a section type and geometry refer to `SECTYPE` and `SECDATA` command respectively. The `SECOFFSET` command can be used to allow for the element offsets at the top, middle, and bottom surfaces. In contrast to some other shell

elements in ANSYS, the SHELL181 element is well-suited for large rotation and/or large strain nonlinear applications.

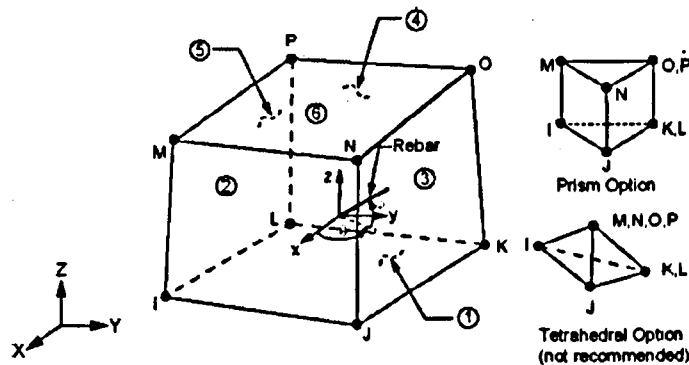


Figure 6.3 Schematic of SOLID65 (ANSYS@Academic Research, 2009)

The SOLID65 element was used in the model for the concrete infill. This is an eight-node element with three degrees of freedom at each node: translations in the nodal x , y , and z directions, as shown in Figure 6.3. The element description herein only refers to concrete with no rebar capability, although it is possible for this element to allow for the reinforcement behaviour. The element is capable of directional integration point cracking and crushing associated with plastic deformation behaviour. For this reason, this element, other than some other solid elements, was selected for the modelling of concrete infill. The assumptions and restrictions are defined in the reference of ANSYS@Academic Research (2009) as follows:

- Cracking is permitted in three orthogonal directional at each integration point;
- If cracking occur at an integration point, the cracking is modelling through an adjustment of material properties which effectively treats the cracking as a 'smeared band' of cracks, rather than discrete cracks;
- The concrete material is assumed to be initially isotropic;

- In addition to cracking and crushing, the concrete may also undergo plasticity, with the Drucker-Prager failure surface being most commonly used. In this case, the plasticity is done before the cracking and crushing checks.

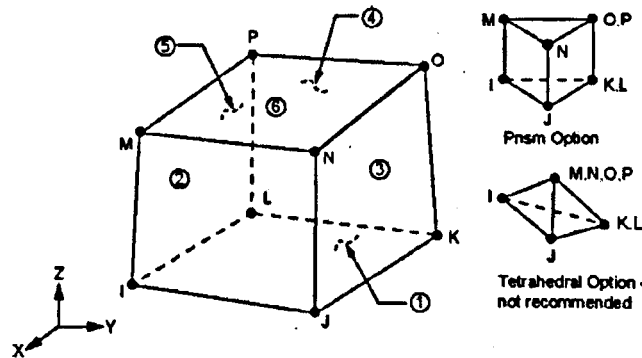


Figure 6.4 Schematic of SOLID185 (ANSYS@Academic Research, 2009)

The SOLID185 element was used for the modelling of the blind bolt, the hollow section column and the endplate. This element is an eight-node element with three degrees of freedom at each node: translations in the nodal x, y, and z directions, as shown in Figure 6.4. The SOLID185 element is the subsequent version of SOLID45 in the ANSYS element library, which has mixed formulation capability in simulating deformation of nearly incompressible elasto-plastic materials. Compared with some other higher order solid elements (such as SOLID186), this element has its advantage of less amount of computation cost. This also means faster analysis for the identical problems and achieves comparable results. Also, it avoids the problem derived from the high order solid element degeneration to the shape of pyramid, for which the due consideration should be given so as to minimize the stress gradients. As for a complicated finite element model, the formation

of tetrahedron and prism shape of the element may be used to better fit irregular element meshes.

The BEAM188 element was used in the model to account for the bolt shank anchored in the concrete infill below the threaded cone. This element has two nodes with six or seven degree of freedom at each node, as shown in Figure 6.5. The cross section can be accurately defined using input command which allows for the bolt shank stress area in the analysis. Use this element in analysis relates to Timoshenko beam theory including shear deformation.

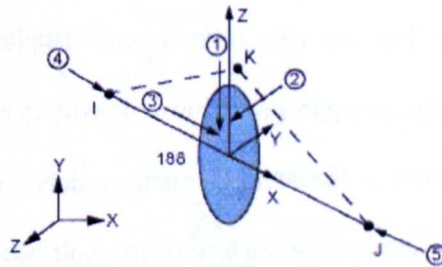


Figure 6.5 Schematic of BEAM188 (ANSYS@Academic Research, 2009)

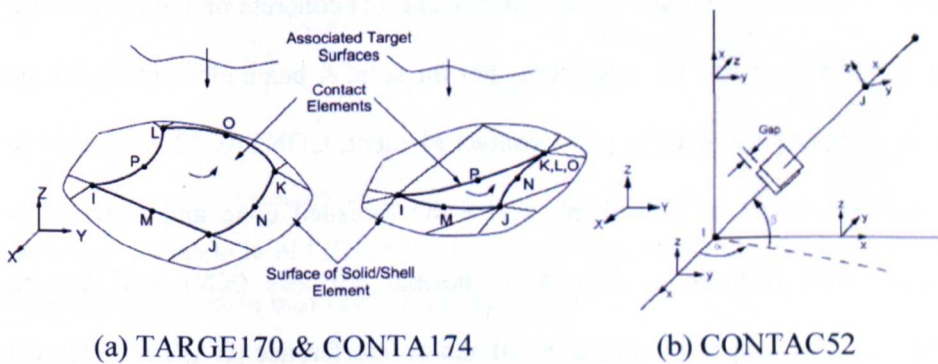


Figure 6.6 Schematic of contact pair (ANSYS@Academic Research, 2009)

The target element (TARGE170) and contact element (CONTA174) were used in the model to ensure proper load transfer between complex interacting surfaces. The coefficient of friction was adopted for sliding resistance while the contact interface is closed. There are four contact algorithms included in

the contact analysis as: pure penalty method, augmented Lagrangian method, pure Lagrange multiplier method and pure Lagrange multiplier on contact normal & penalty on frictional direction method (ANSYS@Academic Research, 2009). As shown in Figure 6.6 (a), this target surface is discretized by a set of target elements and then paired with its associated contact surface. A contact pair is intended for general rigid-flexible and flexible-flexible contact analysis. A real constant set is shared by target and associated contact elements. The contact pair allows for small sliding interaction between a deformable and a rigid body, one of which is defined as master surface and the other as slave surface. For the sake of a smooth distribution of the contact stress along the interface, an appropriate mesh density is required. The contact pairs shown in Figure 6.6 in the solid element models are identified between the following surfaces: (1) bottom surface of the bolt head and top surface of the flat part of the sleeves, (2) endplate surface and tube connecting face, (3) concrete and anchored part of the sleeves, and (4) concrete and anchored bolt shank & nut below the threaded cone. For the solid & beam element model, on the other hand, 3D point to point contact element, CONTACT52, was used to connect the nodes of bolt shank below the threaded cone and concrete in contact. This element is defined by normal stiffness (KN) and sticking stiffness (KS) along with related initial gap or interference (GAP) and element status (START)(ANSYS@Academic Research, 2009).

The PRETS179 element was used in the model for the blind bolt preload. This is a two-node element with one translation degrees of freedom, as shown in Figure 6.7. The PRETS179 element has advantage in its allowance for directly

inputting the bolt preload value. This differs from the use of thermal strain or interference to model preload, which requires trial and error approach to determine an adequate strain and then induce the bolt preload. Before introducing the PRETS179 element, a control node on the pretension section normal to the preload should be defined using the PSMESH command, and the bolt shank is automatically cut along the existing element boundaries at control nodes. The PRETS179 elements are then generated connecting two halves of the bolt shank.

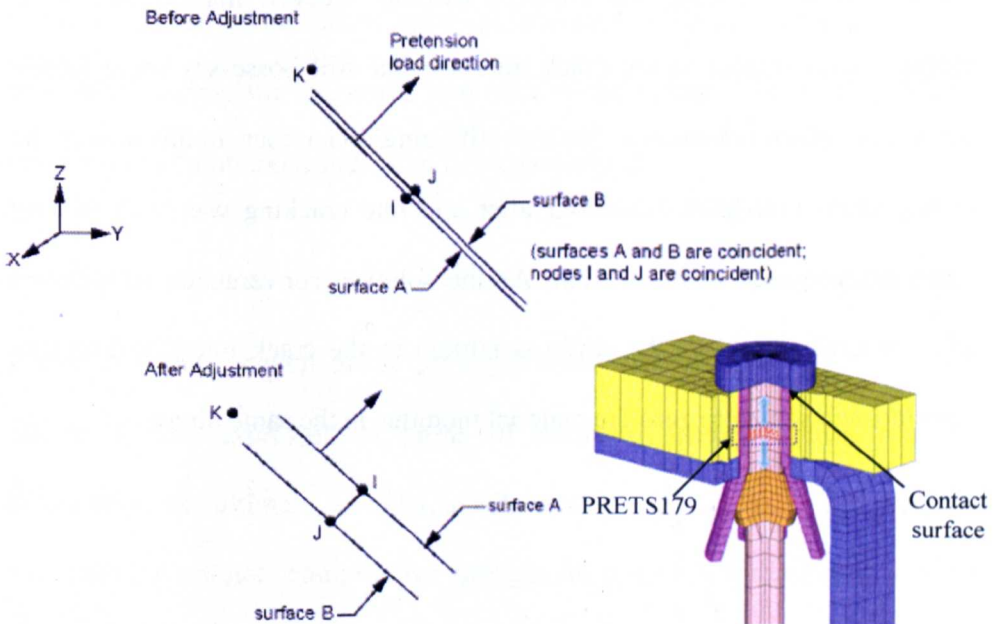


Figure 6.7 Schematic of PRETS179 (ANSYS@Academic Research, 2009) and preload action in blind bolted connection

6.2.2 Concrete failure criteria and modelling

The general yield and failure criteria for finite element analysis are described in Appendix C. The concrete element adopted in finite element analysis takes into account cracking and crushing as discussed below.

Prior to tensile cracking, the concrete behaviour is linearly elastic, in which the elastic modulus is used to obtain the tensile stress, as shown in Figure 6.8. Afterwards, the onset of crack can be assumed as stress-strain relationship achieving uniaxial tensile cracking stress. By introducing a weakness plane normal to the crack face, the related stress-strain relations can be modified thereby the presence of a crack at an integration point is represented. A shear transfer coefficient β_t is used in ANSYS input command to take into account the shear strength reduction for the sliding across the crack interface. Subsequent to cracking, the concrete exhibits reduced normal and shear stiffness with respect to the crack interface but still possesses some tensile capability, which is known as 'tension stiffening' behaviour. In this model, the tensile stress relaxation behaviour after concrete cracking was used to help better convergence in calculation. As the solution convergence is achieved after concrete cracking, the stiffness normal to the crack interface becomes zero through setting to zero the material modulus in the same direction.

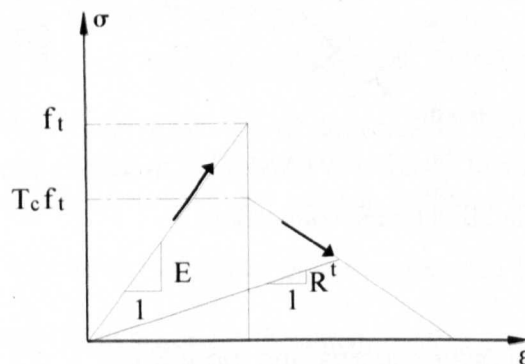


Figure 6.8 Concrete cracking condition adopted in ANSYS (ANSYS@Academic Research, 2009)

The concrete crushing in SOLID65 element is defined as complete deterioration of the structural integrity of the material (ANSYS@Academic Research, 2009). In this case, the material strength is assumed to have significantly degraded so that the contribution to the stiffness of an element at certain integration point can be neglected, i.e. the elastic modulus is set to zero in all directions.

As triaxial stressed concrete often exhibits increased strength with confining pressure, it can be expected that the failure envelope is dependent on three principal stresses. The failure envelope becomes more circular in shape for increasing hydrostatic pressures and vice versa (Chen, 1982). The failure criteria due to multiaxial stress can be expressed as:

$$\frac{F}{f_c} - S \geq 0 \quad \text{Equation 6.1}$$

where, F is the function of the principal stress state (σ_{xp} , σ_{yp} , σ_{zp}). S is the failure surface expressed in terms of principal stresses and five input parameters, as: ultimate uniaxial tensile strength (f_t), uniaxial compressive strength (f_c'), ultimate compressive strength for a state of biaxial compression superimposed on hydrostatic stress state (f_1), ultimate compressive strength for a state of uniaxial compression superimposed on hydrostatic stress state (f_2), and ultimate biaxial compressive strength (f_{cb}). The Equation 6.1 is used in ANSYS to account for concrete cracking or crushing. The failure surface is specified with minimum values of f_t and f_c' , and the other three constants default to Willam and Warnke three-parameter criterion (Willam and Warnke, 1975). F and S are expressed using principal stresses (σ_1 , σ_2 , σ_3), in which

$\sigma_1 = \max(\sigma_{xp}, \sigma_{yp}, \sigma_{zp})$ and $\sigma_3 = \min(\sigma_{xp}, \sigma_{yp}, \sigma_{zp})$. σ_{xp} , σ_{yp} and σ_{zp} are the principal stresses in principal directions. Four concrete failure characterizing domains are then described as: $0 \geq \sigma_1 \geq \sigma_2 \geq \sigma_3$ (compression-compression-compression), $\sigma_1 \geq 0 \geq \sigma_2 \geq \sigma_3$ (tension-compression-compression), $\sigma_1 \geq \sigma_2 \geq 0 \geq \sigma_3$ (tension-tension-compression), and $\sigma_1 \geq \sigma_2 \geq \sigma_3 \geq 0$ (tension-tension-tension). The failure surface in principal stress space with nearly biaxial stress is shown in Figure 6.9 (ANSYS@Academic Research, 2009). As σ_{xp} & σ_{yp} are the most significant nonzero stresses and σ_{zp} varies close to zero, the failure mode is featured by the sign of σ_{zp} , including the cases of concrete cracking and crushing.

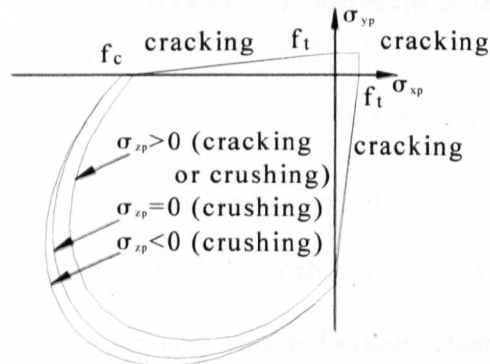


Figure 6.9 Failure surface in principal stress space in nearly biaxial stress state (ANSYS@Academic Research, 2009)

6.2.3 Material model

Steel can be assumed to exhibit identical behaviours in tension and compression. Given that steel behave in ductile manner, true yield and ultimate stresses are considered to allow for large strains. These values can be obtained by converting engineering stresses and strains from uniaxial tensile tests. As the volume change under tension is limited to the small amount

associated with elastic strain, it is reasonable to approximate the volume as constant (Dowling, 2007). Based on this assumption, the true stress (σ_t) and true strain (ϵ_t) can be obtained from engineering stress (σ_{en}) and strain (ϵ_{en}) as:

$$\sigma_t = \sigma_{en} (1 + \epsilon_{en}) \quad \text{Equation 6.2}$$

$$\epsilon_t = \ln(1 + \epsilon_{en}) \quad \text{Equation 6.3}$$

Material properties (such as: elastic modulus, yield stress and ultimate stress) used for blind bolts, beam and tubular columns were obtained from a series of coupon tests conducted in this study and former report (Al-Mughairi, 2009). The initial slope of the input stress-strain relationship was taken as the elastic modulus of the material and the Poisson's ratio for steel was assumed as 0.3. The post yield range of the relationship was represented to have similar fit to original experimental data. The kinematic hardening rule and von Mises yield criterion were chosen for all the steel components. Figure 6.10 and Figure 6.11 present the comparison of actual and true type stress-strain relationships against experimental coupon test results for tubular column and beam & endplate respectively. Figure 6.12 shows the comparison of actual and true type stress-strain relationships for the blind bolt, including the bolt shank and the sleeve. The yield strength and ultimate strength were determined from the tensile tests of machined bolt and full sized bolt respectively, as reported in the literature (Lindapter, 1995; Barnett, 2001; Al-Mughairi, 2009).

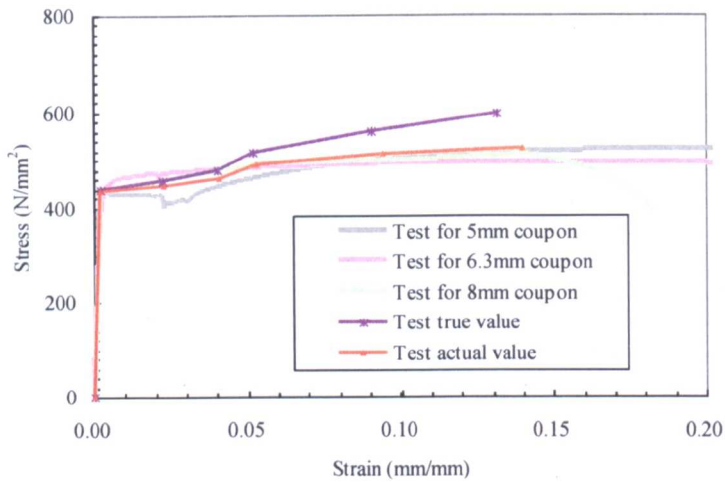


Figure 6.10 Actual and true stress-strain relationship for tubular columns

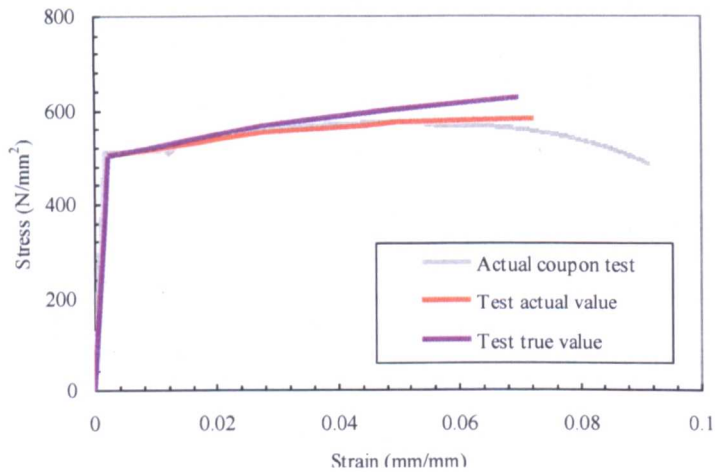


Figure 6.11 Actual and true stress-strain relationship for beam and endplate (Al-Mughairi, 2009)

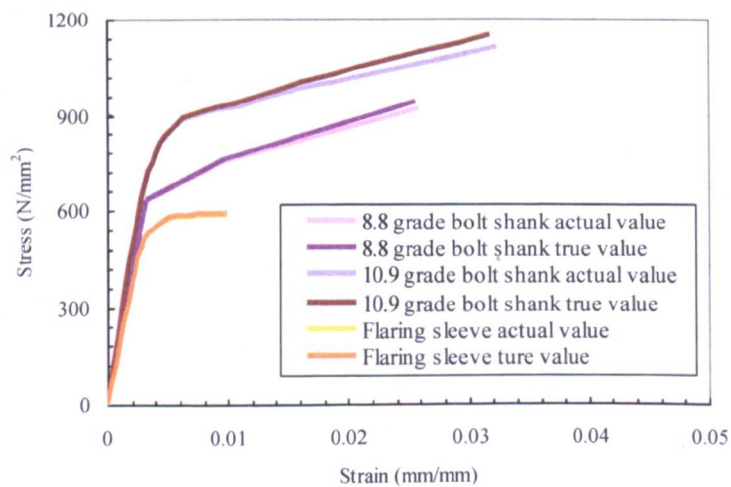


Figure 6.12 Actual and true stress-strain relationship for blind bolts (Al-Mughairi, 2009)

To date, several methods are available in the literature for defining concrete compressive stress-strain relations, ranging from explicit definitions of a particular set of rules or codes to general definitions giving the shape of the curve (ANSYS, 2009). In this study, the multilinear stress-strain relationship for concrete in compression was obtained using the equations suggested by BS EN 1992 (1999). The peak concrete compressive stress is taken as f'_c , which corresponds to a compressive strain of 0.0022. For the curve range between the origin and the strain of 0.0022, the concrete compressive stress, $\sigma'_c(\epsilon)$, can be expressed as:

$$\sigma'_c(\epsilon) = \frac{k\eta - \eta^2}{1 + (k - 2)\eta} f'_c \quad \text{Equation 6.4}$$

where, η is taken as $\epsilon/0.0022$ and k is given as $0.00242E_c/f'_c$. E_c is the elastic modulus of concrete (MPa), which can be written as:

$$E_c = 9500(f'_c + 8)^{1/3} \quad \text{Equation 6.5}$$

The Poisson's ratio of 0.2 was considered for concrete. The ratio of concrete tensile stress to compressive stress at failure was assumed as 0.1. The ultimate compressive strain of concrete was assumed as 0.035. To avoid numerical problem in finite element analysis, the curve at strain range of 0.002 and 0.035 was regarded as stable plateau. The five-parameter model of the Willam-Warnke failure criterion was adopted in ANSYS for the analysis of concrete model. The multi-linear stress-strain relations adopted for concrete with grades C25, C40 and C50 are compared and shown in Figure 6.13.

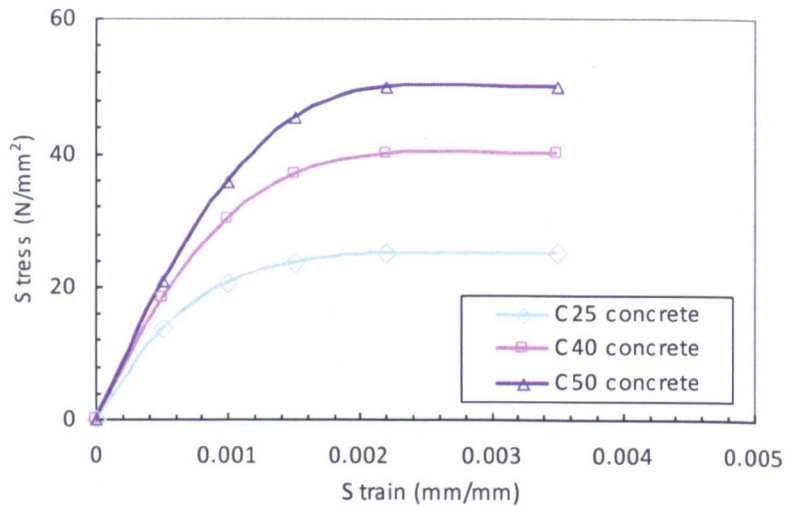


Figure 6.13 Stress-strain relationship of concrete with varying grades

6.2.4 Boundary condition and modelling techniques

The restraints applied for the finite element models are in accordance with those for the test specimens. In view of symmetry about the midline of tube connecting face and beam section, a half model was considered in this analysis and associated nodes of beam, endplate, tube wall, and concrete elements were restrained against lateral translation. The adhesive conditions between different elements were identified and achieved through two modelling techniques described as follows.

To properly join the elements of the steel beam (Shell181 element) to the endplate (Solid185 element) and bolt shank below the threaded cone (Beam188 element) to anchor nut (Solid185 element), a multi-point constraint technique was adopted. This method enforces compatibility at an interface using internally generated constraint equations which eliminates the difficulties of internal force and displacement transfer caused by the elements with different degrees of freedom. Moreover, the transitions from Shell to

Solid and Beam to Solid can be realized without special requirements of nodes alignment and contact stiffness input. The internal multi-point constraints are generated automatically, which improves the solution efficiency over traditional bonded contact and constraint equation methods. In the developed finite element models, the multi-point constraints were created for Shell-Solid and Beam-Solid assemblies.

The contact between the steel components and concrete has been outlined in sub-Section 6.2.1. The constraint condition, however, varies as to whether the concrete infill is taken into account or not. At the initial stage of bolt pretension, it is well recognized that only the steel components of the blind bolt, endplate and unfilled hollow section column rather than concrete are involved in the load transfer. Thereafter, the concrete infill in CFT column will produce anchorage effect for the blind bolt which influences the behaviour of the joints under bending moment. Notwithstanding that, it must be pointed out the difficulty in combining such two stages in finite element analytical process from pre-processing to solution phases. This is because the elements are established only in the pre-processing phase from which a problem arises in incorporating the elements of concrete infill after the analysis of bolt pretension. To solve this problem, an advanced analysis technique called element birth and death option has been introduced to deactivate and activate the concrete elements in both stages corresponding to two load steps thereby properly representing the contributions of concrete infill in the connection system.

The element death option referred by this method is not the removal but deactivation of the killed elements by multiplying the stiffness of those elements by a reduction factor, which is defaulted as $1e^{-6}$ in ANSYS. The deactivated elements in this manner still present in element lists but their strains are set to zero when they are killed. It is worthy of note that the nodes attached to the deactivated elements may float in their response which may cause ill-conditioning solution equations. Consequently, it is advisable to exert artificial restrains on the degrees of freedom of these nodes in the relevant elements. As for subsequent element birth option, on the other hand, the previously killed elements are reactivated in the model and their stiffnesses return to original values. Furthermore, aforementioned artificial constraints generated at the nodes of deactivated elements should be removed in the element reactivation.

6.2.5 *Finite element model illustration*

The geometric configuration and mesh generation constitutes one of the most important parts in the finite element modelling. The finite element models of this innovative blind bolted endplate connection to CFT column consists of several components including a steel beam, an endplate, a CFT column, and blind bolt assemblies. Taking advantage of the symmetry, only a half model was developed in this analysis. The recent finite element analysis of standard bolted endplate connection has become sophisticated, however, problems arise here due to irregular geometric configurations of this innovative blind bolt. This situation becomes even more complicated when the anchorage of blind bolt with concrete infill is introduced. For this reason, it was determined that

the blind bolt model should be developed first, and then the other dependent components could be constructed.

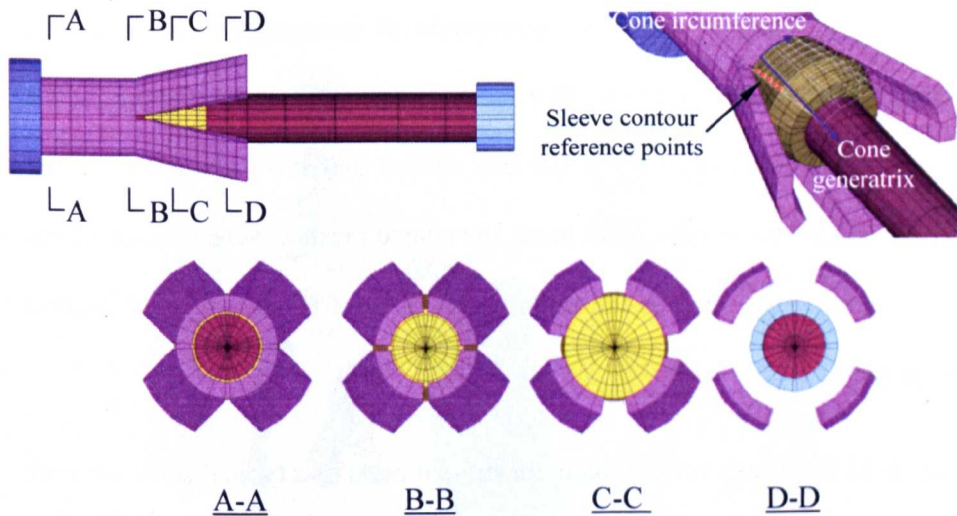


Figure 6.14 Typical finite element meshes for blind bolt assembly

Based on the detailed geometric measurement of this innovative blind bolt, it is relatively easy to develop the component models of the bolt head, shank and anchor nut with the aid of area extruding along coordinate axis. However, the difficulty is recognized for the modelling of the flaring sleeves due to the fact that the contours of flaring sleeves are irregular in the coordinate system. Identifying 3D coordinates of the nodes at the bottom of the flaring sleeve becomes a key point in the configuration. In other words, this requires knowledge of spatial curves & surface (DO Carmo, 1976) and a clear 3D imagination. By assigning node numbers and predetermination of reference points, the flaring sleeves were generated separately and joined together with flat part of the sleeves. Figure 6.14 shows typical finite element meshes of the blind bolt assembly with four typical cross-sectional views along the bolt shank direction as well as geometric location with respect to the threaded cone.

Appropriate finite element mesh is important in reducing errors during the analysis of element matrix. Although ANSYS provides a meshing tool with automatic solutions, the mesh refinement of critical areas would be better determined by users to fulfil the requirement of the analysis. To develop a suitable model for this analysis, fine meshes were used at the regions in the vicinity of the blind bolt where the bolt failure and local high stresses are likely to take place. On the other hand, the coarse meshes were considered for the low stress areas such as the bottom side of the CFT column and column end supports.

Figure 6.15 illustrates several main constituent parts of a typical finite element model. With respect to the steel components on the left, the bolt head and washer are assumed to be rigidly connected to each other, which, as reported in the previous studies (Girão Coelho *et al*, 2006; Bursi & Jaspart, 1997), have no significant influence on the behaviour of the whole structure. The hexahedral brick elements were used for most meshes of the steel tube which represent regular element arrangement in the model. To provide added flexibility of mesh, several wedge elements were also used around the bolt clearance hole as supplement for hexahedral meshes. Regarding the components of concrete infill on the right of Figure 6.15, varied mesh generations were used in the regions near and away from bolt rows. Generally, the element meshing for concrete infill can be taken as similar to that for the steel tube. With the introduction of blind bolt configuration, a practical problem being encountered is the irregular geometric contours of flaring sleeves and threaded cone which must coordinate with those of concrete infill.

Due to difficult 3D view identification and element pickup, it is impossible to refine the mesh using mesh tool as mentioned earlier. Alternatively, the nodes and elements were established with the aid of APDL code which incorporates common commands such as 'Do-loop' and 'If-then' in programming.

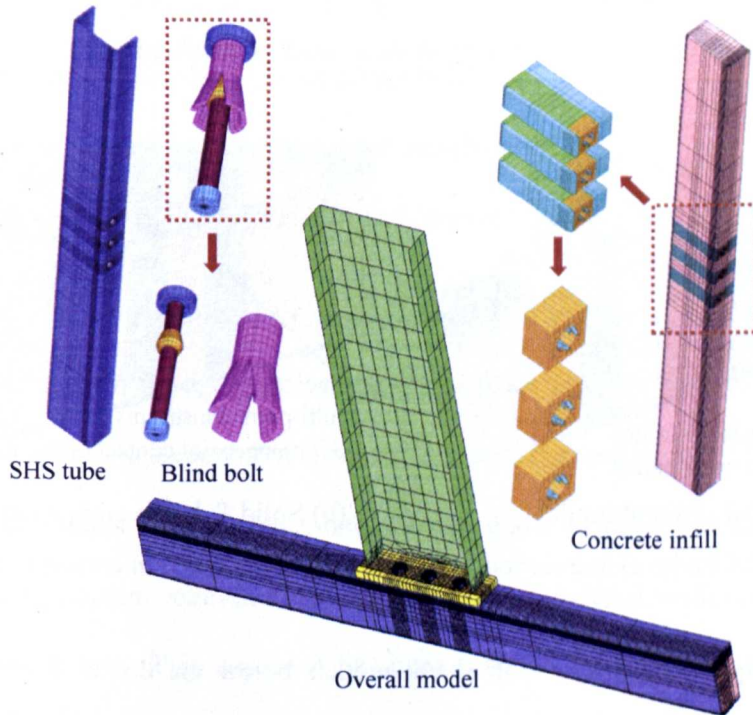


Figure 6.15 Typical finite element model with partitioned components

The model of concrete infill in contact with the blind bolt was modelled with the solid wedge and hexahedral brick elements. Note that the SOLID65 element in the case of large strain and deflection may be accompanied with unconverged or incorrect results when the cracking and crushing nonlinearities are presented simultaneously (ANSYS@Academic Research, 2009). Moreover, the dramatic reduction of stiffness of cracking element in large scale would cause convergence becoming rather difficult. Additionally, the solid wedge elements may pose some problem in regions of relatively high stress gradients. For this reason, the meshes for the concrete infill was adjusted

based on the stress contours. To achieve the analytical stability, some SOLID185 elements were locally inserted into SOLID65 element with refined mesh. As idealized concrete crushing is unlikely with the presence of the secondary tensile strains produced by Poisson's effect, the crushing capability of the element under uniaxial compressive load is disabled for the ease of convergence.

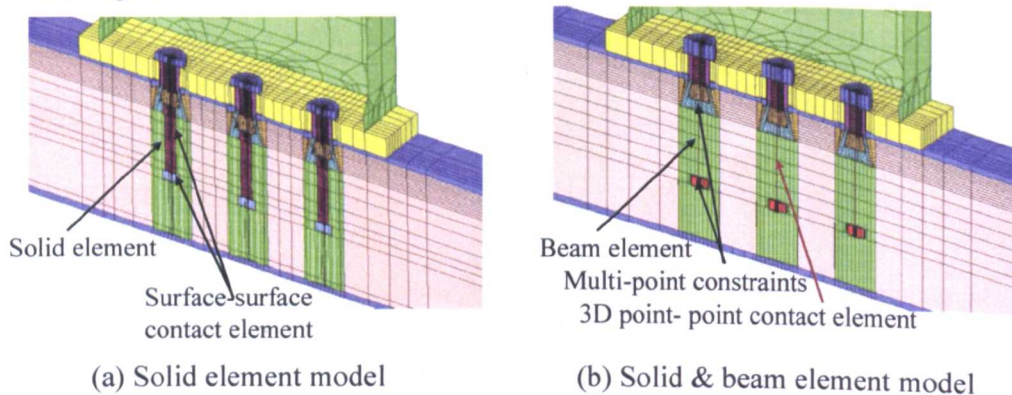


Figure 6.16 Finite element models of blind bolts anchored in concrete infill

In this study, two types of bolt shank models below the threaded cone are introduced as indicated in Figure 6.16. The solid element model as shown in Figure 6.16 (a) displays a realistic geometry in relation to concrete infill nearby. The solid & beam element model as shown in Figure 6.16 (b) uses beam element to model the counterpart bolt shank. The multi-point constraints were adopted to ensure proper conjunction with the threaded cone and anchor nut, while the 3D point-point CONTACT52 element was used to form the interface between the bolt shank and concrete infill with a coefficient of friction equal to 0.45. The contact area between the anchor nut and concrete infill was defined the same as that in the solid model. This model was considered to eliminate local stress concentration problems of concrete at the anchorage locations which may cause early un-converged solution.

6.2.6 Loading condition and solution

The finite element models were first loaded by placing the blind bolt in pretension (also called preload or prestress). The bolt preload value in the unit of force was input with the SLOAD command for predefined PRETS179 elements connecting two halves of the bolt shank. After this part of solution, the bolt shank between the bolt head and threaded cone was preloaded along with the endplate and CFT column face in compression.

The second load step was executed by imposing vertical concentrated load incrementally to the tip of the beam. The displacement control was considered similar to that in experiment to overcome convergence problems. The finite element models were loaded monotonically under bending moments and the resultant moment-rotation relationships were compared with experimental envelope curves. This approach has been justified for the case of composite beam-to-column joints under quasi-static cyclic loading as reported in the recent literature (Vasdravellis *et al.* 2008, Kovács *et al.* 2010).

Regarding the solution phase of the finite element analysis, the element solutions are related to the calculation at integration points in which the simultaneous equations are solved by different methods. The commonly used solvers for linear and nonlinear problems consist of two techniques: direct elimination solver and iterative solver. The former uses equations reordered by alternating diagonal planes while the latter takes two-line successive over relaxation. The sparse direct solvers primarily adopted in this analysis is based on direct elimination equations, where the solution is obtained through an interactive process that successively refines an initial guess to a solution that is

within an acceptable tolerance of the exact solution (ANSYS Version 12.1, 2009).

The standard Newton-Raphson algorithm for nonlinear solution conversion was adopted in the finite element analysis. The load is subdivided into a series of sub-load increments which can be applied over several load steps. The number of iterations is taken as an important influential parameter in this verification. In the case of full Newton-Raphson option, the stiffness matrix is updated at each iteration. Regarding the introduction of element birth and death into this analysis, the option with adaptive descent activated is adopted to yield good results as suggested by ANSYS (ANSYS Version 12.1, 2009).

As the loads are applied incrementally, load step option may be used to represent the actual loading during the test. The solution for each load step is achieved by solving several sub-steps until the convergence criteria are satisfied. The predetermination of the numbers of sub-steps often poses a problem as too few and too many sub-steps may lead to un-converged results and time-consuming analysis respectively. This point becomes an important issue especially when the concrete cracking is encountered in this analysis. In this case, care should be taken to apply the load slowly in smaller increment. As a solution, ANSYS provides an alternate automatic time step option in solution control and the size of the subsequent time step is predicted based on four factors:

- Number of equilibrium iterations used in the last time step;
- Predictions for nonlinear element status change;
- Size of the plastic strain increment;

- Size of the creep strain increment.

This option was selected in the finite element analysis, it was noted that resizing the numbers of sub-steps produces an efficient solution.

Regarding convergence criteria, the L2-norm of force tolerance equal to 0.5% is adopted in ANSYS automatic solution control. The default force convergence is checked by comparing the square root sum of the squares of the force imbalances against the product of tolerance. For nonlinear analyses, it is noticed that the displacement control method is more efficient than load control in the plastic deformation phase, in which the increase of load increment may produce significant increase in the displacement counterpart. The displacement convergence checking was also added into the convergence criteria of modelling. This consideration was observed to improve the convergence of the finite element analysis.

6.3 Finite element analysis results

The finite element models were developed based on the geometric features of the connection tested in the experiment. The analyses were carried out in order to investigate the connection behaviour as a cross validation of the experimental observations. The evidences gained from finite element analysis are regarded as an useful indication of the local failure mode developed inside the tube which is difficult to obtain in physical measurement.

The validation results of the finite element models are presented in this section. First, the results of bolt preload modelling are described in comparison with the strains measured from the tests and reported in the literature. The

connection failure modes of the connection under bending moment are then discussed based on the numerical stress contours. Also, the typical numerical strain distributions of the connection components are compared. Finally, the comparisons of numerical moment-rotation relationships with the experimental cyclic envelopes are plotted and discussed.

6.3.1 *Blind bolt preload*

The bolt preload action is to exert a compressive stress on the endplate and tube connecting face and hold them together to form an assembly. In practice, the bolt preload ensures the connected plates will not separate at initial stage, provided that applied load is less than designed preload. It is apparent that the bolt shank will be stressed along with the plates nearby under compression.

As shown in Figure 6.17, the localized stress contours can be observed around the bolt clearance holes on the tube connecting face and endplate. This is expected as related plates are bolted between the contact surfaces referring to the bolt head and the flaring sleeve. The mechanical interlock within the blind bolted connection system, which transfers the preload from the threaded cone and the flaring sleeve, can also be noted. As such, the flaring sleeve above the threaded cone is stressed to some extent as shown in Figure 6.17.

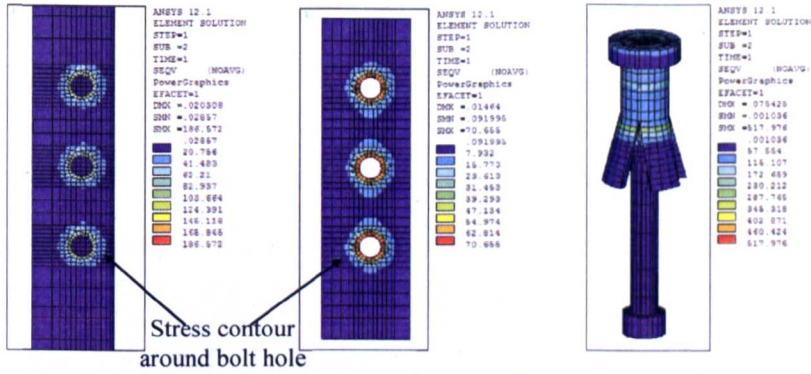


Figure 6.17 Stress contours of tube connecting face, endplate and blind bolt (bolt preload phase)

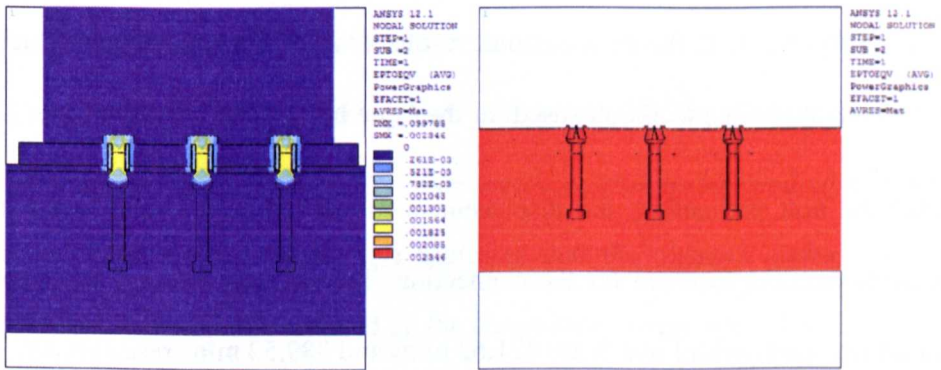


Figure 6.18 Strain contours of overall connection and concrete infill (bolt preload phase)

In order to compare with experimental measurement, the section view of bolt strain contour is plotted along with the overall connection as shown in Figure 6.18. It is observed that the bolt shank above the threaded cone are almost equally strained, while relatively lower strain distributes at the bolt head, the threaded cone and sleeves. For the rest of the connection components, the strains are seen to be negligible. Nearly zero strain contour of concrete infill in Figure 6.18 is also in agreement with the observation which suggests the efficiency of element death option adopted in this analysis to deactivate the concrete element in the modelling of bolt preload. In addition, the strain distribution along the bolt shank also indicates that the bolt preload simulated

by the solid & beam element model and the solid element model mentioned earlier can be regarded as the same.

Four groups of bolt strains from the finite element analysis were compared with those in the experiment and the literature report (Al-Mughairi, 2009). The top shank strain gauges (SGBH) readings at the middle bolt row indicated in sub-Section 3.5.3.3 were used for this comparison. As shown in Figure 6.19, the finite element results of bolt pretension strain appear to be satisfactory when compared with the experimental results and the literature report which justify the modelling technique used for the blind bolt preload modelling.

After the bolt preloading, the displacement is applied at the steel beam to generate bending moment for the connection. The average solution times for connection categories I and II are 421.62 mins and 389.53 mins respectively.

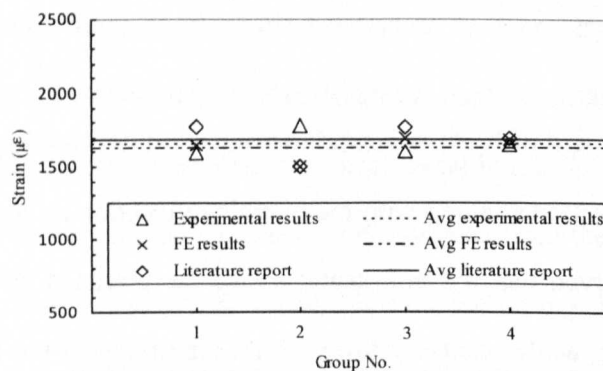


Figure 6.19 Comparison of strains obtained from experiments, finite element analysis and literature report (Al-Mughairi, 2009)

6.3.2 Stress distribution and failure modes identification

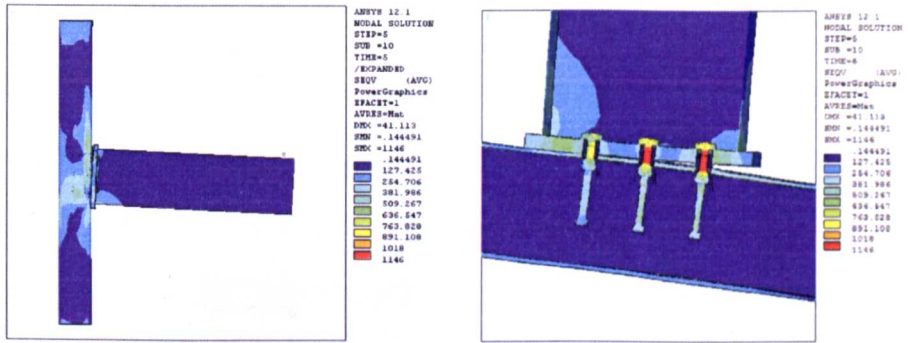
The stress distribution at the connection components are often used in the determination of load transfers and failure modes. Also, it can be adopted in examining the points of interest for structural design. Unlike strain gauge

measurement limited by certain location in the test set-up, the numerical stress contour of the finite element model provides wide range of stress distribution. The stress results obtained from the finite element analysis will be described in this sub-section referring to: overall connection, blind bolt, tube sidewall face & connecting face and concrete infill. The test specimens BBEC-8-10.9-50-LI and BBEC-5-8.8-50-LII were selected in the finite element analysis to represent the test specimens failed in modes I and II.

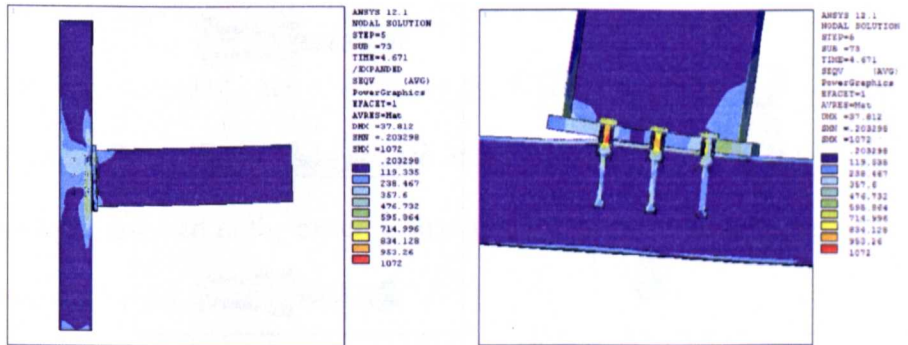
The comparison of numerical stress contours for specimens BBEC-8-10.9-50-LI and BBEC-5-8.8-50-LII are shown in Figure 6.20. The stresses are related to the connections loaded at maximum load condition under bending moments. Visual inspection of these plots indicates that the stresses induced by the bending moment are distributed on the connection components. The stresses in the beam and endplate are mostly in the elastic condition and relatively low in contrast with those in the blind bolt and the tube. The negative bending moment are seen to produce wider stress distribution in the connection components than positive ones. This is expected due to larger lever arm distances from the rotation axis of the connection under negative moment than those under positive moment. The small flexure of the endplate is evident to observe from the contours of deformed shape as well as low stresses distribution on the endplate. The stress contours at the beam web near the flange indicates the compression stresses were developed on the beam flange and endplate. In fact, this effect would be significant when the width of the endplate is larger than that of the tube connecting face; otherwise, the tube

connecting face may attract relatively high stress concentration in the local contact region.

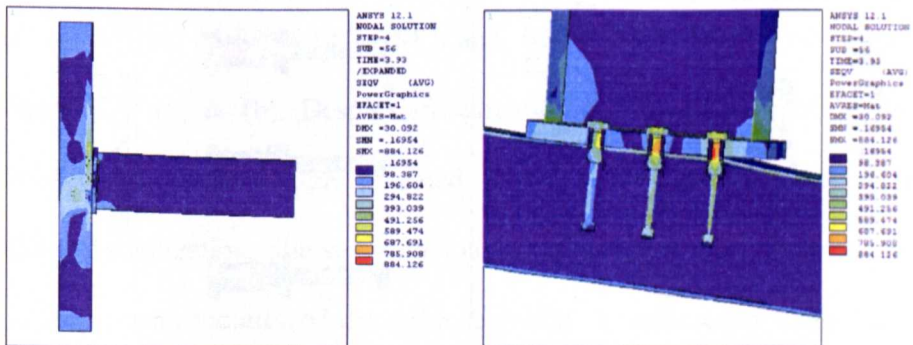
The numerical stress contours in the blind bolts for specimens BBEC-8-10.9-50-LI and BBEC-5-8.8-50-LII are shown in Figure 6.21. Regarding specimen BBEC-8-10.9-50-LI under negative bending moment, relatively high stress distribution of the first and second bolt row can be seen at almost the whole bolt shank regions between the threaded cone and the bolt head. This indicates that the high level of plasticity initially developed at the bolt shank of the first bolt row has extended to that of the second bolt row. Also, the localized stress development can be noticed at the bolt shanks near the anchor nut. By contrast, the stress distribution of the bolt shank under positive bending moment is relatively low due to the lever arm distance as explained earlier. The observations in this case for the bolt shanks under negative and positive bending moment are expected for the connection failure mode I, in which the bolt shank fracture at ultimate load condition as observed in the experiments. In other words, the bolt shank in this mode can be taken as the primary part to carry the tension force in the connection system.



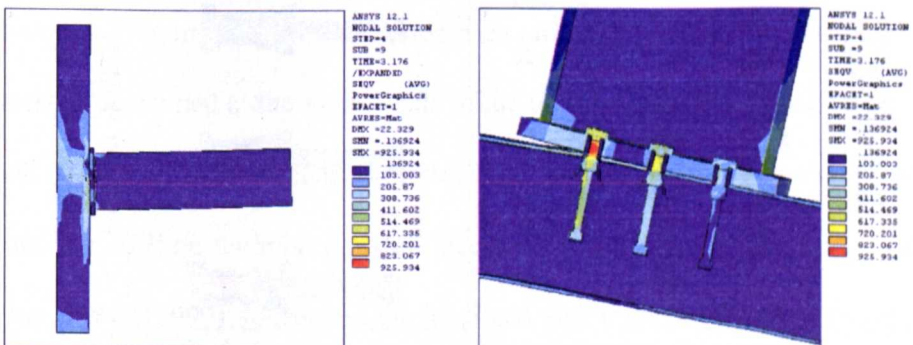
(a) FE analysis for specimen BBEC-8-10.9-50-LI under negative moment



(b) FE analysis for specimen BBEC-8-10.9-50-LI under positive moment

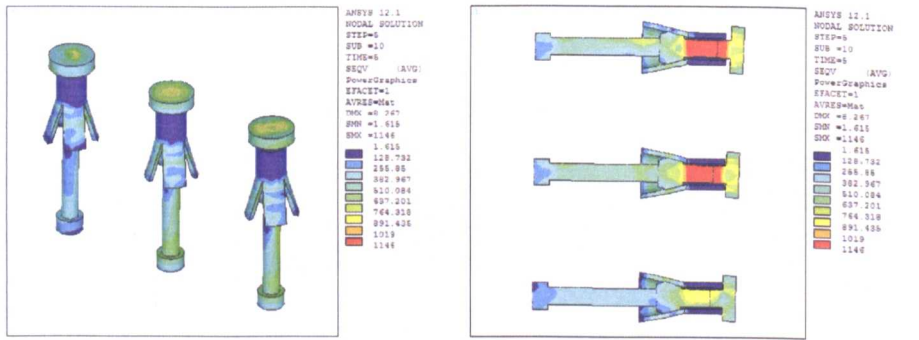


(c) FE analysis for specimen BBEC-5-8.8-50-LII under negative moment

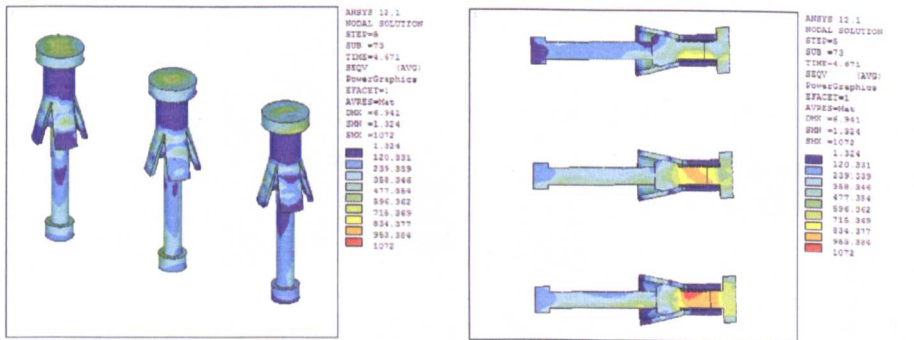


(d) FE analysis for specimen BBEC-5-8.8-50-LII under positive moment

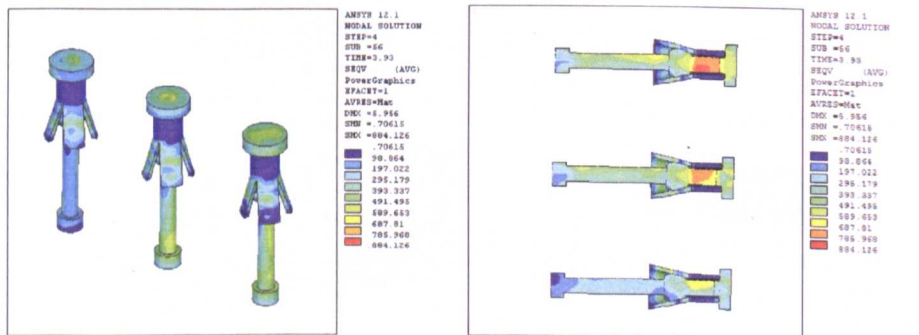
Figure 6.20 Von Mises stress contours of test connections



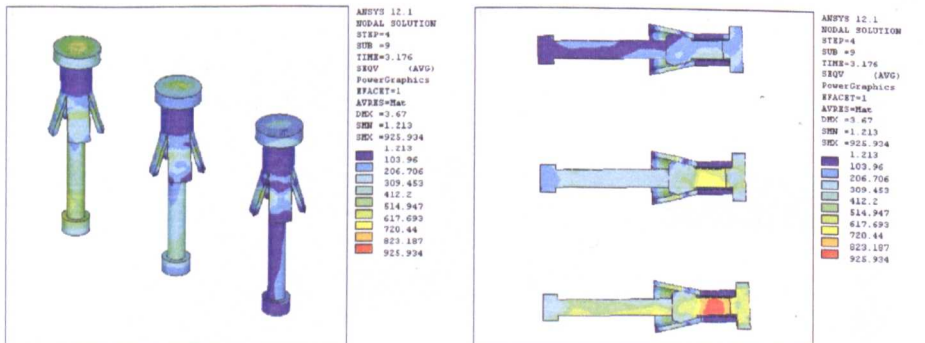
(a) FE analysis for specimen BBEC-8-10.9-50-LI under negative moment



(b) FE analysis for specimen BBEC-8-10.9-50-LI under positive moment



(c) FE analysis for specimen BBEC-5-8.8-50-LII under negative moment



(d) FE analysis for specimen BBEC-5-8.8-50-LII under positive moment

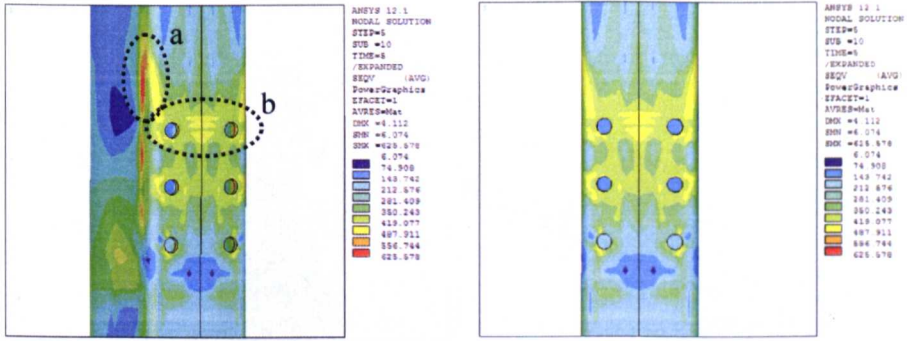
Figure 6.21 Von Mises stress contours of blind bolts

Regarding specimen BBEC-5-8.8-50-LII under negative bending moment, the peak stresses are seen locally at the bolt shank between the threaded cone and the bolt head near the flat part of the sleeves. It seems that the plasticity has not been well developed at the bolt shank of the first bolt row, nor sufficiently extended to that at the second bolt row. This observation implies that the effect of bending rather than axial loading may act effectively in producing localized yielding of the bolt shank. Additionally, the stress contour at the bottom shank below the threaded cone also shows the blind bolts undergo slight bending. The stress results obtained here are in agreement with the connection failure mode II observed in the experiments, in which the bolt shank almost remains intact under this stress condition.

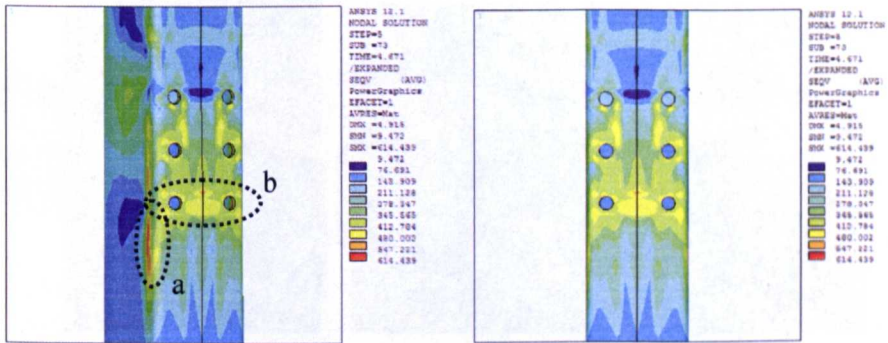
The numerical stress contours on the tube sidewall face and connecting face for specimens BBEC-8-10.9-50-LI and BBEC-5-8.8-50-LII are shown in Figure 6.22 (a) & (b). Despite aforementioned symmetry simplification in finite element modelling, an expanded full tube plot is displayed herein for the sake of visualization. The stress contours indicate significant localized tensile yielding in the vicinity of the edges between the tube connecting face and sidewall face, which are in accordance with the experimental observations as shown in Figure 6.22 (c). On closer examination, it can be seen that the stresses developed at the inner fields of the tube sidewall face close to the first bolt row in tension are relatively low which mirrors the strengthening effect of concrete infill on the tube sidewall face from inside as previously reported by France *et al* (1999). Moreover, the localized yielding can be seen at lower tube sidewall face related to the connection parts in compression.

With respect to the connecting face, it can be observed that numerical yield stress for specimen BBEC-8-10.9-50-LI concentrates locally around the bolt clearance holes and expands downward from the first bolt row to the second bolt row. The maximum stress at tube connecting face are marked in 'region *a*'. This observation from the finite element analysis (Figure 6.22 d & e) agrees with that from the experimental observation (referring to Figure 6.22 f), which refers to the circular yield line pattern suggested by Eurocode 3. By contrast, the relatively high and wide yield stress spreading on the tube connecting face for specimen BBEC-5-8.8-50-LII indicates that the local tube connecting face undergoes significant outward deformation (Figure 6.22 d & e). The further stress contours can be identified from noticeable yielding development around bolt clearance holes at the first bolt row in tension which are in agreement with the experimental observation shown in Figure 6.22 (f). The yield line pattern considered for this case can be related to the category of non-circular yield line pattern.

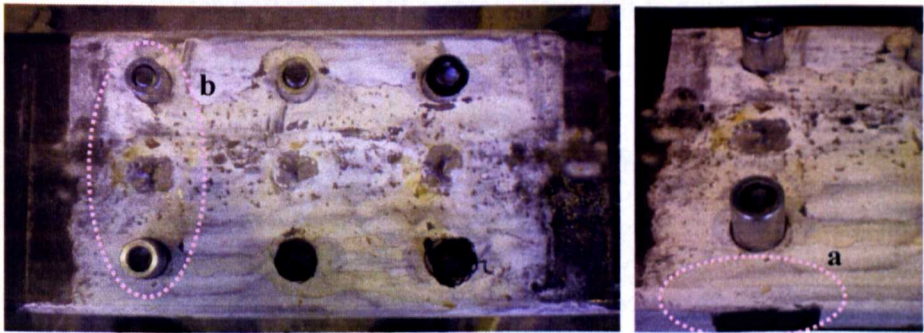
The stress contours at the tube sidewall are also plotted and its maximum value is marked in the 'region *b*'. Likewise, it seems that the plots of specimen BBEC-8-10.9-50-LI exhibits relatively high stress at local regions. With the progress of cyclic loading, however, the tube sidewall of the specimen BBEC-5-8.8-50-LII is expected to undergo wider stress development as the yielding expands downward from the first bolt row to the second bolt row.



(a) FE analysis for specimen BBEC-8-10.9-50-LI under negative moment



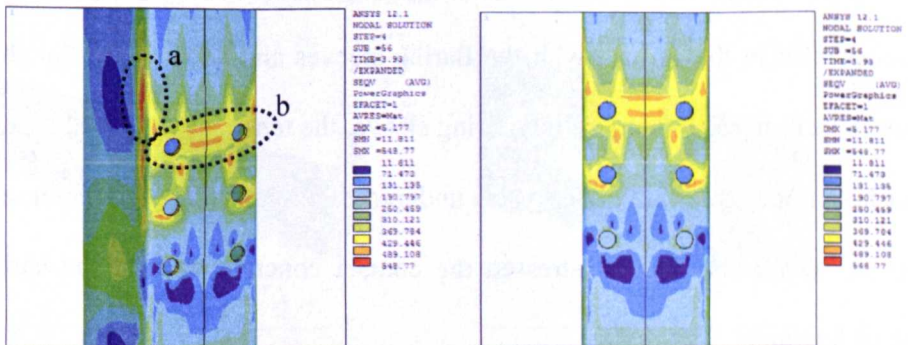
(b) FE analysis for specimen BBEC-8-10.9-50-LI under positive moment



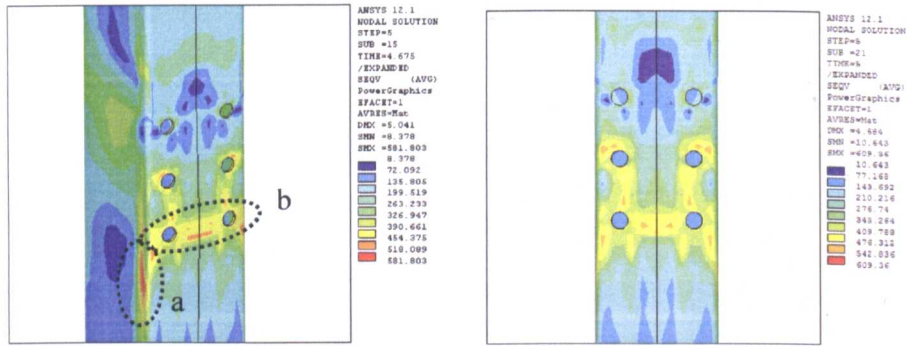
Overall tube connecting face

Tension bolt row

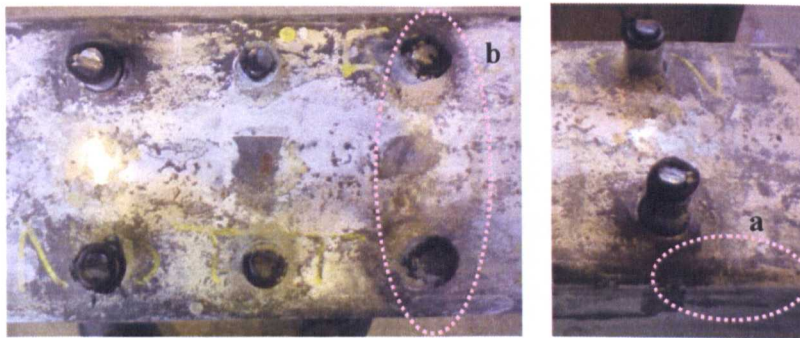
(c) Test graph of tube wall yielding for connection category I



(d) FE analysis for specimen BBEC-5-8.8-50-LII under negative moment



(e) FE analysis for specimen BBEC-5-8.8-50-LII under positive moment



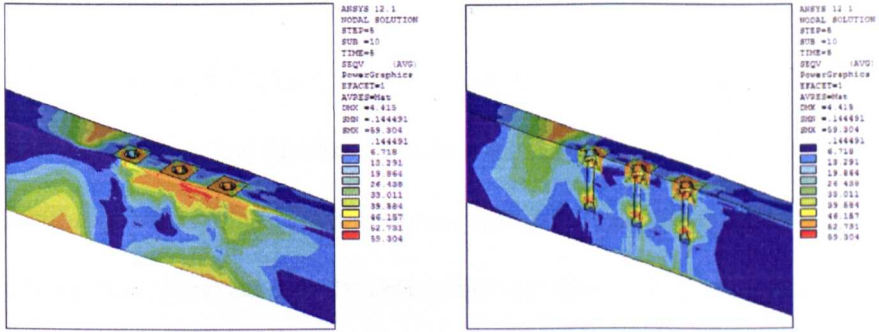
Overall tube connecting face

Tension bolt row

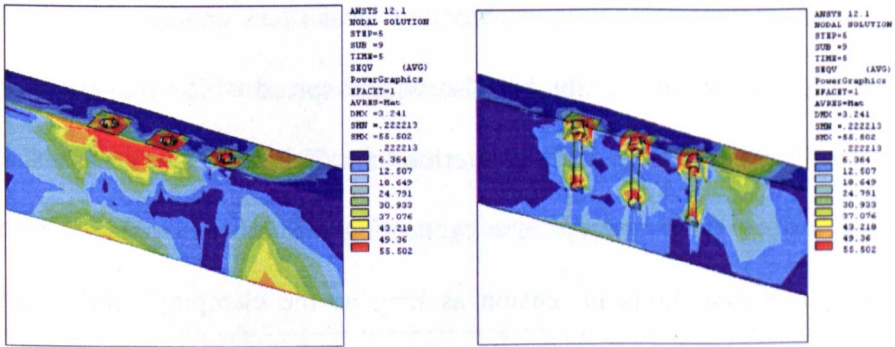
(f) Test graph of tube wall yielding for connection category II

Figure 6.22 Von Mises stress contours of tube sidewall and connecting faces

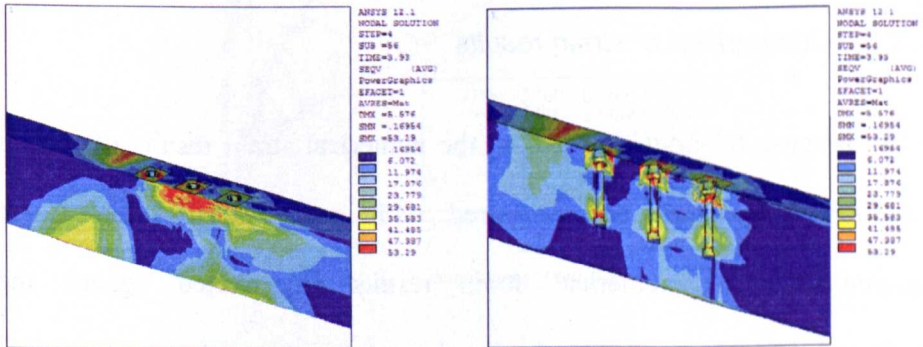
The numerical stress contours at the concrete infill for specimens BBEC-8-10.9-50-LI and BBEC-5-8.8-50-LII are shown in Figure 6.23. Firstly, higher stresses are seen at the corner of concrete block in the vicinity of first and second bolt rows. This phenomenon can be presumed along with the tube face yielding mentioned above. The stress concentrations are also highlighted for concrete infill in the contact with the flaring sleeves and anchor nut. For the concrete infill in the vicinity of the flaring sleeve, the tension transferred to the blind bolt forces the flaring sleeves to undergo deformation along membrane interface which also in turn stressed the contact concrete even at the early stage of loading.



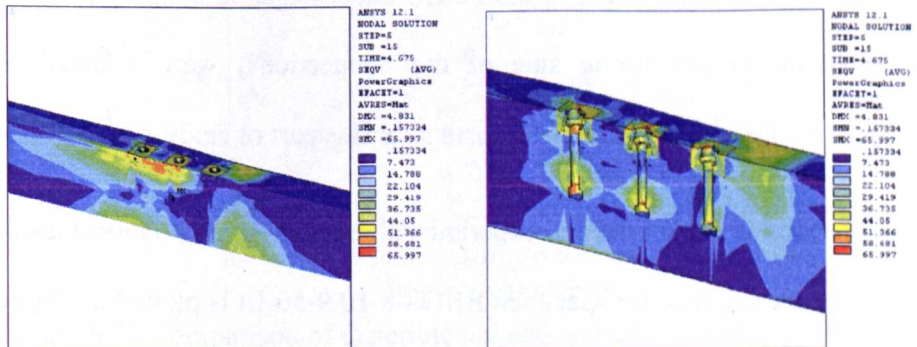
(a) FE analysis for specimen BBEC-8-10.9-50-LI under negative moment



(b) FE analysis for specimen BBEC-8-10.9-50-LI under positive moment



(c) FE analysis for specimen BBEC-5-8.8-50-LII under negative moment



(d) FE analysis for specimen BBEC-5-8.8-50-LII under positive moment

Figure 6.23 Von Mises stress contours of concrete infill

The stress concentrations of the concrete infill localized at the anchor nut for specimen BBEC-8-10.9-50-LI are shown in Figures 6.27 (a) & (b). Along with the yielding at the tube faces, it can be deduced that relatively thick tube face and strong concrete anchorage effectively restrain the pullout of the blind bolt thereby isolating the bolt shank as the primary load carrying part in the connection system. On the other hand, the stress contour of the concrete for specimen BBEC-5-8.8-50-LII shows that the local stress concentrations not only occur at anchor nut location but also widely spread which suggests that concrete infill may undergo widely deterioration. This will result in weaker anchorage on one hand, and the tube connecting face attracts higher tensile force from the blind bolts in tension as long as the clamping mechanism remains effective on the other.

6.3.3 *Comparison of strain results*

For the purpose of model validation, the numerical strain results of related connection components are compared with experimental strain gauge measurements. The numerical strain results are plotted against the experimental envelope curves. Again, the relationships of test specimens BBEC-8-10.9-50-LI and BBEC-5-8.8-50-LII under negative bending moment (corresponding to the strong side of the connections) were selected as representative finite element analysis results for this part of study.

The comparison of numerical and experimental moment-strain relationships of the tube connecting face for specimen BBEC-8-10.9-50-LI is plotted in Figure 6.24. Note that the vertical axis represents the total bending moment of the connection. Apparently, the plotted tube transverse strains on the tube

connecting face are higher than the longitudinal strains. It can be seen that the general trends of the curves predicted by the numerical analyses are similar with those measured in the experiments, especially those in the linear range. An inconsistency is observed in the nonlinear range, in which the moment-strain curves from finite element analysis exhibit higher stiffnesses than those from experimental measurement. At the maximum moment, the finite element models show lower and higher strains than experimental measurements at the longitudinal and transverse directions of the tube connecting face respectively. Either local material imperfections or nonlinear phenomena such as slip between endplate and tube connecting face may cause such inconsistencies.

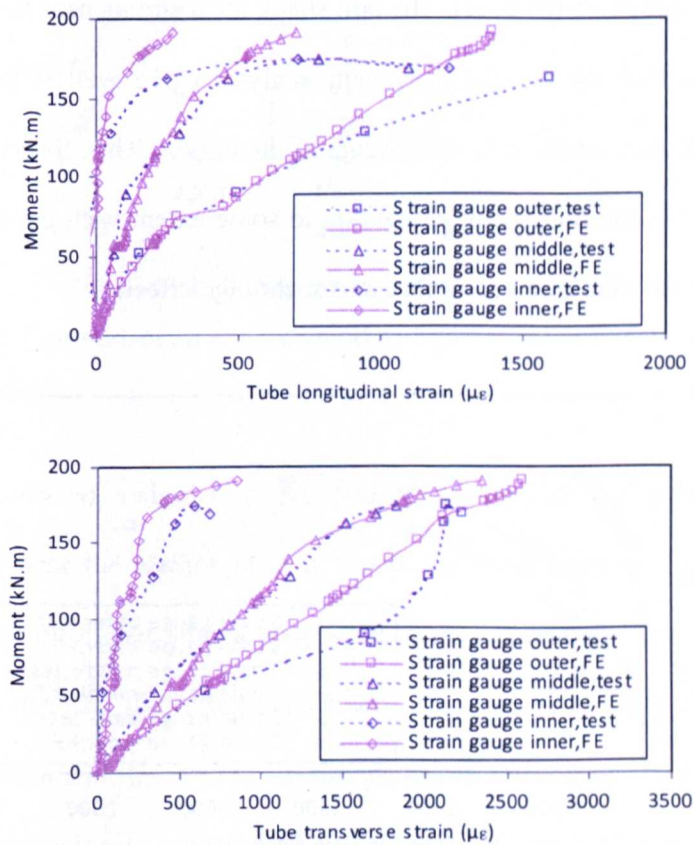
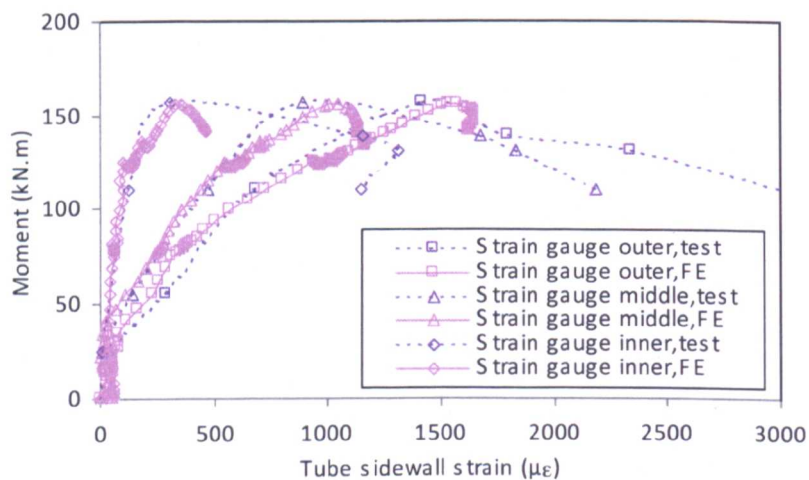


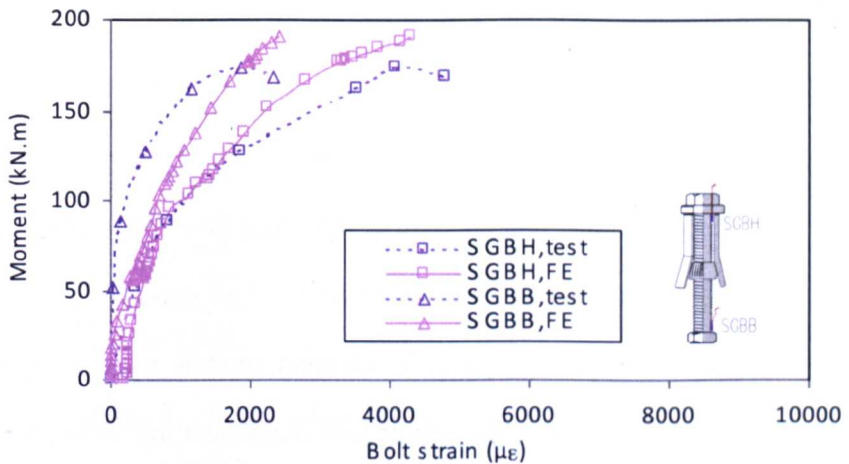
Figure 6.24 Comparison of experimental and numerical moment versus strain curves for tube connecting face of specimen BBEC-8-10.9-50-LI

The comparison of numerical and experimental moment versus strain relation of the tube sidewall face for specimen BBEC-5-8.8-50-LII is plotted in Figure 6.25 (a). For the loading in the finite element analysis from 0 to 22 mrad, only ascending branches of the curves are presented and compared against the experimental measurement. It can be seen that a good correlation of both curves although some slight differences are noticed close to the peak. The accuracy of this simulation is influenced by the consistency of material models as well as local concrete infill deterioration assumed in finite element models.

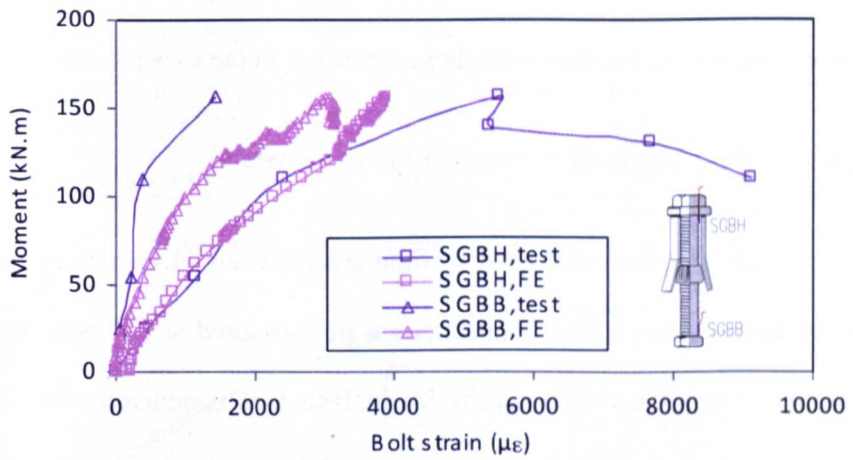
The comparisons of numerical and experimental moment-strain relations of the blind bolts for specimens BBEC-8-10.9-50-LI and BBEC-5-8.8-50-LII are plotted in Figure 6.25 (b) & (c). The bolt shank local strains near the bolt head (SGBH) obtained by the finite element analysis agree well with those by experimental measurement in most range of the curves. This observation may be attributed to the bolt shank elongation to some extent with good restraints provided by the tube connecting face and anchorage effect.



(a) tube sidewall face (Specimen BBEC-5-8.8-50-LII)



(b) Blind bolt (Specimen BBEC-8-10.9-50-LI)



(c) Blind bolt (Specimen BBEC-5-8.8-50-LII)

Figure 6.25 Comparison of experimental and numerical moment-strain curves for blind bolts

On the other hand, a significant difference is observed in the comparisons for the strains near the anchor nut, in which the predictions of finite element analysis exhibit higher strains than those in the experiment. The strains near the anchor nut (SGBB) in both specimens are lower than those at SGBH for the same moment level. The strain profile in this case may be largely attributed to the local anchorage which is greatly influenced by the cracking of concrete infill. Unfortunately, the incorporation of this factor in concrete material model is difficult for finite element analysis. It is also worthy of note

that the smeared crack approach rather than discrete crack approach was used in this finite element model. In the former approach, the nucleation of one or more cracks in the volume attributed to an integration point is translated into a deterioration of the stiffness and strength at that integration point (de Borst *et al.* 2004). Moreover, the tension resistance of cracked concrete elements is ignored as their stiffnesses in the finite element models were assumed as reducing to zero. Consequently, the bottom bolt shank near the anchor nut may exhibit greater local deformation in finite element analysis thereby producing relatively higher local strains than those measured in the experiments.

6.3.4 Comparison of moment-rotation curves

The force and displacement used in finite element model for calculating the moment and rotation of the connections were measured at the same location on the test beam. The mesh sensitivity analysis was conducted with varying mesh densities of tube wall and concrete infill, as shown in Figure 6.26. It turns out that the predictions compare well with each other, so the default model with moderate mesh refinement was adopted for the rest of analyses.

Table 6.1 Comparison of experimental and numerical maximum moment

Test No.	Specimen reference	Finite element analysis results					
		Test results		Solid element model (FE1)		Solid & beam element model (FE2)	
		M_{max}^- (kN.m)	M_{max}^+ (kN.m)	M_{max}^- (kN.m)	M_{max}^+ (kN.m)	M_{max}^- (kN.m)	M_{max}^+ (kN.m)
1	BBEC-8-8.8-50-LI	133.79	163.89	153.62	179.40	154.66	179.41
2	BBEC-8-10.9-50-LI	164.69	188.97	175.35	195.88	176.93	194.51
3	BBEC-8-10.9-50-LII	171.89	189.17	-	-	-	-
4	BBEC-5-8.8-50-LII	115.80	157.72	127.26	155.83	123.76	165.81
5	BBEC-6.3-8.8-50-LII	120.39	160.95	151.89	157.96	151.18	178.36
6	BBEC-6.3-8.8-25-LII	102.95	137.28	107.79	98.69	108.52	140.07

Note: ^{+/−} refers to the variables at positive or negative moment range half cycle of the moment-rotation diagrams

Table 6.2 Comparison of experimental and numerical initial stiffness

Test No.	Specimen reference	Test results		Finite element analysis results (Solid element models)	
		K_{ini}^- (KN.m/mrad)	K_{ini}^+ (KN.m/mrad)	K_{ini}^- (KN.m/mrad)	K_{ini}^+ (KN.m/mrad)
1	BBEC-8-8.8-50-LI	16.92	23.51	16.23	22.55
2	BBEC-8-10.9-50-LI	20.11	27.06	20.79	27.12
3	BBEC-8-10.9-50-LII	20.18	28.62	-	-
4	BBEC-5-8.8-50-LII	14.06	17.95	14.52	19.02
5	BBEC-6.3-8.8-50-LII	15.78	19.15	16.22	21.13
6	BBEC-6.3-8.8-25-LII	13.66	16.18	13.98	17.01

Table 6.3 Ratios of experimental and numerical results

Test No.	Specimen reference	$\frac{K_{ini,test}^-}{K_{ini,FE}^-}$	$\frac{K_{ini,test}^+}{K_{ini,FE}^+}$	$\frac{M_{max,test}^-}{M_{max,FE1}^-}$	$\frac{M_{max,test}^+}{M_{max,FE1}^+}$	$\frac{M_{max,test}^-}{M_{max,FE2}^-}$	$\frac{M_{max,test}^+}{M_{max,FE2}^+}$
		1	BBEC-8-8.8-50-LI	1.04	1.04	0.87	0.91
2	BBEC-8-10.9-50-LI	0.97	1.00	0.94	0.96	0.93	0.97
3	BBEC-8-10.9-50-LII	0.98	1.06	0.98	0.97	0.97	0.97
4	BBEC-5-8.8-50-LII	0.97	0.94	0.91	1.01	0.94	0.95
5	BBEC-6.3-8.8-50-LII	0.97	0.91	0.79	1.02	0.80	0.90
6	BBEC-6.3-8.8-25-LII	0.98	0.95	0.96	1.39	0.95	0.98
Average		0.98	0.98	0.91	1.04	0.91	0.95
St. deviation		0.03	0.05	0.06	0.16	0.06	0.03

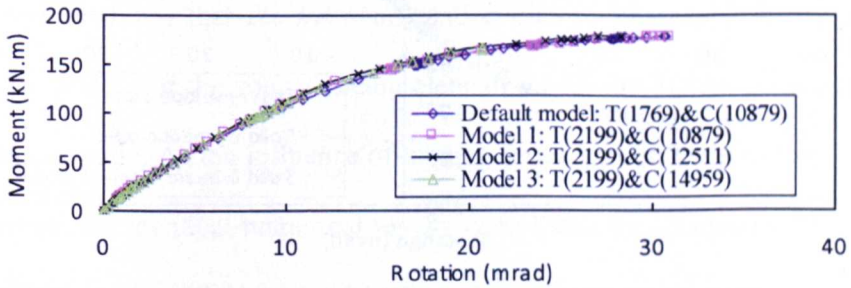
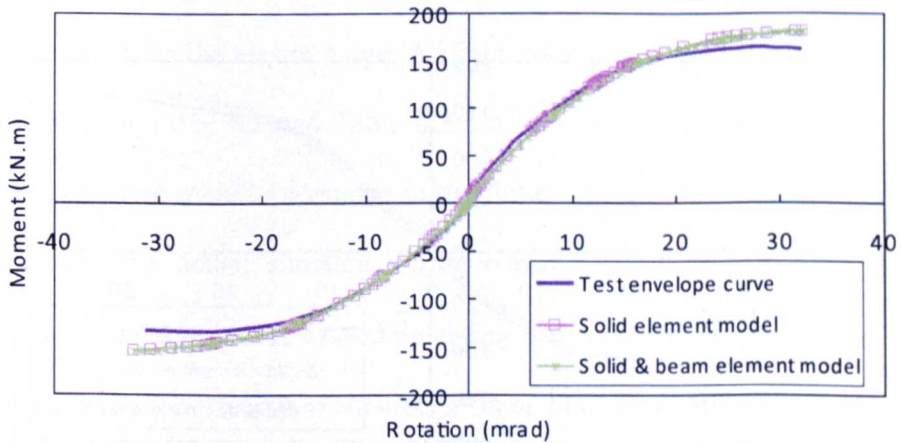
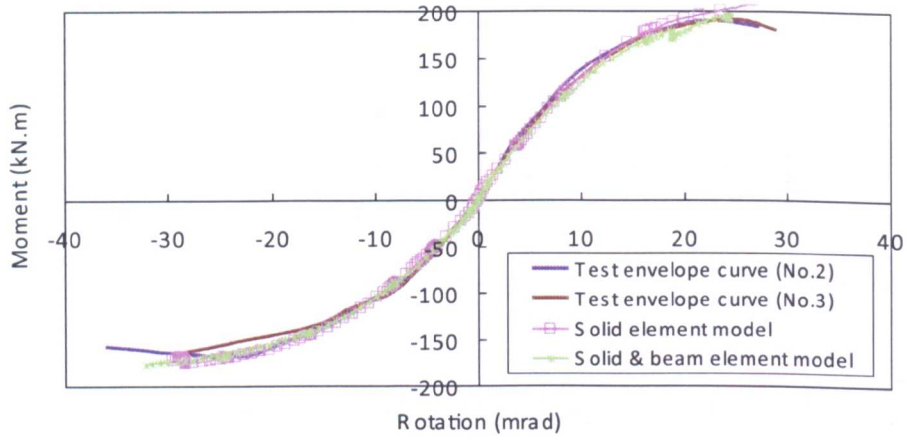


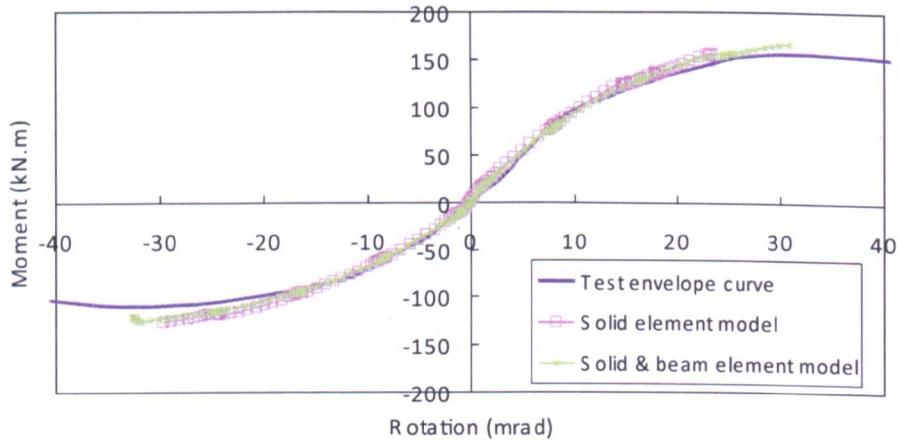
Figure 6.26 Sensitivity analysis- No. elements of tube wall (T) & concrete (C)



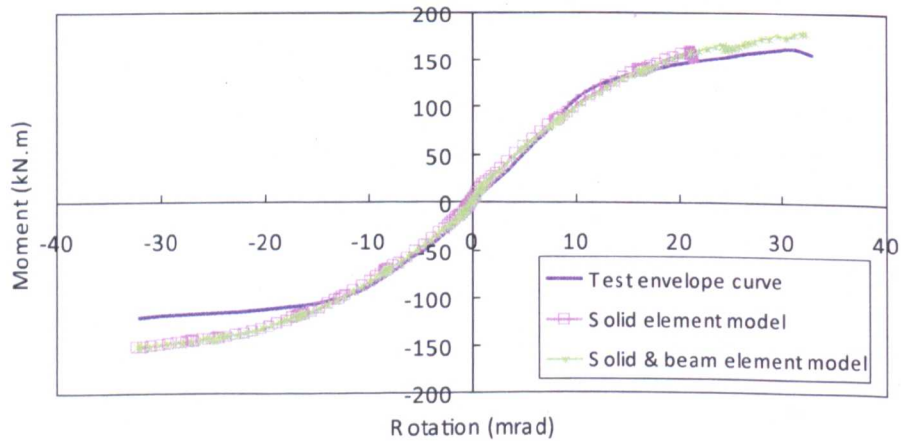
(a) Specimen: BBEC-8-8.8-50-LI



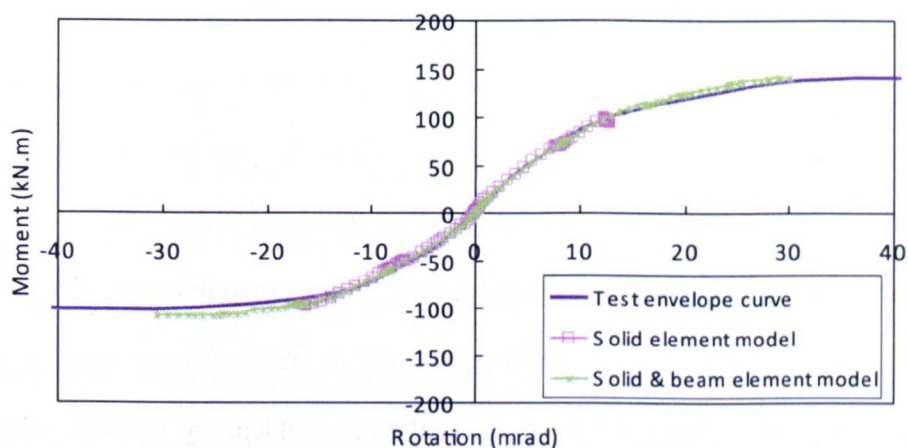
(b) Specimen: BBEC-8-10.9-50-LI & BBEC-8-10.9-50-LII



(c) Specimen: BBEC-5-8.8-50-LII



(d) Specimen: BBEC-6.3-8.8-50-LII



(e) Specimen: BBEC-6.3-8.8-25-LII

Figure 6.27 Comparison of test and numerical moment-rotation curves

The initial stiffness and moment data are listed from Table 6.1 to Table 6.3. The comparisons of test and numerical moment-rotation envelope curves in Figure 6.27 shows that the moment-rotation curves obtained from the solid element model and the solid & beam element model are almost coincident in the elastic range. As the influence of loading procedure on the envelope curve is ignored, the identical numerical results were listed for specimens BBEC-8-10.9-50-LI and BBEC-8-10.9-50-LII. Also, the moment-rotation curves predicted by both finite element models correlate quite well with experimental measurements in the elastic range. A slight discrepancy in the initial stiffness data listed in Table 6.2 and Table 6.3 can be explained by the fact that the perfect concrete material assumed in the finite element models may not fully agree with the actual situation during concrete handling and curing. For example, the micro-cracks caused by drying shrinkage or temperature changes may influence the strength of concrete infill and bond condition to some extent which in turn reduce the stiffness of the connection.

The maximum moment comparison shown in Table 6.1 indicates that the solid element models (FE1) presents to a certain degree lower predictions than the solid & beam element models (FE2), especially for the connections with relatively thin tube under negative bending moment. This is because the concrete undergoing high stress in this case is more susceptible to produce un-converged solution. In other words, the solid & beam element models, as expected, improve the local stress concentration problems of concrete at the bolt shank anchorage range in the modelling which result in relatively higher loading capacities. When comparing the finite element results from the solid & beam element models with the experiments, it is shown that, on average, the predicted values are approximately 5% and 9% higher than the experimental results for the negative and positive bending moments respectively. These discrepancies in the comparison can be attributed to the same reasons mentioned in the previous page. In addition, the imperfections of related concrete and steel material as well as the contact interface conditions may also contribute to such discrepancies. Although the predicted maximum moment results are somewhat overestimated, for most of the moment range the predicted values can be considered to have a close correlation with the experimental results. This demonstrates a reasonable accuracy of finite element models in predicting the ascending branch of the moment-rotation envelope curves. Unfortunately, it seems difficult to model the descending branch of the curves related to connections exhibiting failure mode II. This is because the nonlinear analyses in this study failed to converge when the concrete suffer relatively large local deformation and deterioration.

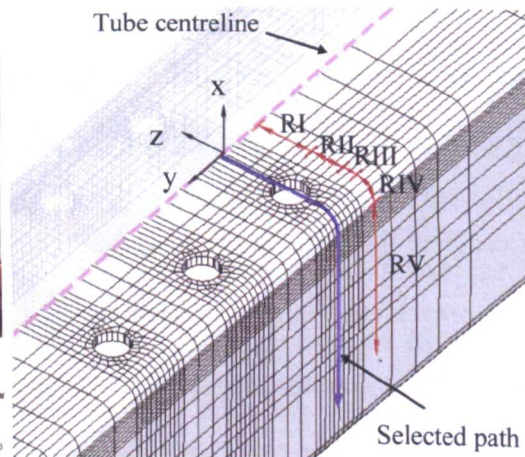
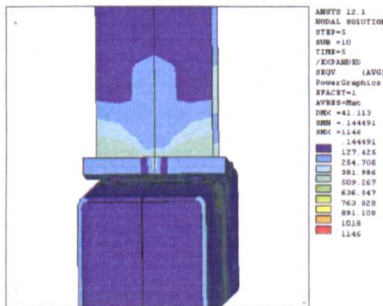
6.3.5 Comparison of tube deformation results

The flexibility of CFT column has been identified to influence the stiffness of the connections. The experiments in this study have incorporated the tube wall thickness and the concrete strength as important influential factors in the connection performance. Due to the limitation of the instrumentation in the experiment, however, it is unlikely that all the information regarding the deformity of the tube is recorded. The numerical approach using finite element analysis was, therefore, adopted to further understanding in such cases.

The concrete infill has been recognized (France *et al*, 1999) to have positive role in preventing the tube connecting face and tube sidewall face buckling outwards in the compression zone of the connection. Moreover, given that the endplate is relatively wide with respect to the tube wall, the local inward bearing of the endplate on the tube connecting face is small. Consequently, the tension zone of the connections can be regarded as the most important source of deformability of the whole joint. A typical deformation illustration at the first bolt row in the tension zone of the connection is shown in Figure 6.28. Tube deformation along a representative path from the tube centreline, through the bolt clearance hole centre and then down to the lower tube sidewall face was examined. Five ranges are identified in this path as shown in Figure 6.28. For the sake of result illustration, the actual curved path along the tube cross section was unfolded to a horizontal line for a distance variable used in the following study. The displacements in UX and UZ denote the directions normal to the tube connecting face and sidewall face respectively. The displacement data was obtained using linear interpolation for related node

results from finite element analyses. For the sake of illustration, only the results referring to the connection subjected to negative bending moment are presented in this comparison. The distance from tube centreline on the aforementioned predefined path is taken as a distance variable for curve comparison.

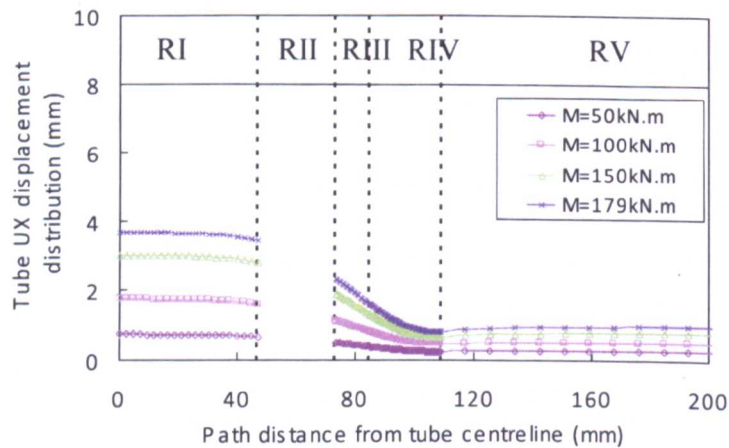
Typical deformation plot at the first bolt row in tension



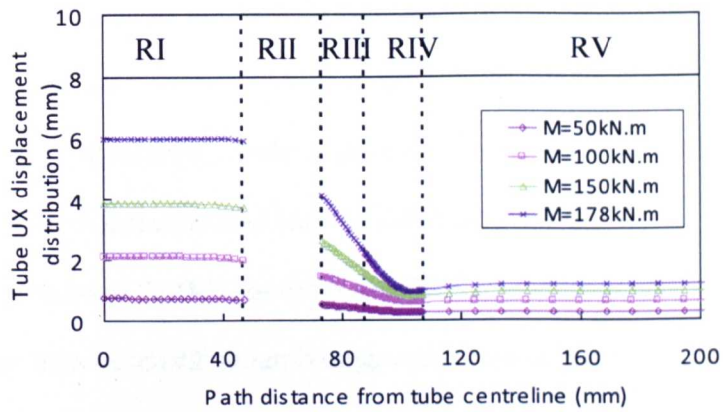
Note:

Path range I (RI)	Centreline to bolt clearance hole
Path range II (RII)	Bolt clearance hole
Path range III (RIII)	Bolt clearance hole to exterior corner
Path range IV (RIV)	Exterior corner
Path range V (RV)	Exterior corner to lower sidewall

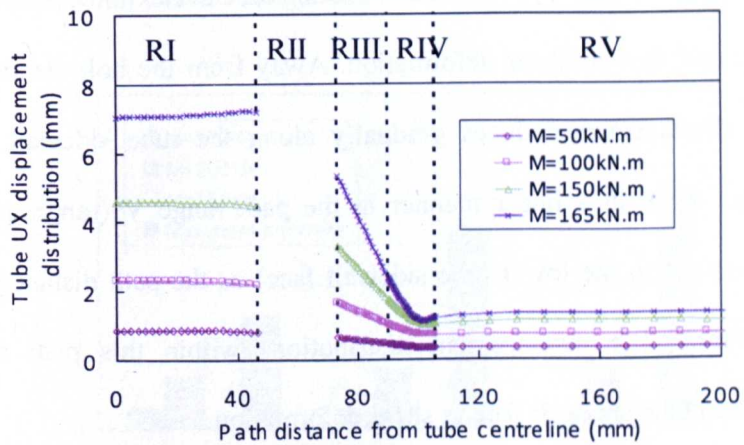
Figure 6.28 Illustration of representative path at the first bolt row



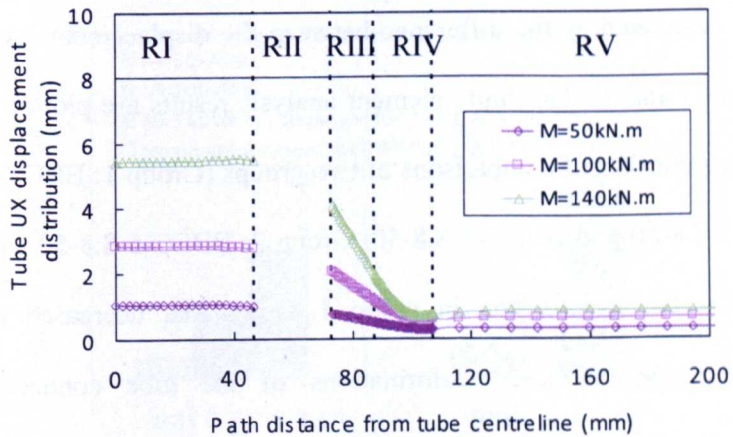
(a) Specimen: BBEC-8-8.8-50



(b) Specimen: BBEC-6.3-8.8-50



(c) Specimen: BBEC-5-8.8-50



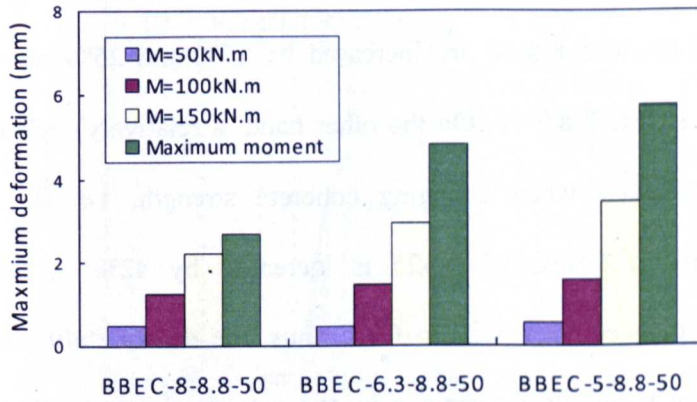
(d) Specimen: BBEC-6.3-8.8-25

Figure 6.29 Comparison of tube UX displacements along assigned path at the first bolt row

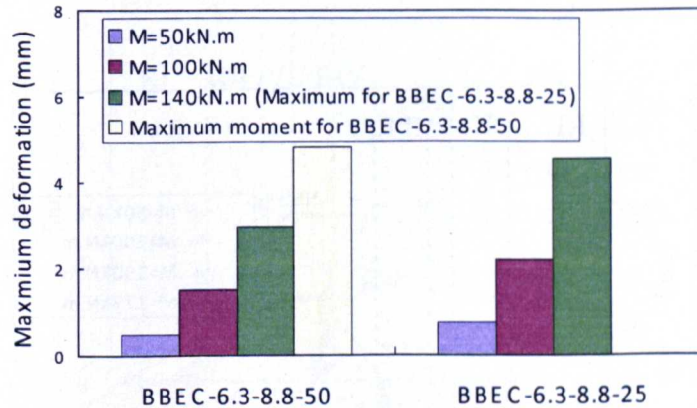
Figure 6.29 shows the UX displacement distribution along the selected path at the first bolt row with respect to three or four moment levels including ultimate moment. It can be observed that relatively high displacement in the path range I (between the tube centreline and bolt clearance hole). Within this path range, the specimens BBEC-5-8.8-50 and BBEC-6.3-8.8-25 present a slight increase of displacement by approximately 2%-5% when approaching the bolt clearance hole. The displacement distributions within the path range I are mostly contributed by the tube connecting face in flexible deformation and tube sidewall face in shear deformation. Away from the bolt clearance hole, the UX displacement reduces gradually along the tube sidewall face and distributes again in a linear manner in the path range V (ranging from the exterior corner to the lower tube sidewall face) as the path distance is larger than 120mm. The displacement distributions within this path range are attributed to tube sidewall face in shear deformation.

For the purpose of further comparison, the deformation of tube connecting face was calculated as the difference between the displacement levels of the path ranges I and V. The finite element analysis results are plotted in Figure 6.30, which consists of comparisons of two groups (Group 1: BBEC-8-8.8-50, BBEC-6.3-8.8-50 and BBEC-5-8.8-50; Group 2: BBEC-5-8.8-50 and BBEC-6.3-8.8-25). The comparison in group 1 shows that decreased tube wall thickness allows increased deformations of the tube connecting face, especially for the cases when the moment level is higher than 100kN.m. The maximum deformations at the moment level of 150kN.m for BBEC-6.3-8.8-50 and BBEC-5-8.8-50 are increased by 31% and 55% in contrast to BBEC-8-

8.8-50 respectively. The comparison in the group 2 shows the deformation of the connecting face is increased with reduced strength of concrete infill for the connections with moment level at 50kN.m and 100kN.m. The maximum deformations at the moment levels of 100kN.m and 140kN.m for BBEC-6.3-8.8-25 are increased by 46% and 54% respectively in contrast to BBEC-6.3-8.8-50. Nevertheless, the maximum deformation of BBEC-6.3-8.8-25 is lower than that of BBEC-6.3-8.8-50 due to an un-converged solution induced earlier termination of finite element analysis as mentioned previously.



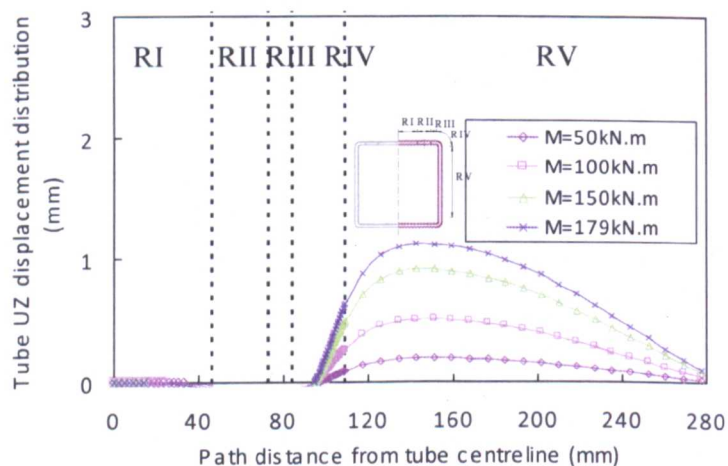
(a) Comparison of specimen group 1



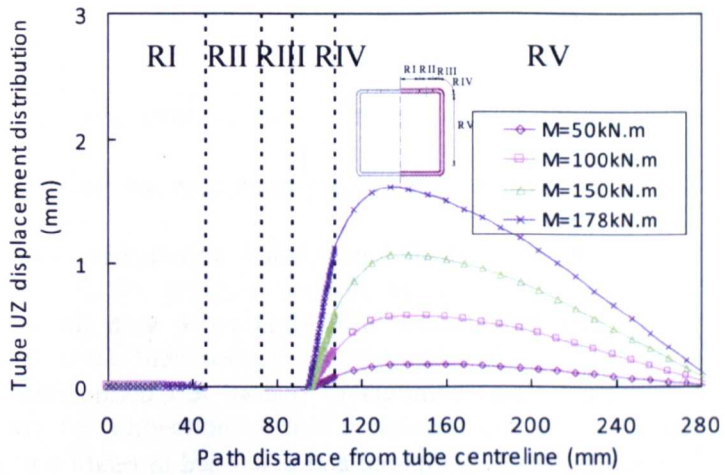
(b) Comparison of specimen group 2

Figure 6.30 Comparison of maximum deformation of tube connecting face at the first bolt row

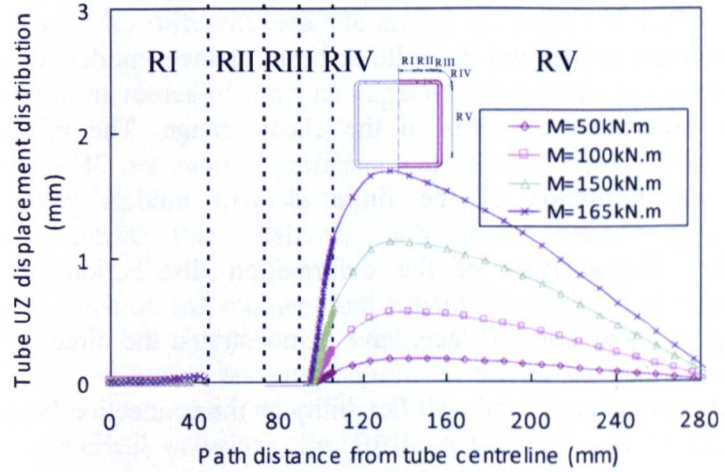
Figure 6.31 shows the UZ displacement distribution along selected path at the first bolt row with respect to generally three or four moment levels including maximum moment. It can be observed that the tube inward deformation mostly initiates at the path range IV and attains the maximum at approximately 30mm away from the exterior corner edge on the tube sidewall face within the path range V. The maximum displacements of the connections under the moment of 100kN.m are nearly 0.5mm-0.8mm, which was deemed to be negligible for the connection performance in elastic range. By contrast, the maximum deformations at the moment level of 150kN.m for BBEC-6.3-8.8-50 and BBEC-5-8.8-50 are increased by 17% and 25% respectively in contrast to BBEC-8-8.8-50. On the other hand, a relatively higher increased trend is observed when changing concrete strength, i.e. the maximum deformations of BBEC-6.3-8.8-25 is increased by 42% as the concrete strength is reduced from C50 to C25. Thus, the deformability on the tube sidewall face is largely determined by the compressive strength of concrete infill and the flexibility of tube wall.



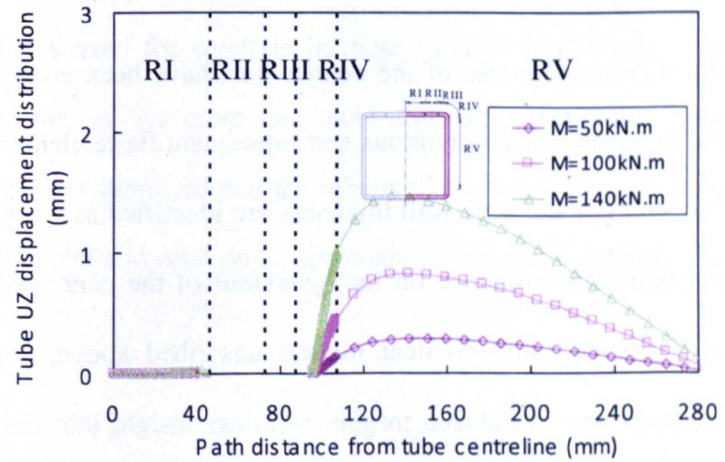
(a) Specimen: BBEC-8-8.8-50



(b) Specimen: BBEC-6.3-8.8-50



(c) Specimen: BBEC-5-8.8-50



(d) Specimen: BBEC-6.3-8.8-25

Figure 6.31 Comparison of tube UX displacement along assigned path at the first bolt row

6.3.6 *Summary of FE modelling results*

This section outlines the results from the finite element analysis and related comparisons with the experiments. The modelling of bolt preload was conducted using element death and pretension approaches. The numerical strain results from the bolt preload modelling agree with the experimental results. The numerical stress contours of overall test connections and their constituent components were compared and discussed in relation to the failure modes of the connections. The moment-rotation envelope curves predicted by the solid element model and the solid & beam element model correlate quite well with experimental results in the elastic range. The brief outcome, accuracy and limitation of the finite element models were discussed accordingly. The analysis of the deformation distribution on the tube connecting face and sidewall face, have demonstrated the direct influence of the concrete strength and tube wall flexibility on the connection behaviour.

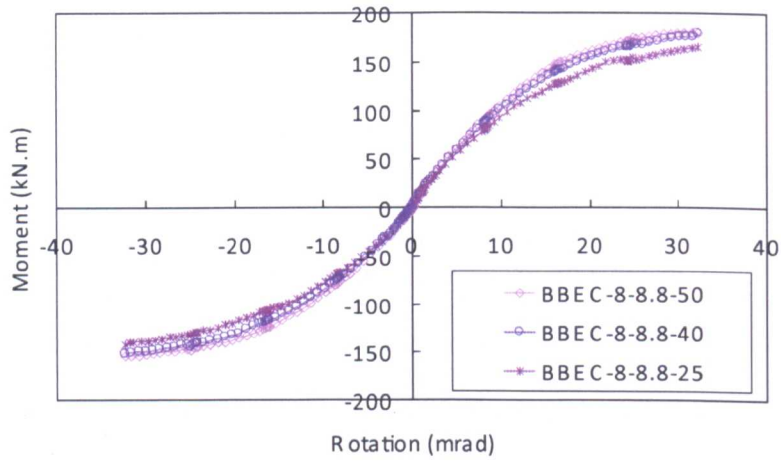
6.4 **Parameter variation analyses**

The moment-rotation response of the connections have been analysed so far based on the experimental observations and subsequent finite element analysis. The concrete strength and tube wall thickness are identified as the parameters which have significant influence on the behaviour of the connection studied herein. Based on the finite element models described above, a parameter variation analyses was introduced to gain a further insight into the moment-rotation relationships of the connections within a given range. For the purpose of comparison of the variation of these parameters, only one selected variable

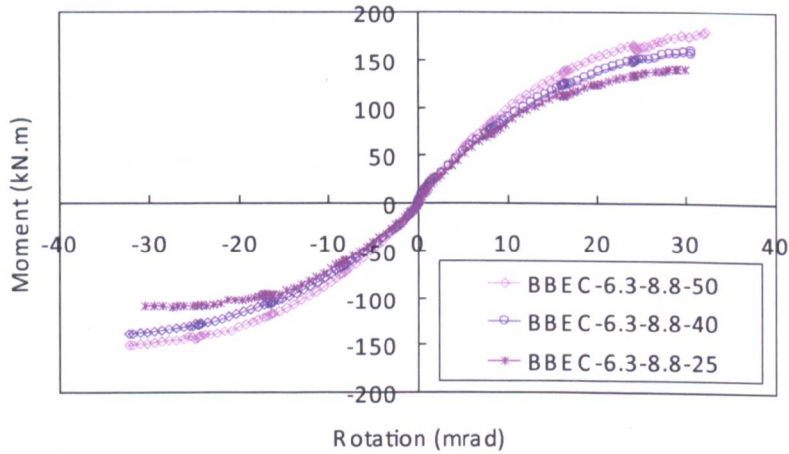
was changed at a time. The maximum moment and rotation results were analysed by taking into account these parameters

6.4.1 *Influence of concrete grade*

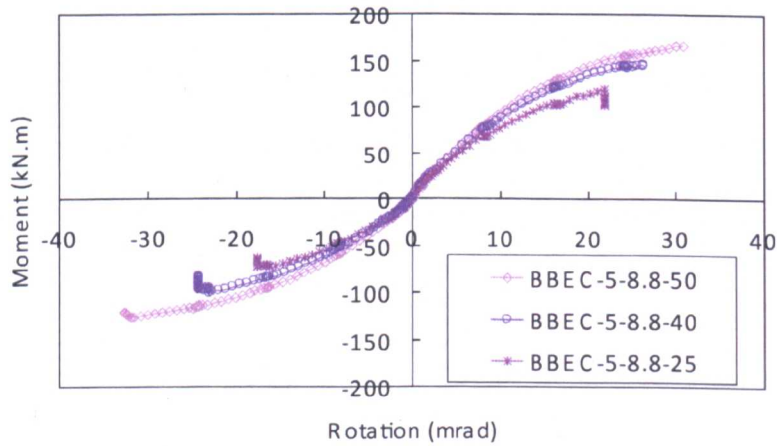
As mentioned in the previous section, the concrete strength influences the deformations of the tube connecting face and sidewall face. To have a closer examination, the connections with the concrete grade of C40 were added for the comparative study described in this section. The comparisons of the numerical results for different concrete grades are shown in Figure 6.32. It is evident that the increases of moment capacity when changing concrete grade from C25 to C40 are more significant than those from C40 to C50. This observation suggests that relatively high grade concrete generally has moderate influence on the moment and rotation capacity of the connections. By contrast, this influence becomes significant for the case of concrete grade C25. The numerical solutions for BBEC-6.3-8.8-25 and BBEC-5-8.8-25 become un-converged earlier than that for BBEC-5-8.8-50 which suggests the solid elements used for concrete in these models most likely undergo large local deterioration. As more and more local concrete failed with the load progressing, it is supposed that the tube wall becomes the main component to carry the moment and rotation for the connections with relatively strong bolt.



(a) $t_c=8\text{mm}$



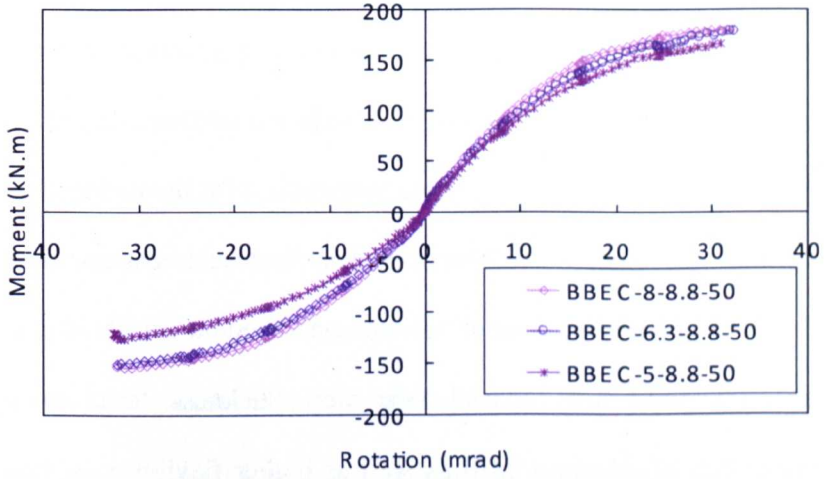
(b) $t_c=6.3\text{mm}$



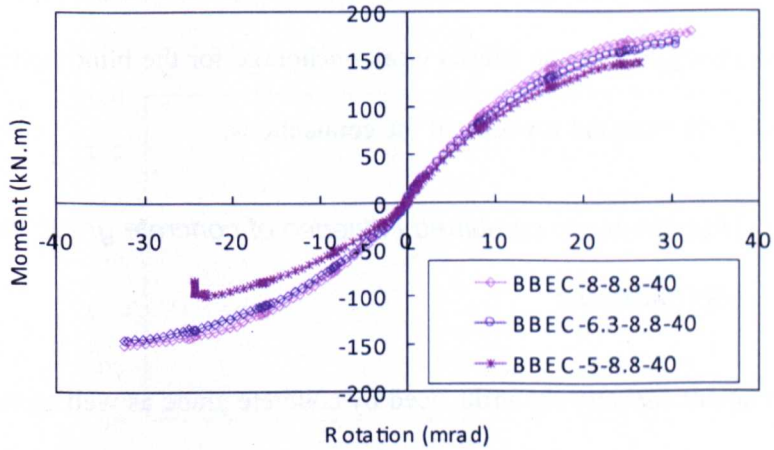
(c) $t_c=5\text{mm}$

Figure 6.32 Comparison of numerical results for varying concrete grades

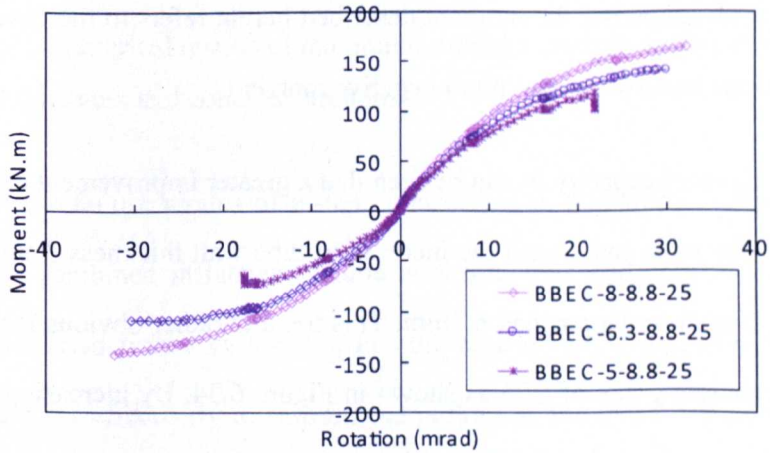
6.4.2 Influence of tube wall thickness



(a) $C_{gr}=C50$



(b) $C_{gr}=C40$



(c) $C_{gr}=C25$

Figure 6.33 Comparison of numerical results for varying tube wall thickness

The comparisons of numerical results for different tube wall thicknesses are shown in Figure 6.33. Three tube wall thicknesses, i.e., 5mm, 6.3mm, and 8mm, are plotted for each concrete grade group for comparison. It can be seen in all cases that when the tube wall was reduced to 5mm, lower moment capacity has resulted. This trend is more pronounced for the connections with relatively low concrete grade. The numerical finite element solutions also resulted in lower resistance—solutions un-converged at earlier steps. This observation suggests that reduced tube wall thickness leads to weaker confining effects of concrete infill as well as higher flexibility of tube wall thereby increasing the local deformation of concrete elements. On the other hand, low strength concrete causes weak anchorage for the blind bolts, which also reduces the moment capacity of the connections.

6.4.3 *Discussion on combined influence of concrete grade and tube wall thickness*

As the moment capacity are influenced by concrete grade as well as tube wall thickness, the finite element results are further summarized and plotted in Figure 6.34. Likewise, the moment described herein refers to the case that the connections underwent maximum negative moment.

For the moment capacity, it can be seen that a greater improvement of moment capacity for most cases with the increase of tube wall thickness from 5mm to 6.3mm than those larger than 6.3mm. This trend is rather obvious for the case of the concrete grade of C25 as shown in Figure 6.34. By increasing the tube wall thickness from 5mm to 8mm, the negative moment capacity is enhanced by 38.2% for the connections with C25 concrete grade while by 22.4% and by

8.2% for the connections with C40 and C50 concrete grades respectively. It turns out that the moment capacity may significantly decrease for the connections with thin tube wall and weak concrete. On the other hand, such increase would become moderate when relatively strong concrete and thick tube wall are adopted. The evidence for this point can also be traced from a previously reported monotonic test with similar joint configuration (Al-Mughairi, 2009). In this test, the moment capacity is almost the same for the connections with varying tube wall thickness from 8mm to 12.5mm. Moreover, for the connections with 10mm and 12.5mm thick tube wall, the most range of the moment-rotation curves are almost coincident, as shown in Figure 6.35.

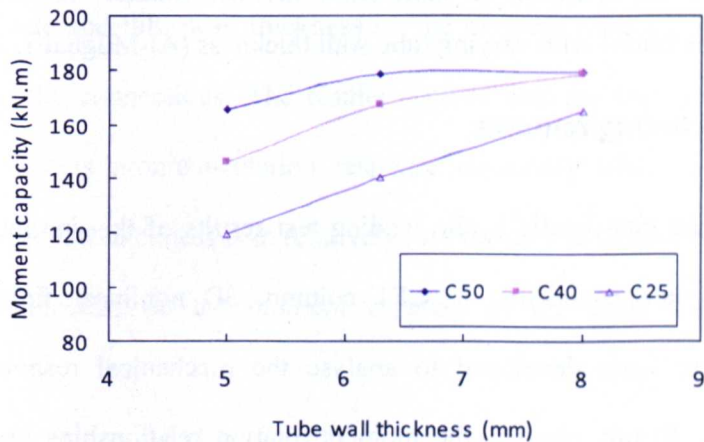


Figure 6.34 Numerical results of maximum moment capacity with varying tube wall thickness and concrete strength

Based on the failure modes of tested connections in this study and previous report, the combined influence of tube wall thickness and concrete strength can be discussed from two aspects. For the case of weak concrete, the tube wall would act effectively to restrain the pullout of the blind bolt as the bolt anchorage is lost. In this sense, the moment capacity of the connections is

determined by the strength of tube wall. Conversely, the concrete strength would become the main influence on the moment capacity of the connections provided that the tube wall is relatively flexible.

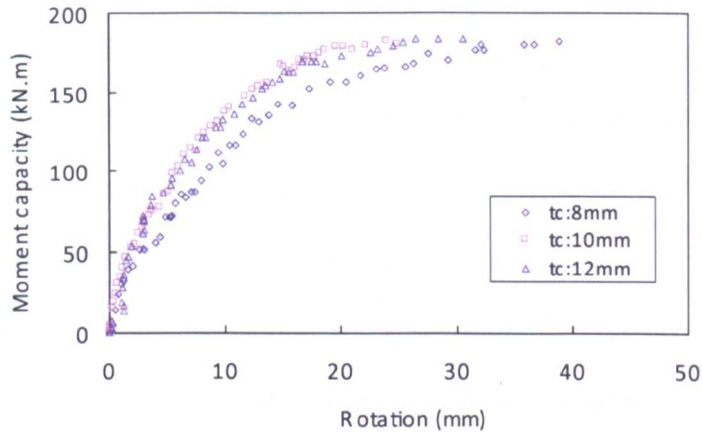


Figure 6.35 Comparison of monotonic moment-rotation relationships of similar connections with varying tube wall thickness (Al-Mughairi, 2009)

6.5 Concluding remarks

Based on the quasi-static cyclic loading test results of this innovative blind bolted endplate connection to CFT column, 3D nonlinear finite element models have been developed to analyse the mechanical response of the connection. In this chapter, the moment-rotation relationships predicted by finite element models were compared with the experimental cyclic envelopes under positive and negative bending moments. The comparison showed that the models are able to predict the initial stiffness and maximum moment capacity with reasonable accuracy (refer to Figure 6.27). The strain results of the blind bolts and tube connecting face and sidewall face were compared against the experimental instrumentations which showed that the finite element model is capable of capturing local strain distribution (refer to Figure

6.24- Figure 6.26). From above analysis, it is concluded that this connection can be simulated numerically in this study.

The validated finite element model was used to draw a comparison of the failure modes of the connection components observed in the tests. Related stress contours of the connection were described and discussed for further understanding of the connection response. The displacement distributions of the tube connecting face and sidewall face were also traced by finite element models which provide a useful supplement for the test recording in the study of tube flexibility.

Parametric analyses were conducted to further investigate the influences of concrete grade and tube wall thickness on the moment capacity and rotation capacity of the connections. The results showed that the increase of either parameter affects moment-rotation response especially when the concrete grade or tube wall thickness is in relatively low value. The combined influence of both parameters on the moment capacity of the connections is also discussed.

The general conclusion to be drawn from the analyses is that this finite element model is capable of predicting the moment-rotation behaviour of this innovative blind bolted endplate connection to CFT column. It offers a reliable and cost-effective alternative to supplement experimental observation and measurement. Based on the numerical predictions of moment-rotation envelopes, the hysteretic moment-rotation relationship will be developed in Chapter 7.

As a note to this chapter, the purpose of the finite element analysis described herein is to supplement the experimental study of the connections with limited range of parameters of the blind bolt, the concrete grade, and the tube section as listed in Table 6.4. As for the general connection design, the understandings obtained from this analysis act as a basis for future work with wider range of related parameters which will also be discussed in Section 8.2.

Table 6.4 Model limitations

Items	Limitations
Blind bolt size, grade & type	M16 (Gr.8.8) Extended Hollobolts
Concrete grade	C25~C50
Slenderness ratio of tube connecting face	$25 \leq b_c/t_c \leq 40$
Ratio of the bolt gauge width (g) to the width of tube connecting face (b_c)	$g/b_c = 0.6$
Ratio between the bolt pitch distance (p) to the width of tube connecting face (b_c)	$p/b_c = 0.5$

CHAPTER 7

JOINT HYSTERETIC MOMENT-ROTATION RELATIONSHIP MODELLING

7.1 Introduction

The discussion of the finite element model in the preceding chapter has provided a satisfactory prediction of the ascending branch of test moment-rotation envelope curves. To simulate the hysteretic moment-rotation relationship of the test connections, analytical models based on the relevant mathematical representations will be presented in this chapter. The descending branch of envelope curve, along with the loading, unloading and reloading segments of hysteresis loop will be incorporated in analytical models with respect to related geometric and material parameters.

Modelling the joint moment-rotation relationship depends on the behaviour of constituent joint components. In the case of practical design for the joints under monotonic loading, the simple component model based analysis eliminates much of the variability arising from the connections. The so-called component method in Eurocode 3 refers to using such simplified mechanical models composed of extensional springs and rigid links to evaluate the joint behaviour by assembling the contributions of individual components. In this study, the components in aforementioned joint tension zone were highlighted and related cyclic models are outlined prior to the analysis of joint hysteretic moment-rotation relationship.

Although mathematical representations are widely used in former studies of joint monotonic behaviour, appropriate hysteretic models incorporating loading and unloading excursions are still needed to simulate the hysteretic moment-rotation relationship of this innovative blind bolted endplate connection to CFT column. The characteristics of strength, stiffness and energy dissipation were incorporated into the hysteretic models in this study. The results of the finite element analysis, which incorporated the information of joint geometric and mechanical properties, were used to provide basic parameters, such as initial stiffness, yield strength and rotation, for the mathematical representations.

This chapter will be structured as follows. The description of three typical mathematical representations is presented in Section 7.2. Their use in the prediction of test envelope curves are also described and discussed. The cyclic material model is outlined in Section 7.3 in which related experiments are referred. The hysteretic moment-rotation models for the tests are presented in Section 7.4 which includes the description for the excursion corresponding to the loading and unloading branches of the envelope curve. The simulation of test hysteretic moment-rotation curves is presented in Section 7.5. Finally, a brief summary and discussion about adopted hysteretic models for the joint behaviour modelling is outlined in Section 7.6.

7.2 Mathematical representations of moment-rotation envelope

To account for the nonlinear moment-rotation curve of the connection, two types of mathematical representation are identified. The first type is related to pure curve fitting formulations, and related parameters do not necessarily have

clear physical meanings. The second type, on the other hand, is developed on the basis of relevant physical parameters. This also means that the representations can be referred as strength, stiffness, and shape factor. In this study, only the latter representation was used and related physical parameter data are derived from finite element analysis. The mathematical representation outlined herein consists of Eurocode 3 based trilinear representation, power representation and exponential representation.

7.2.1 Eurocode 3 based trilinear representation

Eurocode 3 suggests a trilinear representation of joint moment-rotation curve with parameters of clear physical meaning. As shown in Figure 7.1, this curve is assumed to consist of three parts. The curve in the first part is linear elastic until a level of 2/3 of the design moment resistance ($M_{j,Rd}$) is reached, i.e. the relationship between moment and rotation is linear. Thereafter, the curve goes up nonlinearly until a yield plateau with the rotation θ_{xd} corresponding to the moment first reaching $M_{j,Rd}$. In this range, the moment of the connection can be obtained from the product of the values of secant stiffness and rotation. The final part of the curve ends at the joint rotation capacity (θ_{cd}) corresponding to the same load level of $M_{j,Rd}$. The stiffness expressions including initial and secant stiffnesses can be written as follows:

$$K = \begin{cases} K_{int} & \text{when } M < 2/3 M_{j,Rd} & \text{Equation 7.1} \\ \frac{K_{int}}{\left(\frac{1.5M}{M_{j,Rd}}\right)^\xi} & \text{when } 2/3 M_{j,Rd} < M < M_{j,Rd} & \text{Equation 7.2} \end{cases}$$

where, $\xi = 2.7$ is assumed for the endplate and welded joints.

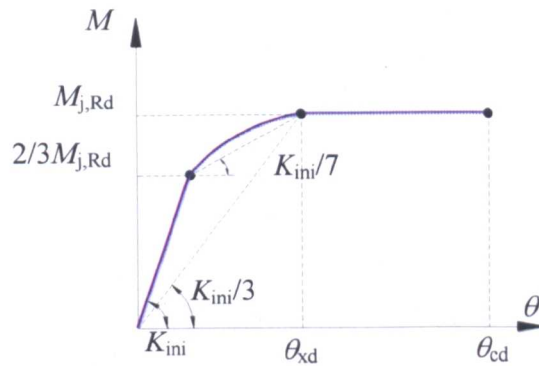


Figure 7.1 Trilinear representation of moment-rotation curve suggested by Eurocode 3 (2005)

It is observed that the moment-rotation curve can be plotted provided that K_{ini} and $M_{j,Rd}$ are available for this representation. This representation was adopted by early researchers in the comparison of test moment-rotation curves (Weynand *et al*, 1995). In this study, these two parameters are obtained from finite element analysis results, and the calculated curve is then compared with test envelope curve, as shown in Figure 7.2. An agreement can be seen at the initial phase of the curve, however, the difference is noticeable regarding the curve starting from the post-yielding point. This indicates that the strain hardening effects are not taken into account by this representation as the rotation varies between θ_{xd} and θ_{cd} .

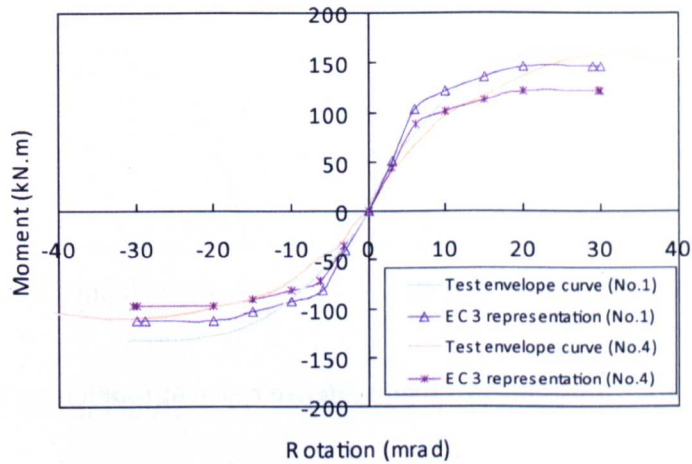


Figure 7.2 Comparison of trilinear representations and test envelope curves (Test No.1 & No.4)

7.2.2 Power representation

A nonlinear power representation of moment-rotation curve was proposed by Richard & Abbott (1975) in modelling material elastic-plastic behaviour. This model was later introduced and applied in the modelling of moment-rotation relationship of beam to column joints, as reported by Faella *et al* (2000) and Simoes *et al* (2001). In this representation, four parameters are required: reference bending moment (M_0), K_{ini} , plastic stiffness (K_p), and shape factor (n). It is noted that this representation is able to account for the moment-rotation curve with plastic development and softening branch, as shown in Figure 7.3.

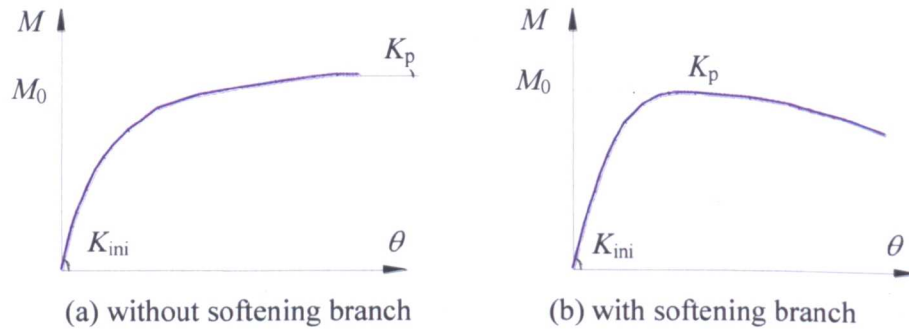


Figure 7.3 Illustration of representative moment-rotation curves

Using above parameters, the power representation can be expressed in Equation 7.3. The tangent to the nonlinear curve can be calculated by the differentiation of Equation 7.3 which yields Equation 7.4. Likewise, the parameters of M_0 , K_{ini} , and K_p are obtained from previous finite element analysis results, and then the shape factor is calculated by these equations which give rise to a close correlation with the test envelope curves, as shown in Figure 7.4. The shape factors in the equations for the negative loading and positive loading curves are listed in Table 7.1. It is noted in the numerical analysis that larger shape factor often produces the curves with greater slope in the ascending branch. For test No.4 and No.6, there are two K_p and n are provided for the curves with and without softening branches. As such, a representative curve correlation for this consideration is shown in Figure 7.5 in which two power representations indicate such difference.

$$M = \frac{(K_{ini} - K_p)\theta}{\left(1 + \left|\frac{(K_{ini} - K_p)\theta}{M_0}\right|^n\right)^{\frac{1}{n}}} + K_p\theta \quad \text{Equation 7.1}$$

$$\begin{aligned}
 K_{\theta} = \frac{\partial M}{\partial \theta} &= \frac{\partial \left\{ \frac{(K_{ini} - K_p)\theta}{\left(1 + \left| \frac{(K_{ini} - K_p)\theta}{M_0} \right|^n\right)^{\frac{1}{n}}} \right\}}{\partial \theta} + K_p \\
 &= \frac{K_{ini} - K_p}{\left(1 + \left| \frac{(K_{ini} - K_p)\theta}{M_0} \right|^n\right)^{\frac{n+1}{n}}} + K_p
 \end{aligned}
 \tag{Equation 7.2}$$

Reference: Richard & Abbott (1975), Faella *et al* (2000)

Table 7.1 Parameters for mathematical representations

Test No.	Specimen reference	Test results				Shape factors			
		Initial stiffness (KN.m/mrad)		Maximum moment (kN.m)		Power		Exponential	
		K_{ini}^-	K_{ini}^+	M_{max}^-	M_{max}^+	n^-	n^+	n^-	n^+
1	BBEC-8-8.8-50-LI	16.92	23.51	133.79	163.89	1.41	1.55	0.19	0.20
2,3	BBEC-8-10.9-50-LI	20.11	27.06	164.69	188.97	1.43	1.51	0.25	0.25
	BBEC-8-10.9-50-LII	20.18	28.62	171.89	189.17				
4	BBEC-5-8.8-50-LII	14.06	17.95	115.80	157.72	1.21	1.42	0.05	0.03
5	BBEC-6.3-8.8-50-LII	15.78	19.15	120.39	160.95	1.19*	1.21*	0.24*	0.23*
6	BBEC-6.3-8.8-25-LII	13.66	16.18	102.95	137.28	1.35	1.35	0.05	0.05
						1.30*	1.31*	0.06*	0.06*

Note: * denotes the representation parameter for the curves incorporating the softening branch

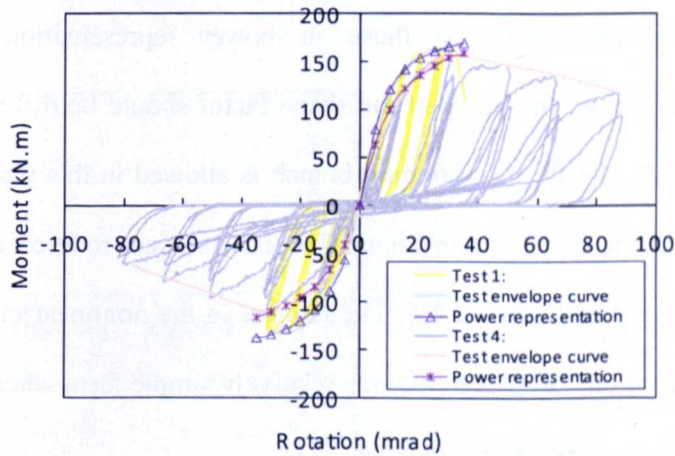


Figure 7.4 Comparison of power representations and test envelope curves (Test No.1 & No.4)

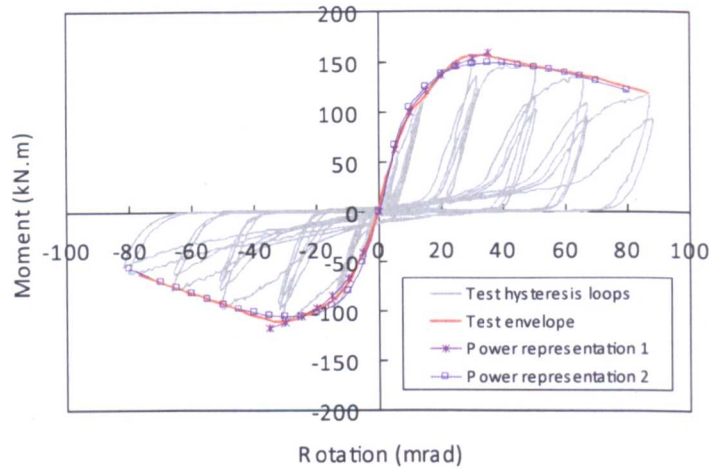


Figure 7.5 Comparison of finite element model based power representations for the curve with or without softening branch (Test No.4)

7.2.3 Exponential representation

Another nonlinear representation of moment-rotation curve is featured by exponential parameters. This representation was firstly proposed by Yee *et al* (1986) for moment-rotation curve modelling. The parameters required in this representation are similar to those in power representation described previously, however, the value of the shape factor should be different due to the formulation. Again, the softening branch is allowed in this representation which also can be illustrated in Figure 7.3. The moment-rotation relationship can be expressed in Equation 7.5. The tangent to the nonlinear curve can be written in Equation 7.6, which presents relatively simple form when compared with the previous power representation.

$$M = M_0 \left[1 - \exp \left(\frac{-\theta (K_{ini} - K_p + n\theta)}{M_0} \right) \right] + K_p \theta \quad \text{Equation 7.3}$$

$$\begin{aligned}
 K_{\theta} = \frac{\partial M}{\partial \theta} &= \frac{\partial \left\{ M_0 \left[1 - \exp \left(\frac{-\theta (K_{ini} - K_p + n\theta)}{M_0} \right) \right] \right\}}{\partial \theta} + K_p \\
 &= (K_{ini} - K_p + 2n\theta) \exp \left(\frac{-\theta (K_{ini} - K_p + n\theta)}{M_0} \right) + K_p \quad \text{Equation 7.4}
 \end{aligned}$$

The curve fitting of the test moment-rotation envelopes with exponential representation was also conducted and an example comparison plotted in Figure 7.6. It is shown that a good agreement between the representation and the test envelopes can be obtained by introducing the shape factors listed in Table 7.1. Based on the numerical analysis results, a similar observation with power representation was made that the slope in the ascending branch is improved with the greater shape factors. However, it is noted that the increasing magnitude of maximum moment predicted by exponential representation is less than that by power representation which in turn produces less agreement of moment in the softening branch.

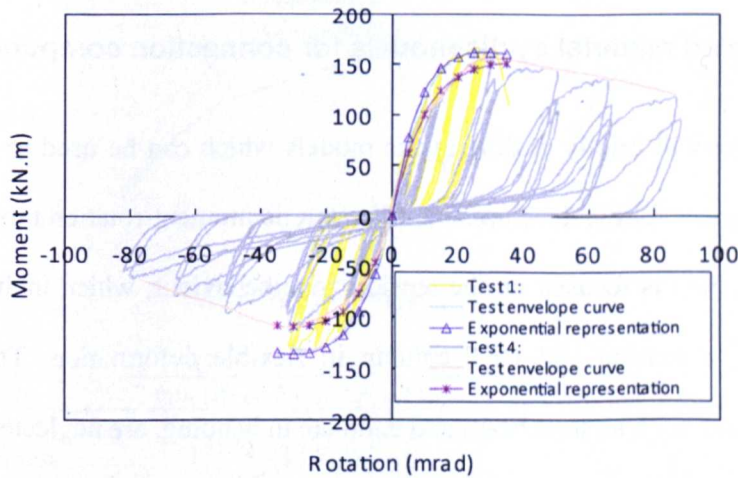


Figure 7.6 Comparison of representative exponential representations and test envelope curves (Test No.1 & No.4)

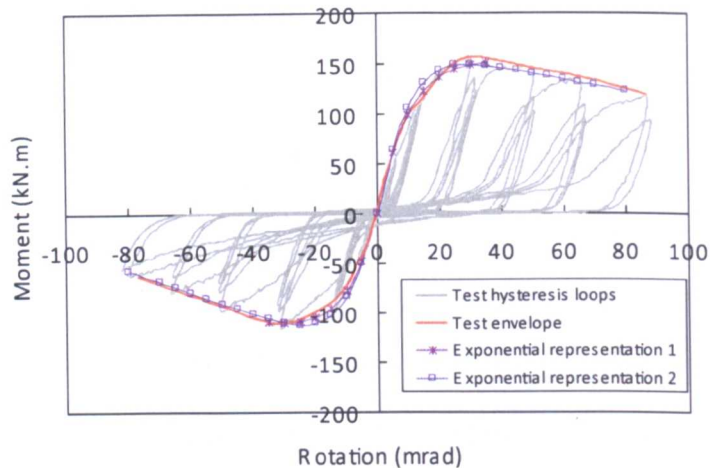


Figure 7.7 Comparison of exponential representations for the curve with or without descending branch (Test No.4)

Similarly, the exponential representation was adopted for the envelope curves of test No.4 and No.6, in which different K_p and n are adopted to allow for the curves with and without softening branches. The basic parameter values are derived from the results of finite element analysis. As shown in Figure 7.7, a close correlation can be seen between the test envelopes and the curves displayed by both representations.

7.3 Related material cyclic models for connection components

This section will briefly outline cyclic models which can be used to provide basic evidences for the development of hysteretic moment-rotation model. The attention herein is focused on the tension zone behaviour, which includes the blind bolt in tension and CFT column in flexible deformation. The other contributions, such as steel beam and endplate in bending, are neglected herein which agree with previous assumptions for test specimens.

In the component method, the connection response is based on the assessment of force-displacement constitutive law of each component. The individual extensional or rotational spring is used to allow for the response of certain part of the connection under specific loading. The joint constituent components are assembled in serial or parallel configuration with equivalent springs as illustrated in Figure 7.8 (Wald & Steenhuis, 1993). The joint cyclic behaviour may be greatly influenced by the weakest components. In the study herein, the bolt & CFT column are taken as the primary components in the tension zone which agrees with aforementioned test observations. Relevant explanations will also be provided in the following study along with the description of proposed analytical models. As a basis for this study, the material cyclic models of steel and concrete are included in Appendix D.

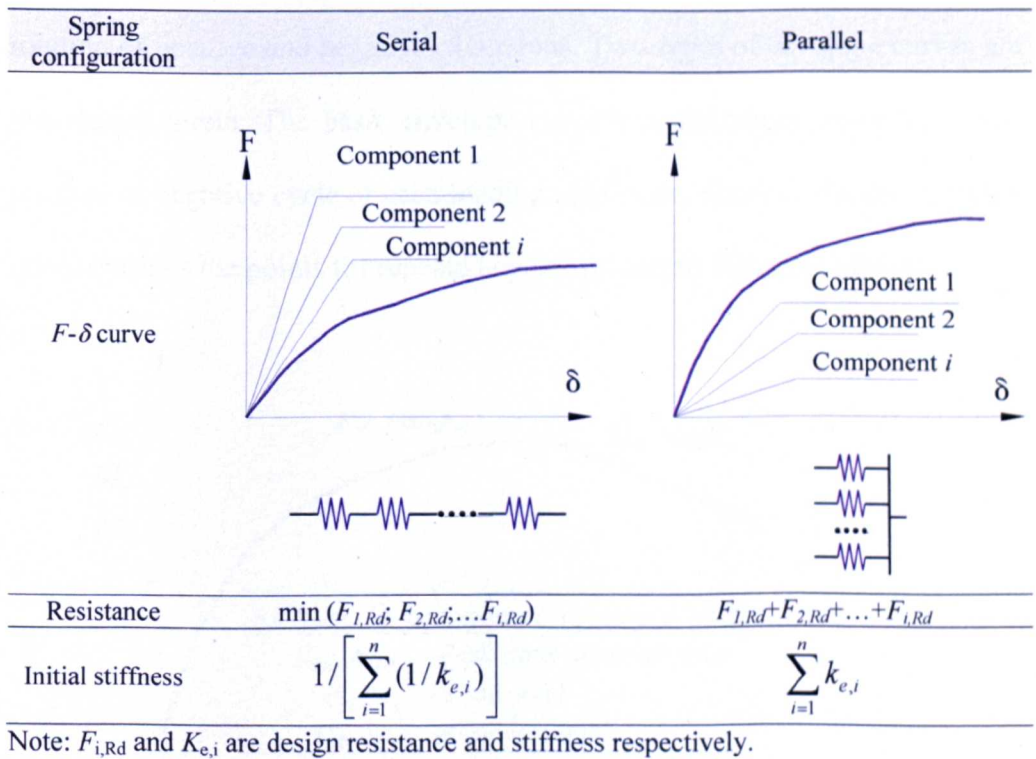


Figure 7.8 Illustration of linear assembling method of connection components

7.4 Development of hysteretic moment-rotation model

7.4.1 Basic envelope curve

Several models for featuring moment-rotation response of bolted endplate connections are reported in the literature (Deng, *et al*, 2000). Using key curve fitting variables, it is possible to characterize the moment-rotation response of the connection which can be incorporated into frame model analysis. For the connections studied herein, however, it is difficult to use reported models due to different degrees of complexity in the joint configuration. To analyse the connection behaviour in this part of work, the envelope response curves were studied as a basis for developing hysteretic moment-rotation relationship. By referring to previous test and numerical results, these curves are formulated using the line of best fit through the maximum moment and its corresponding rotation of positive and negative excursions. Two types of envelope curves are introduced herein. The basic envelope curve accommodates loads from first positive or negative cycle of each loading amplitude; the degradation envelope curve outlines the points for repeated cycles related to load degradation.

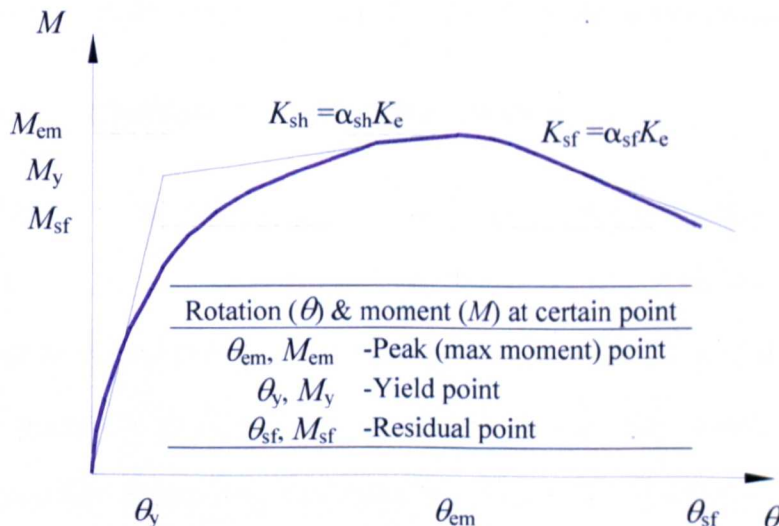


Figure 7.9 Envelope curves for hysteretic moment-rotation models

A representative envelope curve for hysteretic moment-rotation model is illustrated in Figure 7.9. Prior to the peak (maximum moment) point (θ_{em} , M_{em}), the strain hardening stiffness (K_{sh}) is calculated as $\alpha_{sh}K_e$. The moment at the rotation range between θ_y and θ_{em} can be formulated by K_{sh} and θ . If the deterioration is taken into account subsequent to the peak point, the linear descending branch is represented by the softening stiffness K_{sf} which is equal to $\alpha_{sf}K_e$. Apparently, the value of K_{sf} should be negative. Based on the linear relationship in the softening branch, the moment can then be calculated as:

$$M = \frac{(M_{sf} - M_{em})(\theta - \theta_{em})}{\theta_{sf} - \theta_{em}} + M_{em} \quad \text{Equation 7.7}$$

The parameters of α_{sh} and α_{sf} can be obtained from experimental data or analytical model. In this study, the moment-rotation relationships derived from the finite element models mentioned in Chapter 6 were adopted for envelope curve at the rotation range between θ_y and θ_{em} . The softening branch is then predicted using α_{sf} obtained from experimental moment-rotation relationship as referred to Chapter 4. The finite element model based envelope curve serves as a basic step to be further associated with hysteretic model analysis.

7.4.2 Hysteretic moment-rotation models

Referring to the observed cyclic response of the connections, hysteretic models were developed for loading and unloading branches in order to simulate the moment-rotation relationship analytically. It was noted that the test hysteresis loops may not be simplified with the excursions in linear relationship. Rather, the hysteresis loops have to be divided into several

segments to represent the nonlinear behaviour of the connection. In order to mathematically describe these segments, several power and exponential functions were adopted and compared with the test curves in Chapter 4. Implementation of these functions requires several variables restored in the previous hysteresis loops. The strength and energy dissipation deterioration were also taken into account in these models. The hysteretic models for the connection were identified for different behaviours of the connections in categories I & II and will be presented separately below.

7.4.2.1 Hysteretic model for connection category I

As mentioned previously in Section 4.5, the connections in category I are featured by relatively strong CFT column and consequently failed by bolt fracture and developed the full bolt tensile strength. Given the primary contribution of the blind bolt to the response of the connection, the hysteretic model was expected to be similar to that for the bolt in tension. However, it is worthy of note that actual connection behaviour in this category is affected by the mechanical interlock effect between the flaring sleeve, the threaded cone, and the deformation of bolt clearance hole on the tube connecting face as well as local concrete deterioration. The shapes of the unloading curves and reloading curves tend to become nonlinear when approaching the zero moment axis in the hysteretic moment-rotation relationship. On the other hand, the connection capacities are weakened when subjected to consecutive inelastic deformation and cyclic loading. This is especially significant for the foregoing test evidence of dramatic reduction of the energy dissipation (see Figure 4.13 a-c,e) in the repeated cycles subsequent to the first ones of each loading

amplitude. Thus, the hysteretic model developed for the connection in this category should be able to accommodate these changes in the connection behaviour.

An idealization of the proposed moment-rotation hysteresis loops consists of three stages. The whole loading process is featured by combining the hysteresis loops corresponding to each loading amplitude. Also, this idealization allows for repeated cycles under the same loading amplitude. As an illustration, Figure 7.10 shows the transition of the excursions in which only the cycles related to non-recoverable plastic rotation are considered. Stage 1 corresponds to the first hysteresis loop under i th loading amplitude, referring to Figure 7.10 (a). The strength and energy dissipation capacities of the connection commence to degrade during the repeated cycles in Stage 2 (see Figure 7.10b) when local cracks are assumed to appear in concrete. During Stage 3, the hysteresis loop continues as the loading increased to $(i+1)$ th amplitude, referring to Figure 7.10 (c).

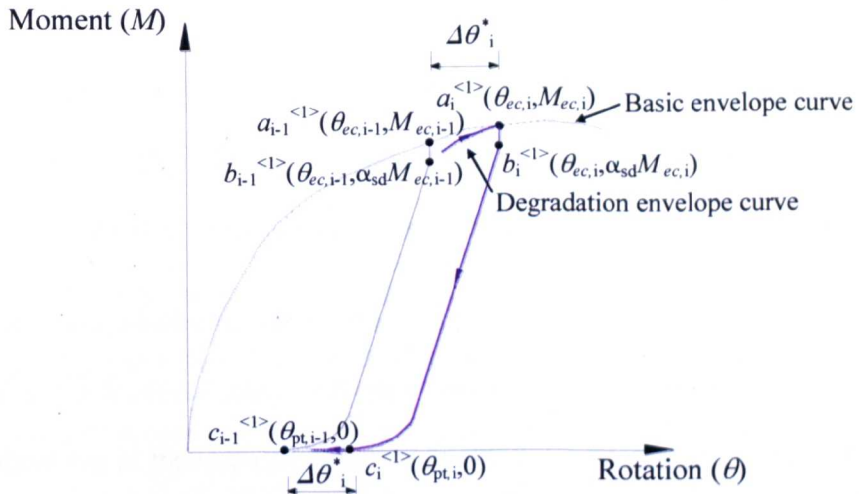
Following the cyclic loading sequence described above, the hysteretic model for the connection category I is outlined in details as follows:

-Stage 1: On initial loading from last cycle under $(i-1)$ th loading amplitude, the curve ascends and intersects basic envelope curve at point $a_i^{<1>}(\theta_{ec,i}, M_{ec,i})$, as shown in Figure 7.10 (a). Afterwards, the unloading segment starts at this point and moves downward linearly to point $b_i^{<1>}$ with decreased moment value of $\alpha_{sd}M_{ec,i}$ but no changes of rotation value. Further unloading beyond point $b_i^{<1>}$ follows a linear segment and descends nonlinearly adjacent to the zero moment axis. The unloading segment ends when it reaches point

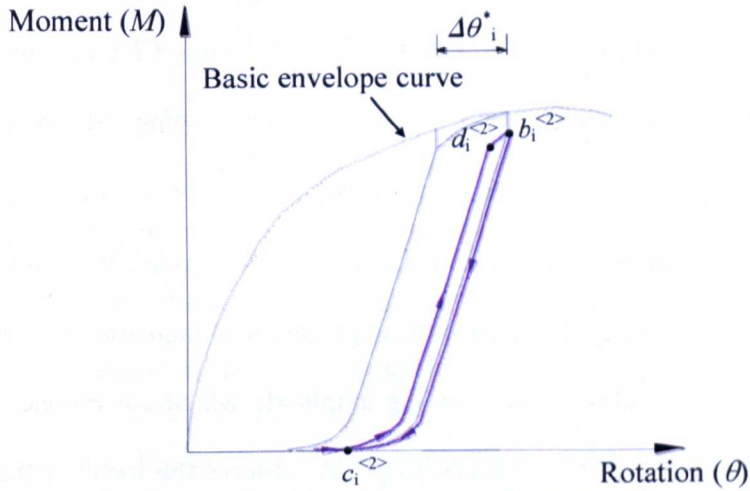
$c_i^{<1>}(\theta_{pt,i}, 0)$, where $\theta_{pt,i}$ can be regarded as the rotation produced by the residual or permanent deformation of the connection. The inelastic rotation difference between point $c_i^{<1>}$ and point $c_{i-1}^{<1>}$, corresponding to the first cycle under current and previous loading amplitudes respectively, on the zero moment axis is assumed to be the same as that on the basic envelope curve which is also referred to as equal inelastic rotation increment. The unloading segment from point $b_i^{<1>}$ to point $c_i^{<1>}$ can be expressed by a power expression in the form of M_{fu} as:

$$M_{fu} = \alpha_{sd} M_{ec,i} \left(\frac{\theta_{fu} - \theta_{pt,i}}{\theta_{ec,i} - \theta_{pt,i}} \right)^{N_c} \quad \text{Equation 7.8}$$

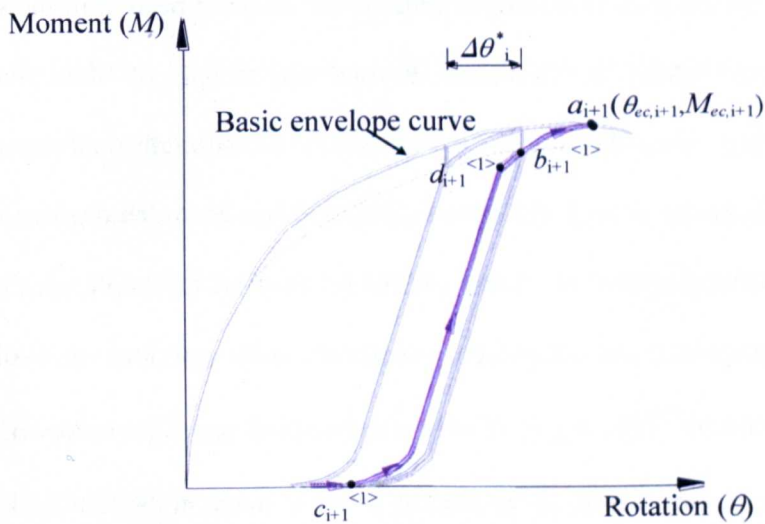
where, θ_{fu} is the rotation variable varying from $\theta_{pt,i}$ to $\theta_{ec,i}$. N_c is the scaling exponent controlling the smoothness of the transition of excursion branch. The envelope curves represent gradual trends of strain hardening to the peak point of envelope curve and deterioration afterwards. Based on the test data calibration, N_c is related linearly with partial ductility ratio (μ_i) which can be given as the value of $1.6\mu_i$ in this study.



(a) First hysteresis loop under i th loading amplitude



(b) Repeated hysteresis loops under i th loading amplitude



(c) Hysteresis loop under $(i+1)$ th loading amplitude

Figure 7.10 Hysteretic moment-rotation model for the connection category I

Following the unloading segment to point $c_i^{<1>}$, no presence of negative moment is considered in the moment-rotation relationship. This is because the compression effect is primarily carried by the compression zone of the CFT column with limited contribution of deformed plate elements in bearing.

-Stage 2: The manners of reloading and unloading in the repeated cycles under i th loading amplitude are similar to those in the first cycle, but the degradation of strength and energy dissipation should be taken into account in the model. For this reason, the aforementioned degradation envelope curve is established as a contour of dropped peak points. Due to relatively strong CFT column in this connection category, a slight reduction of the initial loading stiffness can be assumed in Stage 2. As the repeated cycle continues, a family of dropped peak points can be presumed for the second, third, fourth...cycles. Basically, it is expected that the magnitude of strength degradation is increased with the increased number of cycles at each loading amplitude which corresponds to the drop of the peak point of hysteresis loops. To observe the locus of these points, more cycles at each loading amplitude are actually needed in the test loading history which is, however, beyond the scope of this study. Notwithstanding that, the trends of reduction of strength and energy dissipation during three cycles at each amplitude have been demonstrated in the test results as described in Chapter 4. For the purpose of simplicity, these dropped peak points are idealized to coincide with previous unloading segment at point $b_i^{<1>}(\theta_{ec,i}, \alpha_{sd}M_{ec,i})$ on the degradation envelope curve. α_{sd} is the strength degradation ratio as the fraction of the moment in the first cycle of each loading amplitude. By relating α_{sd} to μ_i , as shown in Figure 7.11 (a), a

power function based on the curve fitting of experimental data can be expressed as:

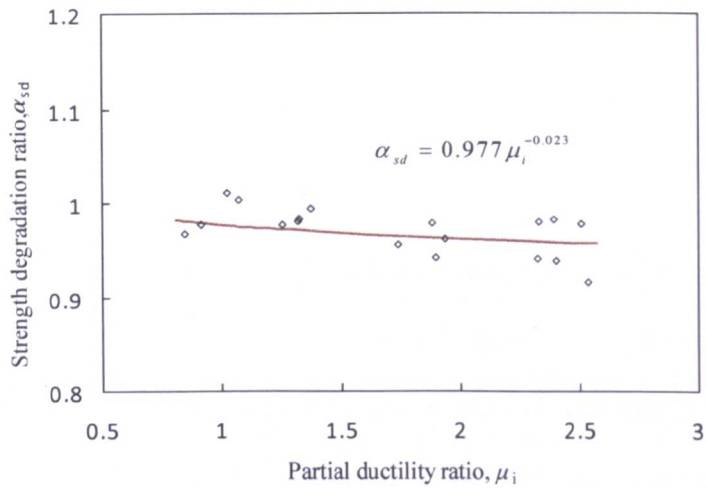
$$\alpha_{sd} = 0.977 \mu_i^{-0.023} \quad \text{Equation 7.9}$$

The energy dissipation degradation ratio, γ_{ed} , is also introduced as the fraction of the dissipated energy in the first cycle of a loading amplitude. Likewise, a simplification was used for the energy dissipation in the consecutive cycles. As illustrated in Figure 7.11 (b), a curve fitting using power functions can be written as:

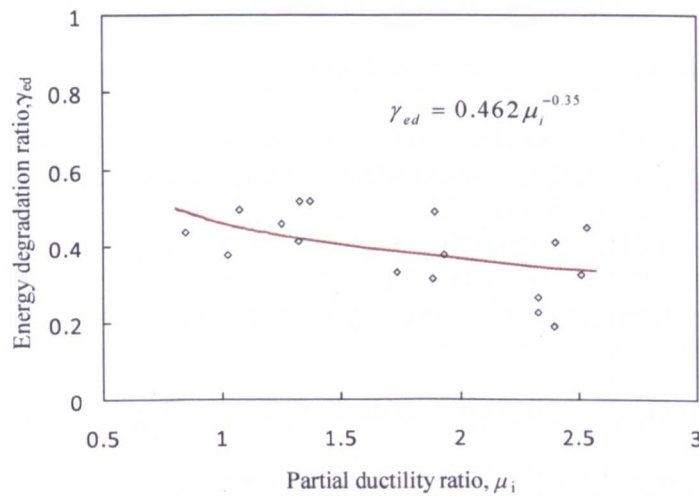
$$\gamma_{ed} = 0.462 \mu_i^{-0.35} \quad \text{Equation 7.10}$$

The parameters α_{sd} and γ_{ed} are calculated with the equations above each time when the reloading & unloading segments cross the degradation envelope curve and hysteretic loops corresponding to the repeated cycles are formed.

As shown in Figure 7.10 (b), the reloading in Stage 2 starts at point $c_i^{<2>}$ and continues up to point $d_i^{<2>}$. This segment ends when it intersects point $b_i^{<2>}$ at the degradation envelope curve. For the purpose of simplicity, point $b_i^{<2>}$ is assumed to be at the same location of point $b_i^{<1>}$ ($\theta_{ec,i}, \alpha_{sd} M_{ec,i}$). Afterwards, the unloading path subsequent to reloading is directed from point $b_i^{<2>}$ to $c_i^{<2>}$. The mathematical expressions for reloading and unloading segments of this stage are similar to the unloading segment for the first cycle under i th loading amplitude except the further consideration of degradations of strength and energy dissipation.



(a) Strength degradation ratio versus partial ductility ratio



(b) Energy degradation ratio versus partial ductility ratio

Figure 7.11 Strength degradation ratio and energy degradation ratio versus partial ductility ratio for the connection category I (Note: test data are obtained from related experiments)

The function for reloading segment c_i - d_i can be expressed in a power expression form of M_{rl} as:

$$M_{rl} = \alpha_{sd} M_{ec,i} \left(\frac{\eta_2 \theta_{fu} - \theta_{pt,i}}{\theta_{ec,i} - \theta_{pt,i}} \right)^{(N_c - \eta_1)} (1 + \eta_1 \gamma_{ed}) \quad \text{Equation 7.11}$$

And, the function unloading segment $b_i^{<2>} - c_i^{<2>}$ can be given by:

$$M_{ru} = \alpha_{sd} M_{ec,i} \left(\frac{\eta_2 \theta_{ru} - \theta_{pt,i}}{\theta_{ec,i} - \theta_{pt,i}} \right)^{(N_c + \eta_1)} (1 - \eta_1 \gamma_{ed}) \quad \text{Equation 7.12}$$

where, η_1 and η_2 are the test calibrated parameters. θ_{fu} and θ_{ru} are the rotation variables varying from point $c_i^{<2>}$ to point $d_i^{<2>}$ and the point $b_i^{<2>}$ to point $c_i^{<2>}$ respectively. The scaling exponents for both equations are controlled by N_c and η_1 .

-Stage 3: After unloading of n th cycle under i th loading amplitude, the reloading is directed towards a new cycle under $(i+1)$ th loading amplitude. As shown in Figure 7.10 (c), the segment from point $c_{i+1}^{<1>}$ to point $d_{i+1}^{<1>}$ follows the similar manner in Stage 2 which can be given by Equation 7.11. Prior to the arrival at point $a_{i+1}(\theta_{ec,i+1}, M_{ec,i+1})$ on the envelope curve, likewise, the intersection point at the degradation envelope curve is updated by point $b_{i+1}^{<1>}$.

7.4.2.2 Hysteretic model for connection category II

The hysteretic behaviour of the connections in category II are characterized not only by the plastic elongation of the bolt shank but also by the flexible deformation of tube face. It was felt that more complex contribution of CFT column to the hysteretic moment-rotation model of the connection should be taken into account in this case. The energy dissipation analysis in Chapter 4 indicates that the flexibility of the tube face may cause deteriorated confinement of CFT column which in turn produces greater concrete deterioration and decreases the moment capacity of the connection. On the

other hand, the tube connecting face as a plate element in flexible deformation improves the energy dissipation capacity of the connection when comparing with relatively independent tensile action of the bolt shank for the connection category I. This behaviour represents larger area enclosed by corresponding hysteresis loops. During the reversed loading, the deformed tube face in the tension zone of the connection will undergo compression thereby allowing certain extension of unloading branch of the hysteresis loop below the zero moment axis. Based on the observations from the test results, the hysteretic model for the connection category II was considered with appropriate mathematical expressions which differ from those for the connection category I.

According to the cyclic loading sequence, three stages are incorporated in the idealized hysteretic moment-rotation relations which are presented in a similar manner as in previous sub-Section shown in Figure 7.10. Stage 1 represents the first hysteresis loop under i th loading amplitude. Due to the damage of concrete infill, compressive deformation of the deformed tube face will occur in this stage. Stage 2 indicates that the strength and energy dissipation capacities of the connection reduce significantly during repeated cycles and subsequent to Stage 1. Finally, the hysteresis loops step forward to Stage 3 which relates to $(i+1)$ th loading amplitude. The hysteretic models for the connection category II are outlined below:

-*Stage 1:* The loading segment starting from point $e_i^{<1>}(0, M_{0,1})$ in this case is similar to that for the connection category I except the change of stiffness at point $g_i^{<1>}(\theta_{ec,i-1}, M_{t,i})$ (here called the turning point) with the same rotation as

the peak point on the basic envelope curve under $(i-1)$ th loading amplitude. Thereafter, the loading segment ends at point $a_i^{<1>}$ on the basic envelope curve, as shown in Figure 7.12 (a).

In order to account for the changing shape before and after the turning point $g_i^{<1>}$, an exponential function and a linear function were considered. The exponential function for the first nonlinear loading segment, $e_i^{<1>}-f_i^{<1>}-g_i^{<1>}$, can be expressed as:

$$M_{f1} = \frac{\chi_c (M_{ec,i} - M_{0,1}) \theta_{f1}}{\theta_{ec,i}} e^{\left(\frac{\theta_{f1}}{\theta_{ec,i-1}}\right) - 1} + M_{0,1} \quad \text{Equation 7.13}$$

The function for the second linear loading segment, $g_i^{<1>}-a_i^{<1>}$, can be given by:

$$M_{f2} = \frac{(M_{ec,i} - M_n)(\theta_{f2} - \theta_{ec,i-1})}{\theta_{ec,i} - \theta_{ec,i-1}} + M_n \quad \text{Equation 7.14}$$

where, χ_c is the test calibrated parameter. θ_{f1} and θ_{f2} are the rotation variables corresponding to the ranges from point $e_i^{<1>}$ to point $g_i^{<1>}$ (i.e., from 0 to $\theta_{ec,i-1}$) and from point $g_i^{<1>}$ to point $a_i^{<1>}$ (i.e., from $\theta_{ec,i-1}$ to $\theta_{ec,i}$) respectively. $M_{0,1}$ is the moment on zero rotation axis at the beginning of the loading path, which is known from the previous negative unloading excursion under $(i-1)$ th loading amplitude.

The segment $a_i^{<1>}-c_i^{<1>}$ represents the unloading path until the zero moment axis is reached. Likewise, the rotation ($\theta_{pt,i}$) at point $c_i^{<1>}$ can be regarded as the rotation produced by the residual or permanent deformation of the

connection. The segment from point $a_i^{<1>}$ to point $c_i^{<1>}$ can be expressed as the first part of unloading by a power expression in the form of $M_{un1,i}$ as:

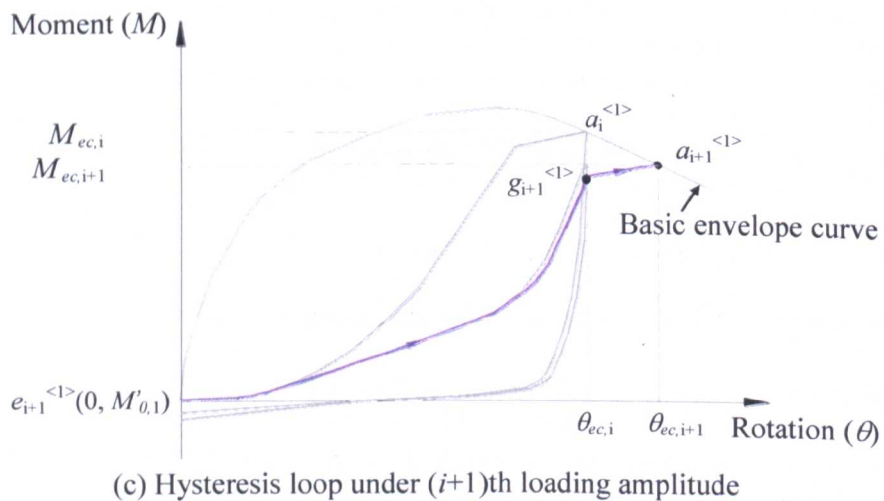
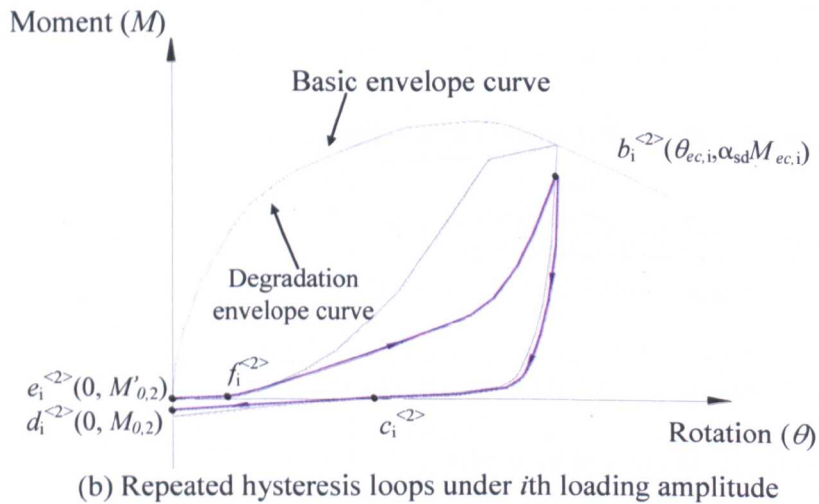
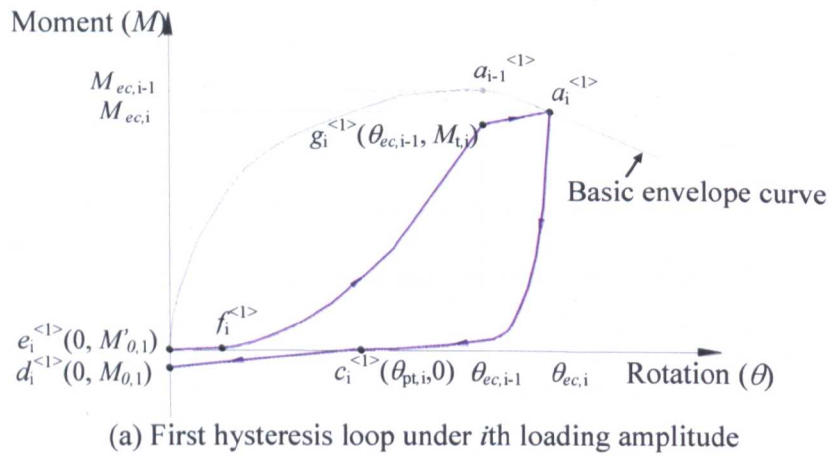


Figure 7.12 Hysteretic moment-rotation model for the connection category II

$$M_{un1,i} = \eta_3 M_{ec,i} \left(\frac{\theta_{un1,i} - \theta_{pr,i}}{\theta_{ec,i} - \theta_{pr,i}} \right)^{N_c} \quad \text{Equation 7.15}$$

where, η_3 is the test calibrated parameter. $\theta_{un1,i}$ is the rotation variable varying from $\theta_{pr,i}$ to $\theta_{ec,i}$. N_c is the scaling exponent which is the same as that defined in Equation 7.8.

The following unloading path is featured by a linear segment targeting at point $d_i^{<1>}$ on zero rotation axis. Based on the experimental data, Figure 7.13 shows the relation between the slope of this segment in first unloading path near the origin of the curve, $K_{0,i}$, and the partial ductility ratio, μ'_i . The linear trend line expression for the first cycle of each loading amplitude is given by:

$$K_{0,i} = -0.19 \mu'_i + 0.82 \quad \text{Equation 7.16}$$

in which, the variable range is given as: $1 \leq \mu'_i < 3.5$. Also, $\theta_{pr,i}$ instead of $\theta_{ec,i}$ is used in the calculation of μ'_i .

The moment, $M_{ul,i}$, for this linear segment can be expressed as:

$$M_{ul,i} = K_{0,i} (\theta_{ul,i} - \theta_{pr,i}) \quad \text{Equation 7.17}$$

where, $\theta_{ul,i}$ is the rotation variable varying from 0 to $\theta_{pr,i}$.

As the connection is subjected to reversed moment, i.e., the moment will develop in the negative excursion of moment-rotation relationship, it is assumed that the following cycles will join the points $e_i^{<1>}$ and $d_i^{<1>}$ on the zero rotation axis.

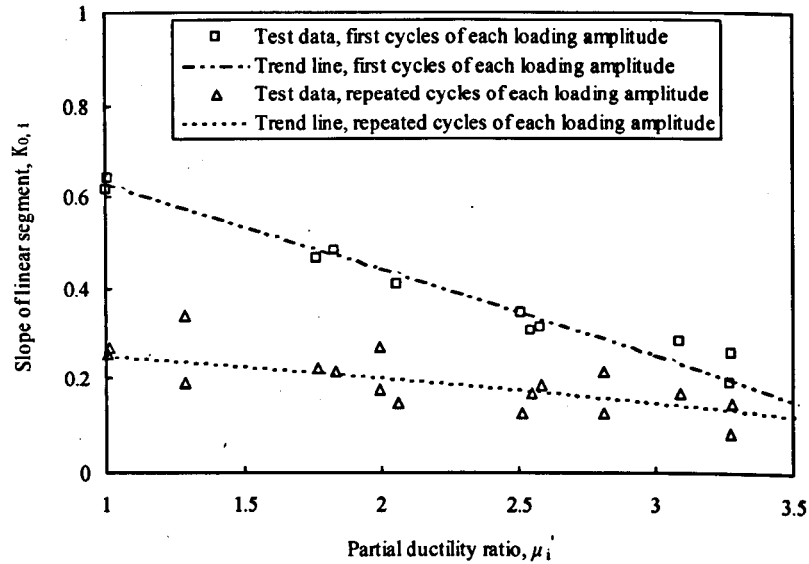


Figure 7.13 Relation between $K_{0,i}$ and μ'_i for the connection category II

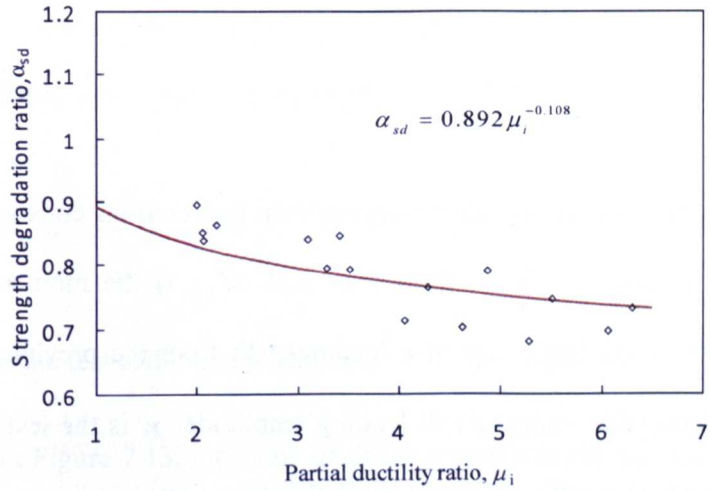
-Stage 2: On reloading in Stage 2, the drop of loading stiffness at the beginning of loading is significantly increased when compared with that for the connection category I. This can be attributed to the presence of more extensive concrete deterioration during the continuous loading. As shown in Figure 7.12 (b), the reloading segment ends when it reaches point $b_i^{<2>}$ on the degradation envelope curve. Similar to the definition in connection category I referring to Figure 7.10, the point $b_i^{<2>}$ in contrast to point $a_i^{<1>}$ has the same rotation as $\theta_{ec,i}$, but reduced moment as $\alpha_{sd}M_{ec,i}$. The relationship between α_{sd} and μ_i is shown in Figure 7.14 (a) and the counterpart equation can be expressed as:

$$\alpha_{sd} = 0.892 \mu_i^{-0.108} \quad \text{Equation 7.18}$$

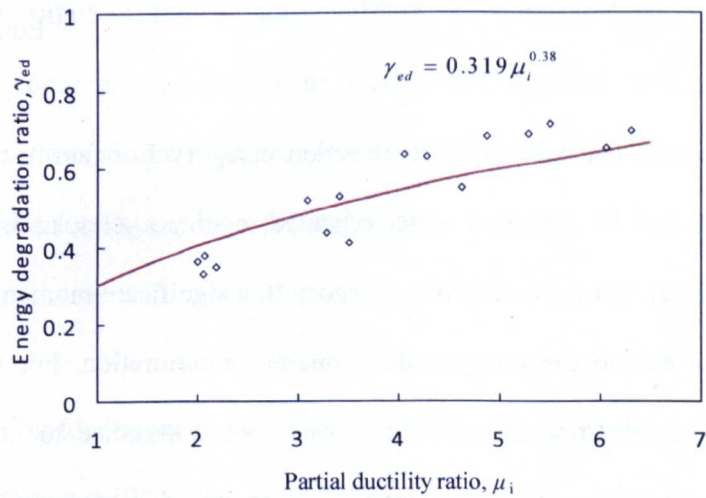
Likewise, the equation for the relationship between γ_{ed} and μ_i can be written as:

$$\gamma_{ed} = 0.319\mu_i^{0.38}$$

Equation 7.19



(a) Strength degradation ratio versus partial ductility ratio



(b) Energy degradation ratio versus partial ductility ratio

Figure 7.14 Strength degradation ratio and energy degradation ratio versus partial ductility ratio for the connection category II

As shown in Figure 7.12 (b), it is also noted that the area enclosed by the hysteresis loop in this case is to some extent limited by point b_1 which also determines the shape of the reloading segment.

The expression for the reloading segment $e_i \leftrightarrow -f_i \leftrightarrow -b_i$ can be formulated in exponential function including the strength degradation as:

$$M_{sl} = \frac{\chi_c (\alpha_{sd} M_{ec,i} - M'_{0,2}) \theta_{sl}}{\theta_{ec,i}} e^{\left(\frac{\theta_{sl}}{\theta_{ec,i}}\right)^{-1}} + M'_{0,2} \quad \text{Equation 7.20}$$

where, θ_{sl} is the rotation variables varying from the rotations corresponding to point e_i to point b_i (i.e., from 0 to $\theta_{ec,i}$). $M'_{0,2}$ is the moment on zero rotation axis at the beginning of a loading path from the previous negative unloading excursion under $(i-1)$ th loading amplitude. χ_c is the test calibrated parameters which can be expressed in relation to γ_{ed} as:

$$\gamma_{ed} = \frac{\chi_c}{1 + 0.5 \chi_c} \mu_i^{\chi_c} \quad \text{Equation 7.21}$$

As discussed in the case of the connection category I, a family of dropped peak points can be supposed under repeated loading cycles, as indicated in Figure 7.12 (b). For the connection category II, a significant moment reduction is expected due to the compounded concrete deterioration. For this study, however, the reloading and unloading paths were assumed to intersect the degradation envelope curve at point b_i . Although this assumption may not be consistent with the test results if more repeated cycles are considered, this simplification was adopted for simplicity in representing basic hysteresis loop. Notwithstanding that, more experimental works are needed to be able to provide test data for accurate expression of the locus of these points. Further development of the detailed paths for the case of repeated loading is a task for future work.

On unloading from the peak point $b_i^{<2>}$ (Figure 7.12b), the segment $b_i^{<2>-c_i^{<2>}$ has similar relation as that for Stage 1. The first part of unloading path is represented by a nonlinear segment; once the zero moment axis is reached (point $c_i^{<2>}$), the path is directed linearly to point $d_i^{<2>}$.

$$M_{un2,i} = \eta_4 \alpha_{sd} M_{ec,i} \left(\frac{\theta_{un2,i} - \theta_{pl,i}}{\theta_{ec,i} - \theta_{pl,i}} \right)^{N_4} \quad \text{Equation 7.22}$$

where, η_4 is the test calibrated parameter.

As shown in Figure 7.13, the slope of linear segment in the second unloading path, $c_i^{<2>-d_i^{<2>}$, is lower than that in the first unloading path, $c_i^{<1>-d_i^{<1>}$. This observation suggests the reduced stiffness of the connection as more substantial concrete crushing occur during the repeated loading thereby indicating further reduced moment capacity of the connection. The linear trend line expression for $K_{0,i}$ can be expressed as:

$$K_{0,i} = -0.05 \mu_i + 0.3 \quad \text{Equation 7.23}$$

The expression for the segment $c_i^{<2>-d_i^{<2>}$ can then be obtained by substituting $K_{0,i}$ into Equation 7.17.

-Stage 3: The loading path in Stage 3 is directed towards a new cycle under $(i+1)$ th loading amplitude. Figure 7.12 (c) shows a nonlinear segment and a linear segment incorporated in the path starting from point $e_{i+1}^{<1>}$ to point $a_{i+1}^{<1>}$. Since this loading path is similar with that in Stage 1, the expressions for both segments can be related to Equation 7.13 and Equation 7.14 respectively in which the input values of rotation and moment are updated

accordingly. Before the turning point at $g_{i+1}^{<1>}$, it is assumed that the loading path is similar to the last loading path under i th loading amplitude, especially when the steel components becomes the main source of deformability of the connection. By computing the equations presented above related to three stages, the overall hysteretic moment-rotation curve can be obtained.

7.5 Validation of proposed hysteretic moment-rotation model

The application of the analytical model described in sub-Section 7.4.2 to compare the test hysteretic moment-rotation curves is presented in this section. The numerical models for the specimens BBEC-8-8.8-50-LI (Test No.1) and BBEC-8-10.9-50-LI (Test No.2) were selected to feature the connection category I, while those for BBEC-5-8.8-50-LII (Test No.4) and BBEC-6.3-8.8-25-LII (Test No.6) were used to feature the connection category II.

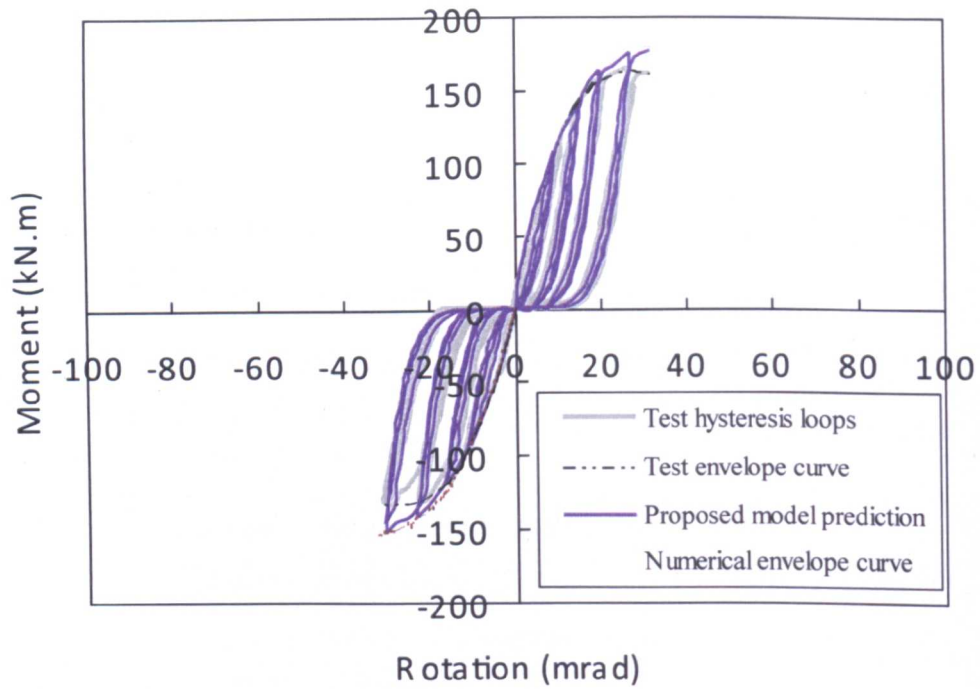
The numerical hysteretic moment-rotation relationships are developed starting from the envelope curves obtained from the calibrated finite element models indicated in Chapter 5. The proposed analytical model in this chapter may also be regarded as a further supplement for the finite element analyses in which the numerical moment-rotation envelope curves were compared with experimental curves (referring to sub-Section 6.3.4). However, it is noted that the curves predicted by finite element models for the connection category II are not able to allow for the descending branch. For this reason, the softening stiffness K_{sf} was accounted for based on the test calibration parameters α_{sf} for specimens of the connection category II, as listed in Table 7.2.

The overall hysteresis loops for the connection can be obtained by computing equations each time for foregoing three stages presented in Section 7.4. The points on the envelope curve were plotted with respect to the controlled displacement increment applied during the inelastic phase of the connection. The mathematical expressions for the nonlinear segments of the moment-rotation relationship were calculated using the test calibrated parameters indicated in Table 7.2.

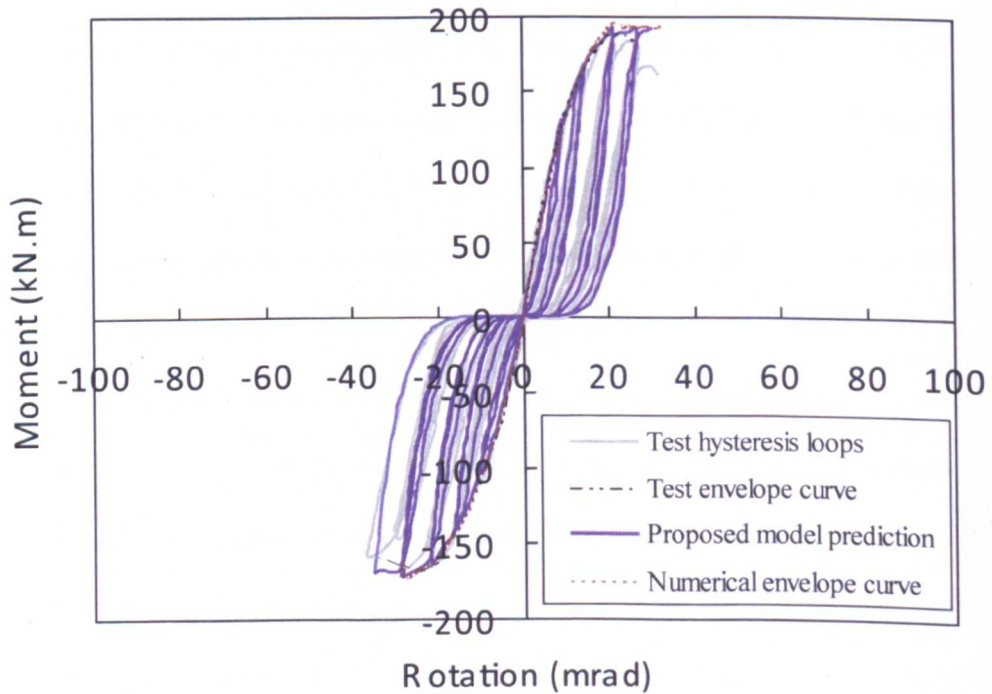
Table 7.2 Summary of test calibration parameters

Connection category		Test calibration parameters				
I	η_1	0.3				
	η_2	1.02				
II	η_3	1.0	$\alpha_{sf}(\text{Test No.4})$	-0.040	χ_c	0.20
	η_4	1.18	$\alpha_{sf}(\text{Test No.6})$	-0.046		

Figure 7.15 illustrates the test moment-rotation envelope curves and hysteresis loops for the specimens of the connection category I, superimposed with relevant results from numerical analysis and proposed model prediction. As can be seen graphically, the predicted hysteretic moment-rotation relationship from numerical analysis matches quite well with experimental curve except for a slight difference in the vicinity of peak point of the excursion. This discrepancy can be attributed to the difference in the envelope curves predicted by finite element model described in sub-Section 6.3.4. It also can be observed that the predicted hysteretic loops corresponding to the repeated cycles of each loading amplitude indicate a good correlation with the test curves.

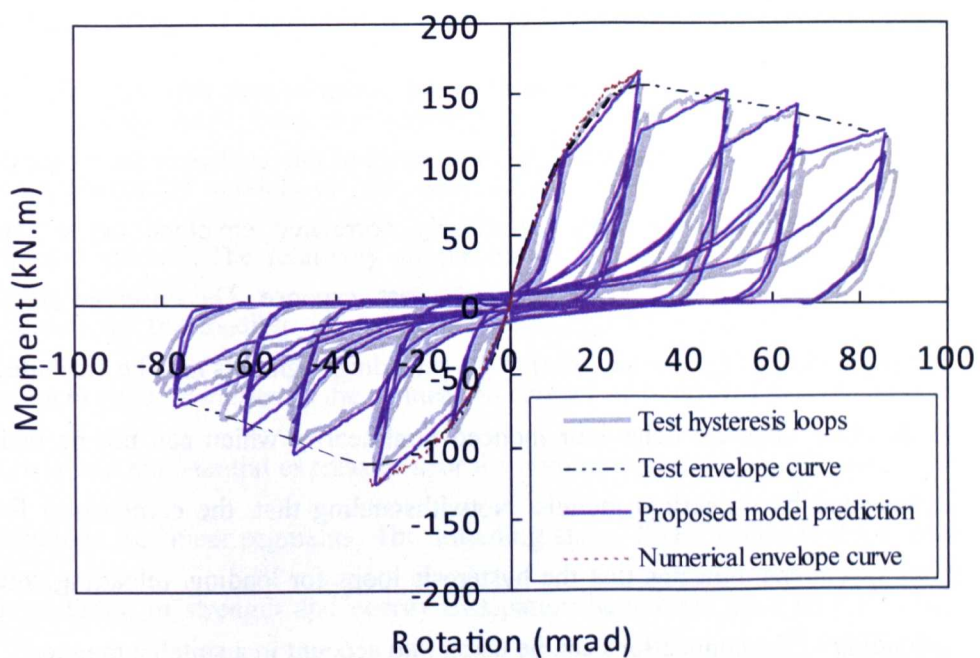


(a) Test specimen BBEC-8-8.8-50-LI

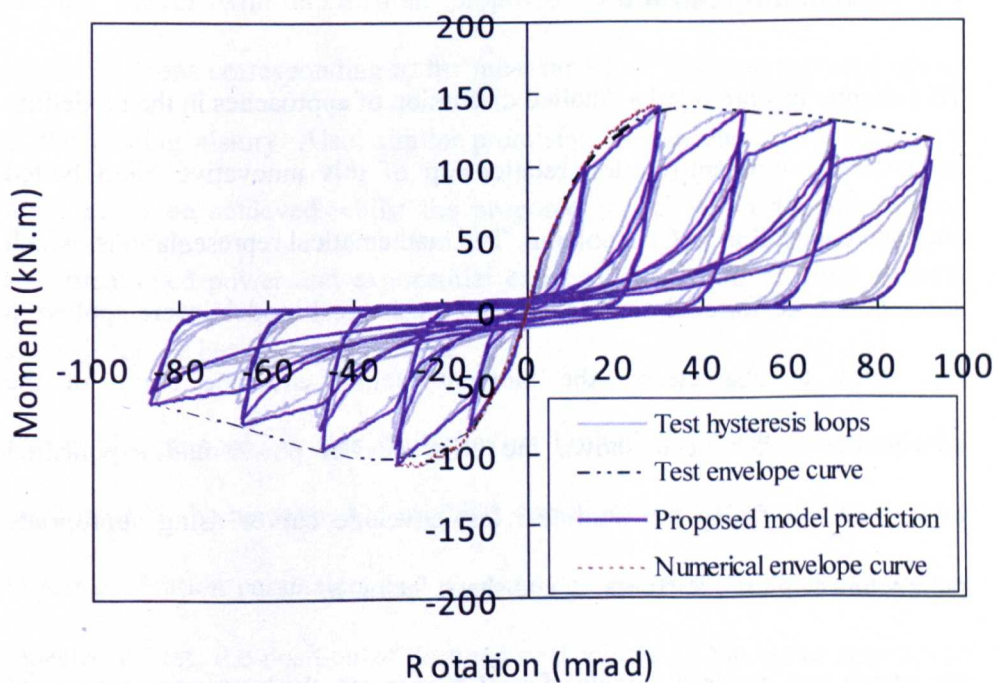


(b) Test specimen BBEC-8-10.9-50-LI

Figure 7.15 Hysteretic moment-rotation experimental and numerical curves for the connection category I



(a) Test specimen BBEC-5-8.8-50-LII



(b) Test specimen BBEC-6.3-8.8-25-LII

Figure 7.16 Hysteretic moment-rotation experimental and numerical curves for the connection category II

Figure 7.16 presents the test envelopes and hysteretic moment-rotation relationships for the specimens of the connection category II together with the analytical predictions of the proposed model. It can be seen that the analytical models yield good predictions of the most range of the test hysteretic moment-rotation relationship. In fact, the closely correlated envelope curve acts beneficially in the good prediction of the test response. The observed slight overestimation of the moment during the reloading segments may be attributed to the local concrete behaviour induced nonlinearity which can not be well represented by numerical models. Notwithstanding that, the comparison for both specimens indicates that the hysteresis loops for loading, reloading, and unloading of the connections can be taken into account in a suitable manner.

7.6 Concluding remarks

This chapter has provided a detailed discussion of approaches in the modelling of hysteretic moment-rotation relationship of this innovative blind bolted endplate connection to CFT column. The mathematical representations, which are widely used for analytical model and mechanical models, were applied in this study to characterize the moment-rotation envelope curve of the connection. It has been shown the efficiency of power and exponential expressions in fitting the nonlinear test envelope curves using appropriate parameters of plastic stiffness, k_p and shape factor, n .

By introducing material models of steel & concrete, the hysteretic response of the connection has been discussed from the viewpoint of constituent components. As the joint cyclic behaviour may be greatly influenced by the weakest component, the introduction of this part of understanding provided a

useful basis for the further analysis of the overall joint behaviour under cyclic loading.

More efforts have been concentrated on the development of hysteretic moment-rotation models on the basis of the envelope curves from finite element models. The relatively simple mathematical functions were used to characterize the loading, unloading and reloading segments of the hysteretic moment-rotation curves of the connection categories I and II. This contains the power and exponential expressions for the nonlinear segments while the linear functions for linear segments. The softening slope, linear segment slope, and degradation of strength and energy dissipation have been allowed for in the proposed models in relation to partial ductility ratios. A good correlation of the test curves with those from proposed model was presented for the hysteresis loops corresponding to the most ranges of first and repeated cycles of the loading history. Also, similar promising predictions of test hysteresis loops could be achieved whilst the proposed model was established using aforementioned power and exponential expressions instead of finite element analysis for the basic envelope curve.

The model proposed in this study has its limitations. Further experimental work needs to be performed to establish consistent methods in the evaluation of test calibration parameters ($\eta_1, \eta_2, \eta_3, \eta_4, \chi_c, \alpha_{sf}, K_{0,i}, \alpha_{sd}, \gamma_{ed}$). As for the repeated cycles, the position of dropped peak points of the curve was traced experimentally which can be used to feature the strength degradation. Due to limited numbers of repeated cycles under each loading amplitude in the ECCS loading procedure, the experimental study was not able to provide sufficient

data to determine the locus of these points. A more accurate prediction of this locus which incorporates stability limit may further improve the accuracy of the proposed model, especially for the hysteresis loops under repeated loading cycles.

CHAPTER 8

CONCLUSIONS AND FUTURE WORK

This thesis has presented the results of a series of full scale joint tests in which open section beams were connected to CFT columns through blind bolted endplates. The connector adopted for these connections is an innovative blind bolt called the Extended Hollobolt which is based on the Lindapter Hollobolt. This chapter summarizes the key findings of this research programme presented in this thesis. Recommendations and further work are outlined in Section 8.2.

8.1 Conclusions from current research programme

Based upon the experimental and analytical investigations conducted, the following conclusions and observations can be extracted from this research programme:

- The full-scale quasi-static cyclic loading tests have shown two representative failure modes: modes I and II. For failure mode I, the bolt shank fractured ultimately with limited CFT column face yielding. For failure mode II, the CFT column face deformed in moderate flexible manner with local damage of concrete infill and slight bolt pullout with likely local crack in the sleeves. The former failure mode is associated with the bolt as a relatively weak component; in contrast, the latter failure mode is referred to relatively strong bolt with tube face in flexible deformation and excessive concrete crushing. As such, the connections

were classified as two categories corresponding to the failure modes mentioned above. The material and geometric parameters, such as bolt grade, tube wall thickness and concrete grade, were shown in this study to have influence on the joint failure modes.

- The experimental observation demonstrated that this innovative blind bolt can be successfully applied in the bolted endplate connections to CFT column subjected to cyclic loads. The tests on the blind bolted connections have indicated that the additional anchorage part of the Extended Hollobolt remains almost intact during the cyclic loading which may provide stable improvement of strength and stiffness of the connection as long as the surrounded concrete maintains certain load carrying capacity. This observation also implies the merit of this blind bolted connection over some other blind bolts developed in Australia (i.e., the extensions welded to the Ajax One-side blind bolts) which posed undesired weld fracture under cyclic loading as reported in the literature.
- The moment-rotation curve presented certain nonlinear characteristics at very beginning of loading. The hysteresis loops for test specimens showed obvious pinching. The connections, which were subjected to loading procedures with varying displacement increments, demonstrated different shapes of hysteresis loops but almost enclosed by similar envelope curves.
- The connections failed in mode I (bolt shank fracture with limited CFT column face yielding) have less ductility than those in failure mode II, i.e. approximately 28-32 mrad and 86-92 mrad for connection categories I and II under negative loading respectively. Based on the ductility requirements suggested by Eurocode 8 for dissipative semi-rigid (and/or)

partial strength connections and ductility classification in accommodating plastic hinge rotation, it is concluded that test connections in category I can provide more than 25 mrad rotation required for the connections in frames of medium ductility class (DCM) with behaviour factor (q) greater than 2.0. On the other hand, the test connection in category II are more likely to have more than 35 mrad rotation required for the connections in frames of high ductility class (DCH).

- It was evident that the bolt grade, tube wall thickness and concrete grade have positive influences on the basic joint moment-rotation behaviours, which are represented by initial stiffness, yield rotation & moment, and maximum rotation & moment. For category II connections, the resistant ratio and full ductility ratio showed more significant drops than those for the connections of category I. As for energy dissipation, throughout all the loading progress the category I connection demonstrated a dramatic drop of energy dissipation ratio subsequent to the first cycle of each loading amplitude, which suggests greater reduction of energy dissipation capacity during the repeated cycles of each loading amplitude. In contrast, a similar trend was shown at the beginning of the inelastic cycles for the connections of category II, but this drop is reduced as the rotations increased.
- The damage indices incorporated into a cumulative damage model analysis have been found to provide an approximation of the damage progression of the connection. The energy based cumulative damage index was noticed to represent a more reasonable evaluation of the observed progressive damage process of the connections. By introducing

the general Park & Ang damage level classification, the hysteretic progress of the connection was further analysed in terms of damage stages which seemed to result in a good agreement with the test observations.

- 3D nonlinear finite element models that incorporate advanced modelling technique have been demonstrated to adequately predict the moment-rotation behaviour of this connection within the limitation of parameters chosen. The numerical predictions of bolt preload and strain distribution of connection components showed good agreement with test data for two connection categories. The stress distributions indicated that the bolt shank in failure mode I is the primary part to carry the tension loads with limited plasticity spreading on the tube walls. On the other hand, the stress distributions suggested the concrete strength and tube wall flexibility play an important role in failure mode II. Through a parameter variation analysis, a comparison and discussion is made for the moment-rotation envelope curves of a limited range of tube wall thickness and concrete strength. These results showed that by increasing the tube wall thickness from 5mm to 8mm, the negative moment capacity is enhanced by 38.2% for the connections with C25 concrete grade while by 22.4% and by 8.2% for the connections with concrete grades of C40 and C50 respectively.
- A hysteretic moment-rotation model, incorporating power and exponential expressions to define the loading, unloading and reloading segments of the hysteresis loops, has been developed. It has been shown that the softening slope, linear segment slope, and degradation of strength and energy dissipation can be allowed for by introducing test calibration parameters ($\eta_1, \eta_2, \eta_3, \eta_4, \chi_c, \alpha_{sf}, K_{0,i}, \alpha_{sd}, \gamma_{ed}$) in relation with partial

ductility ratio. The accuracy of the model has been demonstrated to be reasonable for specimens in the connection categories I and II.

- The conclusions of this study reported herein indicate that the objectives of this research have been satisfied primarily in terms of experimental study based evaluation, finite element modelling and hysteretic moment-rotation model study. The understanding of the progressive damage evolution of these Extended-Hollobolt endplate connections, which mainly relate to the blind bolt and CFT column, provides a basis for further evaluating a range of such connections subjected to cyclic loading. Moreover, incorporated with the contribution of beam endplate, the developed hysteretic model for the hysteretic moment-rotation response of the connection could be further applicable for the seismic performance assessment of steel frames, where the semi-rigid connections are constituent part of the dissipative system. Additionally, for this type of connection with over-strength beam and endplate the ductile performance could be improved whilst relatively thin tube wall and/or weak concrete infill (e.g. less than 6.3mm and/or C40 in this study) are used.

8.2 Recommendations and future work

The work conducted in this program is based on the full scale experimental investigation and finite element analysis of the joint performance. Some additional items are recommended to further develop the understanding of the hysteretic behaviour of this innovative blind bolted endplate connection to CFT columns.

- *Further investigation of the hysteretic moment-rotation response of the connection with varying anchorage condition of the blind bolts.* The connections studied in this research project were based on the blind bolts of the same geometric configuration with the bolt shank length of 150mm. If the blind bolts are perfectly anchored (i.e. capable of developing the full bolt tensile resistance), it is supposed that the bolt shank will ultimately fracture corresponding to the failure mode I. In this case, further improvement of bolt anchorage capacity has little effect on the further increasing the strength and ductility of the connection. Conversely, the reduction and gradual loss of anchorage may lead to some other components instead of the blind bolts to achieve ultimate capacity. This has already been demonstrated by the different failure modes of specimens BBEC-6.3-8.8-25-LII and BBEC-6.3-8.8-50-LII with the change of the failure mode when the bolt anchorage was weakened by reducing the strength of the concrete infill. More material and geometric parameters of the blind bolt and SHS section can be considered in the further study to improve the understanding of the cyclic behaviour of the connections, such as the bond condition between anchored bolt and concrete infill.
- *Additional tests with varying loading procedure.* An important area to consider is the consecutive failure mode of the connections under a given loading amplitude level. This failure mode is unique as it appears to be related to the normal ultimate capacity as well as low cycle fatigue of the connection components. Such observation was made in the tests of this study mainly for the specimens in failure mode II with significant strength

degradation during the repeated loading cycles. This evidence was considered in the proposed hysteretic moment-rotation models as indicated in Chapter 6, however, the ECCS procedure for the tests only allows three cycles (i.e., two repeated cycles following the first cycle) at each loading amplitude which provide very limited data for this part of study. It is therefore recommended to apply a modified loading procedure for future tests to reduce the numbers of the amplitude levels but incorporates more cycles at each amplitude. The test using the suggested modified procedure may clarify the locus of decreased peak points referring to the repeated loading cycles which will in turn lead to a greater understanding and improvement of the proposed hysteretic models.

- *Further full scale joint testing.* The endplate thickness in the study was adopted as 25mm to exclude the endplate flexure for all test specimens. If thinner endplate is used, subsequent reference to Eurocode 3 can be taken in normal joint design to determine the flexure strength and stiffness of the endplate in relation with the component method as indicated in Figure 7.8. On the other hand, the endplate flexure will be added as a dissipative component into the joint hysteretic moment-rotation behaviour. A counterpart experimental study is needed to provide some insights of the improvement of energy dissipation capacity of such joint configuration. A further test programme can also be extended to the more complex issues of cruciform blind bolted connections and composite connections with concrete slabs. These issues have been investigated in the literature for the connections with open section beams welded to tubular columns. The introduction of this innovative blind bolt into those connections will

provide useful data for its further application in the steelwork frame system. Based on such future test data, further development of the joint hysteretic models would also be required for the joint configurations mentioned above.

- *Application of numerical modelling.* The tensile behaviour of this innovative blind bolt was previously determined numerically based on the T-stub assembly model before the starting of this research programme. It demonstrated the good application of finite element model as a cost effective way of investigating the load transfer mechanism and related joint response based on a parametric study. In contrast, the computational cost and convergence problem were highlighted for the joint model in the finite element analysis due to the consideration of complicated joint configuration as well as the incorporation of concrete model. For this reason, the finite element models would also be restricted for small range parametric study especially when some more components were introduced into this connection system. It is therefore recommended that a further development of the finite element models using improved material models and advanced modelling techniques so as to accurately simulate the moment-rotation hysteresis loops of the connection in a more efficient manner.

REFERENCES

1. American Institute of Steel Construction Inc. (AISC), 2005: Steel Construction Manual. 13 Edition, AISC, Chicago, US
2. Tsai KC, Weng YT, LIN ML., Pseudo dynamic tests of a full-scale CFT/BRB composite frame: displacement based seismic design and response evaluations. In: Proceeding of the International Workshop on Steel and Concrete Composite Constructions, Taiwan, 2003: 165-176
3. Tabsh SW, Mourad S., Resistance factors for blind bolts in direct tension. Engineering Structures, Vol.12(19), 1997: 995-1000
4. SHS Jointing. Corus Tubes library publication online. 14 Jun 06, [cite 10 Jun 2009]. Available from:
http://www.corusgroup.com/file_source/StaticFiles/Business_Units/Corus_Tubes/CT46-SHS%20Jointing%2014-06-06.pdf
5. Design Guide for SHS Concrete Filled Columns. Corus Tubes library, 11 Apr 05, publication online [cite 10 Jun 2009]. Available from:
http://www.corusgroup.com/file_source/StaticFiles/Business%20Units/Corus%20Tubes/CT26-Design%20Guide%20for%20SHS%20CFC%2011-04-05.pdf
6. Huck BOM, Alcoa Fastening systems, 2007, publication online [cite 12 July 2009]. Available from:
http://www.alcoa.com/com_transport/en/products/product.asp?country_id=999&market_id=30&market_cat_id=379&cat_id=557&prod_id=884
7. Flowdrill & Hollo-Bolt. Corus Tubes library publication online. 13 Feb 2003, [cite 10 Jun 2009]. Available from:
http://www.corusgroup.com/file_source/StaticFiles/Business%20Units/Corus%20Tubes/TD384-Flowdrill%20&%20Hollo-Bolt%2013-02-03.pdf
8. Type HB Hollo-Bolt, Lindapter, 2008. Download online, exact date unknown, publication online [cite 10 Jun 2009]. Available from:
http://www.lindapter.com/Products/Cavity_Fixings/2/Type_HB_Hollo-Bolt.pdf
9. One side structural fastener, AJAX Engineered Fasteners, 1999, publication online [cite 12 July 2009]. Available from:

References

- <http://www.ajaxfast.com.au/index.asp?d=5A4C5A717251477C70080F080108>
10. Kurobane Y, Packer JA, Wardenier J, Yeomans N., Design Guide for Structural Hollow Section Column Connections. CIDECT and Verlag TÜV Rheinland GmbH, Köln, Germany, 2004.
 11. Ghobarah A, Mourad S, Korol RM., Behaviour of blind bolted moment connection for HSS columns. Tubular Structures V, Proceedings of the Fifth International Symposium, Nottingham, UK, 1993: 125-132.
 12. Mazzolani FM., Moment resistant connections of steel frames in seismic areas. E&FN SPON Press. 2000: 95-96
 13. CEN, Eurocode 8, prEN-1993-1-8, Part 8: General rules, seismic actions and rules for buildings Eurocode 8: Design of structures for earthquake resistance. Stage 49 draft, CEN, European Committee for Standardization, Brussels, Belgium, 2003
 14. American Institute of Steel Construction (AISC). Seismic provisions for structural steel buildings. American Institute of Steel Construction, Chicago, 2005
 15. Dubina D, Stratan A., Behaviour of welded connections of moment resisting beam-to-column joints. Engineering Structures, 24(11), 2002: 1431-1440
 16. SAC, 1997. Protocol for fabrication, Inspection, testing and documentation of beam-column connection tests and other experimental specimens. report No. SAC/BC-97/02, SAC Joint Venture
 17. Mahina S, Malleyb J, Hamburgerc R., Overview of the FEMA/SAC program for reduction of earthquake hazards in steel moment frame structures. Journal of Constructional Steel Research, 58(5), 2002: 511-528
 18. Joints in Steel Construction: Simple Connections, The Steel Construction Institute & The British Constructional Steelwork Association Limited, 2005
 19. Arthur GA., Investigation of the failure mechanism and moment capacity prediction in a ten bolt flush end plate moment connection. University of Akron, USA, in partial fulfillment of the requirements for Master of Science degree. 2010

References

20. Lee J, Goldsworthy HM, Gad EF., Blind bolt T-stub connections to unfilled hollow section columns in low rise structures. *Journal of Constructional Steel Research*, 66(8-9), 2010: 981-992
21. Al-Mughairi A, Tizani W, Owen J., Connection to Concrete Filled Hollow Section using Extended Hollobolt (Moment Connection Tests). *Proceedings of the 9th International Conference on Steel Concrete Composite and Hybrid Structures*. Leeds, UK. 2009: 599-604
22. Al-Mughairi A., The behaviour of moment resisting connection to concrete filled hollow sections using extended hollobolts. University of Nottingham, United Kingdom, in partial fulfillment of the requirements for Ph.D. degree. 2009
23. Jaspart JP, Steenhuis M, Weinand K., The stiffness model of revised Annex J of Eurocode 3. In: *Proceedings of 3rd international workshop on connection in steel structure*, Pergamon, 1995: 115-26
24. Simoes da Silva L, Calado L, Simoes R, Girao Coelho A., Evaluation of Ductility in Steel and Composite Beam-to-Column Joints: Analytical Evaluation. In: Leon R, Easterling WS, editors. *Connections in steel structures IV. Proceedings of the Fourth International Workshop on Connections*, Roanoke, VA, USA, October 22-25. 2000: 223-233
25. Faella C, Piluso V, Rizzano G., *Structural steel semirigid connections: theory, design and software*. CRC Press, 2000
26. Adey BT, Grondin GY, Cheng JJR., Cyclic loading of end plate moment connections. *Canadian Journal of Civil Engineering*, 4(27), 2000: 683-701
27. Zoetemeijer P., A design method for the tension side of statically loaded bolted beam-to-column connections. *Heron*, 20(1), 1974:1-59
28. Agerskov H., High-strength bolted connections subject to prying. *Journal of Structural Engineering*, ASCE, 102(ST1), 1976: 162-75
29. Yee YL, Melchers RE., Moment-rotation curves for bolted connections. *Journal of Structural Engineering*, ASCE, 112(3), 1986: 615-635
30. Jaspart JP, Steenhuis M, Weinand K., The stiffness model of Revised Annex J of Eurocode 3. *Proc., 3rd Int. Workshop on Connection in Steel Struct.*, Pergamon 1995: 115-126

References

31. Shi YJ, Chan SL, Wong YL., Modeling for moment-rotation characteristics for end- plate connections. *Journal of Structural Engineering*, ASCE, 122(11), 1996: 1300-1306
32. prEN 1993-1-8: 2005. Eurocode 3: Design of Steel Structures, Part 1.8: Design of joints, European Standard, CEN, Brussels, 2005
33. Barnett TC., The behaviour of a blind bolt for moment resisting connections in hollow steel sections. University of Nottingham, United Kingdom, in partial fulfillment of the requirements for Ph.D degree, 2001
34. Tanaka T, Tabuchi M., Experimental study on endplate to SHS column connections reinforced by increasing wall thickness with one site bolts. *Tubular Structures VII*, Farkas & Jamai(eds), Balkema, Rotterdam. 1996: 253-260
35. Lee J, Goldsworthy HM, Gad EF., Blind bolted T-stub connections to unfilled hollow section columns in low rise structures. *Journal of Constructional Steel Research*, 66(8-9), 2010: 981-92.
36. France JE, Davison JB, Kirby PA., Strength and rotational stiffness of simple connections to tubular connections using flowdrill connector. *Journal of Constructional Steel Research*, 50(1), 1999: 1-14
37. France JE, Davison JB, Kirby PA., Strength and rotational stiffness of endplate connections to concrete filled tubular columns with flowdrilled connectors. *Journal of Constructional Steel Research*, 50(1), 1999: 15-34
38. France JE, Davison JB, Kirby PA., Strength and rotational response of moment connections to tubular columns using flowdrill connectors. *Journal of Constructional Steel Research*, 50(1), 1999: 35-48
39. Tizani W, Ridley-Ellis D., The performance of a new blind bolt for moment-resisting connections. In: Jaurrieta MA, Alonso A, Chica JA., eds. *Proceedings of the 10th International Symposium on Tubular Structures: Tubular Structures X*, Madrid, Spain, Rotterdam, A.A. Balkema, 2003: 395-401
40. Ellison S, Tizani W., Behaviour of blind bolted connections to concrete filled hollow sections. *The Structural Engineer*, November, 2004: 16-17

References

41. Schneider SP, Alostaz YM., Experimental behavior of connections to concrete-filled steel tubes. *Journal of Constructional Steel Research*, 45(3), 1998: 321-352
42. Goldsworthy H, Gardner AP., Feasibility study for blindbolted connections to concrete-filled circular steel tubular columns. *Structural Engineering and Mechanics*, 24(4), 2006: 463-478
43. Gardner AP, Goldsworthy HM., Experimental investigation of the stiffness of critical components in a moment-resisting composite connection. *Journal of Constructional Steel Research*, 61(5), 2005: 709-726
44. Ghobarah A, Mourad S, Korol RM., Behaviour of blind bolted moment connection for HSS columns. *Tubular Structures V, Proceedings of the Fifth International Symposium, Nottingham, UK, 1993: 125-132*
45. Korol RM, Ghobarah A, Mourad S., Blind bolting W-shape beams to HSS columns. *Journal of Structural Engineering, ASCE*, 119(12), 1993: 3463-3481
46. Harada Y, Arakaki T, Morita K., Structural behaviour of RHS column-to-H beam connection with high strength bolts. *International Journal of Steel Structures*, 2, 2002: 111-121
47. Loh HY, Uy B, Bradford MA., The effects of partial shear connection in composite flush end plate joints Part I-experimental study. *Journal of Constructional Steel Research*, 62(4), 2006: 378-390
48. Loh HY, Uy B, Bradford MA., The effects of partial shear connection in composite flush end plate joints Part II-Analytical study and design appraisal. *Journal of Constructional Steel Research*, 62(4), 2006: 391-412
49. Wang JF, Han LH, Uy B., Behaviour of flush end plate joints to concrete-filled steel tubular columns. *Journal of Constructional Steel Research*, 65(8-9), 2009: 1644-1663.
50. Elghazouli AY, Málaga-Chuquitaype C, Castro JM, Orton AH., Experimental monotonic and cyclic behaviour of blind-bolted angle connections. *Engineering Structures*, 31(11), 2009: 2540-2533
51. Lee J, Goldsworthy HM, Gad EF., Blind bolted moment connection to unfilled hollow section columns using extended T-stub with back face support. *Engineering Structures*, 33(5), 2011: 1710-1722

References

52. Nethercot DA, Davison JB, Kirby PA., Connection flexibility and beam design in non-sway frames. *Journal of Structural Engineering, ASCE*, 3(25), 1988: 99-108
53. Korol RM, Ghobarah A, Osman A., Extended endplate connections under cyclic loading: Behaviour and design. *Journal of Constructional Steel Research*, 16(4), 1990: 253-279
54. Ghobarah A, Osman A, Korol RM., Behavior of extended endplate connections under cyclic loading. *Engineering Structures*, 12(1), 1990: 1-27
55. Tsai KC, Popov EP., Cyclic behavior of endplate moment connections. *Journal of Structural Engineering*, 116(11), 1990: 2917-2930
56. Mourad S, Ghobarah A, Korol RM., Dynamic response of hollow section frames with bolted moment connections. *Engineering Structures*, 10(17), 1995: 737-748
57. Dunai I, Fukumoto Y., Behaviour of steel-to-concrete connections under combined axial force and cyclic bending. *Journal of Constructional Steel Research*, 36(2), 1996: 121-147
58. Bernuzzi C, Zandonini R, Zanon P., Experimental analysis and modelling of semi-rigid steel joints under cyclic reversal loading. *Journal of Constructional Steel Research*, 38(2), 1996: 95-123
59. Adey BT, Grondin GY, Cheng JJR., Cyclic loading of end plate moment connections. *Canadian Journal of Civil Engineering*, 4(27), 2000: 683-701
60. Yorgun C, Bayramoglu G., Cyclic tests for welded-plate sections with end-plate connections. *Journal of Constructional Steel Research*, 57(12), 2001: 1309-1320
61. Simões R, Silva LS., Cyclic behaviour of end-plate beam-to-column composite joints. *Steel and Composite Structures*, 1(3), 2001: 355-376
62. Dubina D, Ciutina A, Stratan A., Cyclic tests of double-sided beam-to-column joints. *Journal of Structural Engineering, ASCE*, 127(2), 2001: 129-136
63. Sumner EA, Murray TM., Behavior of extended end-plate moment connections subject to cyclic loading. *Journal of Structural Engineering, ASCE*, 128(4), 2002: 501-508

References

64. Grecea D, Stratan A, Ciutina A, Dubina D., Rotation capacity of MR beam-to-column joints under cyclic loading. In: *Connections in Steel Structures V - Amsterdam - June 3-4, 2004*: 141-154
65. Kovács N, Calado L, Dunai L., Behaviour of bolted composite joints: experimental study. *Journal of Constructional Steel Research*, 60, 2004: 725-738
66. Nogueiro P., Simões da Silva L, Bento R, Simões R., Experimental behaviour of standardised European end-plate beam-to-column steel joints under arbitrary cyclic loading. *International Colloquium of Stability and Ductility of Steel Structures, Lisbon, Portugal, 2006(6-6-8)*
67. Shi G, Shi Y, Wang Y., Behaviour of end-plate moment connections under earthquake loading. *Engineering Structures*, Vol. 29, No. 1, 2007: 703-716
68. Wang JF, Han LH., Hysteretic behaviour of flush end plate joints to concrete-filled steel tubular columns. *Journal of Constructional Steel Research (2009)*, 65(8-9), 2009: 1644-1663
69. Mirza O, Uy B., Behaviour of composite beam-column flush end-plate connections subjected to low-probability, high-consequence loading. *Engineering Structures*, 33(2), 2011: 647-662
70. Calado L, Castiglioni CA., Low cycle fatigue testing of semi-rigid beam-to-column connections. *Connections in Steel Structures III*, edited by Bjorhovde, Colson and Zandonini, Pergamon, New York, 1995: 371 -380
71. Ballio G, Calado L, Castiglioni CA., Low cycle fatigue behaviour of structural steel members and connections. *Fatigue and Fracture of Engineering Materials and Structures*, 20(8), 1997: 1129-1146
72. Bernuzzi C, Calado L, Castiglioni CA., Ductility and load carrying capacity prediction of steel beam-to-column connections under cyclic reversal loading. *Journal of Earthquake Engineering*, 1(2), 1997: 401-432
73. Plumier A, Agatino MR, Castellani A, Castiglioni CA, Chesi C., Resistance of steel connections to low-cycle fatigue. *Proceeding of 11th European Conference on Earthquake Engineering*, 1998: 317-335

74. Krawinkler H., Loading histories for cyclic tests in support of performance assessment of structural components. The 3rd International Conference on Advances in Experimental Structural Engineering, San Francisco, 2009
75. BS 5950-1: 2000. Structural use of steelwork in building Part 1: Code of practice for design - Rolled and welded sections. 2000
76. BS EN 10210-2:1997. Hot finished structural hollow sections of non-alloy and fine grain structural steels. Tolerances, dimensions and sectional properties. 1997
77. BS 4-1:1993. Structural steel sections Part 1: specification for hot-rolled sections. 1993
78. ECCS. Technical Committee 1-structural safety and loadings-technical working group 1.3-seismic design, recommended testing procedure for assessing the behaviour of structural steel elements under cyclic loads, 1986
79. EN 10002-1, Metallic materials - Tensile testing, Part 1: Method of test at ambient temperature. London: British Standards Institution, 2001
80. EN ISO 898-1, Mechanical properties of fasteners made of carbon steel and alloy steel - Part 1: Bolts, screws and studs (ISO 898-1:1999)
81. Hicks SJ, Newman GM, Edwards M, Orton A., Design manual for SHS concrete filled columns. British Steel Tubes & Pipes, 2002
82. Ryan JC., Evaluation of extended end-plate moment connections under seismic loading. Virginia Polytechnic Institute and State University, USA, in partial fulfilment of the requirements for Master of Science degree, 1999
83. Kovács N, Calado L, Dunai L., Experimental and analytical studies on the cyclic behaviour of end-plate joints of composite structural elements. *Journal of Constructional Steel Research*, 64(2), 2008: 202-213
84. Guidelines for Cyclic Testing of Components of Steel Structures, ATC Applied Technology Council, ATC-24, 1992
85. FEMA 356, Prestandard and Commentary for the Seismic Rehabilitation of Buildings, Federal Emergency Management Agency, November 2000

References

86. Han LH, Yang YF., Cyclic Performance of Concrete-Filled Steel CHS Columns under Flexural Loading. *Journal of Constructional Steel Research*, 61(4), 2005: 423-452
87. Shannag MJ, Abu-Dyya N, Abu-Farsakh G., Lateral load response of high performance fibre reinforced concrete beam-column joints. *Journal of Construction and Building Materials*, 2005(19): 500-508
88. Park HG, Kwack JH, Jeon SW, Kim WK, Choi IR., Frame steel plate wall behavior under cyclic lateral loading. *Journal of Structural Engineering*, ASCE, 133(3), 2007: 378-388
89. Deierlein GG, Reinhorn AM, Willford MR., Nonlinear structural analysis for seismic design-A guide for practicing engineers, National Institute of Standards and Technology (NIST), U.S Department of Commerce, 2010
90. Bose B, Hughes AF., Verifying the performance of standard ductile connections for semi-continuous steel frames. *Proceedings of the Institution of Civil Engineers, Structures and Buildings*, 110, 1995: 441-457.
91. Thomson AW, Broderick BM., Earthquake resistance of flush end-plate steel joints for moment frames. *Proceedings of the Institution of Civil Engineers Structures & Buildings*, 152, Issue 2, 2002: 157-165.
92. Fardis M, Carvalho A, Elnashai A, Faccioli E, Pinto P, Plumier A., Designers Guide to EN 1998-1 and EN 1998-5, Designers Guide to EN 1998-1 and EN 1998-5. Eurocode 8: Design of Structures for Earthquake Resistance. General Rules, Seismic Action and Rules for Buildings, Foundations and Retaining Structures. 2005.
93. Powell GH, Allahabadi R., Seismic damage prediction by deterministic methods: Concepts and procedures, *Earthquake Engineering & Structural Dynamics*. 16(5), 1988: 719-734.
94. Castiglioni CA, Pucinotti., Failure criteria and cumulative damage models for steel components under cyclic loading. *Journal of Constructional Steel Research*. 65(4), 2009: 751-765.
95. Cosenza E, Manfredi G., Ramasco R., The use of damage functionals in earthquake engineering: a comparison between different methods. *Earthquake Engineering & Structural Dynamics*. 22(10), 1993: 855-868.

References

96. Cosenza E, Manfredi G., Damage indices and damage measures. *Progress in Structural Engineering and Materials*, 2(1), 2000: 50-59
97. Williams MS, Sexsmith RG., Seismic Damage Indices for Concrete Structures: A State of the Art Review. *Earthquake Spectra*, 11(2), 1995: 319-349
98. Miner MA., Cumulative damage in fatigue. *Journal of Applied Mechanics*, 12(3), 1945: 159-164.
99. Ballio G, Castiglioni CA., Unified approach for the design of steel structures under low and high cycle fatigue. *Journal of Constructional Steel Research*. 34(1), 1995: 75-101.
100. Krawinkler H, Zohrei M., Cumulative damage in steel structures subjected to earthquake ground motions. *Computers and Structures*. 16(1-4), 1982: 531-541
101. Stephens JE, Yao JTP., Damage assessment using response measurements. *Journal of Structural Engineering, American Society of Civil Engineers*, 113(4), 1987: 787-801
102. Banon H, Biggs JM, Irvine HM., Seismic damage in reinforced concrete frames. *Journal of Structural Engineering, American Society of Civil Engineers*, 107(9), 1981: 1713-1729
103. Banon H, Veneziano D., Seismic safety of reinforced concrete members and structures. *Earthquake Engineering & Structural Dynamics*. 10(2), 1982: 179-193
104. Darwin D, Nmai CK., Energy dissipation in RC beams under cyclic load. *Journal of Structural Engineering, American Society of Civil Engineers*, 112(8), 1986: 1829-1846
105. Kraetzig WB, Meyer IF, Meskouris K., Damage evolution in reinforced concrete members under cyclic loading. *Proceedings of ICOSSAR 89, the 5th International Conference on Structural Safety and Reliability, Part I, August 7, 1989 - August 11, 1989: 795-802*
106. Park YJ, Ang AHS, Wen YK., Seismic damage analysis of reinforced concrete buildings. *Journal of Structural Engineering, American Society of Civil Engineers*, 111(4), 1985: 740-757

References

107. Kumar S, Usami T., An evolutionary-degrading hysteretic model for thin-walled steel structures. *Engineering Structures*, 18(7), 1996: 504-514
108. Altoontash A., Simulation and damage models for performance assessment of reinforced concrete beam-column joints. Stanford University, United States, in partial fulfilment of the requirements for Ph.D. degree. 2005
109. Palazzo B, Petti L, De Iuliis M., Reduction factors for performance based seismic design of structures. *Proceedings of the 13th World Conference on Earthquake Engineering*, 2004: 2286
110. Amziane S, Dubé JF., Global RC structural damage index based on the assessment of local material damage. *Journal of Advanced Concrete Technology*, 6(3), 2008: 459-468
111. ANSYS@Academic Research, Release 12.1, Help System, Structural Analysis Guide, ANSYS, Inc., 2009.
112. ANSYS Parametric Design Language Guide, ANSYS, Inc., Canonsburg, PA, 2009
113. Zienkiewicz OC, Taylor RL., *The finite element method for solid and structural mechanics*. Elsevier Ltd. 2006
114. Kazimi SMA., *Solid Mechanics*. Tata McGraw-Hill. 1982
115. Chen WF, Han DJ., *Plasticity for structural engineering*. Springer-Verlag Publications, New York. 1988
116. Chen WF, Saleeb AF., *Constitutive equations for engineering materials-elasticity and modelling*. Elsevier Ltd. 1994
117. Singh PN, Jha PK., *Mechanics of Solids*. John Wiley & Sons Inc. 1981
118. Lubliner J, Oliver J, Oller S, Onate E., A plastic-damage model for concrete. *International Journal of Solids and Structures*, 25(3), 1989: 299-326
119. Chen WF., *Plasticity in Reinforced Concrete*. McGraw-Hill, New York, 1982
120. William KJ, Warnke EP., Constitutive models for the triaxial behaviour of concrete. *Proceedings of the International Association for Bridge and Structural Engineering*, 19, 1975: 1-30

References

121. Dowling NE., Mechanical behaviour of materials, engineering methods for deformation, fracture, and fatigue. New Jersey: Pearson Education, Inc., 2007
122. Hollofast and Hollobolt, Lindapter International, UK, 1995.
124. Pike D., Manual for the design of concrete building structures to Eurocode 2. Institution of Structural Engineers, 2006
125. BS EN 1992, Eurocode 2: Design of concrete structures, Part 1-1- General rules and rules for buildings. BSI, 1999.
126. Vasdravellis G, Valente M, Castiglioni CA., Behavior of exterior partial-strength composite beam-to-column connections: Experimental study and numerical simulations. *Journal of constructional steel research*, 65(1), 2009: 23-35
127. Kovács N, Dunai L, Calado L., Prediction of the cyclic behaviour of moment resistant beam-to-column joints of composite structural elements. *SDSS'Rio 2010 stability and ductility of steel structures*, Rio de Janeiro, Brazil, September 8-10, 2010
128. DO Carmo M., Differential Geometry of Curves and Surfaces. Prentice-Hall, 1976
129. Girao Coelho AM, Simoes Da Silva L, Bijlaard F., Characterization of the nonlinear behaviour of single bolted T-stub connections. *Proceedings of the 5th International Workshop on connections, Connections in Steel Structures, Behaviour, strength and design*, Amsterdam, Netherlands, 2004
130. Bursi OS, Jaspart JP., Benchmarks for finite element modelling of bolted steel connections. *Journal of Constructional Steel Research*, 43(1-3), 1997: 17-42
131. de Borst R, Remmers JJC, Needleman A, Abellan M-A., Discrete vs smeared crack models for concrete fracture: bridging the gap. *International Journal for Numerical and Analytical Methods in Geomechanics*, 28(78), 2004: 583-607
132. Abdalla KM, Chen WF, Kishi N., Expanded Database of Semi-rigid Steel Connections. *Computers and Structures*, 56(4), 1995: 553-564

References

133. Frye MJ, Morris GA., Analysis of flexibly connected steel frames. *Canadian Journal of Civil Engineers*, 2(4), 1975: 280-291
134. Jones SW, Kirby PA, Nethercot DA., Effect of semi-rigid connections on steel column strength. *Journal of Constructional Steel Research*, 1(1), 1980: 38-46
135. Colson A, Louveau JM., Connections incidence on the inelastic behaviour of steel structures. *Proceedings of the Euromech Colloquium*, October, 1983: 174
136. Kishi N, Chen WF., Moment-rotation relations of semi-rigid connections with angles. *Journal of Structural Engineering*, ASCE, 116(7), 1990: 1813-1834
137. Lui EM, Chen WF., Analysis and behaviour of flexibly jointed frames. *Engineering Structures*, 8(2), 1986: 107-118
138. Wu FS, Chen WF., A design model for semi-rigid connections. *Engineering Structures*, 12(2), 1990: 88-97
139. Richard RM, Abbott BJ., Versatile elastic-plastic stress-strain formula. *Journal of the Engineering Mechanics Division*, ASCE, 101(4), 1975: 511-515
140. Ang KM, Morris GA., Analysis of three-dimensional frame with flexible beam-column connections. *Canadian Journal of Civil Engineering*, 11, 1984: 245-254
141. Weynand K, Jaspart JP, Steenhuis M., The stiffness model of revised Annex J of Eurocode 3. *Connections in Steel Structures III behaviour strength and design*, *Proceedings of the 3rd International workshop on connections*, Trento, Italy, May, 1995: 441-452
142. Wald F, Steenhuis M., The Beam-to-Column Bolted Joint Stiffness according Eurocode 3, in *Proceedings of the State of the Art, Workshop 1992 - COST C1*, Strasbourg, 1993: 503-516
143. Dowling NE. *Mechanical behaviour of materials. Engineering methods for deformation, fracture, and fatigue*, New Jersey: Pearson Education, Inc, 2007.

References

144. Bjorhovde R, Colson A, Brozzetti J., Classification system for beam-to-column connections. *Journal of Structural Engineering, ASCE*, 11, 1990: 3059-3076
145. Sinha BP, Gerstle KH, Tulin LG., Stress-strain relations for concrete under cyclic loading, *ACI Structural Journal*, 61, 1964: 195-211
146. Karsan ID, Jirsa JO., Behavior of concrete under compressive loadings. *Journal of Structural Engineering, ASCE*, 95(12), 1969: 2543-2563
147. Blakely RWG, Park R., Prestressed concrete sections with cyclic flexure. *Journal of Structural Engineering, ASCE*, 99(8), 1973: 1717-1742
148. Darwin D, Pecknold DA., Analysis of cyclic loading of plane R/C structures. *Computer & Structures*, 7(1), 1977: 137-147
149. Yankelevsky DZ, Reinhardt HW., Model for cyclic compressive behaviour of concrete. *Journal of Structural Engineering, ASCE*, 113(2), 1987: 228-240.
150. Mander JB, Priestley MJN, Park R., Theoretical stress-strain model for confined concrete. *Journal of Structural Engineering, ASCE*, 114(8), 1988: 1804-1826.
151. Bahn BY, Hsu CT., Stress-strain behaviour of concrete under cyclic loading. *ACI Materials Journal*, 95(2), 1998: 178-193.
152. Sima J, Climent Molins., Cyclic constitutive model for concrete. *Engineering Structures*, 30(3), 2008: 695-706.
153. De Stefano M, De Luca A, Astaneh A., Modelling of Cyclic Moment-Rotation Response of Double-Angle Connections. *Journal of Structural Engineering, ASCE*, 120(1), 1994: 212-229.
154. Fang LB., The behaviour of SHS and T-stubs under cyclic loading. University of Nottingham, United Kingdom, in partial fulfilment of the requirements for MSC degree. 2010
155. Deng CG, Bursi OS, Zandonini R., A hysteretic connection element and its applications. *Computers and Structures*, 78(1-3), 2000: 93-110
156. ANSYS, Concrete suite-theory manual v12, ANSYS Inc., Canonsburg, 2009.

References

157. Krishnamurthy N, Graddy DE., Correlation between 2D and 3D FE analysis of steel bolted end-plate connections. *Computer & Structures*, (4-5/6), 1976: 381-389.
158. Abolmaali A, Kukreti AR, Murray TM., Finite element analysis of two tension bolt flush endplate connections. Research report No. FSEL/MBMA 84-01, Structural Engineering Laboratory, School of Civil Engineering and Environmental Science, University of Oklahoma, Norman, Oklahoma, 1984.
159. Gebbeken N, Rothert H, Binder B., On the numerical analysis of endplate connections. *Journal of Constructional Steel Research*, 30(1), 1994: 177-C196.
160. Bahaari MR, Sherbourne AN., 3D simulation of bolted connections to unstiffened columns: part 2: extended endplate connections. *Journal of Constructional Steel Research*, 40(3), 1996: 189-C224.
161. Choi CK, Chung GT., Refined three-dimensional finite element model for end-plate connections. *Journal of Structural Engineering*, ASCE, 122(11), 1996: 1307-C1316.
162. Bose B, Wang ZM, Sarkar S., Finite element analysis of unstiffened flush end-plate steel-bolted joints. *Journal of Structural Engineering*, ASCE, 123(12), 1997: 1614-C1621.
163. Bursi OS, Jaspart JP., Basic Issues in the finite element simulation of extended end plate connections. *Computers & Structures*, 69, 1998: 361-382.
164. Sumner EA., Unified design of extended endplate moment connections subject to cyclic loading. Virginia Polytechnic Institute and State University, USA, in partial fulfilment of the requirements for Ph.D. degree. 2003.
165. Shi G, Shi Y, Wang Y, Bradford MA., Numerical simulation of steel pretensioned bolted endplate connections of different types and details. *Engineering Structures*, Vol. 30, No. 1, 2008: 2677-2686.
166. Mazzolani FM., Mathematical Model for Semi-Rigid Joints Under Cyclic Loads, in R. Bjorhovde et al. (eds) *Connections in Steel Structures*:

References

- Behaviour, Strength and Design, Elsevier Applied Science Publishers, London, 1988: 112-120.
167. Chui PPT, Chan SL., Transient response of moment-resistant steel frames with flexible and hysteretic joints. *Journal of Constructional Steel Research*, 39(3), 1996: 221~243.
168. Bernuzzi C., Prediction of the behaviour of top-and-seat cleated steel beam-to-column connections under cyclic reversal loading. *Journal of Earthquake Engineering*, 2(1), 1998: 25-58.
169. Ibarra LF, Medina RA, Krawinkler H., Hysteretic models that incorporate strength and stiffness deterioration. *Earthquake Engineering and Structural Dynamics*, 2005(34): 1489-1511.
170. Chen WF., *Practical Analysis for Semi-Rigid Frame Design*. 2000: World Scientific Publishing Co. Pte. Ltd.

PUBLICATIONS

- Wang ZY, Tizani W, Wang QY. FE analysis of the influence of column axial load on the cyclic behavior of bolted endplate joint. In: Proceedings, ICOSSAR2009, 10th International Conference on Structural Safety and Reliability, Osaka, Japan, September 13-17, 2009, eds. Furuta, Frangopol & Shinozuka, Taylor & Francis Group, London, 2009: 2250-2257, CD.
- Zhiyu Wang. Investigation on moment resisting connection to hollow section - using modified blind bolts. In: Proceedings, YRC2009, 11th Young Researcher's Conference, London, UK, 18th, March, 2009, The Institution of Structural Engineers (IStructE), 2009: 49
- Wang Zhiyu, Tizani Walid. Modelling techniques of composite joints under cyclic loading. In Computing in Civil and Building Engineering, Proceedings of the International Conference, W. TIZANI (Editor), 30 June-2 July, Nottingham, UK, Nottingham, University Press, Paper 254, 2010: 507
- Pitrakkos Theodoros, Tizani Walid, Wang Zhiyu. Pull-out behaviour of anchored blind-bolt: a component based approach . In Computing in Civil and Building Engineering, Proceedings of the International Conference, W. TIZANI (Editor), 30 June-2 July, Nottingham, UK, Nottingham University Press, Paper 255, 2010: 509
- Wang ZY, Tizani W, Wang QY. Strength and initial stiffness of a blind-bolt connection based on the T-stub model, Engineering Structures, 32(9), 2010: 2505-2517.
- Wang ZY, Tizani W, Wang QY. Study on the initial stiffness of blind bolted T-stub connections. In: Proc. 13th. International Symposium on Tubular Structures, HongKong, 2010: 53-61.
- Zhiyu Wang. Assessment of cyclic structural performance of an innovative blind bolted connection to concrete filled steel tubular column. In: Proceedings, YRC2011, 2011 Young Researcher's Conference, London,

UK, 17th, March, 2011, The Institution of Structural Engineers (IStructE),
2011: 62

APPENDIX A Rotation measurements in reported cyclic loading tests

Reference	Connection types	Test description	Joint rotation measurements
Korol (1990)	Extended endplate A490, 25mm diameter bolt	The column stub was rigidly fixed to the testing frame. The deflection at the tips of the beams at first beam yielding were calculated by assuming that the connecting were fully rigid	Dividing deflection at the tips of the beams by the corresponding beam length
Ghobarah (1990)	Extended endplate A490, 25mm diameter bolt	Similar test rig with Korol (1990)	Column flange rotations were recorded for the un-stiffened connection. If these rotations are multiplied by the cantilever length and then a subtraction made from the overall displacement, the resulting displacements are due to a combination of bolt extension and beam & endplate deformations. By recording the rotations of the end-plate relative to the column and multiplying them by the cantilever length, the contribution of the end-plate rotation and bolt extension was determined. What remains will be the elastic and inelastic beam rotation, which could then be separated.
Tsai (1991)	Extended endplate A325 bolt	Similar test rig with Korol (1990)	The joint rotation was mainly contributed by beam rotation. The beam rotations were determined by dividing the cantilever end deflections by the cantilever beam length excluding the elastic effects of beam and column deformations.
Mourad (1995)	Extended endplate HSBB fastener	Similar test rig with Korol (1990)	The joint rotation was mainly contributed by beam rotation. The beam-tip yield displacement is defined as the beam-tip displacement corresponding to the expected beam-tip load which would cause initial yielding in the un-stiffened beam.
Dunai (1996)	Extended endplate SBPR 80/105 bolt	The test concentrates only on the connection zone rather than joint region.	The endplate deformation and the rotation components of the connection are measured by relative displacement measurement devices. The relative displacements are measured between the pertinent points on the edges of the two end-plates.

Table in Appendix A continues

Bernuzzi (1996) . Flush endplate Extended endplate in one/ both sides	The column stub was rigidly fixed to the testing frame. The deflection at the tips of the beams at first beam yielding were calculated by assuming that the connecting were fully rigid	Dividing deflection at the tips of the beams by the corresponding beam length
Adey (2000) Extended endplate A325/A490 bolt	The one batch of the tested samples were designed with endplate significantly weaker than the beam & column and the other were developed to account for plastic moment capacity of the beam. The frames were chosen as horizontal and vertical loading types.	The test results are presented based on the beam end moment versus endplate rotation. The endplate rotation was obtained by subtracting the beam end rotation from the column panel zone rotation.
Yorgun (2001) 16mm diameter & 10.9 grade bolt Extended endplate	The thickness of the panel zone was selected much larger than that of the column web to minimize deformation in the panel zone of the column	The connection rotation was determined by dividing the cantilever beam tip deflection by the cantilever beam length.
Sumner (2001) 32mm diameter bolt (ASTM A490 or ASTM A325) Extended endplate in one side	The reported tests were designed with strong endplate and connecting beam failure. The instrumentation was installed to measure the applied beam rotation and endplate separation.	The total joint rotation is found by dividing the deflection achieved in the last completed cycle by the distance from the load point to the face of the connection, and subtracting the measured rotation of the test column and the measured rigid body motion of the load frame. It is also clear that the primary source of inelastic rotation was the connecting beam.

Table in Appendix A continues

Dubina (2001)	Extended endplate in two side diameter bolt & 10.9 grade bolt	The inelastic deformations were designed to occur in the panel zone, connection, or in the beam. All the moment and rotation were considered at the column face for all configurations.	<p>Anti-symmetrical loading case:</p> $\gamma = \frac{\sqrt{a^2 + b^2} (\delta_5 - \delta_1)}{2ab}$ <p>Panel zone rotation:</p> $\phi_e^{left} = \frac{\delta_5 - \delta_6}{b}, \phi_e^{right} = \frac{\delta_8 - \delta_7}{b}$ <p>Connection rotation:</p> $\phi_{j,i} = \gamma + \phi_e$ <p>Total joint rotation:</p> <p>Symmetrical loading case:</p> $\phi_{j,i} = \frac{1}{L_y} \left(\frac{\delta_1 + \delta_2}{2} - \frac{PL_b^2}{6EI_x} - \frac{PL_b}{2GA_{sb}} \right)$ <p>The last two terms accounts for the elastic rotation of the beam on the length L_b.</p>
Kovács (2004)	Extended endplate 16mm diameter bolt & 8.8 and 10.9 grade bolt	The test programs were performed on endplate type column-base joints to feature different failure modes. The transducer measured the horizontal displacement of loading points.	The rotation is calculated referring the 'joint reference section' which is located at a distance equal to two times the column section height from the endplate.

Table in Appendix A continues

The rotation of the joint is given by following equation:

$$\phi_{\text{joint}} = \phi_{\text{total}} - \phi_{\text{model}} - \phi_{\text{elastic}}$$

It can be obtained from several redundant measurements along the beam, corrected by deducting the elastic rotation of the column and the beam and the rigid body rotations.

$$\begin{aligned} \phi_{\text{total}} &= \tan^{-1} \left(\frac{\delta_{DT20} - \delta_{DT15} - \delta_{DT16}}{L_1} \right) = \tan^{-1} \left(\frac{\delta_{DT11} - \delta_{DT12}}{d_5} \right) \\ &= \tan^{-1} \left(\frac{\delta_{DT1} - \delta_{DT2}}{d_3} \right) + \tan^{-1} \left(\frac{\delta_{DT3} - \delta_{DT4}}{d_4} \right) \end{aligned}$$

The rigid body rotation and the elastic rotation is given by:

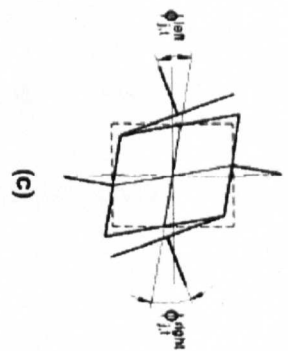
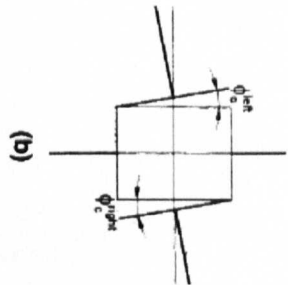
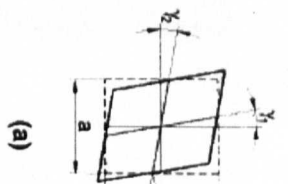
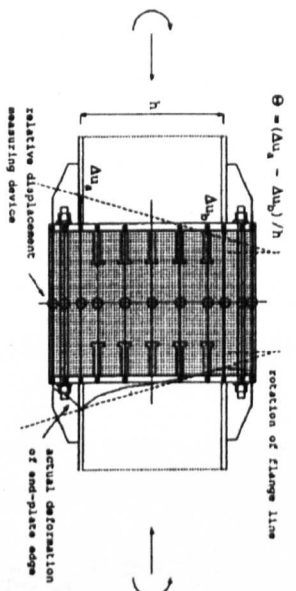
$$\phi_{\text{model}} = \tan^{-1} \left(\frac{\delta_{DT5} - \delta_{DT6}}{d_1} \right), \quad \phi_{\text{elastic}} = \left(Mx - \frac{Fx^2}{2} \right) / EI_b + 0.08898 \frac{ML}{EI_c}$$

The joint rotation is taken including the shearing rotation and endplate gap rotation. d_i is the distance between the centrelines of the beam flanges.

$$\phi_{\text{shearing}} = \frac{\Delta}{d_j}, \quad \phi_{\text{endplate gap}} = \frac{\delta}{d_j}$$

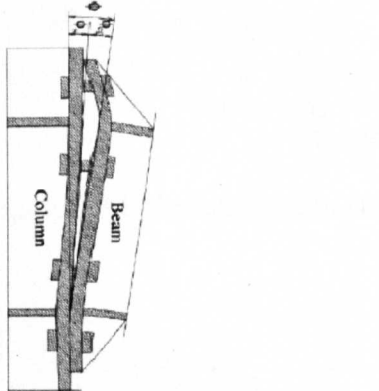
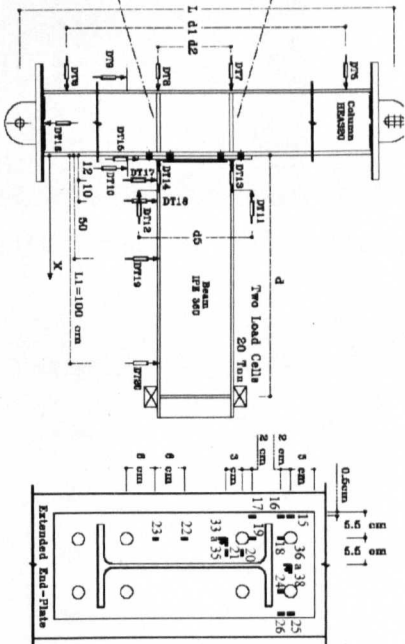
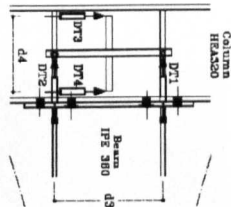
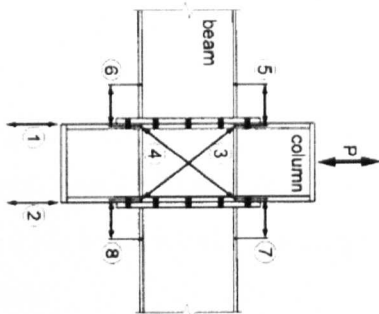
The connection rotations were determined by the difference between the measured beam end rotations and the column rotations.

Shi (2007)	Extended endplate 20/24 mm diameter & 8.8 and 10.9 grade bolt	Eight specimens of endplate joints with various details and welded-plate columns and beams were tested.
Wang (2009)	Flush endplate Lindapter Hollobolt	Four cruciform shape endplate joints to CFT column under symmetrical cyclic loading



Dunai, 1996

Rotation at: (a) Panel zone; (b) Connection; (c) Total joint (Dubina, 2001)



Dubina, 2001

Nogueiro, 2006

Shi, 2007

Figure A1 Illustration of rotation measurements in reports

APPENDIX B Bolt shank tensile test

Bolt shank length: 150mm

Bolt size: M16(Gr 8.8), M16(Gr 10.9)

Test machine: Zwick/Roell 1484 computer controlled universal test machine

Load cell: 200kN

Related codes: BS 5950-1 (2000), BS EN 10210-2 (1997) and BS 4-1 (1993)

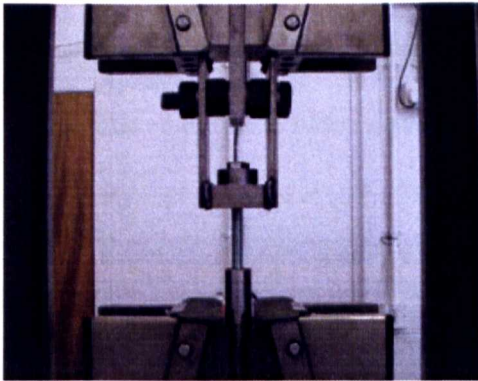


Figure B1 Test set-up



Figure B2 Bolt shank fracture after test

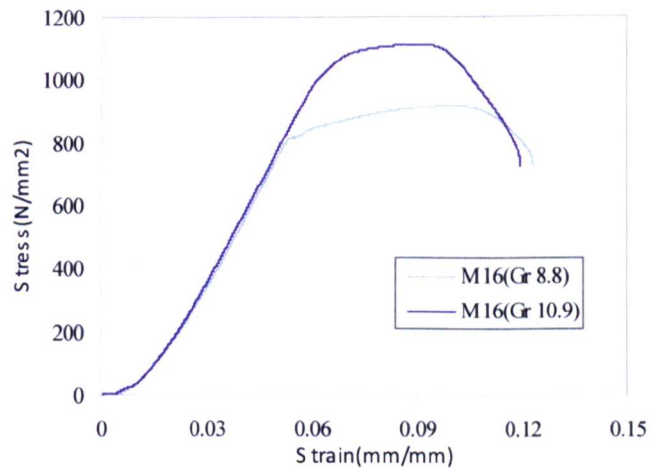


Figure B3 Calculated stress-strain curve of bolt shank

APPENDIX C General yield and failure criteria for finite element analysis

In general, the plasticity theory to predict the inelastic behaviour of metals consists of three main concepts: a yield criterion (predicting the onset of material inelastic response), a plastic flow rule (correlating the plastic strain increments to stress increments under inelastic loading) and a hardening rule (describing the changes of the yield surface due to plastic strains). Although the brittle material is often known for different physical properties, the metal plasticity theory based approaches are often used to model irreversible damage under loads exceeding the elastic limit. The following subsection presents a brief summary of theoretical basis in ANSYS related to the material yield and failure criteria for finite element analysis.

The material yield criteria have been well documented in most solid mechanics books (Kazimi *et al*, 1982; Chen *et al*, 1988). An emphasis herein is given to the von Mises criterion and Drucker-Prager criterion. In the case of multi-axial loading condition, the material yielding is induced by the combination of the stress components, including the hydrostatic pressure and the deviatoric stress. Assuming the yield is independent of the hydrostatic pressure and the solid is isotropic, yield only depend on the second invariants of the deviatoric stress tensor, J_2 , which can be expressed in terms of the principal stresses ($\sigma_1, \sigma_2, \sigma_3$) as:

$$J_2 = \frac{1}{6} [(\sigma_1 - \sigma_2)^2 + (\sigma_1 - \sigma_3)^2 + (\sigma_3 - \sigma_2)^2] \quad \text{Equation C1}$$

or in terms of the stress tensor components ($\sigma_x, \sigma_y, \sigma_z, \tau_{xy}, \tau_{xz}, \tau_{zy}$) as:

$$J_2 = \frac{1}{6}[(\sigma_x - \sigma_y)^2 + (\sigma_x - \sigma_z)^2 + (\sigma_y - \sigma_z)^2] + \tau_{xy}^2 + \tau_{xz}^2 + \tau_{yz}^2 \quad \text{Equation C2}$$

As physical interpretation of the von Mises yield criterion, the yielding begins when the elastic energy of distortion reaches a critical value (Hencky, 1924) and the octahedral shear stress reaches a critical value (Nadai, 1937), corresponding to the maximum distortion strain energy criterion and the maximum octahedral shear stress criterion respectively. The yield equation for the von Mises condition can be expressed in a simple form as:

$$f(J_2) = J_2 - k^2 = 0 \quad \text{Equation C3}$$

where, k is a critical value of the octahedral shear stress, which can be defined as $3^{0.5}$ times lower than the yield stress, σ_e , from uni-axial tension test. The von Mises yield condition can be expressed in a concise manner as follows:

$$(\sigma_1 - \sigma_2)^2 + (\sigma_1 - \sigma_3)^2 + (\sigma_3 - \sigma_2)^2 = 2\sigma_e^2 \quad \text{Equation C4}$$

or

$$(\sigma_x - \sigma_y)^2 + (\sigma_x - \sigma_z)^2 + (\sigma_y - \sigma_z)^2 + 6(\tau_{xy}^2 + \tau_{xz}^2 + \tau_{yz}^2) = 2\sigma_e^2 \quad \text{Equation C5}$$

The use of von Mises yield criteria has been extended to the study of concrete under compressive stresses. As discussed in the book by Chen *et al* (1988), the von Mises yield criteria based one-parameter models are generally used in early finite element analyses. Due to relatively weak tensile capacity of concrete, the criteria are usually supplemented by the maximum principal stress surface or tension cut-off surface. The typical yield surface of von Mises yield criteria is shown in Figure C1.

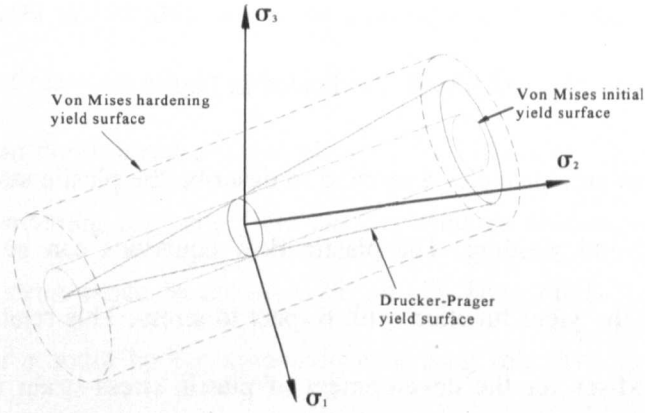


Figure C1 Yield surfaces of von Mises and Drucker-Prager criterion

The Drucker-Prager criterion was developed through a simple modification of the von Mises yield criteria, in which a hydrostatic stress component on failure is considered (Chen *et al.* 1988). This criterion is also known as one of the simplest types of two-parameter pressure-dependent models. This criterion has a good application for concrete. The function of the Drucker-Prager criterion is given as:

$$f(I_1, J_2) = \alpha I_1 + \sqrt{J_2} - k_c = 0 \quad \text{Equation C6}$$

where, I_1 is the second invariants of the deviatoric stress tensor, which can be expressed as ' $\sigma_1 + \sigma_2 + \sigma_3$ '. To feature the outer bound on the Mohr-Coulomb failure surface, the constants, α_c and k_c , can be expressed as:

$$\alpha_c = \frac{2 \sin \phi}{\sqrt{3}(3 - \sin \phi)} \quad \text{Equation C7}$$

$$k_c = \frac{6c \cos \phi}{\sqrt{3}(3 - \sin \phi)} \quad \text{Equation C8}$$

where, ϕ and c are the angle of internal friction and cohesion respectively.

Lubliner *et al.* (1989) suggested ϕ as 32° and c as between 2.8 N/mm^2 to 3.6

N/mm² for concrete. A comparison of yield surfaces of Drucker-Prager criterion with von Mises criterion is indicated in Figure C1.

The plastic flow rule provides a method to describe the plastic strain to stress increments beyond yielding. The plastic flow equations can be derived by differentiating the yield function with respect to stress. This relationship was used by von Mises for the development of plastic stress-strain relations for metal (Chen *et al.* 1988). In ANSYS, the flow rule is given in a simple form, in which the plastic strain increment tensor $\{d\epsilon^{pl}\}$ can be expressed as:

$$\{d\epsilon^{pl}\} = \lambda \left\{ \frac{\partial Q}{\partial \sigma} \right\} \quad \text{Equation C9}$$

where, λ is the plastic multiplier which defines the amount of plastic straining. Q is the function of stress termed the plastic potential which determines the direction of plastic straining.

The hardening rule describes the changes of size and shape of the yield surface with progressive yielding. The most widely used rules include those of isotropic hardening, kinematic hardening, and a combination of both (Chen *et al.*, 1988). The material definition in ANSYS includes the isotropic hardening, and the kinematic hardening rule. For the isotropic hardening rule, the yield surface expands in size which implies an increase for the tension yield stress the same as that for compressive yield stress, as shown in Figure C2. Thus, the isotropic hardening rule ignores the Bauschinger effect, which is described by the fact that metals subjected to an unloading followed by a reloading will exhibit lower yield stress than the original yield stress. The input command 'TB, MISO' is used in ANSYS to allow for the von Mises yield criteria with

associated flow rule and multilinear isotropic hardening rule. The function of the amount of plastic work done can be determined from the equivalent plastic strain, ϵ^{pl} , and the uniaxial stress-strain curve as shown in Figure C4 (a). For kinematic hardening rule, the yield surface remains unchanged in size and translates in stress space, as shown in Figure C3. Thus, the Bauschinger effect is taken into account by the kinematic hardening rule. The input command 'TB, KINH' is used in ANSYS to allow the von Mises yield criteria with the associated flow rule and multilinear kinematic hardening rule. An assumption is made for the material behaviour composed of various subvolumes. All subvolumes are subjected to the same total strain whereas each subvolume exhibits different yield strengths. The portion of total volume and yield stress for each subvolume is obtained by matching the material response to the uniaxial stress-strain curve, as shown in Figure C4 (b). The kinematic hardening rule was adopted in the material definition of steel to allow for the structure subjected to cyclic loading.

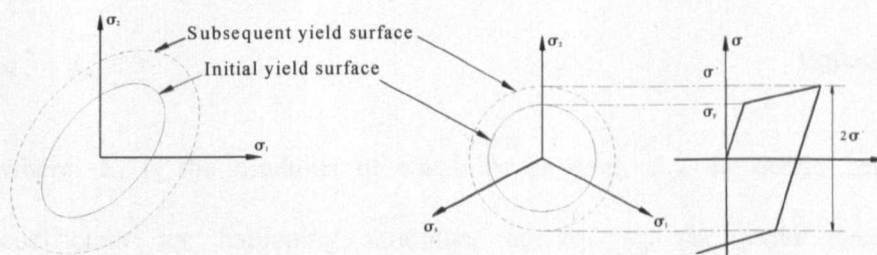


Figure C2 Subsequent yield surfaces for isotropic hardening material

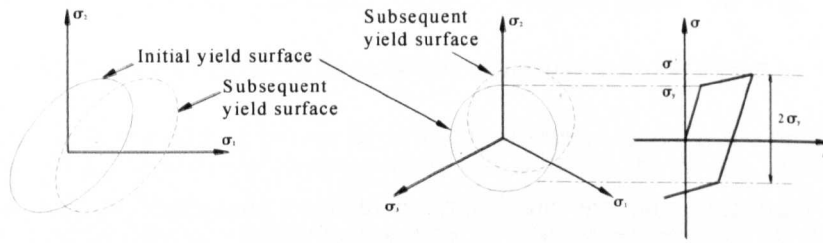
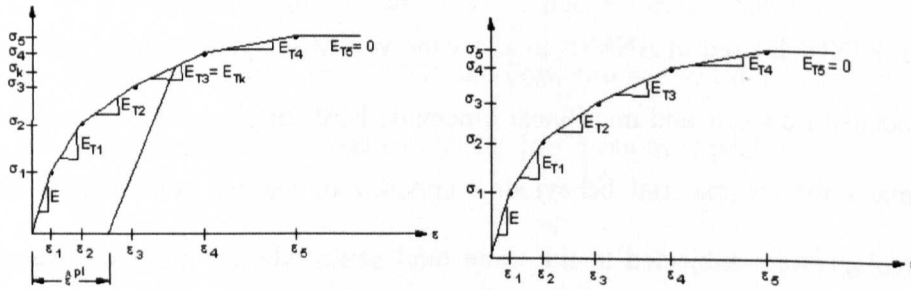


Figure C3 Subsequent yield surface for kinematic hardening material



(a) Multilinear isotropic hardening (b) Multilinear kinematic hardening

Figure C4 Illustration of stress-strain curves for the determination of hardening rule in ANSYS (ANSYS@Academic Research, 2009)

APPENDIX D Cyclic material models of steel and concrete

D1. Material cyclic model of steel

The kinematic hardening model and yield criteria of steel was briefly introduced in sub-Section 6.2.2, the representative stress-strain relationship is described here based on an idealized hysteresis loop with tension and compression excursions as a basis for the cyclic models for connection components.

As shown in D1, unloading and reloading are along a straight line oa or oa' for the strain less or equal to the yield strain ($\epsilon \leq \epsilon_y$). Thereafter, the strain hardening is assumed during the line range of ab or $a'c'$ ($\epsilon > \epsilon_y$). By translating this line to cross the origin of the axis to form a new line od or $d'o$, the residual stress (σ_r^*) and strain (ϵ_r^*) can be obtained at the intersection of this line and related unloading branch (point d or d'). Based on the linear relationship, σ_r^* can be written as:

$$\sigma_r^* = \lambda_{s,h} E_s \epsilon_r^* \quad \text{Equation D1}$$

where, E_s is the modulus of elasticity of steel, $\lambda_{s,h}$ the strain hardening coefficient for hardening modulus, σ_y and ϵ_y the yield stress and corresponding strain respectively.

Besides the previously mentioned Bauschinger effect, the Massing's hypothesis is also taken into account in this kinematic hardening stress-strain relationship as:

$$|\sigma_y^t| + |\sigma_y^c| = 2\sigma_y \quad \text{Equation D2}$$

where, σ_y^t and σ_y^c are the yield stresses for tension and compression loading respectively.

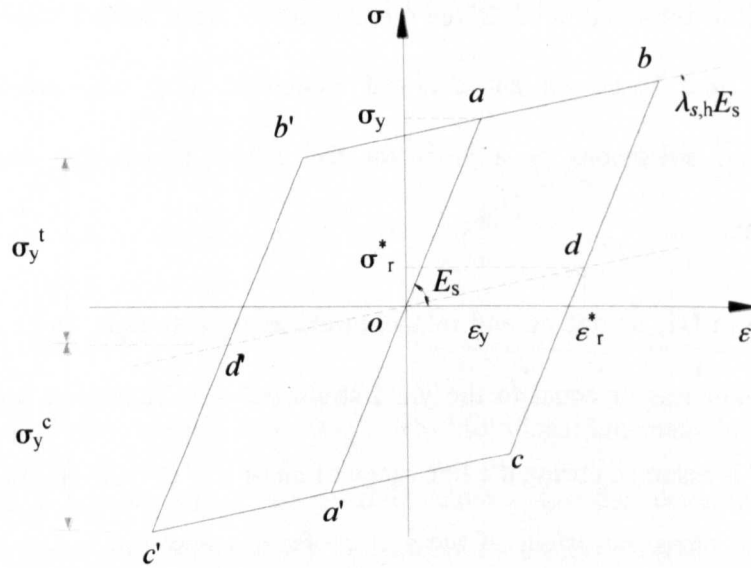


Figure D1 Representative kinematic hardening stress-strain relationship of steel (De Stefano *et al*, 1994)

Unloading prior to σ_r^* , e.g., line bd , the stress-strain relationship is linear and reversible. Given the loading in positive and negative directions, this relationship can be expressed in absolute values form with reloading branch as:

$$|\sigma - \sigma_r^*| = E_s |\varepsilon - \varepsilon_r^*| \quad \text{when } |\varepsilon - \varepsilon_r^*| \leq \varepsilon_y \quad \text{Equation D3}$$

Likewise, the line beyond the yield point can be expressed using points d and d' as reference. The hardening modulus is introduced herein with $\lambda_{s,h}$ and the corresponding relationship in this range can be expressed as:

$$|\sigma - \sigma_r^*| = \sigma_y + \lambda_{s,h} E_s |\varepsilon - \varepsilon_r^* - \varepsilon_y| \quad \text{when } |\varepsilon - \varepsilon_r^*| > \varepsilon_y \quad \text{Equation D4}$$

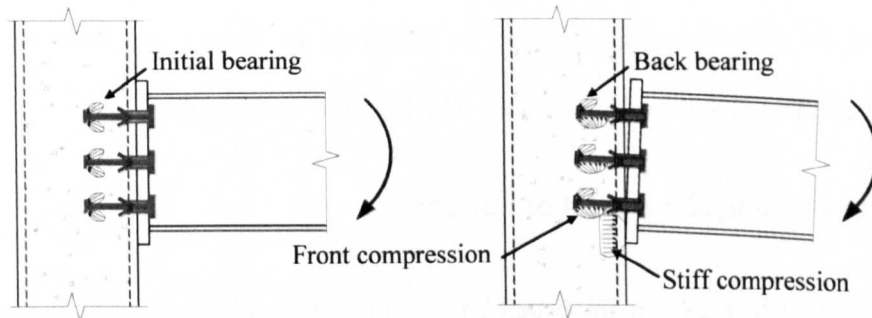
Although an idealized hysteresis loop can be expressed by concise expressions above, its further application may be subjected to change according to the structure details and loading pattern, which will be discussed later.

D2. Material cyclic model of concrete

Concrete infill plays an important role in the rotation behaviour of the joint system subjected to cyclic loading. Through the anchorage and bond interaction between the concrete and the blind bolt, the tensile force from the blind bolt is transferred to the concrete which implies that the concrete is locally compressed. D2 illustrates this concrete compression with respect to two cases of joint rotation. In the case of small joint rotation, the axial tensile force is developed in the blind bolts. The bolt anchorage arises from the anchor nut initially bearing against the associated concrete. As for the compression zone, the tube is assumed to supply sufficient resistance for the compression of the connection.

Whilst large joint rotation takes place, the tube connecting face deforms and the blind bolts inevitably undergo certain rotation in combination with the axial loading. An assumption is made that the concrete infill in contact with the anchor nut and bolt shank is in compression. This effect resists against the separation of these components from concrete infill as the connection is subjected to external loads. The tube in the compression zone is assumed to deform locally which, in turn, compresses the concrete. The compression area

can also be considered with force transferring via a 1 to 1 dispersion through the stiff endplate to the tube connecting face.



(a) Small joint rotation case

(b) Large joint rotation case

Figure D2 Assumed concrete compression with joint rotation

The cyclic stress-strain model of concrete has been investigated by many researchers (Sinha *et al*, 1964; Karsan & Jirsa, 1969; Blakeley & Park, 1973; Yankelevsky & Reinhardt, 1987; Mander *et al*, 1988; Bahn & Hsu, 1998; Sima & Climent-Molins, 2008). It was felt that the general knowledge of loading and unloading relationships of these models could be extended in this study to allow for the contribution of the concrete to the response of the connection.

Based on the uniaxial reversed-cyclic loading tests, simplifications have been made in early concrete models to use similar monotonic stress-strain curves for envelope curves. As shown in D3, the experimental curve reported by Sinha *et al* (1964) illustrates the locus of common points which control the concrete degradation under loading cycles. There are two limits related to common points. The reloading portion of any cycle crosses the unloading portion may be defined as a stability limit. As the loads increase above this

limit and peak stress maintained between cycles, further permanent stain may accumulate. On the other hand, the maximum stress at which a reloading curve intersect the original unloading curve may be taken as common limit. With these two limits, the common point can be adjusted with regard to the envelope curve to control the cycle numbers leading to failure. Besides these common points, Darwin & Pecknold (1977) suggested the locus of turning points which control the energy dissipation, i.e., the lower the turning point, the greater the energy dissipated at a cycle.

A simplified concrete model proposed by Blakeley & Park (1973) is adopted here to form the hysteretic stress-strain curve. As shown in D3, all the loading and unloading branches are plotted by a series of straight lines. If the maximum concrete strain, ϵ , is less than strain corresponding to peak stress (f_c'), ϵ_o , then the unloading and reloading is assumed to take place in linear relationship with a slope equal to the modulus of elasticity, E_c (e.g., straight line ed). This also means that no stiffness deterioration and energy dissipation. The tensile loading is incorporated in this curve from point d to point f if there is no presence of concrete crack, otherwise, the stress will return to point d before a new cycle for compression.

If ϵ is greater than ϵ_o , consecutive stiffness deterioration and energy dissipation is accounted for by the introduction of the reduction factor, λ_f , varying from 0.1 to 0.8 as:

$$\lambda_f = 0.8 - \frac{0.7(\epsilon_{cm} - \epsilon_o)}{\epsilon_{20c} - \epsilon_o} \geq 0.1$$

Equation D5

where, ϵ_{cm} and ϵ_{20c} are the unloading strain on the envelope curve and the strain at which stress drops to $0.2f'_c$, respectively.

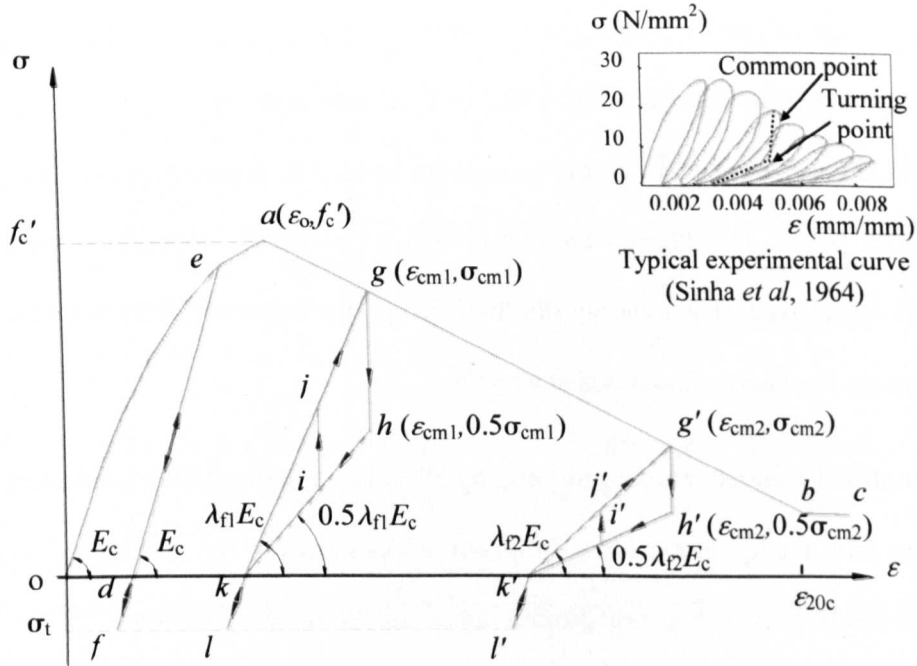


Figure D3 Representative stress-strain relationship for cyclic behaviour of concrete (Blakeley & Park, 1973)

The unloading branch is idealized as a bilinear path. From the point on the envelope curve such as point g , it is assumed that 50% stress (i.e., $0.5\sigma_{cm1}$) is reduced to the point h without decrease of strain. The subsequent path extends with a slope of $0.5\lambda_{f1}E_c$, to point k which is determined graphically. Likewise, if the concrete has not cracked, the tensile stress may develop to point l with a slope of E_c . The reloading is assumed to follow the path kg with slope $\lambda_{f1}E_c$ back to the envelope curve. The case of the reloading occurring prior to unloading attaining zero stress is permitted by following the path of ij instead of kh , and the overall path is $ghij$. This relationship continues until the concrete stress drops to $0.2f'_c$, i.e., point b . Although this relationship is simple

Appendix D Cyclic material models of steel and concrete

in expression, its good applicability not only for concrete but also for the case with adding effect of steel or reinforcement which was also reported in the literature.